Search for $\pi^o \rightarrow$ *invisible* decays with the NA62 experiment

DISSERTATION
ZUR ERLANGUNG DES GRADES

"Doktor der Naturwissenschaften"

AM FACHBEREICH PHYSIK, MATHEMATIK UND INFORMATIK
DER
JOHANNES GUTENBERG-UNIVERSITÄT
IN MAINZ

Letizia Peruzzo
GEBOREN IN BIELLA, ITALIEN
MAINZ, JULI 2020

1. Berichterstatter:
2. Berichterstatter:
Datum der mündlichen Prüfung: 12 März 2021

Preface

The measurement presented in this thesis has been published in a peer-reviewed journal:

"Search for π^0 decays to invisible particles" JHEP 02 (2021) 201

available also as arXiv:2010.07644.

The author of this thesis is one of the two main authors and the main person responsible for the analysis work of the above publication. The work has been carried out by the author within the NA62 collaboration, which is an international collaboration of more than 350 scientists and engineers from 31 institutes in 15 countries. A more technical and detail description of the analysis procedure is available to the NA62 collaboration as internal note.

Abstract

Letizia PERUZZO

Search for $\pi^o \to$ invisible decays with the NA62 experiment

The search for new physics beyond the Standard Model is one of the most active fields in particle physics. Complementary to direct searches for new processes at high-energy scale, $\mathcal{O}(\text{TeV})$, rare or forbidden Standard Model decays are investigated to look for deviations from the predictions. The NA62 experiment at the CERN SPS, designed for the measurement of the ultra-rare decay $K^+ \to \pi^+\nu\bar{\nu}$, investigates new-physics contributions in the kaon and pion sector.

The highly efficient, hermetic photon-veto system makes NA62 a perfect apparatus for a high-sensitivity search for π^o decays into invisible particles. In a fraction of data collected by NA62 in 2017, about 8.4×10^9 π^o mesons have been tagged by the reconstruction of the second most-abundant K^+ decay, $K^+ \to \pi^+\pi^o(\gamma)$. The background rejection inefficiency for visible π^o decays, ranging from $\mathcal{O}(10^{-8})$ to $\mathcal{O}(10^{-9})$, is estimated by the combination of single-photon detection efficiencies measured in data and Monte Carlo simulations of $K^+ \to \pi^+\pi^o(\gamma)$ decays, a novel experimental technique with respect to that used in the most sensitive previous experimental result.

The analysis is performed with the blind technique for a cut-based signal region. The π^+ momentum range is optimized to have the best sensitivity for the estimated upper limit on the $\pi^o \to$ *invisible* branching ratio in absence of a signal. In the signal region with π^+ momentum between 25 and 40 GeV/c, a total of about 4×10^9 tagged π^o mesons are collected out of which 12 events survive the signal selection criteria. Given an estimated rejection inefficiency of $(2.8^{+5.9}_{-2.1}) \times 10^{-9}$, no signal is observed beyond the expected background fluctuations. The resulting upper limit on the branching ratio is

$$\text{BR}(\pi^o \to \textit{invisible}) \leq 4.4 \times 10^{-9}$$

at 90% confidence level, which improves on the previous best limit by a factor of 60. As a by-product of the analysis, the decay $K^+ \to \pi^+ X$ is investigated, where X is a neutral particle escaping detection with a mass in the range 109–155 MeV/c^2. Model-dependent scenarios are investigated with the assumption that X is an axion-like particle with dominant fermion couplings or a dark scalar with mixing with the Standard Model Higgs.

Zusammenfassung

Letizia PERUZZO

Suche nach dem Zerfall $\pi^o \rightarrow$ invisible mit dem NA62-Experiment

Die Suche nach neuer Physik jenseits des Standardmodells ist eine der wichtigsten Aufgaben der Teilchenphysik. Ergänzend und komplementär zur direkten Suche nach neuen Prozessen bei Energien der TeV-Skala können seltene oder verbotene Zerfälle untersucht werden, um Abweichungen von der Standardmodell-Vorhersage zu finden. Das NA62 Experiment am CERN-SPS, konzipiert und gebaut für die Messung des sehr seltenen Zerfalls $K^+ \rightarrow \pi^+ \nu\bar{\nu}$, sucht allgemein nach neuer Physik in Kaon- und Pion-Zerfällen.

Durch das hermetische und hoch-effiziente Photonvetosystem kann NA62 u.a. nach π^o-Zerfällen in nicht sichtbare Teilchen suchen. Die vorliegende Arbeit analysiert von NA62 im Jahr 2017 aufgezeichnete Daten, in denen 8.4×10^9 π^o-Mesonen des zweithäufigsten Kaonzerfalls $K^+ \rightarrow \pi^+\pi^o(\gamma)$ über die Messung der beteiligten K^+- und π^+-Mesonen indirekt rekonstruiert wurden. Der Untergrund aus π^o-Zerfällen in sichtbare, aber nicht detektierte Teilchen wird zu $\mathcal{O}(10^{-8})$ bis $\mathcal{O}(10^{-9})$ abgeschätzt, indem die Effizienzen für den Nachweis von einzelnen Photonen in den Daten gemessen und mit Monte-Carlo-Simulationen von $K^+ \rightarrow \pi^+\pi^o(\gamma)$-Zerfällen kombiniert werden. Dies ist eine neue Technik im Vergleich zu früheren Experimenten.

In der Analyse wird die durch diverse Selektionskriterien definierte Signalregion ausgeblendet. Der π^+-Impulsbereich ist so gewählt, um — bei Abwesenheit eines Signals — das beste erwartete Limit auf das Verzweigungsverhältnis von $\pi^o \rightarrow$ *invisible* zu erhalten. In der Signalregion mit einem π^+-Impuls zwischen 25 und 40 GeV/c werden in 4×10^9 $K^+ \rightarrow \pi^+\pi^o$-Zerfällen insgesamt 12 Kandidaten des Zerfalls $\pi^o \rightarrow$ *invisible* gefunden, die alle Selektionskriterien überlebt haben. Bei einer abgeschätzten Untergrundunterdrückung von $(2.8^{+5.9}_{-2.1}) \times 10^{-9}$ sind die Ereignisse in Übereinstimmung mit dem erwarteten Untergrund. Die gemessene obere Grenze auf das Verzweigungsverhältnis ist

$$\mathrm{BR}(\pi^o \rightarrow \mathit{invisible}) \leq 4.4 \times 10^{-9}$$

bei einem Konfidenzniveau von 90% und liegt einen Faktor 60 unter dem bisherigen besten Limit. Ein Nebenprodukt der Messung ist die Suche nach dem Zerfall $K^+ \rightarrow \pi^+ X$ mit einem nicht beobachteten, neutralen Teilchen X mit einer Masse zwischen 109 MeV/c^2 und 155 MeV/c^2. Unter der Annahme, dass X entweder ein axion-ähnliches Teilchen mit fermionischen Kopplungen oder ein skalares, mit dem Higgsboson mischendes Teilchen ist, werden stringente Grenzen auf die entsprechenden Kopplungen gesetzt.

Contents

Introduction

The Standard Model (SM) of particle physics is a very successful theory providing a mathematically elegant and consistent description of nature as well as precise predictions. However, there are nowadays many evidences of its incompleteness, the neutrino masses, the existence of dark matter and energy, the predominance of matter over antimatter are just a few examples which suggest that the SM would be an effective theory as part of a more general framework which manifests itself at a higher energy scale. In this perspective, over the last decades, many theories have been developed to extend the SM and look for new-physics processes. The neutral pion, which has historically played an important role in our understanding of the dynamics of elementary particles, presents itself as a promising field for the search of physics processes beyond the SM. One of the most interesting processes is the decay $\pi^o \to \mathit{invisible}$, historically connected to the study of neutrino properties, evidence for this decay would be a clear sign of new physics.

The search for the $\pi^o \to \mathit{invisible}$ decay presented in this work is carried out within NA62, a fixed-target experiment at the CERN SPS, with the use of the $K^+ \to \pi^+\pi^o(\gamma)$ process as tagged source for the neutral pion. The experiment began physics data taking in September 2016 in order to search for new-physics effects in kaon decays by measuring the branching ratio of the rare decay $K^+ \to \pi^+\nu\bar{\nu}$ with a precision of about 10%. The NA62 apparatus was intrinsically built for a high-sensitivity search for π^o decays into *invisible* (undetectable) particles, seen as a natural by-product of the search for the decay $K^+ \to \pi^+\nu\bar{\nu}$. In fact, the suppression of the main K^+ decays, which have branching fractions several orders of magnitude higher than the $K^+ \to \pi^+\nu\bar{\nu}$ signal, is crucial for the success of NA62. In particular, the background from $K^+ \to \pi^+\pi^o(\gamma)$ (the second most abundant kaon decay with a branching ratio of about 21%) has to be suppressed by a factor 10^{12} by exploiting both the precise reconstruction of the kinematics, $\mathcal{O}(10^4)$, and the detection of the π^o decay products, $\mathcal{O}(10^8)$. A detailed understanding of the π^o rejection performances is hence mandatory to perform the main analysis of the experiment.

The thesis is organized as follows. The theoretical framework of the SM is presented in Chapter 1 with focus on the physics motivations for the search for $\pi^o \to \mathit{invisible}$ decays described in Chapter 2. Part I of the thesis is mainly dedicated to introduce the NA62 experiment, with a brief introduction to the long tradition of kaon experiments given in Chapter 3. The NA62 physics program is presented in Chapter 4, the beam and the experimental apparatus in Chapter 5 and Chapter 6, respectively. The software framework adopted in the search for $\pi^o \to \mathit{invisible}$ decays is described in Chapter 7. The data taking conditions used in the run period 2016–2018 (also referred to as NA62 Run I) are described in Chapter 8.

The search for $\pi^o \to invisible$ decays is reported in Part II of this thesis. The strategy of the analysis is presented in Chapter 9. The selection of $K^+ \to \pi^+\pi^o(\gamma)$ events is contained in Chapter 10, while the algorithm for detection of additional activity from visible π^o decays is given in Chapter 11. It is important to underline that the signature for $K^+ \to \pi^+\pi^o$ with $\pi^o \to invisible$ is the same as that for a $K^+ \to \pi^+\nu\bar{\nu}$ decay. In this respect, the selection applied to this analysis directly follows the criteria applied for the search for $K^+ \to \pi^+\nu\bar{\nu}$ decays with 2016 data [1, 2]. The two analyses are performed with the data collected with the same trigger stream (the $\pi\nu\bar{\nu}$ trigger), the efficiency of which is discussed in Chapter 12. The study of the single-photon efficiencies, with the so-called "Tag&Probe" method, and the evaluation of the expected π^o rejection are explained in Chapter 13 and 14, respectively. The background estimation is presented in Chapter 15 and the statistical treatment of the data is described in Chapter 16. Chapter 17 contains the validation of the adopted method after the analysis of the sideband regions. The expected results for the signal region are detailed in Chapter 18 together with the comparison with the previous most sensitive search. Chapter 19 summaries the results obtained. Conclusions are presented in Chapter 20.

Chapter 1
The Standard Model of Particle Physics

Years of theories and discoveries have led to a remarkable knowledge of the fundamental structure of matter: everything in our universe is made from a few basic blocks, the fundamental particles, governed by four fundamental forces. The Standard Model of particle physics (SM), as a result of those theories and discoveries, describes our knowledge of how the fundamental particles and three of the forces (*electromagnetic*, *weak* and *strong*) are related. [1] The first milestone in the formulation of the SM, as known nowadays, is dated to 1960 with the unification of the electromagnetic and weak interaction in the *Electroweak theory* by S. Glashow. Seven years later, S. Weinberg and A. Salam incorporated into Glashow theory the mechanism proposed in 1964 by P. Higgs to give mass to the elementary particles: the *Higgs mechanism*. In the 1970s the theory of strong interaction acquired its modern form: experimental observations confirmed that protons and neutrons are composed by smaller fundamental particles, which become quasi free as the energy scale at which they are observed increases.

The SM is a *gauge quantum field theory*, renormalizable and mathematically self-consistent, containing the internal symmetry of the unitary product group

$$\mathrm{SU}(3)_\mathrm{C} \times \mathrm{SU}(2)_\mathrm{L} \times \mathrm{U}(1)_\mathrm{Y} \tag{1.1}$$

where $\mathrm{SU}(3)_\mathrm{C}$ represents the symmetry structure of the strong interaction, $\mathrm{SU}(2)_\mathrm{L}$ the weak isospin symmetry and $\mathrm{U}(1)_\mathrm{Y}$ the weak hypercharge symmetry. The symmetry of Equation (1.1) is spontaneously broken at an energy scale of $\approx$ 100 GeV (the electroweak energy scale), thus providing mass to the elementary particles through the coupling with the Higgs field. Only the $\mathrm{SU}(3)_\mathrm{C} \times \mathrm{U}(1)_\mathrm{Q}$ symmetry remains unbroken, where $\mathrm{U}(1)_\mathrm{Q}$ is the symmetry group of the electromagnetic interaction. A review of the SM can be found in References [3, 4].

The basic blocks of matter consist of 61 elementary particles: 48 fermions, 12 gauge bosons and the Higgs boson. Fermions are particles of half-integer spin that, according to the spin-statistics theorem, follow the Pauli exclusion principle. Elementary fermions, *leptons* and *quarks*, have spin $S = 1/2$ and are divided into three families (see Table 1.1). All the known stable matter in the universe is built by the lightest and most stable fermions (the *electron*, the *up* and the *down quarks*) which compose the first family. The heaviest and less stable fermions belong to the second and third generations. Additionally, for each family the lepton sector is completed by a corresponding neutrino type. Fermions interact in different ways. All of them couple with the weak interaction. The charged leptons (e, μ and

[1] Only *gravity*, the fourth fundamental force, is not included.

τ) and the six quark types (u, d, c, s, t and b) are also affected by the electromagnetic force, which does not couple with the three neutrinos (ν_e, ν_μ and ν_τ) as they do not have electromagnetic charge. Quarks can also couple with the strong interaction, since they carry an additional quantum number, the *color charge*, and manifest themselves in three different colors: red, green and blue. Each of the 24 fermions has a corresponding antiparticle with opposite electromagnetic charge and quantum numbers.

	First Family	Second Family	Third Family	Electric charge
Leptons	e^- electron (m=0.511 MeV/c^2)	μ^- muon (m=105.7 MeV/c^2)	τ^- tau (m=1.777 GeV/c^2)	-1
	ν_e electron-neutrino (m<2 eV/c^2)	ν_μ muon-neutrino (m<0.19 MeV/c^2)	ν_τ tau-neutrino (m<18.2 MeV/c^2)	0
Quarks	u up (m≈2.2 MeV/c^2)	c charm (m≈1.3 GeV/c^2)	t top (m≈173 GeV/c^2)	$+2/3$
	d down (m≈4.7 MeV/c^2)	s strange (m≈93 MeV/c^2)	b bottom (m≈4.2 GeV/c^2)	$-1/3$

TABLE 1.1: Fermions in the SM. Mass values are taken from Reference [5].

Bosons are particles with integer spin. The elementary bosons have spin $S = 1$, the *gauge bosons*, and spin $S = 0$, the *Higgs boson*. Gauge bosons (see Table 1.2) are the force carriers that mediate the electromagnetic (*photons*), strong (*gluons*) and weak (W and Z) interactions: these forces are explained by the exchange of gauge bosons among matter particles. Due to the non-abelian [2] structure of the symmetry groups SU(3) and SU(2), the interaction between gauge bosons is also possible. This means that gluons couple with other gluons, $W^\pm$ and Z couple with themselves and also with photons.

Force	Bosons	Number	Electric charge	Mass [GeV/c^2]
Electromagnetic	γ	1	0	–
Weak	$W^\pm$ Z	3	±1 0	80.4 91.2
Strong	g	8	0	–

TABLE 1.2: Gauge bosons in the SM. Mass values are taken from Reference [5].

The Higgs boson is the visible manifestation of the Higgs scalar field, which itself is a complex doublet of SU(2). Due to the particular shape of the field potential (the so-called "Mexican hat"), a spontaneous breaking of the electroweak symmetry SU(2) × U(1)

[2] The internal operation of the group is not commutative.

occurs. In this mechanism of spontaneous symmetry breaking, three components of the SU(2) doublet are absorbed by the gauge bosons of the weak interaction ($W^{\pm}$ and Z) which acquire mass. The remaining electrically neutral component, which corresponds to the vacuum expectation of the field, results to be non-zero and manifests itself as the Higgs boson. This implies that all fermions, which interact via Yukawa coupling with the Higgs field, acquire mass. Photons, gluons and neutrinos [3] that do not interact with the Higgs field, remain massless. The mass values of the elementary particles are therefore connected to how strongly each particle couples to the Higgs field. However, these values are not predicted by the theory and can only be measured experimentally.

A solid model ...

The architecture of the SM has been confirmed over the years by several discoveries such as the existence of the $W^{\pm}$ and Z bosons [6, 7], the *gluons* [8], and the *charm* [9, 10], *bottom* [11] and *top* [12, 13] quarks. The agreement between theoretical predictions and experimental measurements of the quantum numbers of these particles gives validity to the model. As last piece, on July 2012, the discovery of a Higgs-like particle in the mass region around 125 GeV/c^2 was announced [14, 15]. The following tests of its properties confirmed that this new particle is consistent with the Higgs boson [16], predicted in the SM and sought for about forty years.

... with some leaks

Despite the SM is our best description of the subatomic world, there are opened questions which are still not yet answered: *which is the origin of the observed matter-antimatter asymmetry?*, *why are the mass values of the elementary particles so different?* and *what about the remaining 96% of yet unknown matter/energy of the universe?* are just a few hints that new physics must be present. In addition, the SM includes only three of the fundamental forces of the universe: gravity, the most familiar force, is excluded and any attempt of adding it into the SM framework so far was unsuccessful.

Forefront experiments, looking for discrepancies between observations and SM predictions, are carried out to search for new-physics processes, allowing to go further in the understanding of the mechanisms of the universe. Although so far, new physics does not reveal itself with direct searches at the high-energy frontier at $\mathcal{O}$(TeV), it can be complementary looked for at lower energy with high-intensity experiments which search for very rare processes. This is the case of the NA62 experiment with both the precise measurement of the branching ratio of the rare kaon decay $K^+ \to \pi^+ \nu\bar{\nu}$, as main goal of the experiment (see Section 4.1), and the search for $\pi^o \to$ *invisible* decays, the subject of this work.

[3] In the SM, neutrinos are considered massless particles. However, the evidence of neutrinos oscillation suggests that the flavor neutrinos (ν_e, ν_μ and ν_τ) are a combination of three neutrino-mass eigenstates and therefore neutrinos have a discrete mass. The three mass values are smaller than the other fermions masses, but still unknown.

Chapter 2
The $\pi^o \to invisible$ Decay

The history of the neutral pion dates back to 1935, when the existence of a massive neutral scalar particle coupling both to protons and neutrons was postulated in order to describe the nuclear forces [17]. The first hint of the existence of such a particle [18, 19] was connected to the observation of mixed cosmic-ray showers, where γ-rays were observed together with a meson shower. The emitted γ-rays were interpreted as the decay products of a new neutral particle, produced in the interaction of high-energy protons with the atmosphere [20]. The discovery of the new particle was confirmed in 1950 [21]: protons with an energy of approximately 290 MeV were made to interact in a nuclear target and the emission of photons with an energy of about 70 MeV was observed. This was interpreted as due to the existence of a neutral meson, called *neutral pion* (π^o), which decays into two photons and with a mass about 300 times the electron.

The decay modes of the lightest unflavored meson have been the subject of many searches in past and present experiments, with improvements of QED and QCD [1] predictions and tests of new-physics scenarios beyond the SM [22]. Following Reference [23], different rare and forbidden decays of the neutral pion can be investigated in NA62. Among them, one of the most interesting is given by $\pi^o \to invisible$ events. Historically, the interest on this decay was related to the study of neutrino properties such as the mass, the helicity and the number of families [24, 25], where the invisible final state is represented by a neutrino-antineutrino pair. At present, more than determining neutrino properties, the interest moves to new-physics scenarios which the invisible final state can open. In this case, any observation of this decay would be a sign of new physics.

2.1 Connection with the neutrino mass: $\pi^o \to \nu\bar{\nu}$

In the SM, neutrinos are considered purely left-handed [2] massless particles and the decay of a π^o into a neutrino-antineutrino pair is forbidden by angular momentum conservation: the two outgoing neutrinos have opposite chirality and the total angular momentum should be equal to one in the π^o rest frame. Therefore, the pseudoscalar meson cannot decay into a $\nu\bar{\nu}$ pair. However, the observation of neutrino oscillations demonstrated non-zero masses of the neutrinos, and therefore neutrinos can be left-handed or right-handed. As a consequence, the $\pi^o \to \nu\bar{\nu}$ decay can occur within the weak interaction via a Z-boson exchange as shown in the Feynman diagrams of Figure 2.1. Assuming a mass for the neutrino below half of the π^o mass, the branching ratio (BR in the following) for a single

[1] *Quantum Electro-Dynamics* (QED) and *Quantum Chromo-Dynamics* (QCD) are the theories of the electromagnetic and strong interactions, respectively.

[2] Neutrinos have always negative chirality in the weak interaction.

neutrino type is [24–26]:[3]

$$\mathrm{BR}(\pi^o \to \nu\bar{\nu}) = 3.8 \times 10^{-8} \left(\frac{m_\nu}{m_{\pi^o}}\right)^2 \sqrt{1 - 4\left(\frac{m_\nu}{m_{\pi^o}}\right)^2} \tag{2.1}$$

where m_ν is the neutrino mass and $m_{\pi^o} \simeq 135\ \mathrm{MeV}/c^2$ the neutral pion mass. The branching ratio has a maximum value of $\mathrm{BR}(\pi^o \to \nu\bar{\nu}) = 3 \times 10^{-9}$ at $m_\nu = 55\ \mathrm{MeV}/c^2$.

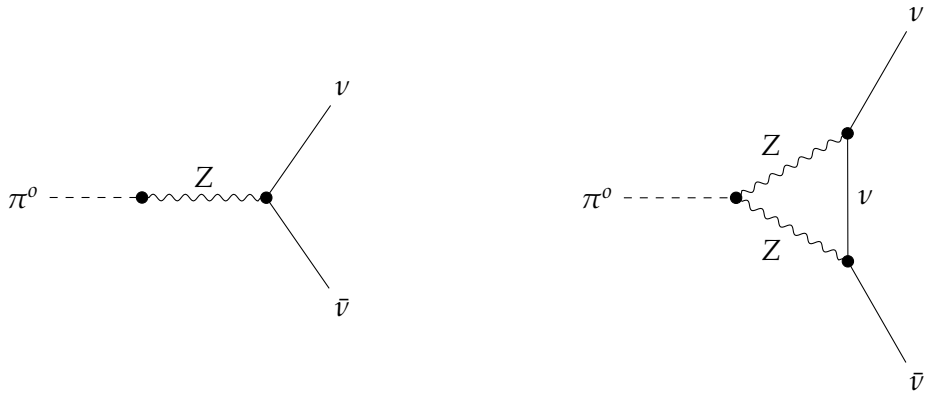

FIGURE 2.1: Feynman diagrams for the process $\pi^o \to \nu\bar{\nu}$. Forbidden in the SM due to angular momentum conservation, the decay is possible for massive neutrinos via the exchange of a Z boson.

As pointed out in Equation (2.1), the branching ratio for $\pi^o \to \nu\bar{\nu}$ decays is closely connected to the neutrino mass. Constraints on the mass of the neutrino can be directly interpreted as constraints on the branching ratio and *vice versa*. The experimental direct limit on the tau neutrino mass ($m_{\nu_\tau} < 18.2\ \mathrm{MeV}/c^2$ at 95% confidence level) from the ALEPH experiment [28] would correspond to a theoretical upper limit of $\mathrm{BR}(\pi^o \to \nu_\tau\bar{\nu}_\tau) < 5 \times 10^{-10}$ at 90% confidence level. [4] However, a more stringent limit is set by cosmological constraints on the sum of neutrino masses $\sum m_\nu < 1\ \mathrm{eV}/c^2$ [5], which implies $\mathrm{BR}(\pi^o \to \nu\bar{\nu}) < 10^{-24}$, far from the present and future experimental sensitivity to observation.

The decay $\pi^o \to \nu\bar{\nu}$ has astrophysical relevance. It has been largely studied in the process of neutrino emission in stellar cooling at the temperature of the pion mass through the pion-pole mechanism $\gamma\gamma \to \pi^o \to \nu\bar{\nu}$ [29–32]. In this condition, the pion propagator can be modified by the presence of a dense baryonic medium [33, 34] with conditions similar to the primordial universe and the $\pi^o \to \nu\bar{\nu}$ decay can occur even if neutrinos are massless particles.

[3] Equation (2.1) represents the branching ratio for a single type Dirac neutrino. In case of a Majorana nature (particle and antiparticle are identical) the branching ratio is a factor of two larger to account for the identical particles in the final state [27].

[4] From direct experimental limits on the electron and muon neutrino mass the theoretical branching ratio would be several orders of magnitude smaller.

2.2 New-physics searches: $\pi^o \to invisible$

The search for the $\pi^o \to \nu\bar{\nu}$ decay can be easily interpreted as a search for $\pi^o \to invisible$, where *invisible* stays for any undetectable final state produced by different processes beyond SM physics. These include for example the study of helicity-flipping (chirality-changing) pseudoscalar interactions, lepton flavor-violating transitions $\pi^o \to \nu_1\bar{\nu}_2$ with two different neutrino flavors in the final state, and any new processes involving feebly-interacting long-lived particles. Any observation of $\pi^o \to invisible$ at the present sensitivity achievable would mean that new physics has been found.

2.3 Present experimental limit

In order to perform a search for $\pi^o \to invisible$ decays, one needs to select a pure sample of π^o mesons. A possible approach to tag a pure π^o "beam" (first proposed in Reference [35]) is to use the decay chain $K^+ \to \pi^+\pi^o$. This, historically, implied a close connection with experiments dedicated to measure the branching ratio of the rare decay $K^+ \to \pi^+\nu\bar{\nu}$ [36–39], where a highly efficient detection of $\pi^o \to \gamma\gamma$ decays is crucial to suppress background contributions from the second most abundant kaon decay, $\mathrm{BR}(K^+ \to \pi^+\pi^o) = 20.67(8)\%$ [5]. Two recent examples are the experiments E787 [40] and its successor E949 [41] at the Brookhaven National Laboratory (BNL), which measured the branching ratio of $K^+ \to \pi^+\nu\bar{\nu}$ and set limits on $\pi^o \to invisible$ decays.

The most stringent present experimental limit on the $\pi^o \to invisible$ branching ratio was established by the E949 experiment [41]. The $K^+ \to \pi^+\pi^o$ and $\pi^o \to invisible$ decay chain was investigated with a decay-at-rest technique for the kaon. The $\pi^o \to invisible$ events were searched for from a sample of tagged 205 MeV/c π^o mesons, selected solely by the use of the charged pion kinematics and the requirement of no additional activity other than that due to the K^+ and π^+ particles. Potential non-$K^+ \to \pi^+\pi^o$ events were identified as $K^+ \to \mu^+\nu_\mu$ decays and scattered beam pions, for a total of 3 background events. After all of the analysis conditions were applied, 99 events were observed. The signal sample was probably dominated by $\pi^o \to \gamma\gamma$ decays with both photons undetected, but since this background contribution was not estimated *a priori*, all of the 99 events were conservatively considered as $\pi^o \to invisible$ candidates. [5] The following formula was used to set the upper limit on the branching ratio:

$$\mathrm{BR}(\pi^o \to invisible) = \frac{N_\mathrm{s}}{N_{\pi^o}} \times \frac{1}{C_{dis}\, C_{acc}} \tag{2.2}$$

with N_s the number of signal events; N_{π^o} the total number of tagged π^o mesons given the selection of $K^+ \to \pi^+\pi^o$ events; C_{dis} and C_{acc} corrections due to mis-reconstruction of the π^+ and to signal losses due to accidental activity, respectively. The number of signal

[5] A different analysis technique is used in this thesis and a comparison with that of the E949 experiment is given in Section 18.2.

events was evaluated with the Poisson statistics, given 99 observed events and 3 background events. In total about 3×10^9 π^o mesons were collected and the resulting upper limit at 90% confidence level is [41]:

$$\mathrm{BR}(\pi^o \to invisible) < 2.7 \times 10^{-7}. \tag{2.3}$$

2.4 Extension to new-physics searches in $K^+ \to \pi^+ X$ decay

In the past years direct searches for new physics have been performed at always increasing energy scales. However, so far there has not been any clear evidence of new processes, leading to an increased interest for scenarios where new physics lies at or below the electroweak energy scale and is only feebly interacting with the SM particles (often referred to as *hidden sector*). The interaction between the SM and the hidden sector may proceed in different ways through new mediators, represented as gauge-invariant operators, that can be light and long-lived and seen as possible Dark Matter candidates. Given the feeble coupling with the SM particles, the new-physics searches are performed at high-intensity experiments and rare and forbidden processes represent golden channels for such searches.

Rare meson decays, such as $K^{\pm} \to \pi^{\pm} + X$ and $B^{(*)} \to K^{(*)} + X$, are a good framework to search for new-physics processes beyond the SM. These decays proceed through *Flavor-Changing Neutral Current* (FCNC) processes, $s \to d$ and $b \to s$ respectively, and the presence of new mediators X emerging in the loops would modify and most probably enhance the decay rate with respect to the SM predictions. These processes are discussed for example in References [42–46].

In the work described in this thesis, two new-physics scenarios are considered in the decay channel $K^+ \to \pi^+ X$: a search for axion-like particles (ALPs) with dominant fermion coupling as presented in References [42, 43] and for dark scalars with mixing with the SM Higgs as presented in Reference [43]. The X particle is considered to decay to an invisible final state in the experimental apparatus or to escape detection being feebly interacting and long-lived, with a mass around the π^o mass.
The decay width for the process $K^+ \to \pi^+ X$ is [42, 47]:

$$\Gamma(K^+ \to \pi^+ X) = \frac{1}{16\pi\, m_{K^+}^3} \times \lambda^{1/2}\left(m_{K^+}^2, m_{\pi^+}^2, m_X^2\right) \times \left(\frac{m_{K^+}^2 - m_{\pi^+}^2}{m_s - m_d}\right)^2 \times |h_{ds}^S|^2 \tag{2.4}$$

where $\lambda(a,b,c) = (a-b-c)^2 - 4\,bc$, and h_{ds}^S is a complex parameter representing the effective coupling for the $s \to d$ transitions. [6] It is important to underline that Equation (2.4) is independent from any model of new-physics search, only the effective coupling contained in the parameter h_{ds}^S is model dependent.

[6] For completeness, Equation (2.4) should be multiplied by a form factor $|f_0^{K^+}(m_X^2)|^2$, which is neglected since its value is close to 1 [27].

2.4.1 Axion portal

Axion particles were introduced in 1977 as a solution of the so-called *strong CP problem*, namely the observation that in the strong interactions the violation of the CP symmetry [7], even if theoretically allowed, does not seem to manifest itself. The solution proposed by R. Peccei and H. Quinn [48] was to add an additional $U(1)$ symmetry group to the QCD Lagrangian. The potential of the field associated to the new $U(1)_{PQ}$ group spontaneously breaks the symmetry and the non-zero vacuum expectation value cancels the non-CP conserving term of the QCD Lagrangian. A new particle, called *Axion*, was associated with the $U(1)_{PQ}$ field [49, 50]. Although QCD axions are excluded by strong constraints, the QCD-axion model can be generalized and a large variety of axion-like particles (ALPs), in the following denoted as a, can be postulated and looked for. [8] ALPs appear as well-motivated candidates to extend the SM particle field: either as direct Dark Matter candidates or as mediators between Dark Matter and SM particles. Their interactions with SM particles can arise through different scenarios [42, 43, 51], for example involving ALP-photon and/or ALP-fermion couplings. In particular, the ALP coupling to quarks can induce a mixing between ALP and neutral pion (or η meson) with the result that any process involving a π^o meson could generate an axion as well. [9]

Following the model presented in Reference [42], ALPs can be produced in FCNC kaon and B-meson decays. The interaction between the pseudoscalar mediator a and the SM fermions f is of the form:

$$\mathcal{L}_{\text{SM}} = \sum_{f=q,\ell,\nu} i g_f \, a \, \bar{f} \gamma^5 f \tag{2.5}$$

where g_f is the effective coupling. Different scenarios are considered for the coupling structure to charged fermions, g_f in Equation (2.5), while the coupling to neutrinos g_ν is assumed to be zero:

- *Yukawa-like*: the interactions between the ALP a and the charged SM fermions arise from a mixing with the Higgs boson and the couplings are proportional to the Yukawa couplings, g_Y: $g_f = \sqrt{2} g_Y m_f / v$, where m_f is the fermion mass and $v \simeq 246$ GeV is the vacuum expectation value of the SM Higgs field. [10]
- *Quark universal*: the ALP a has a universal coupling only with quarks, $g_f \equiv g_q$. In this case, coupling structures other than those involved by the minimal flavor violation of the Yukawa-like type would be expected.
- *Quark third generation*: the ALP a interacts only with quarks of the third family and the coupling g_Q is assumed equal for b and t quarks.

[7] *Charge conjugation* and *Parity symmetry*, which changes a particle in its antiparticle (C symmetry) and inverts the spatial coordinates creating a mirror system (P symmetry).

[8] QCD axions are connected with an exact global $U(1)$ symmetry and their mass is fixed given the coupling strength ($ma \propto 1/f_a$), while ALPs are more generally referred to accidental global $U(1)$ symmetries and they do not have a fix relation between mass and coupling strength.

[9] ALPs have the same quantum numbers of the π^o mesons, being pseudoscalar particles.

[10] As a derivation of this model, *Quark-Yukawa-like* couplings, where the coupling is non-zero only for quarks, are also considered.

Figure 2.2 shows the excluded regions in the space of the coupling as a function of the ALP mass m_a, for Yukawa-like, Quark-universal and Quark-third-generation coupling scenarios, for an invisibly decaying a produced in K and B decays as considered in Reference [42].

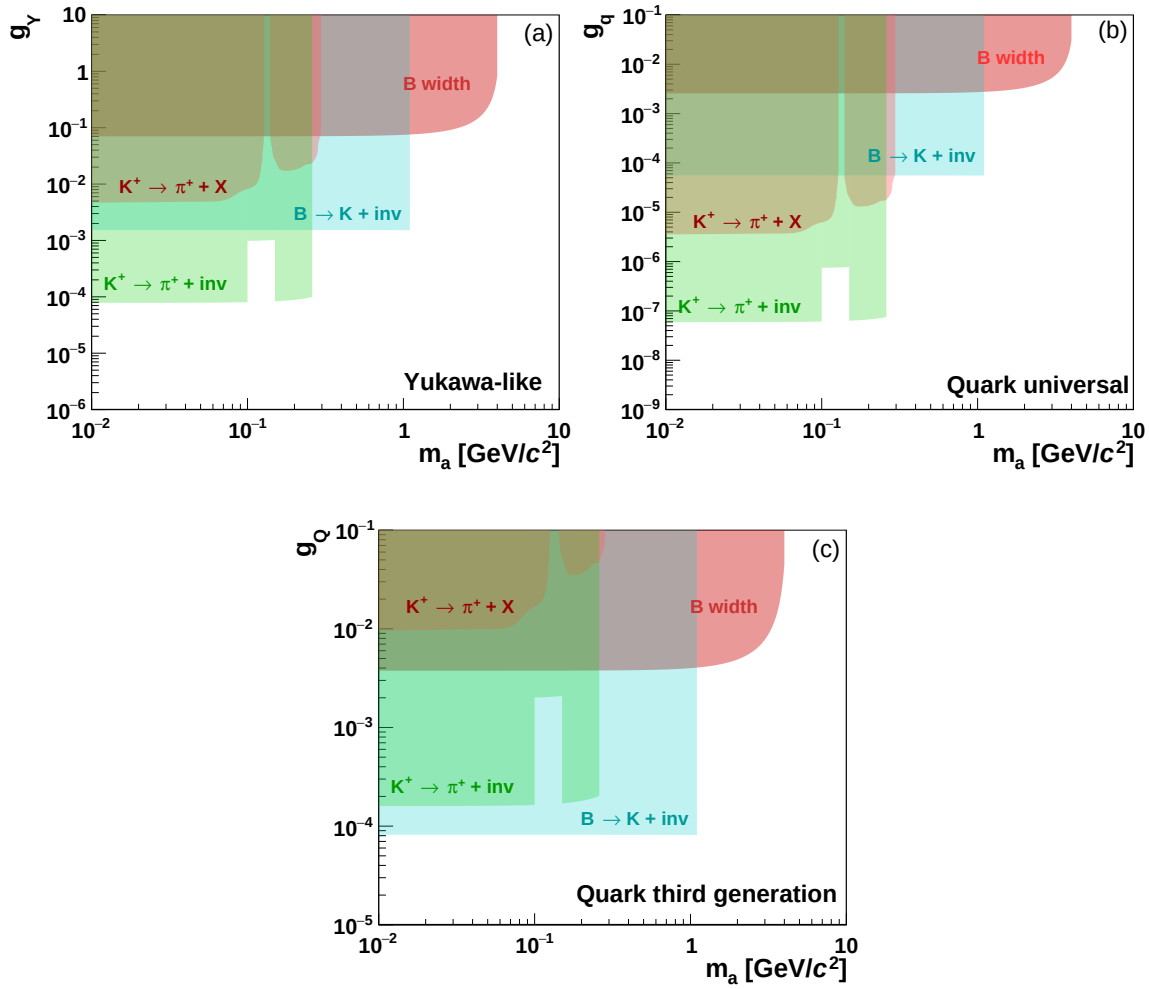

FIGURE 2.2: Excluded parameter regions for an invisibly decaying pseudoscalar a produced in FCNC decays of K and B mesons. The contributions from $K^+ \rightarrow \pi^+ + invisible$ (E949 experiment [41, 52, 53]), $K^+ \rightarrow \pi^+ X$ ($K_{\mu 2}$ experiment [54]), $B \rightarrow K + invisible$ (CLEO experiment [55]) and the B width measurement (PDG [5]) are shown. Three different coupling scenarios are considered as explained in the text: (a) Yukawa-like; (b) Quark universal; (c) Quark third generation. Picture reproduced from Reference [42].

In the corresponding axion portal model with fermion dominance of Reference [43], denoted as *BC10*, the axion-fermion interaction is of the form:

$$\mathcal{L}_{\text{SM}} = \frac{\partial_\mu a}{f_\ell} \sum_\alpha \bar{\ell}_\alpha \gamma_\mu \gamma_5 \ell_\alpha + \frac{\partial_\mu a}{f_q} \sum_\beta \bar{q}_\beta \gamma_\mu \gamma_5 q_\beta \tag{2.6}$$

where ℓ and q represent the charged leptons and quarks, respectively; f represents the

coupling strength and for simplicity it is assumed $f_q = f_\ell$. In this case, only the Yukawa-like scenario is considered with $g_Y = \frac{2v}{f_q}$. [11] The expressions of Equations (2.5) and (2.6) are equivalent at tree-level, but the two approaches differ at loop level, which plays a role in the FCNC processes. Figure 2.3 shows the excluded regions in the space of the coupling as a function of the ALP mass m_a, for a produced in K and B decays as considered in Reference [43].

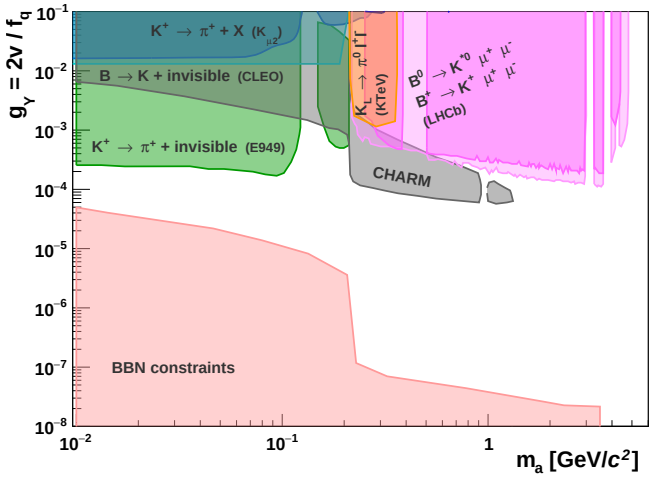

FIGURE 2.3: Search for an axion-like particle a according to the *BC10* model of Reference [43]. The contributions from $K^+ \to \pi^+ + invisible$ (E949 experiment [52, 53]), $K^+ \to \pi^+ X$ ($K_{\mu 2}$ experiment [54]), $B \to K + invisible$ (CLEO experiment [55]), the search for visible a decays (CHARM experiment [56]), $K_L \to \pi^o \ell^+ \ell^-$ (KTeV experiment [57]), $B \to K^{(*)} \mu^+ \mu^-$ decays (LHCb experiment [58–60]) and constraints from the Big Bang nucleosynthesis are shown. Picture reproduced from Reference [43].

2.4.2 Dark scalar portal

The discovery of the Higgs boson in 2012 [14, 15] confirmed the existence of a fundamental scalar particle. Lots of efforts, both from the theoretical and experimental point of view, have been made to extent the scalar sector of the SM and new additional light Higgs-like particles have been postulated and looked for. The light dark scalar particles are considered as mediators between SM and Dark Matter particles and may themselves be Dark Matter candidates allowing to answer some still open questions. The scalar fields do not couple directly to quarks and leptons but their interaction arise through the mixing with the SM Higgs boson. The minimal extension of the SM scalar sector [61] introduces one extra singlet field S, which is not associated to any particular gauge symmetry (i.e. it does not have any gauge quantum numbers) and two couplings μ and λ are added:

$$\mathcal{L}_{\text{scalar}} = -(\mu S + \lambda S^2) H^\dagger H \tag{2.7}$$

where μ leads to the S-Higgs mixing and λ to the coupling of the Higgs boson to a pair of S particles. In Reference [43] two scenarios are considered for the S couplings. The minimal

[11] Note that the definition of g_Y adopted in Equation (2.6) [43] differs by a factor $\sqrt{2}$ with respect to that defined in the Yukawa-like scenario of Reference [42].

scenario (denoted as *BC4*) assumes for simplicity that $\lambda = 0$ and all production and decay processes of the dark scalars are controlled by the same parameter $\mu = \sin\theta$, where θ is the S-Higgs mixing angle. For small values of the mixing angle, this can be written as [43]

$$\theta = \frac{\mu\, v}{m_h^2 - m_S^2} \tag{2.8}$$

where v is the vacuum expectation value of the Higgs field, and m_h and m_S the masses of SM Higgs and dark scalar, respectively. A more general approach (*BC5* model) consists in having both λ and μ being different from zero, and the λ coupling dominates the dark scalar production. Since FCNC transitions at loop level can induce the production of dark scalar particles, the scalar sector can be investigated in kaon and B-mesons decays such as $K \rightarrow \pi\, S$ and $B^{(*)} \rightarrow K^{(*)} S$ [44, 45] and similarly in case of S pair production [62]. The *BC4* model is investigated in this work within the search of light dark scalars production in the channel $K^+ \rightarrow \pi^+ S$. Figure 2.4 shows the excluded regions in the space of the coupling as a function of the dark scalar mass m_S, for S produced in K and B decays as considered in Reference [43].

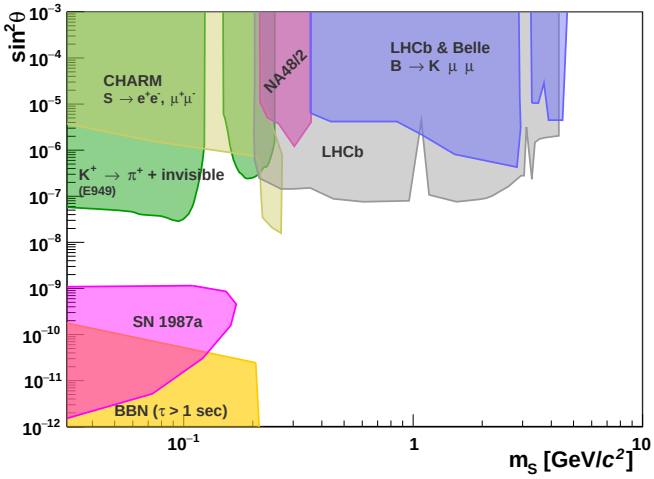

FIGURE 2.4: Search for a dark scalar S according to the *BC4* model of Reference [43]. The contributions form $K^+ \rightarrow \pi^+ + invisible$ (E949 experiment [63]), the search for visible S decays (CHARM experiment [56, 64]), $K \rightarrow \pi\mu\mu$ (NA48/2 experiment [65]), $B \rightarrow K\mu\mu$ (LHCb [59, 60] and Belle [66] experiments), astrophysical constraints (SN1987a [67–70]) and constraints from the Big Bang nucleosynthesis are shown. Picture reproduced from Reference [43].

Part I

THE NA62 EXPERIMENT

Chapter 3
Kaon Experiments

Kaons have played a fundamental role in our understanding of particle physics. With their discovery in cosmic rays in 1947 [71] a new quantum number, the *strangeness*, was introduced. Within the quark model (proposed in 1965 by M. Gell-Mann [72]), the strangeness was interpreted as the existence of a new fundamental particle: the *strange* quark (s). The peculiarity of this new quantum number is that, while it is conserved in strong and electromagnetic interactions, it is not conserved in processes involving the weak force. This observation led to the idea by N. Cabibbo in 1963 [73], that in weak interaction processes the u quark couples with a mixture of down-type quarks (only d and s quark were known at that time) proportional to the *Cabibbo mixing angle*. In 1970 S. Glashow, J. Iliopoulos and L. Maiani [74] suggested the presence of a forth quark (*charm*), extending the concept of the Cabibbo angle to a 2×2 matrix: the *Cabibbo Matrix*. Kaon mesons were also the central actors in improving our understanding of the *Charge conjugation* and *Parity* (CP) symmetry. In 1964, studies on the decays of neutral kaons led to the discovery of the CP violation in weak interactions [75]. In order to explain this observation, a third quark family was introduced by M. Kobayashi and T. Maskawa (1973), arriving to the current formulation of the *Cabibbo-Kobayashi-Maskawa* (CKM) matrix [76].

Nowadays kaons are important to search for new-physics effects in rare and forbidden SM processes. These searches are complementary to the hunting for new processes performed in high-energy experiments, and are carried out at the high-intensity frontier. Currently two kaon experiments (also referred to as *Kaon Factories*) are collecting data: the NA62 experiment at CERN and the KOTO [77] experiment at J-PARC (Japan). A new experiment, KLEVER [78], has been proposed at CERN for 2024. A review of the state of art of both theoretical and experimental studies in the kaon sector can be found in Reference [79].

The NA62 experiment is the latest in a series of fixed-target experiments located in the North Area of the CERN [1] *Super Proton Synchrotron* (SPS) facility, dedicated to explore the kaon sector. The tradition began in 1980s with the NA31 experiment [80]. The neutral kaon sector was investigated in order to detect direct CP violation, by measuring the relative decay rates of K_L and K_S (the long- and short-lived neutral kaons) into pairs of neutral and charged pion final states ($\pi^o\pi^o$ and $\pi^+\pi^-$, respectively). This parameter, called ε'/ε ratio, was known to be small but expected different from zero in the SM and represents the relative strength of direct CP violation with respect to the indirect CP violation. The measurement performed in 1988 by NA31, led to the first observation of direct CP violation. However, at the same time, the experiment E731 at Fermilab reported a measurement

[1] CERN is the acronym of the french name *Conseil Européen pour la Recherche Nucléaire* (European Council for Nuclear Research), founded in 1954 on the French-Swiss border near Geneva.

consistent with zero and therefore a new measurement with better precision was needed. A new experiment, NA48 [81], was therefore proposed at CERN in 1990 to measure with higher accuracy the ε'/ε ratio and quantify the presence of direct CP violation. About 10 years later the first observation from NA31, the NA48 experiment confirmed the presence of direct CP violation [82]. The second phase of the experiment (2003–2004), called NA48/2, was dedicated to study the charged kaon sector [83]. In 2006 the successor experiment, NA62, was proposed [84] in order to measure the ultra-rare kaon decay $K^+ \to \pi^+\nu\bar{\nu}$. In its first phase (2007–2008) the experiment benefited of the beam and detector of NA48/2 and studied lepton flavor universality in the decays $K^\pm \to \ell^\pm\nu$ ($\ell = e, \mu$) [85]. NA62, with a new apparatus, has started to collect physics data in 2016 with the aim to precisely measure the $K^+ \to \pi^+\nu\bar{\nu}$ branching ratio, looking for deviations from the SM prediction and, therefore, indirectly searching for new physics. The experiment successfully completed its first data taking period in 2016–2018 (NA62 Run I) and will continue in 2021 after the long shutdown of the CERN accelerator system.

Chapter 4
The NA62 Physics Program

A broad physics program is available in NA62 with the focus on new-physics searches. The main goal of NA62 is the measurement of the rare decay $K^+ \to \pi^+\nu\bar{\nu}$ for which the entire experimental apparatus is optimized. A description of this decay channel is given in Section 4.1, while the combined analysis of 2016 and 2017 data with the corresponding results is presented in Section 4.2.

In parallel to the measurement of the $K^+ \to \pi^+\nu\bar{\nu}$ branching ratio, the flavor physics sector is also explored to search for lepton flavor (LFV) and lepton number (LNV) violation processes in rare and forbidden kaon and pion decays. An example is the search for lepton number violation in the decay $K^+ \to \pi^-\ell^+\ell^+$ ($\ell = e, \mu$) [86]. Complementary new-physics searches are carried out with the study of the so-called hidden sector, where long-lived particles in the MeV/c^2 – GeV/c^2 mass range feebly coupled with SM particles are looked for. Examples are the search for heavy neutral leptons [87] and dark photons [88].

Table 4.1 lists some of the searches currently in progress with the data collected in the data taking period 2016–2018 (referred to as NA62 Run I).

Physics case	**Decay mode**
Rare and forbidden kaon decays	$K^+ \to \pi^+\nu\bar{\nu}$ [89]
	$K^+ \to \pi^-\ell^+\ell^+$ [86], $K^+ \to \pi^+\ell^+\ell^-$ ($\ell = e,\ \mu$)
	$K^+ \to \pi\mu e$
	$K^+ \to e^\pm\nu\ell^+\ell^\mp$, $K^+ \to \mu^\pm\nu\ell^+\ell^\mp$ ($\ell = e,\ \mu$)
	$K^+ \to \ell^+\nu\gamma$ ($\ell = e,\ \mu$)
	$K^+ \to \pi^+\gamma\gamma$
Rare π^o decays	$\pi^o \to e^+e^-$, $\pi^o \to \gamma e^+e^-$
	$\pi^o \to \gamma\nu\bar{\nu}$ [88]
	$\pi^o \to$ *invisible* [This work]
Hidden sector searches:	
Heavy neutral leptons N	$K^+ \to \ell^+N$ ($\ell = e, \mu$) [87, 90]
Dark photon A'	$K^+ \to \pi^+\pi^o$, $\pi^o \to \gamma A'$ [88]
Dark scalar S	$K^+ \to \pi^+S$, $S \to \mu^+\mu^-$
Axion-like particle a	$a \to \gamma\gamma$ (dump mode)

TABLE 4.1: Examples of currently on-going NA62 analyses with the data collected in the run period 2016–2018. Searches for new-physics processes are focused in rare and forbidden kaon and pion decays, as well as in the hidden sector.

4.1 The golden channel $K^+ \to \pi^+ \nu\bar{\nu}$

The $K^+ \to \pi^+ \nu\bar{\nu}$ decay proceeds through a flavor-changing neutral current (FCNC) process with the coupling of an s quark with a d quark and a neutrino/antineutrino pair. Since the change of flavor within a neutral current is forbidden at tree level, the process occurs at loop level with box and penguins diagrams as shown in Figure 4.1.

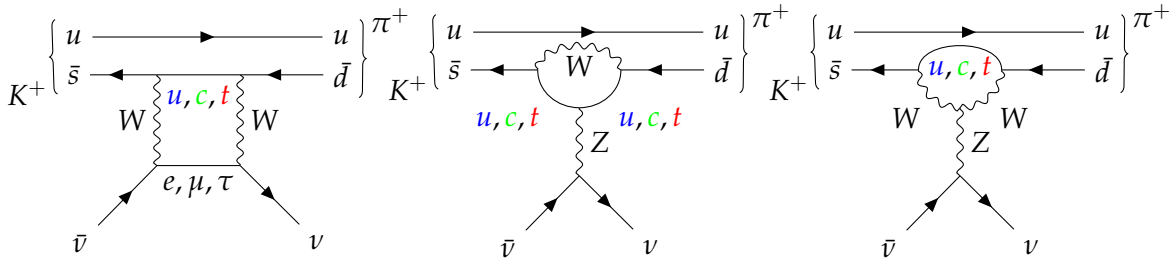

FIGURE 4.1: Feynman diagrams of the process $K^+ \to \pi^+ \nu\bar{\nu}$.

The loops are dominated by the *top* quark with a small contribution of *charm*. The presence of the CKM matrix element $|V_{td}|$ in one vertex of the loops makes the decay extremely suppressed and therefore rare. However, it is theoretically very precisely predicted in the SM [91] to

$$\mathrm{BR}_{\mathrm{SM}}(K^+ \to \pi^+ \nu\bar{\nu}) = (0.84 \pm 0.10) \times 10^{-10} \tag{4.1}$$

with the inclusion of next-to leading order QCD and electroweak corrections, and with hadronic contributions obtained via isospin rotation from those very well measured in the semi-leptonic decay $K^+ \to \pi^o \ell^+ \nu_\ell$ ($\ell = \mu, e$) [92]. The major uncertainties come from the actual precision with which the CKM parameters used in the branching ratio calculation are known. Together with the neutral decay $K_L \to \pi^o \nu\bar{\nu}$, new constraints can be set on the CKM parameters completing analogous studies performed in the B-meson sector. Several new-physics models predict significant deviations of the $K^+ \to \pi^+ \nu\bar{\nu}$ branching ratio with respect to the SM expectation, due to the contribution of new particles involved in the process, making the decay sensitive to physics beyond the SM [93–100].

The actual experimental measurement comes from the combined data of the E787 and E949 experiments at BNL [52, 101]. With the use of a decay-at-rest technique, they observed in total 7 events obtaining a branching ratio of

$$\mathrm{BR}(K^+ \to \pi^+ \nu\bar{\nu}) = \left(1.73^{+1.15}_{-1.05}\right) \times 10^{-10}. \tag{4.2}$$

NA62 aims to improve this result and to measure the $K^+ \to \pi^+ \nu\bar{\nu}$ branching ratio with 10% accuracy using a decay-in-flight technique.

4.2 First NA62 results on $K^+ \to \pi^+\nu\bar{\nu}$

Analysis principle Given the topology of $K^+ \to \pi^+\nu\bar{\nu}$ events (one incoming kaon, one charged pion in the final state and nothing else), the squared missing mass parameter, defined as

$$M^2_{\text{miss}} = (P_{K^+} - P_{\pi^+})^2 \tag{4.3}$$

where P_{K^+} and P_{π^+} are the kaon and pion 4-momenta, respectively, allows to kinematically select the desired events by defining two signal regions (so-called *Region 1* and *Region 2*) on the left and right side of the $K^+ \to \pi^+\pi^o$ peak as shown in Figure 4.2.

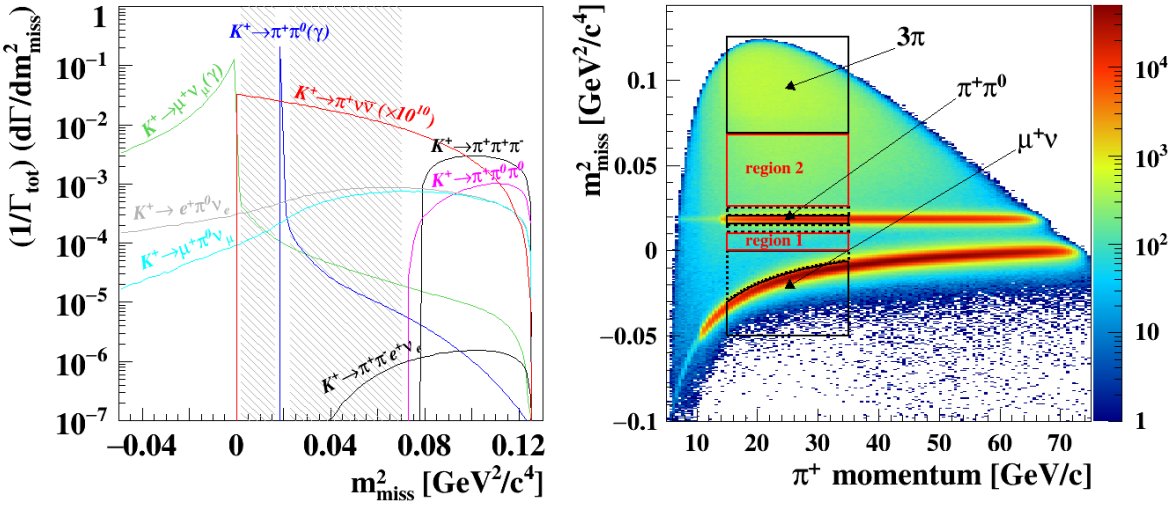

FIGURE 4.2: ***Left:*** True M^2_{miss} distribution of $K^+ \to \pi^+\nu\bar{\nu}$ events and the main K^+ decays. For the latter M^2_{miss} is computed under the π^+ mass hypothesis. The $K^+ \to \pi^+\nu\bar{\nu}$ signal (red line) is multiplied by a factor 10^{10} for visibility. The dashed grey areas show the two signal search regions, so-called *Region 1* and *Region 2*, on the left and right side of the $K^+ \to \pi^+\pi^o$ peak, respectively. ***Right:*** Reconstructed M^2_{miss} distribution as a function of the charged pion momentum from minimum bias data, without applying particle identification and photon rejection. The $K^+ \to \pi^+\nu\bar{\nu}$ signal search regions are showed together with those of the main kaon decays $K^+ \to \mu^+\nu_\mu$, $K^+ \to \pi^+\pi^o$ and $K^+ \to \pi^+\pi^+\pi^-/\pi^+\pi^o\pi^o$. Both panels are taken from Reference [89].

Since the expected branching ratio is several orders of magnitude lower than the usual kaon decays (e.g. $\text{BR}(K^+ \to \mu^+\nu_\mu) \simeq 63\%$ and $\text{BR}(K^+ \to \pi^+\pi^o) \simeq 21\%$), a good π/μ separation together with a strong π^o suppression is required on top of the kinematic selection. The analysis is performed in the π^+ momentum region 15–35 GeV/c leaving at least 40 GeV of energy in the final state in addition to the π^+. This condition allows to further improve the suppression of background such as $K^+ \to \pi^+\pi^o$ and $K^+ \to \mu^+\nu_\mu$, ensuring the presence of a high energy π^o and a better pion/muon separation, respectively.

Results About 1.2×10^{11} and 2×10^{12} kaons decays have been analyzed in the data collected in 2016 [89] and 2017 [102], respectively. From the combined data the Single Event Sensitivity, the ratio between the SM branching ratio and the number of expected

$K^+ \to \pi^+\nu\bar{\nu}$ events ($N^{\rm exp}_{\pi\nu\bar{\nu}}$),

$$\text{S.E.S} = \frac{\text{BR}_{\text{SM}}(K^+ \to \pi^+\nu\bar{\nu})}{N^{\rm exp}_{\pi\nu\bar{\nu}}} \tag{4.4}$$

has been determined to be $(0.346 \pm 0.017) \times 10^{-10}$ [102]. The estimated number of background events has been evaluated to be 1.65 ± 0.31, dominated by pileup events due to beam activity. After the unblinding of the two signal regions three events have been observed as shown in Figure 4.3: one in 2016 and two in 2017 data, respectively. Using the CL_s statistical method [103] the 90% confidence level upper limit on the branching ratio has been computed to be [102]

$$\text{BR}(K^+ \to \pi^+\nu\bar{\nu}) < 1.85 \times 10^{-10}\,. \tag{4.5}$$

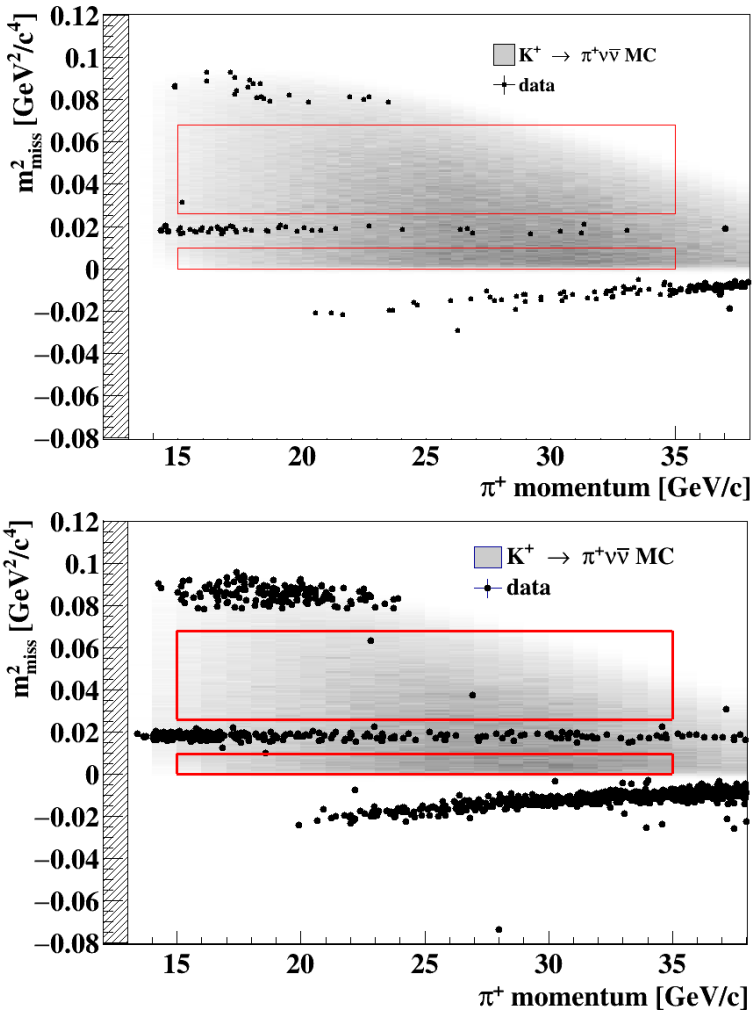

FIGURE 4.3: Reconstructed $M^2_{\rm miss}$ distribution as a function of the π^+ momentum for events (black markers) satisfying the $K^+ \to \pi^+\nu\bar{\nu}$ selection in 2016 [89] (***top***) and 2017 [102] (***bottom***) data, respectively. The grey area corresponds to the expected distribution of $K^+ \to \pi^+\nu\bar{\nu}$ simulated Monte Carlo events. The signal search regions are delimited by the red counters. Three events have been observed after the unblinding of the $K^+ \to \pi^+\nu\bar{\nu}$ signal regions: one in 2016 and two in 2017 data, respectively.

Chapter 5
The Beam

NA62 benefits of the high-energy proton beam of the *Super Proton Synchrotron* (SPS) accelerator, from which a secondary kaon beam is obtained. Since the kaon production cross section increases with the energy, a high-energy beam allows to reduce the non-kaon-related accidental background. As a disadvantage, pions and protons cannot be efficiently separated from the kaon component at beam level. Starting from the SPS proton beam (Section 5.1), a description of the NA62 beamline is presented in Section 5.2. More detailed information can be found in Reference [104].

5.1 The SPS proton beam

The SPS is the second largest ring of the CERN accelerator system with a circumference of 7 km. It accelerates particles up to an energy of 450 GeV. Since its construction in 1976 it has been used to accelerate different particles such as protons and electrons (as well as their corresponding antiparticles) and heavy ions. In particular, between 1981 and 1991 it was employed as a hadron collider for protons and antiprotons (Sp$\bar{\text{p}}$S), contributing to the discovery of W and Z bosons in 1983 [6, 7].

Nowadays the SPS operates in a double mode: I) as injector for the LHC [1] and II) providing proton beams to several fixed-target experiments present at CERN. When the SPS operates as injector for the LHC, protons are accelerated from 25 to 450 GeV and then injected in the two main LHC rings, reaching here an energy of 7 TeV per beam. Instead, when operating for the fixed-target experiments, protons in the SPS are accelerated up to 400 GeV and slow-extracted to be directed to the transfer lines which serve the different experimental areas. The slow-extraction technique is preferred in order to have a constant flux of particles over several seconds. Typically an SPS extraction (also referred to as spill) consists of about 3×10^{13} protons in 4.8 s.

The accelerator chain starts with a bottle of hydrogen gas where an electromagnetic field separates the electrons, leaving a pure source of protons that enter the first stage of acceleration in the *Linear Acceleration 2* (LINAC2). After reaching an energy of 50 MeV, protons are injected in the *Proton Synchrotron Booster* (PSB), a booster composed of four synchroton rings, where they are accelerated to an energy of 1.4 GeV before being injected in the *Proton Synchrotron* (PS) ring. The PS was the first synchroton built at CERN (1959) and is able to accelerate particles up to 25 GeV. Finally, after the PS, protons reach the SPS.

[1] The *Large Hadron Collider* (LHC) is a proton-proton collider with a circumference of 27 km. It is the largest accelerator machine of the world.

5.2 The kaon beam

The proton beam extracted from the SPS is split in the North Area into different beamlines through the usage of the T4 primary target. The P42 beamline (840 m in length) transports protons from T4 to a 400 mm long beryllium target of 2 mm diameter called T10, where the NA62 beamline [105] begins: from the interactions of protons with the T10 target the secondary K12 hadron beam is produced.

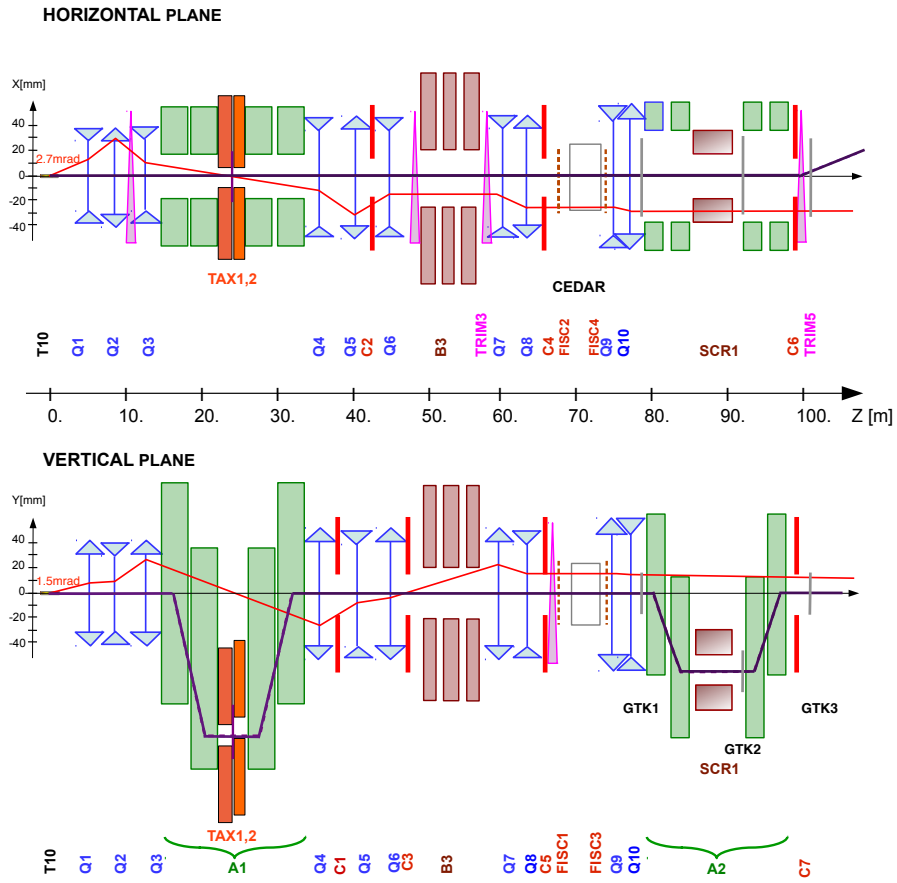

FIGURE 5.1: K12 beam layout from the T10 target to the entrance of the decay region [104]. The red solid line shows the trajectory of a 75 GeV/c particle leaving the target at the maximum accepted angle to be focused in a beam, while the black solid line corresponds to the trajectory of a 75 GeV/c particle leaving the target at zero angle.

The K12 beamline connects the T10 target with the center of the electromagnetic liquid krypton calorimeter (placed about 240 m downstream) in a straight line, defining the z direction of the coordinate system. [2] During an SPS spill a 750 MHz flux of particles gives origin to the NA62 secondary positive beam. It contains a 6% fraction of kaons, resulting in a 5 MHz rate of K^+ decays in the fiducial detector volume.

[2]The y-axis is vertically upwards directed, while the horizontal x-axis forms a right-handed coordinate system.

Beam layout in the upstream region Figure 5.1 shows the upstream part of the beam layout, from the T10 target to the entrance of the decay region. Particles from the target are focused in a beam by a triplet of quadrupole magnets (Q1, Q2, Q3 in Figure 5.1) and the 75 GeV/c momentum component is selected (with 1% precision) by a front-end achromat (A1), which consists of four vertically-deflecting dipole magnets and two beam dump units of copper. The latter, called TAX1 and TAX2, are a series of graduated holes in which the beam passes through, while non-interacting primary protons and unwanted secondary particles are absorbed. Between the two TAXes a radiator of tungsten plates is introduced to degrade by bremsstrahlung the energy of positrons produced in the target, which become separated enough from the hadron beam to be absorbed in a collimator (C3). After a series of quadrupoles and collimators (Q4, Q5, Q6 and C1, C2, C3 in Figure 5.1) a bending magnet (B3), made of three 2 m long dipole magnets, is used to sweep away muons of both positive and negative charge which surround the beam. Only the μ^+ component at 75 GeV/c cannot be separated by the hadron beam and constitutes the muon halo of the beam. To refocus the beam, that could be affected by the B3 magnetic field, two steering dipoles (TRIM2 and TRIM3) are placed just before and after the B3 magnet. The beam is kept parallel to the axis of the first detector in the beamline, the Kaon tagger (CEDAR in Figure 5.1), by another series of quadrupoles and collimators (Q7, Q8 and C4, C5), and focused (Q9, Q10 quadrupoles) again before reaching a second achromat (A2) placed between the first and last stations of the beam spectrometer (GTK in Figure 5.1). The A2 achromat, made of four vertically-deflecting dipole magnets, allows the beam spectrometer to measure the momenta and divergences of the beam particles. An iron collimator, called scraper (SCR1 in Figure 5.1), is placed inside the A2 achromat to complete the separation of the non-75 GeV/c muons from the rest of the beam. Immediately before the last station of the beam spectrometer, the TRIM5 steering magnet is used to deflect the beam by an angle of $+1.2$ mrad on the x-axis. This is done in order to compensate the -3.6 mrad deflection of the MNP33 spectrometer magnet (Figure 5.2), placed downstream to measure the momentum and direction of the kaon decay products.

Beam layout in the downstream region Figure 5.2 shows the downstream part of the beam layout. At about 100 m from the target (after the last station of the beam spectrometer) the beam tube is replaced by a 177 m long tank. It contains the so-called fiducial region where the kaons are expected to decay (with a rate of 4.5×10^{12} kaon decays per year), the downstream spectrometer (STRAW) and part of the photon-veto system. The full tank, and consequently the detectors inside, are kept under vacuum (10^{-6} mbar) in order to minimize interactions of the beam particles and improve the kinematic resolution of the reconstructed events. The vacuum tank ends about 220 m after the target and is followed by a beam pipe of thin aluminium. Finally, after being deflected by a dipole magnet (BEND in Figure 5.2) at the very end of the beamline, the beam ends its path in a dump unit of iron and concrete placed about 270 m downstream the target.

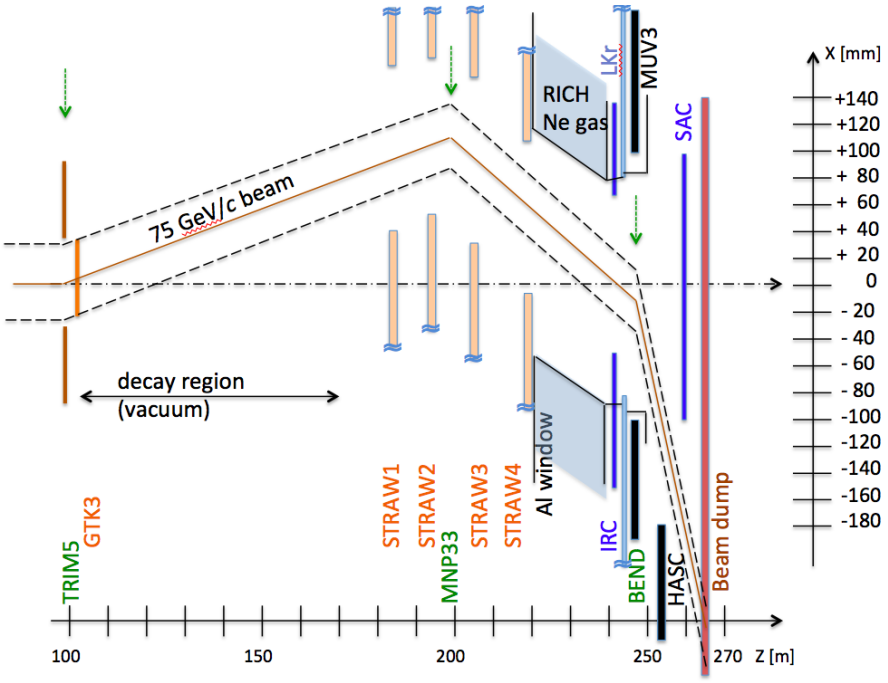

FIGURE 5.2: K12 beam layout from the entrance of the decay region (after the last station of the beam spectrometer) to the end of the beam dump [104]. The fiducial region is contained in the first 60 m of the vacuum tank which hosts the downstream spectrometer (STRAW) with the MNP33 magnet. The BEND magnet, placed downstream the muon-veto system, deflects the undecayed beam particles in the dump unit. The dashed lines correspond to two sigma width of the beam profile.

Pairs of filament scintillator counters, called FISCs, are placed along the beam in proximity of the Kaon tagger and the liquid krypton electromagnetic calorimeter (LKr in Figure 5.2) regions to measure and tune the divergence of the beam. Near the dump unit an ionization chamber and a wire chamber monitor the beam intensity and profile.

Beam configurations The kaon beam, as described above, is the standard beam configuration employed for most of the physics searches. However, dedicated run periods profit of special beam configurations:

- **Muon runs**: the TAXes of the A1 achromat are closed to produce a relatively pure flux of muons by stopping all other secondary beam particles. The muon sweepers are switched off. These runs are mainly used for detector calibrations and efficiency studies.

- **Beam dump runs**: the beryllium target is removed and the primary proton beam is directly sent to the two TAX collimators which, with 22 interaction lengths, act as a beam dump unit. The muon sweepers are kept on. At nominal beam intensity, 10^{18} protons on target (POT) per year are expected, producing for example $\mathcal{O}(10^{15})$ D-mesons and $\mathcal{O}(10^{11})$ b-hadrons in the dump. Together with data collected in the standard kaon beam mode with specific trigger configurations (also referred to as

"parasitic beam dump mode" [3]), these runs allow to search for long-lived exotic particles [106].

[3] In the standard kaon beam configuration about 40% of the primary protons impinge on the TAX collimators. Dedicated trigger configuration can look for pairs of particles in the fiducial volume whose vertex points back to the dump unit.

Chapter 6
The Experimental Apparatus

Distributed over about 200 m, the experimental apparatus can be divided into two parts: the so-called ***upstream*** region dedicated to tag the presence of a kaon in the beam and to measure its momentum and direction, and the ***downstream*** region for reconstructing the final state of the kaon decays. Most of the detectors have a cylindrical shape around the beam, with an evacuated passage to allow the undecayed beam particles to pass through without interacting with the detector material.

The challenging requirements imposed by the measurement of the very rare decay $K^+ \to \pi^+\nu\bar{\nu}$ led the design for the experimental apparatus. The keystones of the experiment are:

- A resolution in the time matching between sub-detectors of $\mathcal{O}(100$ ps$)$.
- A precise reconstruction of the kinematic variables of the event.
- An efficient photon-veto to reach a π^o rejection of $\mathcal{O}(10^8)$.
- A good pion-muon identification with a muon rejection of $\mathcal{O}(10^7)$.

Each request is fulfilled by the construction of very specific detectors employing different techniques and a state-of-the-art trigger and data acquisition system. A view of the whole apparatus is shown in Figure 6.1.

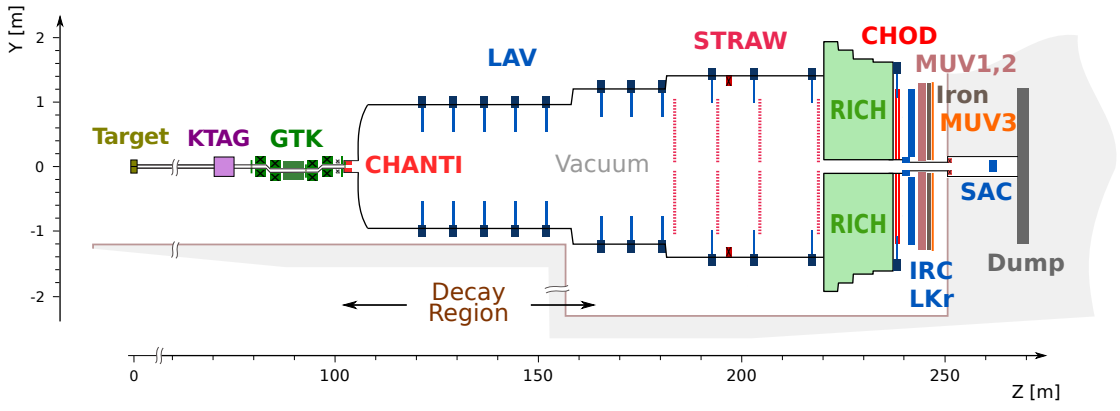

FIGURE 6.1: Vertical view of the NA62 experimental apparatus from the target to the dump unit (from the left to the right) [104].

The Cherenkov detectors **KTAG** and **RICH**, with a very precise time resolution, identify the kaon and the daughter particles, respectively. Their momenta and directions are measured by two spectrometers **GTK** and **STRAW**. Electromagnetic calorimeters with different techniques (**LAV**, **LKr**, **IRC** and **SAC**) form an hermetic photon-veto system up to

50 mrad. A muon-veto system made of two hadron calorimeters (**MUV1** and **MUV2**) and a muon counter (**MUV3**) complete together with the RICH the particle identification system. Two hodoscopes for charged particles (**CHODs**) are used for triggering and timing purposes, while the **CHANTI** counter has to detect inelastic interactions of the beam particle in the GTK. Additional counters (**MUV0** and **HASC**) complete the experimental apparatus by providing hermetic coverage for charged particles produced in multi-track kaon decays.

A description of the NA62 apparatus is given in Section 6.1 (upstream region), Section 6.2 (downstream region) and Section 6.3 (photon-veto system); the trigger and data acquisition system is described in Section 6.4 and the control applications in Section 6.5. More detailed information can be found in Reference [104].

6.1 The upstream region

6.1.1 Kaon tagger (KTAG)

The first detector that the beam encounters on its path is the Kaon tagger or KTAG (Figure 6.2 left panel). It is a Cherenkov counter based on the CERN W-type CEDAR, developed in the 1970s to discriminate particles in an unseparated charged beam extracted from the SPS. In order to stand the high-intensity flux of beam particles in NA62 and to meet the required time resolution of 100 ps, the original optics and readout of the CEDAR were modified for the KTAG detector. The radiator of the CEDAR is filled with 0.94 m^3 of nitrogen (N_2) at room temperature and with a pressure of 1.75 bar. NA62 keeps the possibility to replace the nitrogen gas with hydrogen (H_2) in order to reduce the material budget and, therefore, the beam emittance.

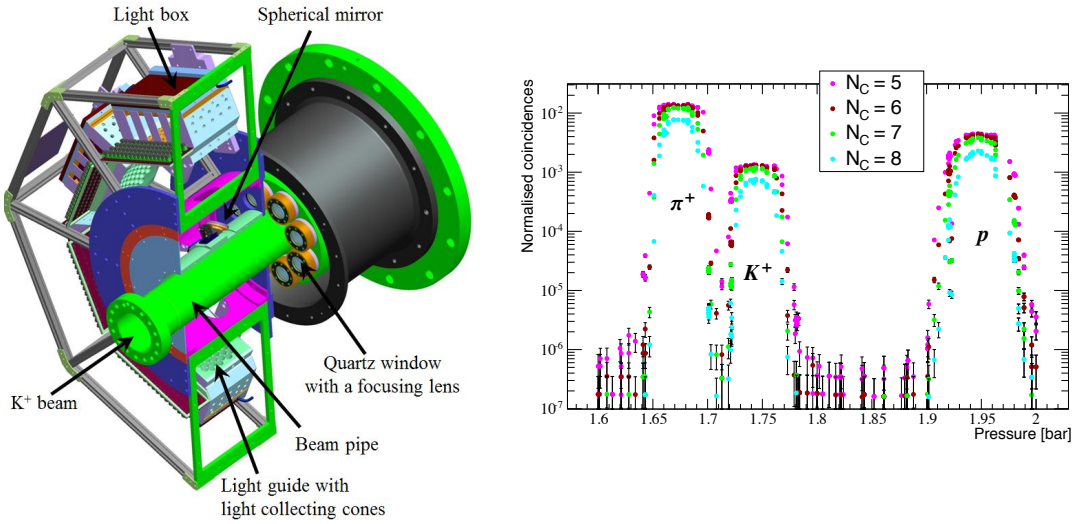

FIGURE 6.2: ***Left:*** Upstream part of the KTAG detector [104]. The emitted Cherenkov light exits the radiator gas through 8 quartz windows and then is focused on the light boxes. ***Right:*** Pressure scan of the N_2 gas at the nominal diaphragm aperture of 1.5 mm [104]. At 1.75 bar the presence of a kaon is required with at least 5 sectors in coincidence.

Given the momentum and a fixed pressure of the gas, the Cherenkov angle only depends on the particle mass. Therefore, by varying the pressure the detector can be made blind to the Cherenkov light of the unwanted particles. The pressure inside the CEDAR can be varied from vacuum up to 5 bar. It is adjusted (as shown in Figure 6.2 right panel) to allow only the Cherenkov light of K^+ particles, once reflected back by the mirror placed at the end of the vessel, to pass through an annular diaphragm with varying radial aperture and to exit the vessel through eight quartz windows. Outside the vessel, the light is focused into eight spherical mirrors which reflect it radially out in eight light boxes (called sectors) placed in an insulated Faraday enclosure filled with nitrogen gas. Each sector hosts 48 photomultipliers which are read out by ultra-fast discriminators [107] in groups of 8 channels. The discriminators output is transmitted as low-voltage differential signal (LVDS) to Time-to-Digital Converter (TDC) boards attached to the TEL62, the main readout system of NA62 (see Section 6.4.1).

At the beginning of each data taking period, in order to ensure the proper operation of the detector, an angular alignment between the optical axis and the beam axis is performed as well as a gas pressure optimization.

6.1.2 Gigatracker (GTK)

The beam spectrometer, made of three stations of silicon pixel detectors, measures the momenta and directions of beam particles with a precision of 0.2% and 16 μrad, respectively. Between the first and last stations, four vertically-deflecting magnets (composing the A2 achromat) are placed. They deviate the beam trajectory allowing the momentum measurement. In the center of the achromat, where the second station is housed, the 75 GeV/c beam component has a parallel vertical displacement of -60 mm.

The required precision on the momentum and direction measurements led the choice of the geometry of the detector: each station is a matrix of 200×90 pixels with an active area of 60.8×27 mm^2 (300×300 μm^2 each pixel). The detector has to sustain the full beam rate of 750 MHz, that goes up to 1.5 MHz/mm^2 in the central detector region, and a high radiation level. Because of the high beam rate, the name Gigatracker (GTK) was chosen. In order to minimize the interaction with the detector material, the material budget of each station is less than 0.5% X_0 corresponding to about 500 μm of silicon. The pixel readout is attached directly to the sensor via bump-bonding in order to satisfy the requirement on the precise time resolution (better than 200 ps). It is composed by application-specific integrated circuits (ASICs), called TDCPix, equipped with a Time-over-Threshold (ToT) discriminator and a TDC. The chips are arranged in a matrix of two rows and five columns, serving 40×45 pixels each as shown in Figure 6.3.

The detector operates in a cooled environment (approximately -15° C), in order to reduce the effect of the radiation damage. 150 micro-channels, acting as heat exchangers, are incised on a thin flat silicon wafer glued on the back side of the readout chip. A cooling

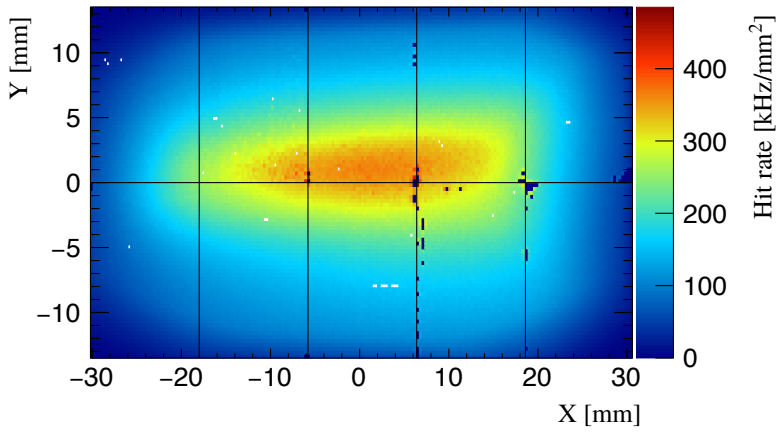

FIGURE 6.3: Illumination of the first station of the Gigatracker (GTK1) operated at 30% of the nominal beam intensity [104]. The black lines delimit the 10 readout chips boundaries, containing each 40×45 pixels.

liquid flows through the micro-channels and removes the heat produced by the TDCPix, ensuring a uniform cooling of the whole detector. The last station (GTK3) marks the beginning of the decay region, contained in the first 60 m of the vacuum tank.

6.1.3 Charged anti-coincidence detector (CHANTI)

The charged anti-coincidence detector (CHANTI) is made of six hodoscope stations with a cross section of 300×300 mm^2, placed in the same vacuum vessels hosting the GTK3 and surrounding the beam. The purpose of this detector is to veto the inelastic interactions of beam particles with the GTK3, to detect the muon halo which surrounds the hadron beam as well as charged particles generated in decays upstream of the GTK3.

The first hodoscope station is placed 28 mm downstream of the GTK3. The distance between each station and the next one doubles to hermetically cover the region between 49 mrad and 1.34 rad for particles generated on GTK3. Each station contains 48 scintillator bars with triangular cross section arranged to form one vertical and one horizontal plane. The bars are read out by fast wavelength-shifting fibers (WLS) connected with silicon photomultipliers (SiPMs). The readout consists of a custom front-end board (CHANTI-FE) to set the SiPM voltage and a LAV-FE board (Section 6.3.2) to digitize the analogue signal in an LVDS signal. The latter is connected with a TEL62 board (Section 6.4.1). The overall rate on the CHANTI detector is expected to be about 7.2 MHz at nominal intensity with a measured time resolution of about 800 ps.

6.2 The downstream region

6.2.1 STRAW spectrometer

Four STRAW chambers and a dipole magnet (MNP33) form the downstream spectrometer that measures the directions and momenta of charged particles produced in the kaon

decays. It starts about 20 m after the decay volume and extends over 35 m along the beamline. In order to minimize multiple scattering, the STRAW spectrometer is placed inside the vacuum tank and was built with light material, corresponding to a total material budget of 1.8% X_0 seen by crossing particles.

Each of the four chambers is composed of two modules with two views: X (0°) and Y (90°) in the first module, U (−45°) and V (+45°) in the second. The layout of the four views (Figure 6.4) results in an active circular area of 2.1 m outer diameter with an octagonal gap of 6 cm apothem around the z-axis to accommodate the passage of the beam. Since the dipole magnet, placed between the second and third chambers, changes the beam angle in the horizontal plane from +1.2 to −3.6 mrad the octagonal gap of each chamber is not centered in the xz plane. In order to have high detection redundancy, each view has four straw layers, which guaranties that at least two straw tubes per view get hit when a particle crosses one chamber. In average a track counts 27 straw hits when all the four chambers are crossed.

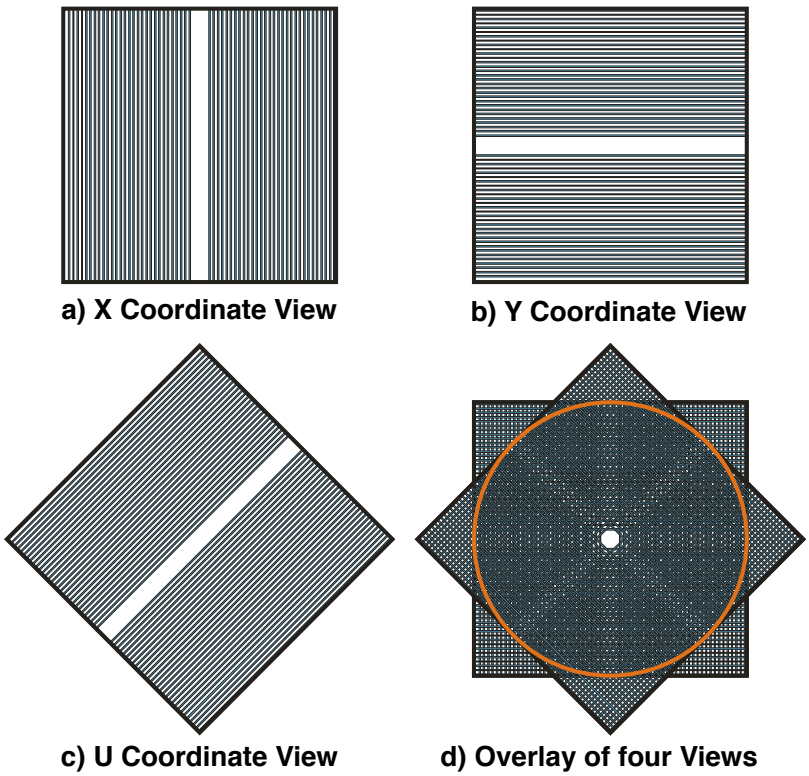

FIGURE 6.4: Layout of the 4 views composing a STRAW chamber [104]. Each chamber has an octagonal shape with a inner gap for the passage of undecayed beam particles.

Each straw is a tube of 216 cm length and 9.82 mm diameter of polyethylene terephthalate (PET) coated inside with copper and gold. The gas inside is a mixture of 70% argon and 30% carbon dioxide at atmospheric pressure, while the anode wires are made of gold-plated tungsten. The gas volume is closed by the front-end readout board (COVER), which

has a modularity of 16 straw tubes and is designed to sustain the force of a pressure difference of 1 bar in case of the break of one tube.

Between the second and third chambers the MNP33 magnet, inherited from the NA48 experiment, is placed. It provides an integral magnetic field of 0.9 Tm [108] pointing in the direction of the negative y-axis and resulting in a transverse momentum kick of 270 MeV/c for positively charged tracks. The STRAW spectrometer provides a momentum resolution of

$$\frac{\sigma_p}{p} = 0.30\% \oplus 0.005\%\ p\ [\text{GeV}/c]\ , \tag{6.1}$$

while the angular resolution is 60 μrad at 10 GeV/c track momentum and decreases to 20 μrad at 50 GeV/c.

6.2.2 Ring Imaging Cherenkov counter (RICH)

The Ring Imaging Cherenkov (RICH) detector is part of the particle identification system of NA62, which has to efficiently discriminate pions from muons. It is optimized for the track momentum range 15–35 GeV/c and provides a muon suppression of about a factor 100.

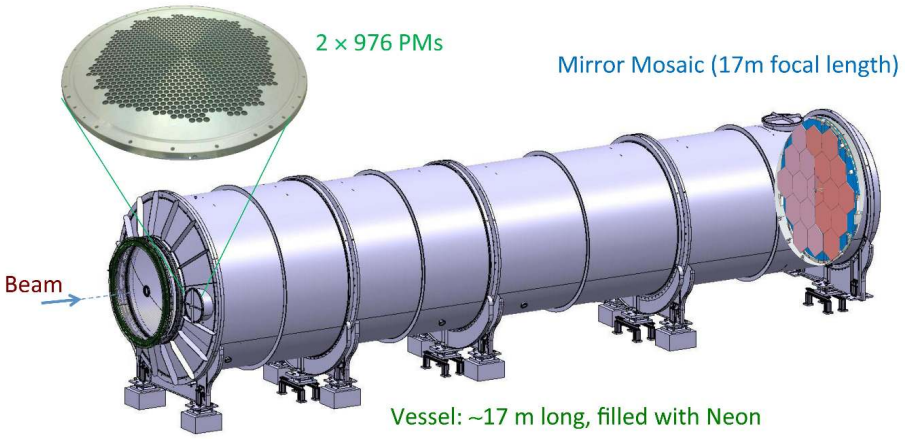

FIGURE 6.5: Layout of the RICH detector [104]. The vessel, 17 m long, is filled with neon gas at atmospheric pressure. The mirror mosaic and the photomultiplier flanges are visible in the downstream and upstream parts of the vessel, respectively.

Neon gas at atmospheric pressure and room temperature fills the 17.5 m long cylindrical vessel (Figure 6.5), which is divided in four sections with decreasing diameter. The entrance window is the only element that separates the vacuum of the decay volume from the neon gas. Outside of its active area (1.1 m radius) two flanges of 976 photomultipliers each are accommodated in the focal plane. They detect the ring produced by the Cherenkov light cone, which is reflected back by a mosaic of 20 mirrors located at the exit window (1.4 m active radius). The reconstruction of the ring produced at the focal plane provides a direct measurement of the particle velocity and, therefore, of the mass when combined

with the momentum measured by the STRAW spectrometer.

In order to avoid the light absorption by the thin aluminium beam tube, placed inside the vessel for the passage of undecayed particles, the mirror mosaic is divided in two halves, one for each side of the beam pipe. The mirrors are made of 25 mm thick glass coated with aluminium. They have a hexagonal shape of 350 mm side with the exception of the inner one, which is made of two half hexagons with a central hole for the beam tube. Piezoelectric motors are attached to the mirror supports allowing to remotely control the mirror position and to perform fine alignment after the installation. This is possible, during the data taking, by selecting particles with the Cherenkov light contained in only one mirror and using the track directions provided by the STRAW spectrometer.

The photomultipliers are read out by 8-channel ASIC discriminators [107] with a 50 ps time resolution leading a crossing particle time resolution of 100 ps. The boards operate as Time-over-Threshold discriminators, whose LVDS output is then sent to a TEL62 board (Section 6.4.1).

6.2.3 Hodoscopes for charged particles (CHODs)

A system of two independent scintillator detectors (hodoscopes) is used to detect the presence of charged particles produced in the kaon decay. They cover the region downstream of the RICH detector and upstream of the LKr calorimeter with the main purpose of providing a fast time input to the trigger for charged particles. The hodoscope system consists of the old CHOD detector, inherited from the NA48 experiment, and the new CHOD, built specifically for the high-intensity environment of NA62. They are located upstream and downstream of the last LAV station, respectively.

NA48-CHOD

The NA48-CHOD is made of 128 scintillator counters (slabs) assembled in one vertical and one horizontal plane, to form four quadrants with 16 slabs on each plane and resulting in an octagon of 1 210 mm apothem with a central hole for the beam tube (Figure 6.6 left panel). Each slab is a plastic scintillator of 20 mm thickness, with different width to take into account the higher rate in the detector center. The slabs are read on one side by photomultipliers through light guides. The front-end electronics consists of four LAV-FE boards (Section 6.3.2) reading each one quadrant and sending signals to one TEL62 board (Section 6.4.1). The NA48-CHOD provides a time resolution of about 200 ps for charged particles.

CHOD

The CHOD hodoscope is a single plane of 152 scintillator tiles covering an annulus of 140 mm and 1 070 mm for the inner and outer radius, respectively. The choice to use scintillator tiles instead of strips was driven by the possibility to optimize the hit rates and

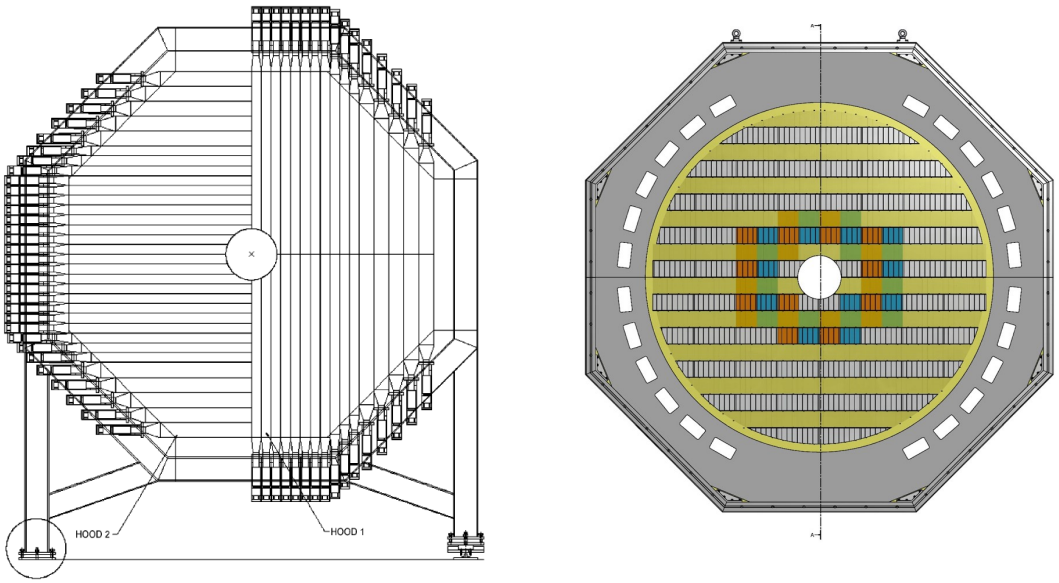

FIGURE 6.6: ***Left:*** Layout of the NA48-CHOD detector [104]. The 128 slabs are assembled on a vertical and horizontal plane forming four quadrants. ***Right:*** CHOD layout with 152 tiles mounted in a octagonal aluminium structure [104]. Short tiles (134 mm) are placed in the central part of the detector around the beam pipe (orange and blue), surrounded by larger ones (twice the width).

to select specific tile groups for the trigger. The tiles form horizontal rows alternating on the upstream and downstream sides of a support foil, to guarantee overlap on the vertical axis, and are placed inside an aluminium structure with the dimension of an octagon with 1 550 mm apothem (Figure 6.6 right panel). Each tile is connected through WLS fibers to a pair of SiPMs mounted outside the detector acceptance in the aluminium structure. The SiPM signals are discriminated by constant fraction discriminators (CFDs) and sent to a TEL62 board (Section 6.4.1). The CHOD provides a time resolution better than 1 ns.

6.2.4 Muon-veto system (MUV)

The muon-veto system completes, together with the RICH detector and the LKr calorimeter, the particle identification system and provides an $\mathcal{O}(10^5)$ muon suppression for the $K^+ \to \pi^+ \nu\bar{\nu}$ measurement. It consists of two modules of hadron calorimeters called MUV1 and MUV2 (together referred to as HAC), a 80 cm iron wall to stop all detectable particles except muons, and a fast scintillator detector called MUV3. The entire system (Figure 6.7) can participate in the trigger in order to have an online selection of events with muons in the final state.

Hadron calorimeter (HAC)

The hadron calorimeter (HAC) is made of two modules of sampling calorimeters with alternating layers of iron and scintillators for a total of about 8 interaction lengths. The active layers are connected to photomultipliers, whose fast signals are first shaped to LKr-like pulse shapes by NIM modules (used in the NA48-HAC) and then read out by Fast Analog-to-Digital Converters (FADCs) implemented in the CREAM boards. The latter are readout

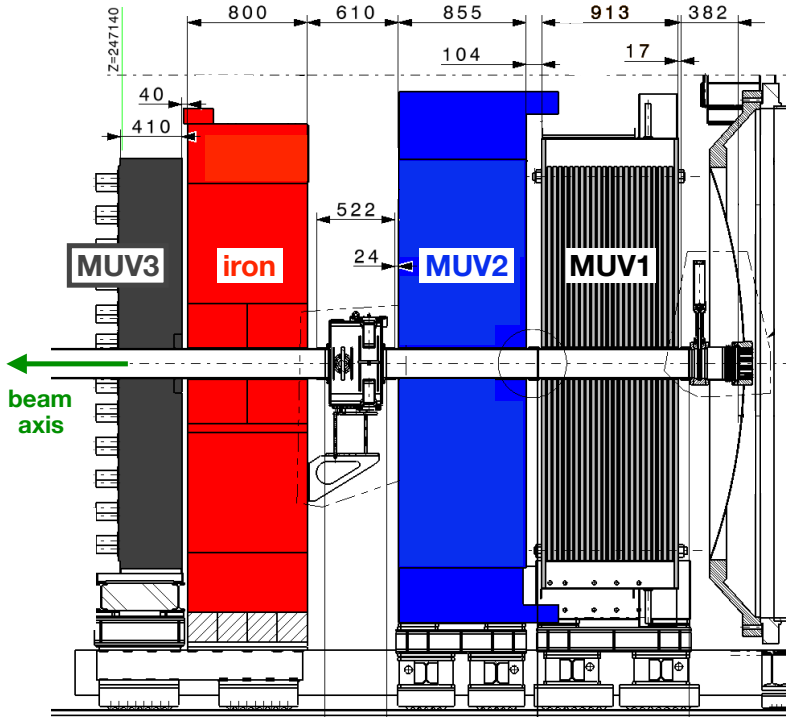

FIGURE 6.7: The muon-veto system layout [109] with the two modules of hadron calorimeters (MUV1 and MUV2), the iron wall, and the fast muon counter (MUV3).

boards developed specifically for the LKr calorimeter and described in Section 6.4.1. In order to have a precise energy response, a detector calibration was performed with the use of high-energy pions crossing the detector and muons completely stopped inside [110], resulting in an energy resolution of:

$$\frac{\sigma_E}{E} = \frac{0.460}{\sqrt{E[\text{GeV}]}} \oplus 0.093 \,. \tag{6.2}$$

MUV1 The MUV1 is the HAC front module, newly built for the NA62 experiment. It consists of 24 layers of iron interleaved with 23 layers of scintillator strips spanning the whole length of the detector. Exceptions are the outer and inner strips, which are shorter (to accommodate the support structure) and half length (to accommodate the beam pipe and to sustain a higher particle rate), respectively. Each layer has the dimension of 270×260 cm^2, with the two outer iron layers larger to serve as support structure. The scintillator layers are alternately oriented, resulting in 12 horizontal and 11 vertical layers. The strips are read out on both sides (except for the half strips in the central region) by two WLS fibers connected to photomultipliers. Strips at the same transverse position in all layers are connected to the same photomultipliers for a total of 176 channels.

MUV2 The HAC back module, MUV2, is the refurbished front module of the NA48 hadron calorimeter [81]. It consists of 24 layers both of iron and scintillator strips. Due to space constraints, the module was rotated by 180° with respect to the NA48 configuration leading to two consecutive iron layers between MUV1 and MUV2. Each scintillator layer

is made of 44 strips spanning half of the detector length (130 cm long), connected via two light guides to the photomultipliers. As in the MUV1 module, the strips are alternately oriented providing 12 horizontal and 12 vertical layers. Strips with identical transverse alignment are connected with the same photomultiplier for a total of 88 channels.

Fast muon-veto (MUV3)

The MUV3 is a fast scintillator detector devoted to tag the presence of charged particles (muons) that traverse the whole calorimeter system (LKr+HAC) and survive 80 cm of iron wall, for a total of more than 14 interaction lengths. Thanks to a fast time response when a particle crosses the detector (time resolution of about 500 ps) it is used at trigger level to efficiently identify events with muons in the final state. The detector is a square of 264 cm side consisting of 148 scintillator tiles of size $22\times22\times5$ cm^3, with the inner ones smaller to sustain the higher particle rate. Each tile is read out by two photomultipliers. Their signals are discriminated by CFDs and then sent to a TEL62 board (Section 6.4.1).

6.2.5 Additional veto detectors

In order to detect $K^+ \to \pi^+\pi^+\pi^-$ ($K_{3\pi}$) decays, where pions escape the lateral acceptance of the STRAW spectrometer, two additional veto detectors were built: a peripheral muon-veto detector (MUV0), and a hadronic sampling calorimeter (HASC). In addition to identify multi-track kaon decays, they can also be used to detect products of photon conversions which escape laterally the photon-veto system acceptance. Both detectors are read out by LAV-FE (Section 6.3.2) and TEL62 (Section 6.4.1) boards.

MUV0 The MUV0 is designed to detect negative pions of $K_{3\pi}$ decays with momenta below 10 GeV/c which, deflected by the MNP33 magnet towards positive x, escape the lateral acceptance near the RICH detector. It is a scintillator hodoscope with two layers of 48 scintillator tiles ($200\times200\times10$ mm^3 each) mounted on the downstream flange of the RICH. It covers the lateral acceptance of $1.545 < x < 2.945$ m and $|y| < 0.7$ m. Tiles are grouped into 9 so-called super-tiles, read out by WLS fibers connected to photomultipliers.

HASC The HASC has to detect π^+ mesons emitted in $K_{3\pi}$ decays with very high momentum (above 50 GeV/c) and traversing the beam hole in the center of the STRAW spectrometer. Those pions are swept away from the beam axis towards negative x by the BEND magnet placed downstream of the MUV3 detector (see Figure 5.2). The detector covers the acceptance region of $-0.48 < x < -0.18$ m and $|y| < 0.15$ m. It is made of 9 identical modules: a sandwich of 60 lead plates alternated with scintillator plates with a transverse dimension of 100×100 mm^2. Each module has 10 longitudinal readout sections where the tiles are optically coupled to WLS fibers, read by SiPM sensors.

6.3 The photon-veto system

The photon-veto system has to identify events with photons in the final state. The $K^+ \to \pi^+\pi^o$ ($K_{2\pi}$) decay with a branching ratio of BR $= (20.67 \pm 0.08)\%$ [5] is the second most abundant kaon decay. For the $K^+ \to \pi^+\nu\bar{\nu}$ measurement it is required to reject this kind of events at the level of 10^{12}. Kinematic constraints on the missing 4-momentum $M^2_{\text{miss}} = (P_{K^+} - P_{\pi^+})^2$, measured combining GTK and STRAW information, provide a rejection of $\mathcal{O}(10^4)$. The additional requirement on the π^+ momentum to be between 15 and 35 GeV/c ensures an energy for π^o from $K_{2\pi}$ events of at least 40 GeV, leaving the remaining $\mathcal{O}(10^8)$ to be achieved by the photon-veto detectors.

Starting from the existing electromagnetic calorimeter of NA48 [81], new detectors were specifically built for NA62 in order to have an hermetic photon-veto system from 0 to 50 mrad. The system is divided in three angular regions, as shown in Figure 6.8, which employ different detector technologies:

- Twelve stations of Large Angle Vetoes (LAVs) covering the region between 8.5 and 50 mrad.
- The NA48 Liquid Krypton electromagnetic calorimeter (LKr) covering the region between 1 and 8.5 mrad.
- Two Small Angle Vetoes (SAV) covering the region below 1 mrad.

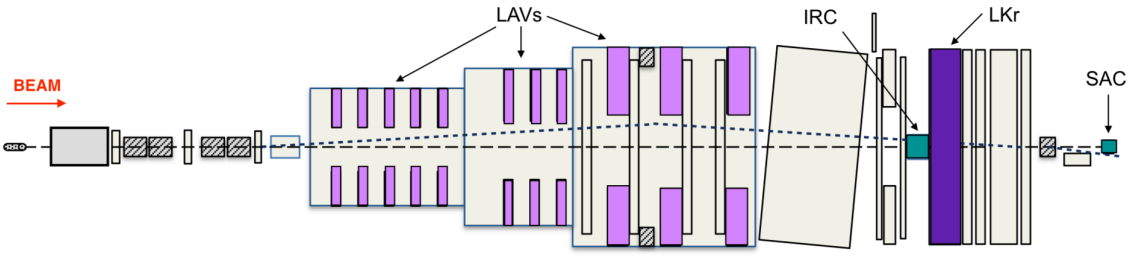

FIGURE 6.8: Layout of the NA62 photon-veto system with 12 stations of Large Angle Vetoes (LAVs), the Liquid Krypton electromagnetic calorimeter (LKr) and the two Small Angle Vetoes (IRC and SAC) [111].

The geometry is conceived in a way that only three configurations are possible for photons coming from π^o decays under the requirement that the π^o comes from $K^+ \to \pi^+\pi^o$ events with the π^+ momentum below 35 GeV/c. In the majority of the cases, about 82%, both photons have an energy above 20 GeV and are detected by the LKr and SAV calorimeters. In almost all of the remaining 18% of the cases, one photon is detected by the LKr or SAV and the other hits one station of the LAVs, leaving only 0.2% of π^os with only one photon hitting a detector and the other photon missing at large angle (above 50 mrad) in between two LAV stations. The energy of this escaping photon is below 200 MeV by kinematic constraints.

In order to reach the required $\mathcal{O}(10^8)$ π^o rejection, each photon-veto detector has to have an inefficiency of 10^{-4} or lower. Test beam measurements of the LAV [112] and SAV [113] prototypes, and data collected in 2004 and 2006 by the LKr with the NA48 apparatus [114] showed that the measured efficiencies satisfy the design requirements. A simulation of the $K^+ \to \pi^+\pi^o$ decay kinematics and of the geometrical acceptance was done in order to estimate the total π^o rejection. Using the detector inefficiency as expected by design (see Table 6.1), each photon was weighted with the corresponding inefficiency of the hit detector at the photon energy. After applying the π^+ momentum cut between 15 and 35 GeV/c, the total π^o rejection inefficiency was computed to be 1.6×10^{-8} [115].

Photon-veto detector	**Angular coverage [mrad]**	**Design inefficiency**
LAV	8.5 – 50	10^{-4} for $E_\gamma > 200$ MeV
LKr	1 – 8.5	10^{-3} for $E_\gamma > 1$ GeV 10^{-5} for $E_\gamma > 10$ GeV
SAV	0 – 1	10^{-4} for $E_\gamma > 5$ GeV

TABLE 6.1: The photon-veto system angular coverage and design inefficiency [104].

6.3.1 Liquid Krypton calorimeter (LKr)

The Liquid Krypton calorimeter has been inherited from the (previous) NA48 [81] experiment, devoted to detect direct CP violation in the kaon sector. The calorimeter was required to have high granularity and high-energy resolution to be able to measure photon energies and transverse coordinates with high precision. It was built as an ionization calorimeter filled with 9 000 ℓ of liquid krypton. The noble gas was chosen to have a material with long recombination lifetime and short radiation length, and to have a homogeneous calorimeter (the liquid krypton acts as both absorber and active material) with dimensions to fully contain the development of electromagnetic showers. The assembly of the calorimeter was completed in 1996 and since then operated in the NA48 experiment and, after a major upgrade of the readout system, in NA62.

The calorimeter active volume has an octagonal shape of 128 cm apothem with an inner hole of 8 cm radius for the beam pipe and a length of 27 X_0 along the z-axis (about 127 cm). It is divided in 13 248 cells of dimension $2\times2\times127$ cm^3, with each cell having a central anode at high voltage (3 kV) in the middle of two cathodes kept at ground. The electrodes (Figure 6.9 left panel) are made of copper-beryllium (Cu-Be) ribbons 40 μm$\times$18 mm in cross section displaced by 1 cm in x and 2 mm in y. In order to achieve a good accuracy in the transverse dimension of the cells, the electrodes ribbons are forced to go through five spacers (Figure 6.9 right panel), which constrain the transverse positions with ±45 μm precision. The spacer plates, made of epoxy-fiberglass composite material, are spaced by 21 cm and shifted along the horizontal axis by 10 mm resulting in a zig-zag trajectory for

the Cu-Be ribbons. This configuration avoids that the shower core of an incident photon is aligned with the anode electrode, causing inefficiency in the photon detection. At the downstream end of the ribbons the anodes are directly connected to the high voltage, which produces the drift field for the ionization, and to preamplifiers which read out the signal.

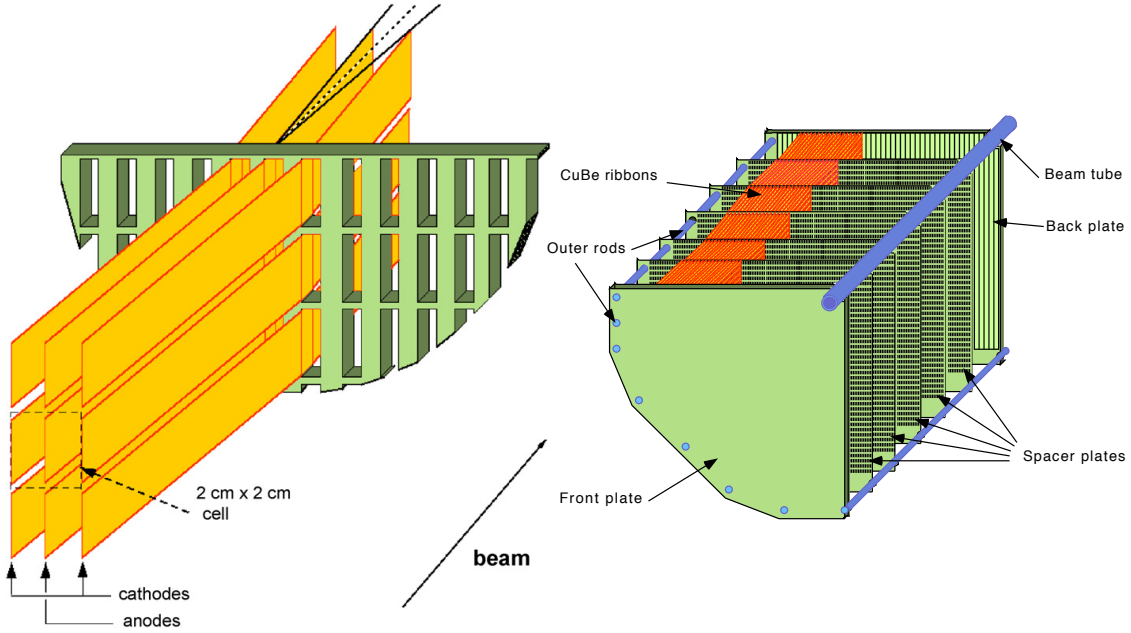

FIGURE 6.9: ***Left:*** LKr cells design [81]. The Cu-Be ribbons are placed to form 13 248 cells of 2×2 cm^2 cross section spanning the full length of the detector (127 cm). The high voltage (3 kV) is applied on the anode, while the two cathodes are at ground. ***Right:*** One quadrant of the calorimeter [104]. The ribbons pass through 5 spacer plates to form a zig-zag configuration.

The electrode structure, the liquid krypton, and the preamplifiers are housed in a vacuum-insulated cryostat of horizontal cylindrical shape and a vertical cylindrical neck. The cryostat outside warm windows are made of 4 mm aluminium sheets. The cold front window is double walled: the outer wall is a convex 2 mm thick stainless steel foil and the inner one is flat and 0.5 mm thick, leading to a total amount of material upstream the sensitive volume of 0.58 radiation lengths. The krypton is kept at a temperature of 120 K being in thermal contact with a bath of saturated liquid argon at 10 bar, itself cooled down by liquid nitrogen.

LKr Front-End electronics Electrons and photons entering the active volume of the LKr produce electromagnetic showers by repeated pair production and bremsstrahlung processes. Charged particles of the shower ionize the atoms of the krypton with the free electrons produced drifting toward the anode of the cells. Their total numbers is a direct measure of the incoming particles energy. The lateral distribution of the electromagnetic shower is peaked to the direction of the incoming electron/photon with up to 40% of its total energy deposited in one single cell. The signal produced on the anode is read out by charge-integrating preamplifiers hosted inside the cryostat and directly attached to the

anodes ribbons. [1] The preamplifiers are connected by coaxial cables to the transceivers on the warm side of the cryostat, whose signal has a quasi ideal triangular shape with raising time of about 22 ns. The calorimeter pulses are continuously digitized by 40 MHz fast ADC in the CREAM readout boards, described in Section 6.4.1.

Calorimeter performances In the NA48 setup, energy and position resolutions were measured to be [81]:

$$\frac{\sigma_E}{E} = \frac{0.032}{\sqrt{E[\text{GeV}]}} \oplus \frac{0.09}{E[\text{GeV}]} \oplus 0.0042 \,, \tag{6.3}$$

$$\sigma_{x,y} = \frac{0.42 \text{ cm}}{\sqrt{E[\text{GeV}]}} \oplus 0.06 \text{ cm} \,. \tag{6.4}$$

In the NA62 apparatus an energy resolution of

$$\frac{\sigma_E}{E} = \frac{0.048}{\sqrt{E[\text{GeV}]}} \oplus \frac{0.11}{E[\text{GeV}]} \oplus 0.009 \tag{6.5}$$

has been obtained [104], which is worse than in NA48 due to the presence of non-linear energy response (induced by the zero-suppression algorithm implemented in the new electronics) and extra material, mainly from the RICH detector, upstream of the calorimeter.

6.3.2 Large Angle Veto (LAV)

The Large Angle Veto (LAV) system consists of 11 ring-shaped stations placed in the vacuum of the decay volume and a 12^{th} station, operated in air, located 3 m upstream of the LKr calorimeter. The twelve stations have to provide hermetic coverage for photons produced in decays inside the fiducial volume and emitted at an angle between 8.5 and 50 mrad. For the construction of the LAV system the lead-glass blocks from the OPAL electromagnetic barrel calorimeter [116], which became available in 2007, were used. A prototype was tested at the low-energy electron beam of the Frascati Beam-Test Facility (BTF) [112], fulfilling the required photon detection efficiency.

The modules of the central part of the OPAL electromagnetic calorimeter are lead-glass blocks of about 75% lead oxide (PbO) by weight manufactured in the mid 1980s. Each block (Figure 6.10 left panel) has a trapezoidal shape: the front and rear face are 10×10 cm^2 and 11×11 cm^2 respectively, while the length is about 37 cm. They are read out at the back side by a photomultiplier optically coupled via a 4 cm long cylindrical light guide. Electromagnetic showers in the lead-glass blocks are detected via their Cherenkov light. Before the construction of the LAV system, particular care was taken in reinforcing the stainless steel cover of each block and in replacing the original wrapping to make the detector compatible with vacuum operation [117].

[1] The choice of cold preamplifiers was made to minimize the time of charge transfer achieving a fast shaping of the pulses.

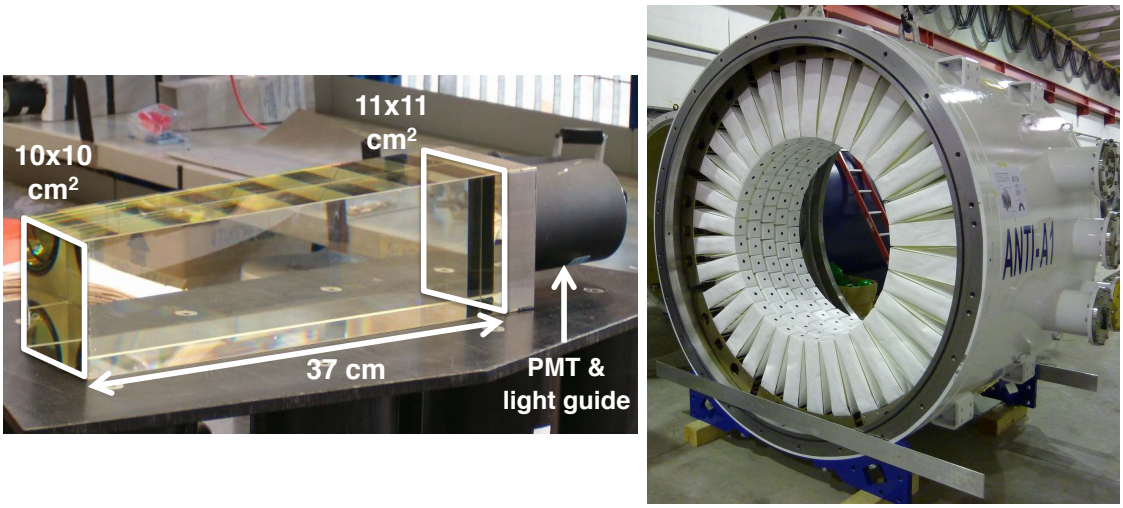

FIGURE 6.10: ***Left:*** Module of the OPAL calorimeter used in the construction of the LAV stations [104]. It consists of a lead-glass block with trapezoidal shape, connected via a light guide to a photomultiplier. ***Right:*** Completed LAV1 station before the installation in the NA62 beamline [104].

A LAV station (Figure 6.10 right panel) is made by the lead-glass modules arranged around the inside of a segment of the vacuum tank, with the blocks aligned radially to form an inward-facing ring. In order to provide the required depth for an efficient photon detection, multiple rings staggered in the azimuth angle and a 1 cm longitudinal distance are used in each station. Since the spaces between the blocks are significantly smaller in the larger diameter stations, here fewer layers are necessary. As a result of the geometry, blocks in at least three rings (effective depth of 21 X_0) are hit by particles incident on each station. The geometry of the stations is summarized in Table 6.2. The complete construction of the stations operated in vacuum (LAV1–11) started in 2009 and took three years, while the last LAV12 station was completed and installed in 2014.

Stations	**Outer wall diameter [mm]**	**Ring radius [mm]**		**Number of layers**	**Number of modules**
		Inner	**Outer**		
LAV1 – LAV5	2 168	537	907	5	160
LAV6 – LAV8	2 662	767	1 137	5	240
LAV9 – LAV11	3 060	980	1 350	4	240
LAV12	3 320	1 070	1 440	4	256

TABLE 6.2: Geometry of the 12 LAV stations [104]. The first 11 LAVs are placed in the vacuum (10^{-6} mbar) of the decay volume inside the steel vessel. LAV9 and LAV10 are placed astride of the STRAW spectrometer magnet. The 12^{th} station operates in air and is placed between the hodoscopes for charged particles.

LAV Front-End (LAV-FE) electronics At nominal beam intensity the rate of the LAVs is dominated by the muon halo with about 4 MHz. In order to keep this accidental rate at the percent level, a time resolution of 1 ns is required for energies above 1 GeV. A custom

front-end board based on Time-over-Threshold (ToT) discriminators [118] has been developed. Since the LAV system is exposed to photons with a wide range of energies (from a few hundreds of MeV to tens of GeV), the photomultiplier signals vary from tens of mV to tens of V. Therefore, before being discriminated, the signal is clapped for protection at 0.6 V, maintaining the time of the rising and falling of the pulse. The signal is then passively split: one copy is summed with signals of adjacent channels for diagnostic purpose, while the other is amplified by a factor of 5 and discriminated by two different thresholds. The resulting output of the discriminator boards are two low-voltage differential signals (LVDS) with the width equal to the duration in which the analogue signal is above the specified threshold (about 5 mV and 15 mV for the low and high thresholds, respectively). Each LAV-FE board has hence 32 input channels and 64 output channels. The LVDS signals are then sent to TEL62 boards (Section 6.4.1).

6.3.3 Small Angle Veto (SAV)

The Small Angle Veto (SAV) system provides detection of high-energy (mostly above 5 GeV) photons down to 0 mrad. It consists of two shashlyk calorimeters of lead and plastic scintillator plates crossed by wave-length scintillating fibers (WLS): the Intermediate-Ring Calorimeter (IRC) and the Small-Angle Calorimeter (SAC). They are located, respectively, immediately upstream of the LKr calorimeter and at the end of the experiment before the beam dump unit. At nominal beam intensity, the two detectors are exposed to a photon rate of 1 MHz, with the IRC reaching about 10 MHz due to the muon halo being concentrated in a few cm diameter spot on negative x. The photon detection efficiency was tested in 2012 with a prototype of the SAC detector at the Frascati Beam-Test Facility [113], resulting in an inefficiency of $\mathcal{O}(10^{-4})$ for 600 MeV electrons.

Intermediate-Ring Calorimeter (IRC)

The Intermediate-Ring Calorimeter (IRC) covers the inner region of the LKr. It has a cylindrical shape with an outer radius of 145 mm centered on the z-axis and an inner radius of 60 mm with a 12 mm offset towards negative x, to take into account the beam deflection given by the STRAW magnet. The detector (Figure 6.11 left panel) is composed of two modules (spaced by 4 cm) with 25 and 45 layers, respectively in the upstream and downstream parts, for a total detector depth of 19 X_0. Each layer is made of a lead absorber and a scintillator plate, both 1.5 mm thick, and has 570 holes to host the WLS fibers. The hole matrix is shifted by 4.8 mm along the y-axis in the downstream module with respect to the upstream one in order to avoid that photons traverse the detector inside a fiber. The lead/scintillator rings are divided into four isolated quadrants, whose WLS fibers are connected with one photomultiplier resulting in a 4-channel detector.

Small-Angle Calorimeter (SAC)

The Small-Angle Calorimeter (SAC) consists of 70 plates of both lead and plastic scintillators, each of 1.5 mm thickness and 205×205 mm^2 transverse dimension. The total depth of

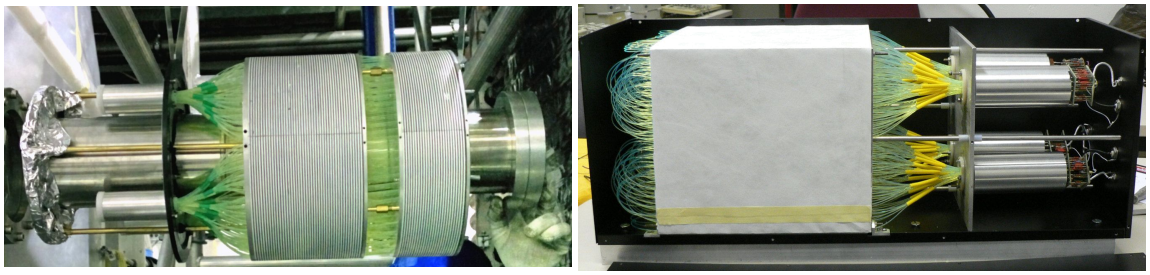

FIGURE 6.11: ***Left:*** IRC detector installed in the NA62 beamline, with the beam coming from the right [104]. The two modules are visible, together with two (out of four) bunches of WLS fibers connected to photomultipliers. ***Right:*** SAC detector after completion and assembly [104]. The WLS fibers connected to the four photomultipliers are visible.

the detector (Figure 6.11 right panel) is about 19 X_0. Each plate (both lead and scintillator) has a grid of 484 holes in order to accommodate 240 WLS fibers. The fibers traverse the whole detector and are bent into a U-shape allowing the readout of both ends at the back of the detector, where the fibers are grouped in four bunches, each connected to a photomultiplier. However, since the scintillator plates have no transverse segmentation the SAC is basically a single-channel detector. It is placed inside the beam vacuum at the end of the experiment, just before the beam dump unit, and it is rotated by 23 mrad with respect to the z-axis to guarantee that photons traveling parallel to the beam axis cannot traverse the detector along a WLS fiber without encountering any lead plates.

SAV readout system

Both IRC and SAC are read out by LAV-FE boards connected with a TEL62 (Section 6.4.1). The output of each channel (four in both detectors) is discriminated against two thresholds, 10 and 30 mV for the low and high thresholds respectively, and converted in LVDS as described in Section 6.3.2. During the 2016 data taking, the additional CREAM (Section 6.4.1) readout based on fast ADCs was added in order to improve the SAV efficiency in discriminating photons arriving close in time. A linear amplifier with two outputs per channel splits the photomultiplier signals and sends them to the two different readout boards. Before being sent to the CREAM modules, the signal is shaped into a LKr-like pulse by a NIM module as for the HAC calorimeter. The SAV time resolution is about 1 ns.

6.4 The trigger and data acquisition system

A unified trigger and data acquisition (TDAQ) system has been designed in order to fulfill the requirements of having a high-performance and versatile system, to sustain a total particle flux of 750 MHz, and to change trigger configurations during the data taking. The NA62 TDAQ is rather unique in a high-energy experiment since any information recorded by the detector is available to build the trigger response and no additional hardware is used for the trigger. The trigger logic is based on three different levels, as shown in the data flow of Figure 6.12, with a reduction factor of 10 at each step (from 10 MHz to 10 kHz): a

hardware-based level zero trigger (L0) and two software-based levels one and two triggers (L1 and L2) are used.

Data Flow When a particle crosses the experimental apparatus a set of sub-detectors generates the so-called trigger primitives, digital words encoding the event characteristics, and sends them to the L0 Trigger Processor (L0TP). It sorts the trigger primitives in time and search for a match with any of the active trigger configurations. In case of success a trigger signal is sent to all the sub-detectors which, with the only exception of the GTK detector and the calorimeters (acquired later due to the high bandwidth requirement), send their data to the PC farm. Here the software triggers refine the event selection by requiring simple correlations between conditions computed by individual detectors.

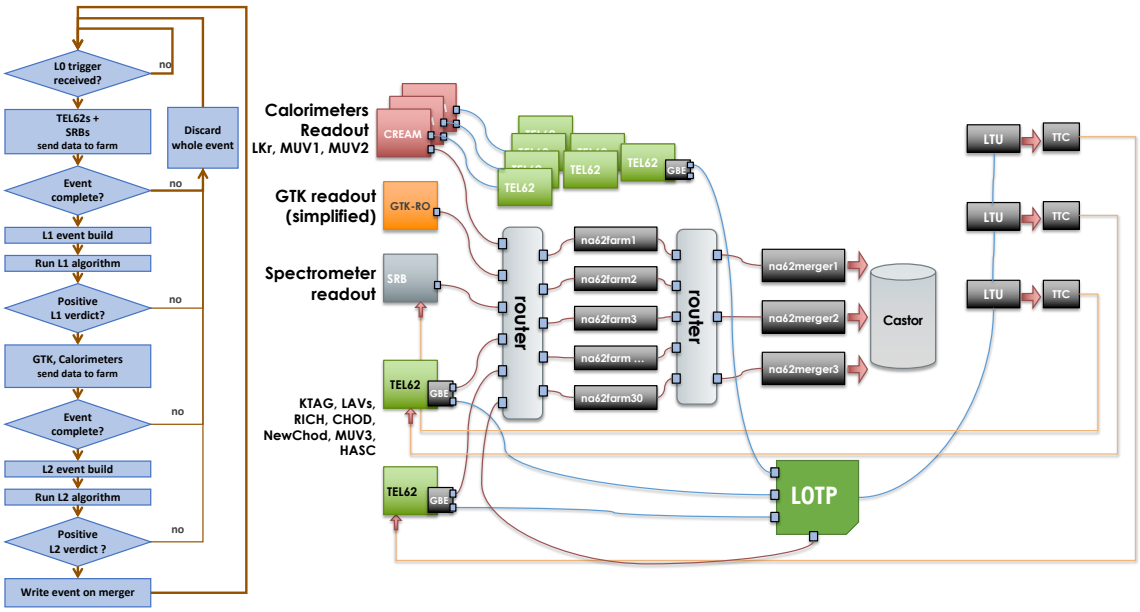

FIGURE 6.12: Data flow and overview of the unified trigger and data acquisition system [119].

In order to maintain high-trigger efficiency, all elements that compose the readout and trigger system have to work in a synchronized way. In contrast to collider experiments where the particles arrive in short bunches, in a fixed-target experiment beam particles are delivered for the entire duration of the extraction. Hence, the SPS machine spill (also referred to as burst) is the data taking unit of NA62. Events inside a burst, which pass all trigger levels, are transferred to a merger PC and written in a common raw data file saved on tape by the *Central Data Recording* (CDR) system. A high-quality clock generator with a frequency of 40.079 MHz in the experimental area produces the NA62 main clock, thus ensuring the synchronization of the complete apparatus. The clock and the trigger distribution are based on optical fiber transmission using the *Timing Trigger Control* (TTC) [120] and the *Local Trigger Unit* (LTU) [121] infrastructures.

6.4.1 Readout

The experiment consists of 15 sub-detector systems. Most of them share similar requirements in terms of precision timing response and readout capabilities and use a common readout system based on TDCs and FPGAs, the TEL62 boards. The STRAW spectrometer is the only TDC-based detector where a dedicated solution has been chosen due to the large number of channels and the intrinsic poorer time resolution. The GTK detector, with the largest number of channels, and the LKr, HAC, and SAV calorimeters, with a continuous pulse sampling, require dedicated readout systems. In the following a brief description of the different readout systems is given.

TEL62 based readout The TEL62 [122] board is the common readout system of NA62. It is equipped with four TDC boards (TDCBs) developed inside the collaboration, hosting four high-precision HPTDC chips [123]. Each TDCB is under the control of an FPGA with up to 2 GB of RAM. The TDCBs are connected to up to 128 detector channels with an LVDS output signal and can digitize the leading and trailing edge times. Therefore a TEL62 can readout and trigger on 512 detector channels. Data from the detector front-end electronics are digitized in the TEL62 and merged in an event fragment, which is sent to the PC farm. The sub-detectors with the TEL62 readout are listed in Table 6.3.

Detector	Number of channels	Number of TEL62
KTAG	384	6
CHANTI	288	2
RICH	1 952	5
LAV	2 496	12
NA48-CHOD	128	1
CHOD SAV MUV0	304 8 9	1
MUV3	296	1
HASC	360	1

TABLE 6.3: NA62 sub-detectors sharing the TEL62 and TDC readout system.

STRAW readout Two CARIOCA [124] chips and 32 TDCs implemented within an FPGA compose the on-detector electronics of the STRAW spectrometer, a custom front-end board named COVER [125]. It is built gas and vacuum tight since it is also used as a cover for the gas operation. The back-end of the readout are custom-made Straw Readout Boards (SRBs), located 10–15 m from the detector. Each SRB reads 16 COVER boards (16$\times$16 straw tubes) for a total of 8 SRBs per chamber.

GTK readout The GTK readout system (GTK-RO) is composed of 10 custom boards containing an FPGA, acting as an interface between the TDCPix [126] on-detector readout and the clock and trigger distribution performed by the TTC. Signals from the TDCPix are sent via 200 m long optical fibers to the corresponding GTK-RO, located outside the experimental area. When an event satisfies the L0 requirements, data temporally stored inside the GTK-RO boards are sent to the GTK PC farm. This is made of six PCs (two per each station) which, after the L1 trigger response, send the data to the NA62 PC farm. The GTK can in principle be read either after the L0 or the L1 level but, since its data are not used to build the L1 response, it was decided to read it at a lower trigger rate (after L1) to put lower stress on its readout system.

CREAM based readout A dedicated readout system, based on the CREAM (Calorimeter REadout Module [127]), was developed by CAEN specifically for the NA62 LKr calorimeter. The system is also used in the HAC and SAV detectors which, however, represent only 2% of the total number of channels as shown in Table 6.4. A CREAM module manages 32 detector channels and is made of a daughterboard and a motherboard. In the daughterboard the signal from the detectors is shaped, resulting in a pseudo-Gaussian signal with 70 ns FWHM, and digitized by four 14-bit fast ADCs (FADCs) using the 40 MHz clock distributed by the TTC. The digitized signal of each FADC is sent to an FPGA, placed on the CREAM motherboard, that stores the data in its large memory (8 GB) and waits for the L1-trigger response to send them to the PC farm. In order to reduce the amount of data to be read, a channel-based zero-suppression algorithm is implemented: if the difference between the largest and smallest samples of the digitized signal is lower than a programmable value (usually 20 ADC counts) the channel data are not transferred.

Detector	Calorimeter type	Number of channels	Trigger channels
LKr	electromagnetic	13 248	864
MUV1	hadronic	176	12
MUV2	hadronic	88	6
IRC	electromagnetic	4	1
SAC	electromagnetic	4	1

TABLE 6.4: NA62 sub-detectors using the CREAM readout system.

6.4.2 Trigger system

As already mentioned, the NA62 trigger logic is based on three different trigger levels with a factor 10 of data reduction at each step (starting from 10 MHz in input to 10 kHz in output). In the run period 2016–2018 only two trigger levels were implemented since the third level was not needed due to the reduced (with respect to the nominal) beam intensity.

L0-hardware trigger

A small set of sub-detectors provides the information to build the L0-hardware trigger. This includes the CHODs hodoscopes, the RICH detector, the LAV system, the MUV3 detector, the electromagnetic and hadron calorimeters. These detectors produce the so-called trigger primitives, 64-bit words containing timing and encoding information about the events based on the specific characteristics of the detector. They are generated asynchronously by each L0 source and sent via Gigabit Ethernet, in periodic bunches every 6.4 μs, as UDP [2] packets to the L0TP. It verifies the primitives time matching and compares them with programmable reference trigger masks. In total up to 16 trigger masks (or trigger streams) can be used. The L0TP [128], which has a maximum design output rate of 1 MHz, works completely in hardware elaborating the trigger matching inside an FPGA. When one of the trigger masks is satisfied, the L0TP sends a synchronized TTC signal to all detectors, which have to reply sending data to the PC farm. The only exceptions are the GTK and CREAM-based detectors which wait for the L1-trigger response, due to their large data flux. Like any other detector, the L0TP sends data directly to the PC farm so that also the trigger information is recorded.
In the following a brief description of the generated primitives is given.

NA48-CHOD and **CHOD L0** primitives are based on hit coincidences in the same slab/tile of the detector. Primitives are generated for any charged track, and triggers are provided for either single-track or multi-track events.

RICH L0 generates primitives for charged tracks above the Cherenkov threshold based on the number of fired channels in the detector. The RICH has about 2 000 readout channels spread on four TEL62 boards. Primitives are produced by a fifth TEL62, where information from the whole detector is available using the digital OR of groups of 8 channels, called supercells.

LAV L0 has to detect the presence of photons and halo muons in the event. Primitives are based on the coincidence of both high and low discriminator thresholds in a lead-glass block. Signals close in time from adjacent blocks are assumed to belong to the same events, and a single primitive is produced. The trigger implementation used during the 2016–2018 data taking exploits information from only one of the twelve TEL62s used in the LAV system, the LAV12.

MUV3 L0 has to detect events with muons in the final state and can be used either in positive or as veto in the trigger logic. Primitives are generated by a coincidence of the two PMTs signals of the same tile of the detector.

[2] *User Datagram Protocol.*

A dedicated **Level 0 Calorimeter Trigger** (Cal-L0) [129], based on TEL62 boards with custom mezzanine cards instead of TDCBs, has been built for the detectors read out by the CREAM system: the electromagnetic (LKr, IRC and SAC) and the hadron (MUV1 and MUV2) calorimeters. In order to obtain at the L0-trigger level the rejection power required by the measurement of the $K^+ \to \pi^+\nu\bar{\nu}$ branching ratio, the calorimeter information is fundamental. However, due to bandwidth rate, they cannot be fully exploited to build the L0 response. The solution found is to sum the digitized signals from 4×4 channels (super-cells) inside the CREAM boards every 25 ns and send this sum to the Cal-L0 processor, which builds the calorimeter L0-trigger response by performing the search for clusters and computing the time, position, and energy of each cluster. Primitives are based on the number of reconstructed clusters and on the total energy released in the calorimeters. During the 2016–2018 data taking only the LKr participated in the Cal-L0.

There are two special roles in the L0-trigger logic: the Control and the Reference detectors. The Reference detector gives the time of the trigger and must always be present. Instead, the Control detector is used to generate triggers that are independent from the Reference detector, and it is fundamental for trigger-efficiency studies. During the 2016–2018 data taking the Reference and Control detectors were typically the RICH and NA48-CHOD detectors, respectively.

High Level Triggers (HLT)

The available bandwidth for permanent data storage is of $\mathcal{O}$(10 kHz). Since the L0 output rate is 1 MHz, a factor 100 of data reduction is achieved by the L1 and L2 software triggers, also referred to as High Level Triggers (HLT), which run in the online PC farm. The L1 algorithms are based on standalone information from individual sub-detectors while the L2, which uses partially reconstructed events, can exploit correlations among sub-detectors. An example is the combined information from the GTK and STRAW detectors to compute the vertex of the event. The L2 architecture was available since 2015, but no algorithms have been implemented during the 2016–2018 data taking. At that stage, an event is simply re-built by merging all the detector information after the L0 and L1 triggers. Only the detectors whose data are acquired after the L0 trigger can be used in the L1, meaning that the GTK and CREAM-based detectors are excluded. For each of the L0-trigger masks a different set of L1 algorithms can be used and some conditions can be changed independently in each mask. Special L1 triggers are the so-called autopass events, which consist of a few percents of the total L0 rate. Also if they do not satisfy the L1 requests they are collected and used for L1-trigger studies.
In the following, a brief description of the L1 algorithms is given.

KTAG L1 algorithm identifies events with a beam kaon, reducing the L0 triggers due to accidental beam particles. The algorithm requires the presence of a minimum number of KTAG sectors (typically 5 out of 8) in time with a L0 trigger.

LAV L1 algorithm uses the information from all the twelve stations in order to identify events with photons emitted at large angles. The algorithm requires the coincidence of at least two hits in a specific set of LAV stations to tag events with photons in the final state.

STRAW L1 algorithm partially reconstructs tracks in the spectrometer and computes the vertex using the nominal beam momentum and directions. Information on the track momentum and vertex is used to select either one-track or multi-track events.

PC farm The digitized data from the detector electronics are sent, after receiving a trigger signal, as UDP packets through Gigabit Ethernet optical links to the computers of the online PC farm, housed on the surface of the experimental area. The main function of the 30 PCs of the farm is to build the HLT response and verify which events pass them. The events are processed in a Round-Robin way, meaning that each node of the PC farm handles 1/30 of the events. Three merger PCs complete the NA62 PC farm. Their main task is to aggregate events that pass all the trigger levels and belong to the same burst in a common raw data file. The mergers also host the Central Data Recording (CDR) system which takes care of the transfer of the raw data files to the CERN tape system CASTOR [130] for permanent storage. For online monitoring of the data taking conditions, part of the raw files are directly reconstructed on dedicated PCs hosted within the PC farm.

6.5 The NA62 control applications

The operation of the experiment requires several control systems related both to the hardware equipment (e.g. detector power supplies, electronic boards) and the software (e.g. run conditions). For this reason three control applications have been developed: the Run Control (RC), the Detector Control System (DCS), and the Detector Safety System (DSS). The Run Control [131] manages all the devices involved in the data acquisition (from the single electronic board to the PC farm nodes), being the central control and monitoring software of the TDAQ system. It keeps track of all the run configurations, from the TDAQ settings to the beam, and saves them in a database for bookkeeping. The DCS [104] is dedicated to detector monitoring and operations, like for example the setting of high voltages in the detector power supplies. The DSS [104] is used to spot safety issues, which could be related both to hardware systems and people. Examples are the detector cooling system, the gas supplies and the vacuum system.

The three control applications are based on WinCC Open Architecture [132], a widely used industrial software developed at CERN, and implemented on a hierarchy of finite state machines (FSMs): each device connected to the system is modeled as a list of states and transitions between them. The communication among these systems and the connected hardware is handled through the DIM protocol [133].

Chapter 7
The NA62 Software Framework

The NA62 Software Framework (NA62FW) [134] has been developed by the NA62 Collaboration in order to have a common environment for event simulations, data reconstruction, and analysis. It is a ROOT [135] based environment, written in the C++ programming language plus some Fortran routines inherited from the NA48 experiment, and consists of three modules:

- The simulation package **NA62MC** for the generation of simulated events using the Monte Carlo (MC) method.
- The reconstruction package **NA62Reconstruction** for the reconstruction of both the collected data and the MC events simulated by NA62MC.
- The analysis package **NA62Analysis** for the development of simple and complex analysis. Template classes, called *Analyzer*, are the basic module of the analysis and can work independently or in complex chain.

The management of the NA62FW source code is performed using Git [136] as distributed version-control system. Any significant change of the source code defines a new NA62FW software revision identified with a label of the form *rXXX*. The software revisions employed in the central MC production as well as in the data reprocessing are further labeled in the form *vX.X.X* for better bookkeeping.

7.1 The NA62MC package

The NA62MC package is dedicated to the generation of simulated events with the Monte Carlo method. A pure beam optics without particle interactions is simulated upstream of the KTAG detector with TURTLE (*Trace Unlimited Rays Through Lumped Elements*) package [137], a beam tracking and simulation program. The GEANT4 [138], *GEometry ANd Tracking*, software toolkit developed by CERN is used for the simulation of the full experimental apparatus (geometry and material), the magnetic field and the beamline downstream of the KTAG detector. The decay of the beam particles is managed by a set of custom decay generators (mostly for kaons) inherited from the NA48/2 experiment, which include form factors and radiative corrections. In these generators, the daughter particles are generated in the rest frame of the beam and boosted according to the beam momentum in the laboratory frame. The decay region, in which the beam particles are forced to decay, can be set as external parameter of the NA62MC. Usually for kaon decays, the fiducial volume is set between 102 and 180 m from the target. The (eventual) decay of the secondary particles, those produced in beam particle decays, is normally handled by GEANT. Anyway, it can

also be handled directly by NA62MC through the internal generators in case of specific needs: in particular, neutral pions are usually forced to decay into two photons.

The simulation is kept as much as possible independent from the experimental conditions, with the only exception of the beam parameters which are supposed to be tuned on a reference run per year of the data taking. MC samples are reconstructed within the NA62Reconstruction package similarly to the data, where the detector response is modeled to reproduce as much as possible the data taking conditions. MC samples are centrally generated and reconstructed through the NA62 GRID [139] and both reconstructed and true values (those properties that particles have at generation time) are stored in the final output files. More information about the MC samples can be found in Reference [140]. In Section 7.1.1 a description of the MC samples used for this analysis is given.

7.1.1 MC samples

This work makes use of large samples of centrally produced $K^+ \to \pi^+\pi^o$ events, including radiative corrections due to internal bremsstrahlung (IB) $K^+ \to \pi^+\pi^o\gamma_{\rm IB}$. The IB amplitude is completely determined by the $K^+ \to \pi^+\pi^o$ amplitude after QED corrections [141]. It, therefore, includes the effect of multiple soft photon emission: the energy of all the soft photons is summed up providing the energy of the single photon emitted, and the momentum spectrum of the charged pion accounts for the total energy radiated. The samples were produced with the so-called KLOE generator described in Reference [142]. The radiative photon is only passed to GEANT if its energy in the K^+ rest frame is greater than 10 keV. Two different samples have been considered:

- An abundant sample of 60×10^6 $K^+ \to \pi^+\pi^o(\gamma_{\rm IB})$ events with $\pi^o \to \gamma\gamma$, resulting in events with two or three photons in the final state. This sample, referred to as $K_{2\pi(\gamma)}$ in the following, has been used to evaluate the expected background rejection. The sample was produced with the software revisions *v1.0.1* (50×10^6 events) and *v0.11.3* (10×10^6 events).

- A sample of $K^+ \to \pi^+\pi^o(\gamma_{\rm IB})$ events with the π^o undergoing the so-called Dalitz decay, $\pi^o \to \gamma e^+ e^-$. This sample, referred to as $K_{2\pi_D}$ in the following, consists of 50×10^6 simulated events (software revision *v0.11.1*) and has been used to compare the LKr energy resolution simulated by the MC to that measured in the data.

Due to the software revisions used for the production of the two samples, the beam parameters were tuned on the beam setup used during the 2016 data taking (run 6610 as reference). In all the MC samples accidental activity is added at analysis level in the GTK and KTAG detectors by the ***UpstreamPileUpGenerator*** tool as described in Section 7.3.2. No accidental activity is emulated in all the other detectors.

7.2 The NA62Reconstruction package

The collected data are stored in raw data files which contain the readout outputs of each sub-detector. During the reconstruction phase, those information are decoded and simple objects (*hits*) are created containing the time, amplitude, and channel of a specific pulse. However, MC files produced by the NA62MC module contain only the physics signal generated in the detectors. In order to have the very same reconstruction algorithms running on both data and simulation, MC events undergo a digitization stage where the response of the detector electronics is emulated and the hits are created. Grouping in-time and adjacent hits, more complex objects containing higher level information, *candidates*, are created. Examples used in this work are tracks in the STRAW spectrometer and clusters in the LKr calorimeter (see Section 7.2.1 and Section 7.2.2, respectively). In particular, the latter ones play a key role in the photon identification. Reconstructed files for both data and MC are written as ROOT files for storage on EOS [143], the CERN disk-based data storage system.

7.2.1 STRAW track reconstruction

Track candidates are reconstructed starting from the signals of hit straws in each plane of a view module of a chamber. The drift time, measured using as reference the average time of the NA48-CHOD hits recorded within 25 ns from the trigger, is converted into a position information (the distance from the anode wire of the hit straw) using a GARFIELD simulation [144]. View-hits are formed by at least two hit straws placed in consecutive planes of a view in one chamber. A pattern recognition algorithm is used to determine the position of the view-hit in the NA62 reference frame. View-hits are clustered in each chamber in order to identify the space points due to the trajectory of a particle. The space points are grouped in track candidates: segments between chamber 1(3) and 2(4) are formed using a pattern recognition algorithm and their compatibility with the bent of the magnetic field in the xz plane is verified. The quality and the parameters of the track (momentum and directions) are obtained with a fit employing a recursive Kalman filter technique [145], which takes into account the mapping of the magnetic field produced by the MNP33 magnet. More detailed information about track reconstruction in the STRAW spectrometer can be found in Reference [146].

7.2.2 LKr cluster reconstruction

The LKr reconstruction code has been inherited from the NA48 software [147]. A digital filter compares the digitized signals of a CREAM board to reference pulses and assigns the corresponding energy and time to the hit. Templates of reference pulses are obtained with special runs without beam using an internal charge injection system in order to calibrate the response of the LKr cells. Hits are clustered starting from a seed, which is defined as a cell with energy of at least 250 MeV and greater than the neighboring 8 cells. All hits around 11 cm from the seed are considered for the cluster. The cluster time corresponds to

the seed time, while the energy is the sum of the hit energies and the position the energy-weighted average of the hit positions. Corrections to cluster energies and positions are applied to treat clusters close in space and in time, and to handle the presence of dead cells. The energy of the clusters is also corrected to account for the non-linearity induced by the online zero-suppression algorithm. These corrections are applied at the analysis stage by the ***LKrClusterCorrections*** [134] tool. The clustering algorithm implemented within the NA62Reconstruction module, the so-called *LKr standard cluster reconstruction*, is optimized for the energy resolution. However, a non negligible inefficiency in the photon detection is introduced. In order to achieve the best result in terms of photon rejection, an additional reconstruction, called *LKr auxiliary*, has been implemented. In this reconstruction, hits from adjacent cells (less than 10 cm spatial distance) with an energy of at least 40 MeV are clustered together. Time, energy and position of an auxiliary cluster are defined as for the standard reconstruction.

7.3 The NA62Analysis package

The NA62Analysis package has been conceived in order to handle most of the technicalities in reading and writing the input and output ROOT files. A set of standard tools and analysis algorithms (usually referred to as Analyzer) are available within the NA62FW. Among others, tools for the association of the reconstructed STRAW tracks with candidates in the other sub-detectors, as well as those used to apply, at the analysis stage, energy and momentum corrections to the reconstructed candidates are available. Two examples, used in this work, are given in the following: the algorithm ***GigaTrackerRecoAlgorithm*** and the tool ***UpstreamPileUpGenerator***.

7.3.1 GigaTrackerRecoAlgorithm

Kaon candidates in the GTK detector are reconstructed at analysis level using the algorithm ***GigaTrackerRecoAlgorithm*** [134]. Hits in the three stations within a specific time window with respect to a reference time are considered. As default, the time window is ± 10 ns and the reference time is the trigger time. Hits are combined along directions compatible with the beam particle trajectories. Only combinations of three hits (one for each station) are considered as candidate. A least squared fit is performed to measure the slope of the trajectory in the xz plane, with the positions in the GTK3 station corrected by the kick of the TRIM5 magnet. The momentum and the slope in the yz plane are computed analytically assuming the nominal value of the magnetic field of the achromat dipoles. The following conditions are required on the momentum, direction, and time of a candidate:

- The momentum must lie in the range 72–78 GeV/c.
- The slope in the xz plane must be between 0.9 and 1.6 mrad.
- The slope in the yz plane must be between -0.3 and 0.4 mrad.

Fine corrections on the candidate momentum and direction are also applied. These are obtained by the comparison of the corresponding value from $K^+ \to \pi^+\pi^-\pi^+$ events selected kinematically on data using only information from the STRAW tracks.

7.3.2 UpstreamPileUpGenerator

The effect of accidental beam particles is emulated by the ***UpstreamPileUpGenerator*** [134] tool, which injects accidental activity in the KTAG and GTK detectors on the fly while analyzing MC samples. Pileup hits are added synchronously in both detectors according to the distribution of the instantaneous beam intensity (assuming 300 MHz integrated beam intensity) and with different response depending on the beam particle type as extracted from data. The reconstruction algorithms are then re-run again, in order to update the event candidates.

Chapter 8
The NA62 Run I

The first data taking period (Run I) of NA62 started in April 2016 and finished in November 2018, with about 6 months per year of running. After the full detector installation in 2015, few months of 2016 were dedicated to the final commissioning of the GTK detector and the deployment of the full trigger chain. The main physics sample in the 2016 run period, was acquired from mid September to mid October at an average beam intensity of 35–40% of the nominal intensity, corresponding to an integrated flux of about 5×10^{11} kaon decays in the fiducial volume. This represents the first data set recorded by the experiment suitable for the measurement of the $K^+ \to \pi^+\nu\bar{\nu}$ branching ratio, whose results [89] proved the validity of the decay-in-flight technique.

The improvement in the data taking stability achieved at the end of the 2016 run period, as well as the better handling of the spikes in the instantaneous beam intensity, allowed for the 2017 data taking to increase the beam intensity to about 60–65% of the nominal. This resulted in about 2×10^{12} kaon decays in the fiducial volume collected in the 2017 run period. Since the work presented in this thesis is based on a sub-sample of data collected in 2017, a more detailed description of the data taking conditions adopted for this run period is given in Section 8.1.

The data taking conditions in the 2018 run period were very similar to those in 2017. Data were acquired at an average beam intensity of 60–70% of the nominal intensity. In total about 4×10^{12} kaon decays were recorded and available for physics analysis. In the $K^+ \to \pi^+\nu\bar{\nu}$ analysis of 2016 data [89], the main background contribution was identified to be due to beam-related in-time activity like, for example, the simultaneous passage of a beam pion with a kaon decaying between two stations of the GTK detector. In order to mitigate this category of events, referred to as upstream background, at the beginning of the 2018 data taking the adjustable collimator placed between the last two GTK stations was replaced with a fixed collimator providing a wider shielding against beam activity generated upstream.

In parallel to the main trigger stream, dedicated to collect $K^+ \to \pi^+\nu\bar{\nu}$-like events, different trigger configurations were implemented to study lepton number and flavor violation in kaon decays and to explore the dark sector. In addition, a few hours of data taking in 2016 and 2017 and more than one full week in 2018 were dedicated to run in beam dump mode. The experiment will restart the data taking in 2021 after the long shutdown (LS2) of the CERN accelerator machines.

8.1 The 2017 data taking

During the 2017 run period about 2×10^{12} kaon decays were recorded. Data were divided in four physics data sets (denoted as *Samples A*, *B*, *C* and *D*) defined by homogeneous data taking conditions concerning both the trigger and the detectors configurations. The four samples were named in reverse order of the time of the data taking and after quality checks of the data:

- *Sample D*: same experimental setup as in the 2016 run period with upgrade on the CHOD electronics.
- *Sample C*: final trigger conditions with 12.5 ns L0TP granularity [1] and the CHOD detector completely integrated in the trigger chain.
- *Sample B*: final trigger conditions with 6.25 ns L0TP granularity.
- *Sample A*: same as *Sample B* with a temporary shielding against upstream background inserted in the final collimator between the last two GTK stations. [2] This sample is the highest quality data set collected in the 2017 run period.

Table 8.1 lists the data sets collected in the 2017 run period, while the trigger conditions are described in Section 8.1.1.

Sample	Period	Runs	Number of bursts
D	15 June – 03 July	7615 – 7721	42 218
C	06 July – 22 July	7735 – 7873	31 537
B	23 July – 18 September	7876 – 8107	151 466
A	21 September – 22 October	8134 – 8282	83 940

TABLE 8.1: Four physics data sets were acquired in the 2017 data taking at an average beam intensity of 60–65% of the nominal intensity.

The search for $\pi^o \rightarrow$ *invisible* decays is based on the *Sample A*. In total 75 runs have been analyzed, which correspond to about 5.5×10^{11} kaon decays in the fiducial volume. The amount of data in this sub-sample is comparable with those collected in the 2016.

8.1.1 Trigger configurations

In the 2017 data taking eight physics-trigger streams were acquired together with a control-trigger stream used for normalization and trigger efficiency studies.

The $\pi\nu\bar{\nu}$ trigger mask is mainly devoted to the $K^+ \rightarrow \pi^+\nu\bar{\nu}$ analysis, and performs a partial particle identification and π^o rejection already at trigger level. However other analyses with a similar final state (one track and nothing else) can profit of the data collected

[1] The granularity is the time window in which only one primitive is expected by the L0TP. The sub-detector trigger systems encode all the events happening in this time window into a single primitive.

[2] The temporary shielding was then replaced before the 2018 data taking with a new fixed collimator.

through this trigger stream, like the search for $\pi^o \to invisible$ decays.

The **Non-muon** trigger mask provides a sample of events without muons in the final state. Precision SM measurements like the branching ratio of the $K^+ \to e^+\nu_e\gamma$ and $K^+ \to \pi^+\gamma\gamma$ decays use this trigger stream.

The **Muon multi-track** and the **Electron multi-track** trigger masks allow to select events with multiple charged particles in the final state with at least one muon or one electron, respectively. $K^+ \to \pi\mu e$, $K^+ \to \pi ee$ [86], $K^+ \to Xee$ and $\pi^o \to Xee$ decays are examples of analyses that can be performed on data collected with these two trigger streams. A more general **Multi-track** trigger mask was also implemented in order to select $K^+ \to \pi^+\pi^+\pi^-$ decays, which are used as normalization and control sample for multi-track analyses.

The **Di-Muon** trigger mask selects events with a muon pair in the final state, like the decays $K^+ \to \pi\mu\mu$ [86]. Thanks to the absence of the KTAG condition at L1, searches for long-lived exotic particles produced in the beryllium target or in the TAXes and decaying into a muon pair in the fiducial volume are also possible.

Data collected with the **Muon-exotic** trigger mask are employed to search for $\pi\mu$ and $\mu\mu$ final states, produced by the decay of long-lived exotic particles originating from the beryllium target. Those data acquired in the so-called parasitic beam dump mode extend the NA62 potential in the search for exotic particles.

The **Neutrino** trigger mask is intended to search for neutrino to muon conversions within the calorimeters by fully reconstructing $K^+ \to \mu^+\nu_\mu$ decays. This trigger stream was implemented at the beginning of the 2017 data taking for preliminary studies of neutrino oscillations ($\nu_\mu \leftrightarrow \nu_e$) at NA62 [148].

In addition to the physics-trigger masks, an independent **Control** trigger stream were also implemented. It is a minimum bias trigger which involves only the NA48-CHOD detector and allows to select control samples for trigger efficiency studies.

The nine trigger streams are listed in Table 8.2, each with its L0 and L1 conditions, which are described in the following.

L0-trigger conditions

Starting from a common L0-trigger source, the RICH detector used as reference time, different configurations of primitives were used for the L0, combining information from the CHOD and MUV3 detectors and the LKr calorimeter. Primitives from the NA48-CHOD detector were used to generate the independent control-trigger stream. In the following a brief description of the L0 primitives used in the trigger masks of the 2017 data taking is given.

Trigger mask	L0 conditions	D	L1 conditions
$\pi\nu\bar{\nu}$	RICH×!Q_x × UMTC×!MUV3×!E30	1	KTAG×!LAV×STRAW
Non-muon	RICH × Q1×!MUV3	200	KTAG
Muon multi-track	RICH × Q_x × MO1 × E10	10	KTAG×$\text{STRAW}_{\text{Ex.}}$
Electron multi-track	RICH × Q_x × E20	8	KTAG×$\text{STRAW}_{\text{Ex.}}$
Multi-track	RICH × Q_x	100	KTAG×!LAV×$\text{STRAW}_{\text{Ex.}}$
Di-muon	RICH × Q_x × MO2	2	$\text{STRAW}_{\text{Ex.}}$
Muon-exotic	RICH × Q2 × MO1 × E10	5	!KTAG×!LAV×$\text{STRAW}_{\text{Ex.}}$
Neutrino	RICH × MOQ_x×!Q2	20	KTAG
Control	NA48-CHOD	400	–

TABLE 8.2: Eight physics- and one control-trigger masks were used during the 2017 data taking. Due to the limited availability of the trigger bandwidth different downscaling factor (D) were applied to the L0-trigger conditions.

The **RICH** primitive gives the reference time of the L0 trigger and has to be present in all the physics-trigger masks. It requires at least three hits in the detector within few ns.

The **CHOD** primitives are used to define the event topology by selecting single or multi-track events. The configurations of primitives used in the 2017 data taking are:

- The Q1 and Q2 conditions require at least one and two hits in the detector, respectively. These conditions select events with at least one and two charged tracks in the final state, respectively.
- The Q_x condition requires at least two hits in diagonally-opposite quadrants of the detector. This condition selects final state with at least two tracks with opposite charge, resulting very efficient in the selection of processes like $K^+ \to \pi^+\pi^+\pi^-$ and $\pi^o \to e^+e^-\gamma$.
- The UMTC (*Upper Threshold Multiplicity*) condition requires that less than 6 tiles have fired in the detector. This requirement is very effective in the suppression of multi-track events as well as events with photons converting within the RICH mirrors.

The **MUV3** primitives are used to select events with muons in the final state. They can also define the topology of the events by requiring the number of muons that must be present in the final state. The configurations of primitives used in the 2017 data taking are:

- The MUV3 condition requires the presence of at least one hit in the detectors, indicating the presence of at least one muon in the event.
- The MO1 and MO2 conditions require at least one and two hits in the detector outer tiles, respectively. These conditions select events with at least one and two muons in the final state, respectively. The exclusion of the inner part of the detector allows to strongly reduce the contribution of muons from beam pion decays, which tend to hit the inner tiles.

- The MOQ_x condition requires at least two hits in the outer tiles from opposite quadrant of the detector. Analogously to the MO2 condition, this requirement selects final states with two muons but preferring the component where the muons have opposite charge.

The **LKr** primitives allow to identify events with electromagnetic showers inside the calorimeter. The configurations of primitives used in the 2017 data taking are:

- The E10 and E20 conditions require more than 10 GeV and 20 GeV, respectively, deposited in the LKr calorimeter. These conditions prefer events with at least one electromagnetic shower.
- The E30 condition requires more than 30 GeV deposited in the calorimeter or more than one reconstructed cluster with energy greater than 1 GeV. This condition, usually applied negatively as a veto, is used to detect events with electrons or neutral pions in the final state.

The **NA48-CHOD** is used to produce the control-trigger mask and requires one or more time coincidences between hits from the horizontal and vertical scintillator planes of the detector. This condition provides a sample of events with at least one track in the final state.

L1-trigger conditions

Three L1-trigger algorithms were used during the 2017 data taking exploiting the information from the KTAG, STRAW and LAVs detectors. In the following a brief description of the L1 algorithms employed in the trigger masks of the 2017 data taking is given.

The **KTAG** algorithm is used to detect a kaon in time with the final state selected by the L0 masks. It is mainly used in positive with the exception of the Muon-exotic trigger mask, which is sensitive to long-lived particles produced in the target. The algorithm requires at least five (out of 8) fired sectors when a beam particle crosses the detector in a ± 10 ns time window around the L0-trigger time.

The **LAV** algorithm requires a time coincidence of at least three hits in all the LAV stations, in order to identify events with photons emitted at large angles. It is mainly used as a veto for $K^+ \to \pi^+\pi^o$ events where at least one photon from the π^o is inside the acceptance of the LAV system. [3]

The **STRAW** algorithm implements a lighter version of the STRAW reconstruction software. It verifies the quality and the number of tracks in the final state. Using the closest distance of approach (CDA) technique, a vertex is computed between each track and the nominal beam direction. Tracks are selected if the longitudinal position of the vertex

[3] Starting with run 8025 (*Sample B*) the first LAV station was excluded in the algorithm to reduce the rate of accidental veto of the LAV system.

(z_{vertex}) is below 180 m and the CDA<20 cm with respect to the beam axis. In order to suppress events with beam pions scattering on the last station of the GTK detector, the track momentum is required to be lower than 50 GeV/c. Two different algorithms were implemented, sharing the track quality requirements described above: the first is mainly used to select single-track events and requires a positively charged track in the final state not forming a vertex (CDA larger than 3 cm) with any negatively charged track present in the event; the second, denoted as $\text{STRAW}_{\text{Exotic}}$, is mainly used to select multi-track events and requires a negative track in the final state.

8.2 The Data processing

The offline data processing of the raw data consists of 4 steps: calibration, reconstruction, filtering and post-processing. During the calibration step offline corrections, to be applied at the reconstruction stage, are evaluated. These include detector time alignments, the LKr energy scale, the GTK and STRAW momentum scales and alignments. During the entire Run I period more than 4 PB of raw data have been stored on tape in the CERN permanent storage system. The size of the reconstructed files is not far from those of the raw files. The handling of such a large amount of data is inconvenient at the analysis stage. Therefore, after the reconstruction, data are filtered in different output streams: events with particular signature are selected according to the analysis topic in order to skim the amount of data to analyze. The post-processing stage is dedicated to the assessment of the data quality. A specific set of analysis routines has been developed for this purpose: events where reconstruction problems are spotted, as well as entire bursts showing hardware issues, are flagged as *bad* in order to be skipped during the analysis stage. These analysis routines are also used for a quasi-online data quality monitoring during the data taking.

The *Sample A*, which is used for the search for $\pi^o \to invisible$ decays, has been reconstructed with the software revision *v1.0.2*, and filtered with the ***PNNFilter*** filter-analyzer described in Section 8.2.1.

8.2.1 PNNFilter

The *PNNFilter* [134] has been developed to select events with a single-track topology for the $K^+ \to \pi^+\nu\bar{\nu}$ analysis. This filter uses data collected with the $\pi\nu\bar{\nu}$- and the control-trigger masks. Different conditions are applied in the two trigger streams, after requiring no general reconstruction errors in any of the detectors. In case an event is flagged as pertaining to both the control and the $\pi\nu\bar{\nu}$ streams, the control-trigger filtering conditions are applied.

$\pi\nu\bar{\nu}$-trigger stream A quality check of the event is performed, by requiring: at least two NA48-CHOD hits, one in a vertical and one in a horizontal slab of the detector, belonging to the same quadrant; at least one and no more than ten tracks reconstructed in the STRAW

spectrometer. Among all the reconstructed STRAW tracks at least one must be classified as good quality according to the following requirements:

- The track is formed by hits reconstructed in all of the 4 spectrometer chambers.
- The difference in the reconstructed track momentum measured before and after the fit ($\Delta p_{\rm fit}$) is less than 25 GeV/c and the chi square of the fit ($\chi^2_{\rm fit}$) is less or equal to 30.
- The track is inside the geometrical acceptance of the NA48-CHOD, CHOD, LKr and MUV3 detectors.
- The track momentum lies in the range 8–50 GeV/c.
- The track must not form a good vertex (using the closest distance of approach, CDA) with any other track which have hits reconstructed in all 4 chambers and $\chi^2_{\rm fit} \leq 30$. A vertex is defined as good if its longitudinal coordinate ($z_{\rm vertex}$) is between 80 and 180 m, the CDA less than 10 mm and the two tracks are in time within 10 ns.

STRAW tracks classified as good quality must be associated to a horizontal-vertical pair of hits in the NA48-CHOD detector (whose time is taken as reference time for the track) and to a KTAG candidate (reconstructed with at least 4 fired sectors), but not associated to a MUV3 signal. At least one hit in each of the three GTK stations must be present within $\pm$2 ns from the track reference time. A partial photon rejection is already applied at filter level by the requirement of no in-time photons detected in the LKr calorimeter or in the LAV system. The conditions applied for the photon identification are softer than those needed in the analysis: photons in the LKr calorimeter are detected by the presence of standard LKr clusters at least 18 cm away from the STRAW track impact point at the LKr surface and within $\pm$5 ns from the track reference time; photons in the LAV system are defined as signal in any block of the 12 stations within $\pm$2 ns from the track reference time.

Control-trigger stream More relaxed conditions are required with respect to those applied in the $\pi\nu\bar{\nu}$-trigger stream. A quality check of the event is performed, by requiring: at least two NA48-CHOD hits, one in a vertical and one in a horizontal slab of the detector, belonging to the same quadrant; at least one track reconstructed in the STRAW spectrometer. Among all the reconstructed STRAW tracks at least one must satisfy the following requirements:

- The track is formed by hits reconstructed in all of the 4 spectrometer chambers.
- The track is inside the geometrical acceptance of the NA48-CHOD, LKr and MUV3 detectors.
- The track is associated to a horizontal-vertical pair of hits in the NA48-CHOD detector, providing the track reference time.

At least one hit in each of the three GTK stations must be present within $\pm$2 ns from the track reference time.

Part II

SEARCH FOR $\pi^o \rightarrow$ *invisible* DECAYS

Chapter 9
The Analysis Strategy

A pure sample of tagged π^o mesons is available in NA62 from the selection of events with a decay $K^+ \to \pi^+\pi^o(\gamma)$ by means of the sole information on the K^+ and its daughter π^+. Both charged particles are individually tracked, their particle-identification is positively determined, and a time and spatial consistency among the two is required to reconstruct the decay vertex in the detector fiducial volume. The two-body kinematics of the $\pi^+\pi^o$ final state is enforced by the requirement for the squared missing mass, M^2_{miss}, computed from the measured kaon and pion 4-momenta (P_{K^+} and P_{π^+}) as

$$M^2_{\text{miss}} = (P_{K^+} - P_{\pi^+})^2 \ , \tag{9.1}$$

to be compatible with the squared π^o mass. A tight condition on this kinematic variable rejects the background due to other kaon decays to a 10^5 level and, secondly, reduces and softens the contribution of the $\pi^+\pi^o\gamma$ radiative decay. The selection algorithm, as presented in Chapter 10, is called "$K_{2\pi}$ selection" and the selected sample is referred to as "$K_{2\pi}$ sample". The $K_{2\pi}$ sample corresponds to the tagging of a pure π^o beam with an event-by-event determination of momentum and, given the very short π^o lifetime, decay point. A $K_{2\pi}$ sample selected on control-trigger data is used as normalization sample for the analysis and determines the number of tagged π^o mesons, N_{π^o}. [1]

The search for $\pi^o \to$ *invisible* decays is performed after applying the $K_{2\pi}$ selection to $\pi\nu\bar{\nu}$-trigger data (see Section 8.1.1 for the trigger conditions). Due to the topology of the desired events, π^o decays into *"invisible"* (undetectable) particles, stringent requirements are applied to detect and to reject events with any additional activity correlated in time to the incoming K^+ or its daughter π^+ due to π^o visible decays. The ensemble of these requirements is referred to as "photon-rejection algorithm" and is described in Chapter 11.

After rejecting any event incompatible with the signature of $\pi^o \to$ *invisible*, how can the remaining sample be interpreted? Crucially, how many background events are expected to be present in the selected sample? After the photon-rejection conditions, the dominant background left is due to $K^+ \to \pi^+\pi^o(\gamma)$ decays with $\pi^o \to \gamma\gamma$, when all the photons are undetected. Therefore, having an *a priori* knowledge of the $\pi^o \to \gamma\gamma$ rejection power leads to an estimate of the expected number of background events. The expected contamination from $\pi^o \to \gamma\gamma$ background events is determined from a combination of data-based and MC simulations studies, as presented in Chapter 13 and Chapter 14. The strategy adopted consists in studying the response of the photon-veto system to visible

[1] Since the selection criteria of the normalization sample efficiently reject events with a Dalitz π^o decay ($\pi^o \to e^+e^-\gamma$), the normalization sample consists of $K^+ \to \pi^+\pi^o(\gamma)$ events with $\pi^o \to \gamma\gamma$ decays.

products of π^o decays, by evaluating in control-data samples "single-photon" efficiencies guaranteed by the sub-detectors composing the photon-veto system. Using an abundant MC sample of $K^+ \to \pi^+\pi^o(\gamma)$ decays, the single-photon efficiencies are combined to evaluate the probability that each single event might survive the signal selection. The estimate of the expected π^o rejection inefficiency (ε_{π^o} in the following) is obtained as the average of the survival event probabilities and is the figure of merit to determine the expected background contributions, which depend on the π^+ momentum, and ranges from a few 10^{-7} to less than 10^{-8}. The number of expected background events (Chapter 15) is evaluated as:

$$N_{\rm bkg} = N_{\pi^o} \times \varepsilon_{\pi^o} \times \varepsilon_{\rm trigger} \tag{9.2}$$

where N_{π^o} is the number of tagged π^o mesons evaluated on control-trigger data after applying the $K_{2\pi}$ selection; ε_{π^o} is the expected rejection inefficiency provided by the photon-rejection algorithm; $\varepsilon_{\rm trigger}$ is the $\pi\nu\bar{\nu}$-trigger efficiency evaluated for a $\pi^o \to invisible$ signal. Any background source other than the dominant is found to be negligible: as discussed in Chapter 15, the total contamination from other sources is at the level of a few 10^{-11} and, in general, at most $\simeq 1\%$ with respect to the π^o-induced contamination.

For method validation (Chapter 17), data sub-samples where no signal is expected standing to past searches for $\pi^o \to invisible$ are defined, with an expected background contamination of $\mathcal{O}(10^{-7})$. The data in these samples are compared to the expected background and systematic uncertainties are derived from these cross checks. The statistical treatment of the CL_s method [103] is used to evaluate the 90% confidence level (CL) upper limit for the number of signal events. The analysis is performed in bins of the π^+ momentum, with the momentum signal region chosen in order to optimize the analysis sensitivity in the hypothesis of absence of signal (Chapter 18).

The branching ratio for $\pi^o \to invisible$ is computed as:

$$\mathrm{BR}(\pi^o \to invisible) = \mathrm{BR}(\pi^o \to \gamma\gamma) \times \frac{N_{\rm s}}{N_{\pi^o} \times \varepsilon_{\rm signal} \times \varepsilon_{\rm trigger}} \tag{9.3}$$

where $N_{\rm s}$ is the number of signal events obtained after background subtraction from the observed event counts, after applying the $K_{2\pi}$ selection, the photon-rejection algorithm, and the momentum-cut requirements to $\pi\nu\bar{\nu}$-triggered events; N_{π^o} is the number of tagged π^o mesons evaluated after applying the $K_{2\pi}$ selection on control-trigger data and without any of the conditions in the photon-rejection algorithm; $\varepsilon_{\rm signal}$ and $\varepsilon_{\rm trigger}$ are the efficiencies for the conditions of the photon-rejection algorithm and of the $\pi\nu\bar{\nu}$ trigger, respectively, evaluated for a $\pi^o \to invisible$ signal.
In the above Equation (9.3), the efficiency of the $K_{2\pi}$ selection for $\pi^o \to \gamma\gamma$ cancels at first order with that for $\pi^o \to invisible$, while the control-trigger efficiency for $\pi^o \to \gamma\gamma$ is equal to one within a few per mil.

The $\pi^o \to invisible$ analysis has been set up with a sub-sample of data collected in

the 2016 run period. It is important to underline that the signature for $K^+ \to \pi^+\pi^o$ with $\pi^o \to$ *invisible* events is the same as that for a $K^+ \to \pi^+\nu\bar{\nu}$ decay. In this respect, both the $K_{2\pi}$ selection and the photon-rejection algorithm directly follow the selection criteria applied for the analysis of $K^+ \to \pi^+\nu\bar{\nu}$ decays with 2016 data [1, 2]. Since the photon-rejection algorithm was optimized for the $K^+ \to \pi^+\nu\bar{\nu}$ analysis on the 2016 sample, the complete $\pi^o \to$ *invisible* analysis has been performed blind with a sample of data collected in the 2017 data taking leaving unchanged/frozen both the $K_{2\pi}$ selection and the photon-rejection conditions. The analyzed sample, 2017 Sample A (see Chapter 8 for the data taking conditions), consists of about 5.5×10^{11} kaon decays collected in the fiducial volume. The NA62 Software Framework, described in Chapter 7, has been adopted regarding the MC simulations, the data reconstruction, and the analysis tools.

Chapter 10
The $K^+ \to \pi^+\pi^o(\gamma)$ Selection

$K^+ \to \pi^+\pi^o(\gamma)$ events ($K_{2\pi}$ in the following) are selected by the use of only the information from the two charged particles involved in the process, the K^+ and the π^+. The two particles are individually tracked and, time and spatial consistency among them is required to reconstruct the decay vertex. Cuts are applied against the so-called upstream background (which includes early kaon decays, beam pion decays, or kaon-pion mis-matching) and a good particle identification is required to identify the particle in the final state as a charged pion. The variable used to kinematically select the $K_{2\pi}$ signal events is the squared missing mass M^2_{miss}, defined according to Equation (9.1). The selection can be divided into four different steps:

1. Selection of events with a single track in the final state (single-track events).
2. Selection of K^+ decays in the fiducial volume.
3. Particle identification of the π^+ candidates.
4. Definition of the $K_{2\pi}$ signal region.

At the reprocessing level important actions were taken in order to ensure the good quality of the collected and reconstructed data (see Section 8.2). Preliminary conditions are applied at the analysis level to pre-select clean events: no global readout errors in any detector must be present; at least one and less than ten track candidates must be reconstructed in the STRAW spectrometer; at least one hit in both the NA48-CHOD and the LKr detectors must be reconstructed and no more than 2 000 hits must be present in the LKr calorimeter.

10.1 Single-track events

Events with a single charged particle in the final state are selected starting from all tracks reconstructed (according to Section 7.2.1) in the STRAW spectrometer. A correction on the three-momentum of each STRAW track is applied by the ***SpectrometerTrackCorrections*** [134] tool, which acts on all reconstructed STRAW tracks according to the formula:

$$p_{\text{corr}} = (1+\beta)(1+\alpha\, q\, p_{\text{uncorr}})\, p_{\text{uncorr}} \tag{10.1}$$

where q is the charge of the track, p_{uncorr} the track three-momentum measured at the reconstruction stage, and α and β are run-dependent parameters centrally evaluated at the reprocessing level with an independent selection of $K^+ \to \pi^+\pi^+\pi^-$ events [149]. α is a quadratic correction interpreted as a mis-alignment of the STRAW chambers 1 and 4, which is extracted looking at the stability of the reconstructed 3-pion mass $M(3\pi)$ as a function

of the momentum of the negative pion. β is connected with the difference between $M(3\pi)$ and the nominal kaon mass and due to a mis-measurement of the spectrometer magnetic field. Typical numbers are of the order 10^{-5} GeV^{-1} for α and 10^{-3} for β.

Among all tracks reconstructed in the STRAW spectrometer, only those being inside the geometrical acceptance of the downstream detectors (see Table 10.1), having positive charge and classified as having good quality are considered for the selection. The label of good quality is given to STRAW tracks that meet the following conditions:

- The track has hits in all the 4 STRAW chambers.
- The chi square of the track fit χ^2_{fit}, performed at the track reconstruction stage, is ≤ 20.
- The difference between the track momenta measured before and after the fit (Δp_{fit}) must be ≤ 20 GeV/c.

Detector	z_{detector} **[m]**	x_{detector} **[mm]**	r_{inner} **[mm]**	r_{outer} **[mm]**
Track required inside detector acceptance				
STRAW chamber 1	183.508	101.2	75	1 000
STRAW chamber 2	194.066	114.4	75	1 000
STRAW chamber 3	204.459	92.4	75	1 000
STRAW chamber 4	218.885	52.8	75	1 000
RICH entrance	219.445	34	101	1 100
RICH exit	237.326	2	101	1 100
CHOD	238.132	0	140	1 070
NA48-CHOD v. plane	239.009	0	125	1 100
NA48-CHOD h. plane	239.389	0	125	1 100
LKr	241.093	0	150	1130 (octagon apothem)
MUV1	243.418	0	130	1 100 (square)
MUV2	244.435	0	130	1 100 (square)
MUV3	246.800	0	130	1 200 (square)
Track required outside detector acceptance				
LAV12 front face	238.313	0	1 070	-
LAV12 back face	238.783	0	1 070	-
IRC	239.700	0	145	-

TABLE 10.1: Position of the detector centers in the xz plane (all detectors are centered at $y = 0$). The acceptance conditions are applied as circular cuts, except for the outer part of the LKr calorimeter and of the MUVs detectors.

The good-quality STRAW tracks must not form a vertex with any other "not-fake" track. [1] The two-track vertex is defined as the median point between the two STRAW tracks

[1] A STRAW track is classified as fake if it is reconstructed in the spectrometer with the information from only three chambers and has either $\chi^2_{\text{fit}} > 30$, or one or more hits in common with another track.

at their closest distance of approach (CDA). The good-quality STRAW track is classified as having a multi-track-vertex and discarded if the longitudinal position of the two-track vertex is between 60 and 200 m, the CDA less than 15 mm and the time difference between the two STRAW tracks less than 50 ns.

10.1.1 Association to downstream detectors

For all the STRAW tracks passing the above selection, matching conditions with candidates reconstructed in the NA48-CHOD, CHOD, and LKr detectors are required. These conditions are called "downstream selection". For the RICH and the MUVs (MUV1–3) detectors, at this stage of the selection the presence of one associated candidate is registered but not enforced. The matching criteria make use of timing and spatial information, using detector candidates from the standard reconstruction and applying for the association to the STRAW track standard routines present in the ***NA62Analysis*** package of the software framework. The two exceptions are the NA48-CHOD and RICH detectors, where the candidates are reconstructed at analysis level.

Track–NA48-CHOD association

Candidates are reconstructed at analysis level [1] by pairing horizontal and vertical hits belonging to the same quadrant of the NA48-CHOD detector. The time of the candidate ($T_{\text{NA48-CHOD}}$) is taken as the average of the hit times in the horizontal and vertical planes (t_{vhit} and t_{hhit}). The coordinate of the transverse position of the candidate, $\vec{r}_{\text{NA48-CHOD}}$, is taken as the x and y hit coordinates at the vertical and horizontal planes, respectively. The candidate associated to the STRAW track is selected by minimizing the discriminant:

$$\text{Discr}_{\text{NA48-CHOD}} = \left(\frac{t_{\text{vhit}} - t_{\text{hhit}}}{3\sigma_t}\right)^2 + \left(\frac{T_{\text{NA48-CHOD}} - T^{\text{STRAW}}_{\text{track}}}{3\sigma_T}\right)^2 + \left(\frac{|\vec{r}_{\text{NA48-CHOD}} - \vec{r}^{\,\text{NA48-CHOD}}_{\text{track}}|}{2\sigma_{\vec{r}}}\right)^2, \tag{10.2}$$

where $T^{\text{STRAW}}_{\text{track}}$ is the track time as measured by the spectrometer and $\vec{r}^{\,\text{NA48-CHOD}}_{\text{track}}$ the extrapolated track position at the vertical (x) and horizontal (y) planes of the NA48-CHOD detector. The resolutions $\sigma_t = 3$ ns, $\sigma_T = 7$ ns and $\sigma_{\vec{r}} = 13$ mm are taken from the corresponding distributions. [2] A discriminant less than 15 and a time coincidence with the STRAW track time in ± 20 ns are required for the association. In case no association is found, the STRAW track is rejected.

Track–CHOD association

Candidates in the CHOD hodoscope are defined as hits that fire at least one pad of the detector. The output of the standard tool ***SpectrometerNewCHODAssociation*** [134] is used: all hits overlapping a circle around the extrapolated track impact point are associated to the STRAW track. Among all the associated candidates only those in a time window of ± 5 ns

[2] The coefficients in front of the resolutions optimize the impact of the single contributions of the variables on $\text{Discr}_{\text{NA48-CHOD}}$ [1].

with respect to the time of the previously selected NA48-CHOD candidate (used here as reference time for the STRAW track) are considered. The best associated CHOD candidate is the one closest in space with the extrapolated track position $\vec{r}^{\,\mathrm{CHOD}}_{\mathrm{track}}$ at the detector plane, and it must satisfy the following condition on a discriminant variable:

$$\mathrm{Discr}_{\mathrm{CHOD}} = \left(\frac{T_{\mathrm{CHOD}} - T^{\mathrm{STRAW}}_{\mathrm{track}}}{2\sigma_T}\right)^2 + \left(\frac{|\vec{r}_{\mathrm{CHOD}} - \vec{r}^{\,\mathrm{CHOD}}_{\mathrm{track}}|}{2\sigma_{\vec{r}}}\right)^2 < 10, \qquad (10.3)$$

where the resolutions are $\sigma_{\vec{r}} = 16$ mm and $\sigma_T = 7$ ns. In case the condition on $\mathrm{Discr}_{\mathrm{CHOD}}$ is not satisfied, the STRAW track is rejected.

Track–LKr association

The STRAW track association with the LKr calorimeter is made using either information from clusters provided by the standard reconstruction (see Section 7.2.2) or from clusters reconstructed at analysis level with an additional cell-based algorithm, if the standard cluster is not found.

For the standard cluster the associated candidate is selected as the closest in space with the extrapolated position of the STRAW track at the calorimeter surface. The two following conditions are applied: $|\vec{r}_{\mathrm{LKr}} - \vec{r}^{\,\mathrm{LKr}}_{\mathrm{track}}| < 10$ cm and $|T_{\mathrm{LKr}} - T^{\mathrm{STRAW}}_{\mathrm{track}}| \leq 20$ ns.

If no standard clusters are associated to the STRAW track, a cell-based cluster is built by collecting all the hits in a radius of 10 cm from the extrapolated track impact point and within ± 40 ns with respect to the track time. The time of the cell-based cluster is taken as the time of the most energetic hit (seed), which must have at least 40 MeV, and the energy as the sum of all the hit energies. The transverse position of the cell-based cluster is computed as the average of the hit positions weighted by their energies. The cell-based cluster is associated to the STRAW track if the distance from the track impact point is less than 10 cm and the time difference less or equal than 20 ns.

The associated LKr cluster (standard or cell-based) has to be in time with the previously associated NA48-CHOD candidate: $|T_{\mathrm{LKr}} - T_{\mathrm{NA48\text{-}CHOD}}| \leq 6$ ns. In case no LKr cluster is associated to the STRAW track, this is rejected.

Track–RICH association

The association to the STRAW track is checked using the output of the standard tool ***SpectrometerRICHAssociation*** [134]: here a candidate is reconstructed by extrapolating the track position at the mirror plane in order to identify the ring center, and a prediction on the ring radius is made for different mass hypotheses (electron, muon, pion and kaon). To the candidate associated to the STRAW track, called RICH-likelihood candidate in the following, a probability, based on a likelihood calculation [150], of being compatible with one

of the four particle categories is assigned together with the most probable mass hypothesis.

Due to the importance of detecting the track in the RICH detector (required later for the particle identification) a second method is used exploiting a standalone ring reconstruction [1]: in-time hits are grouped and a ring is fitted assuming the passage of a single particle. The standalone reconstruction method allows to measure the momentum of a particle under a given mass hypothesis (π^+ in this case) independently from the STRAW track information. For each of the standalone-reconstructed ring candidates, a discriminant is built as follows:

$$\text{Discr}_{\text{RICH}} = \left(\frac{|\vec{r}_{\text{center}} - \vec{r}_{\text{fp}}|}{\sigma_{\vec{r}}}\right)^2 + \left(\frac{T_{\text{RICH}} - T_{\text{NA48-CHOD}}}{2\sigma_T}\right)^2, \tag{10.4}$$

where $\vec{r}_{\text{center}}$ is the transverse position of the ring center, $\vec{r}_{\text{fp}}$ the STRAW track position extrapolated at the focal plane of the RICH mirrors, T_{RICH} the time of the reconstructed ring candidate, $T_{\text{NA48-CHOD}}$ the time of the associated NA48-CHOD candidate (used as reference), and the resolutions are $\sigma_{\vec{r}} = 3$ mm and $\sigma_T = 0.3$ ns. The best ring candidate (called RICH single-ring candidate in the following), selected by minimizing $\text{Discr}_{\text{RICH}}$, is associated to the STRAW track if it satisfies the conditions:

- $\text{Discr}_{\text{RICH}} < 50$.
- Probability of the ring fit greater than 0.01.
- $|T_{\text{RICH}} - T_{\text{NA48-CHOD}}| < 2$ ns.

At this stage of the selection events are kept even if no RICH candidates are associated to the STRAW track. [3]

Track–MUVs association

The standard tool ***SpectrometerCalorimeterAssociation*** [134] is used for the STRAW track association to the candidates in the MUV1 and MUV2 detectors. A candidate in the MUV1–2 is built by looking at all hits in a ± 25 ns time window around the STRAW track time and close to the extrapolated track impact point both in the x and y detector plane. The output of the tool contains information about the MUV1–2 candidates associated to the STRAW track (one for each track) and the results of the particle identification based on a Multivariate analysis (MVA) [110]. The tool searches also for a LKr cluster associated to the STRAW track. In case no LKr cluster is found the STRAW track is rejected, while no conditions are applied on the presence of MUV1 and MUV2 candidates at this stage of the selection.

For the MUV3 detector, the output of the standard tool ***SpectrometerMUV3Association*** [134] is used, which provides all MUV3 candidates in a time coincidence of ± 5 ns with the STRAW track and geometrically compatible with the extrapolated track position

[3] The presence of both a RICH-likelihood and RICH single-ring candidate associated to the STRAW track is required at the particle identification step.

at the detector plane. A MUV3 candidate is associated to the STRAW track if the candidate time is within ± 5 ns from $T_{\text{NA48-CHOD}}$ (used as reference). At this stage of the selection events are kept even if a MUV3 candidate is associated to the STRAW track. [4]

Track time

Despite its association to NA48-CHOD, CHOD, and LKr candidates, a STRAW track is rejected if the associated NA48-CHOD candidate is out of time (± 25 ns time window) with respect to the trigger time. An event is rejected if more than 9 downstream-track associations pass the trigger time condition. A weighted time is defined for each downstream associated track using the timing information from the STRAW, NA48-CHOD, LKr and RICH single-ring (if any) candidates as follow:

$$T_{\text{downstream}} = \frac{w_{\text{STRAW}}^{-1} T_{\text{STRAW}} + w_{\text{NA48-CHOD}}^{-1} T_{\text{NA48-CHOD}} + w_{\text{LKr}}^{-1} T_{\text{LKr}} + w_{\text{RICH}}^{-1} T_{\text{RICH}}}{w_{\text{STRAW}}^{-1} + w_{\text{NA48-CHOD}}^{-1} + w_{\text{LKr}}^{-1} + w_{\text{RICH}}^{-1}} \quad (10.5)$$

where the weighting factors are $w_{\text{STRAW}} = 10$ ns, $w_{\text{NA48-CHOD}} = 0.5$ ns, $w_{\text{LKr}} = 1$ ns, and $w_{\text{RICH}} = 0.2$ ns [1]. In the following, $T_{\text{downstream}}$ will be used as the reference time for the downstream track.

Figure 10.1 shows the reconstructed squared missing mass (Equation (9.1)) under the pion mass hypothesis as a function of the track momentum, as measured by the STRAW spectrometer, for all the tracks which satisfy the downstream selection. The nominal beam momentum and direction are assumed for the kaon: $p_{\text{kaon}} = 74.9$ GeV/c, $\theta_x = 1.21$ mrad, and $\theta_y = 0.026$ mrad.

10.1.2 Association to upstream detectors

The presence of a kaon is required in the upstream detectors KTAG and GTK. The kaon detection proceeds in two different steps: first, kaons are positively identified among all the beam particles (mostly protons and pions); then, after measuring the momenta and directions in the GTK stations, kaon candidates are associated to each STRAW track passing the downstream selection, and the best kaon-track association is selected. In case no upstream association is found, the STRAW track is rejected. While for the KTAG detectors, candidates from the standard reconstruction are considered, GTK candidates are reconstructed at analysis level with the ***GigaTackerRecoAlgorithm*** tool [134]. The kaon-track association is based on the method discussed in Reference [1].

Kaon tagging

Kaons are identified by the selection of KTAG candidates with at least 5 (out of 8) fired sectors and a time within ± 2 ns with respect to $T_{\text{downstream}}$. A signal candidate is formed

[4] A STRAW track associated to a MUV3 candidate indicates that the charged particle in the final state is a muon. This kind of events are rejected later in the particle identification step.

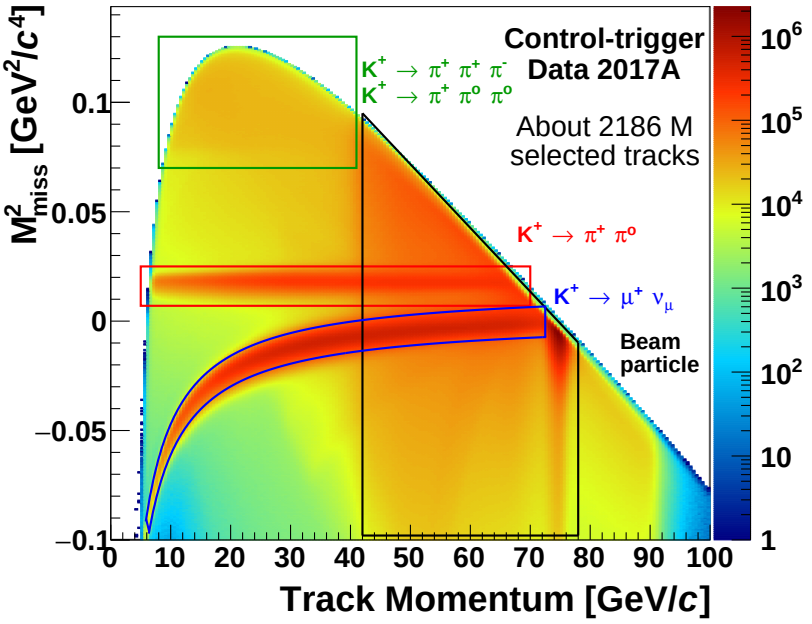

FIGURE 10.1: Distribution of the squared missing mass as a function of the STRAW track momentum for all the tracks that satisfy the downstream selection (full data sample 2017A). For the STRAW track 4-momenta the pion mass is assumed, while for the kaon 3-momentum the nominal beam momentum and direction are used. The main kaon decays are visible together with the distribution of scattered beam particles.

by clustering iteratively in-time hits in different sectors. In case more than one KTAG candidate is tagged as a kaon only the candidate closest in time is considered.

Kaon candidate selection

GTK candidates are built at analysis level with the standard algorithm ***GigaTrackerRecoAlgorithm*** [134] as discussed in Section 7.3.1. The time of the selected KTAG candidate serves as reference time to ***GigaTrackerRecoAlgorithm***. Among all the reconstructed GTK candidates only those which are classified as good quality and consistent with the beam profile in terms of momentum and directions are considered as kaon candidates. The following requirements are made:

- $\chi^2_{\text{event}} = \left(\frac{p_{\text{K}} - p_{\text{beam}}}{\sigma_p}\right)^2 + \left(\frac{\theta_x - \theta_{x,\text{beam}}}{\sigma_{\theta x}}\right)^2 + \left(\frac{\theta_y - \theta_{y,\text{beam}}}{\sigma_{\theta y}}\right)^2 < 20\,,$
  where p_{K}, θ_x, and θ_y are the reconstructed momentum and directions of the GTK candidate; $p_{\text{beam}} = 74.9$ GeV/c, $\theta_{x,\text{beam}} = 1.22$ mrad, and $\theta_{y,\text{beam}} = 0.025$ mrad are the beam nominal momentum and directions, respectively. The nominal resolution of the beam parameters are $\sigma_p = 0.9$ GeV/c, $\sigma_{\theta x} = 0.12$ mrad, and $\sigma_{\theta y} = 0.1$ mrad.
- $|T_{\text{GTK}} - T_{\text{KTAG}}| < 0.6$ ns.

The event is rejected if more than 10 GTK candidates satisfy the above conditions.

Kaon–track association

For each selected downstream track, the best association to a kaon (GTK candidate) is taken. A vertex is defined as the median point at the closest distance of approach (CDA) between the selected STRAW track and any of the kaon candidates. In order to determine the best associated GTK candidate, the measured values of the vertex CDA and the time difference between the GTK and KTAG candidates are used to build the discriminant

$$\mathrm{Discr}(\mathrm{CDA}_{\mathrm{meas}}, \Delta T_{\mathrm{meas}}) = \left(1 - \mathrm{p}_{\mathrm{CDA}}\right)\left(1 - \mathrm{p}_{\Delta T}\right), \tag{10.6}$$

which represents the probability to have values for the CDA and the ΔT larger than those observed. In the above Equation (10.6), $\mathrm{p}_{\mathrm{CDA}}$ ($\mathrm{p}_{\Delta T}$) is the integral of the Probability Density Function (PDF) for the CDA (ΔT) to lie in the range between 0 and $\mathrm{CDA}_{\mathrm{meas}}$ (between $-\Delta T_{\mathrm{meas}}$ and ΔT_{meas}). According to Reference [1] the following PDFs [5], also shown in Figure 10.2, are used to build the discriminant:

$$\begin{aligned}\mathrm{PDF}(\mathrm{CDA}) = {} & 0.0702\, e^{-\frac{1}{2}\left(\frac{\mathrm{CDA}}{1.47}\right)^2} + 0.0229\, e^{-\frac{1}{2}\left(\frac{\mathrm{CDA}}{2.60}\right)^2} + 0.015\, e^{-\frac{\mathrm{CDA}}{2}} + \\ & - 0.0000016\,\mathrm{CDA} + 0.000033,\end{aligned} \tag{10.7}$$

$$\mathrm{PDF}(\Delta\mathrm{T}) = 0.024\, e^{-\frac{1}{2}\left(\frac{\Delta\mathrm{T}}{0.13}\right)^2} + 0.0032\, e^{-\frac{1}{2}\left(\frac{\Delta\mathrm{T}}{0.21}\right)^2}. \tag{10.8}$$

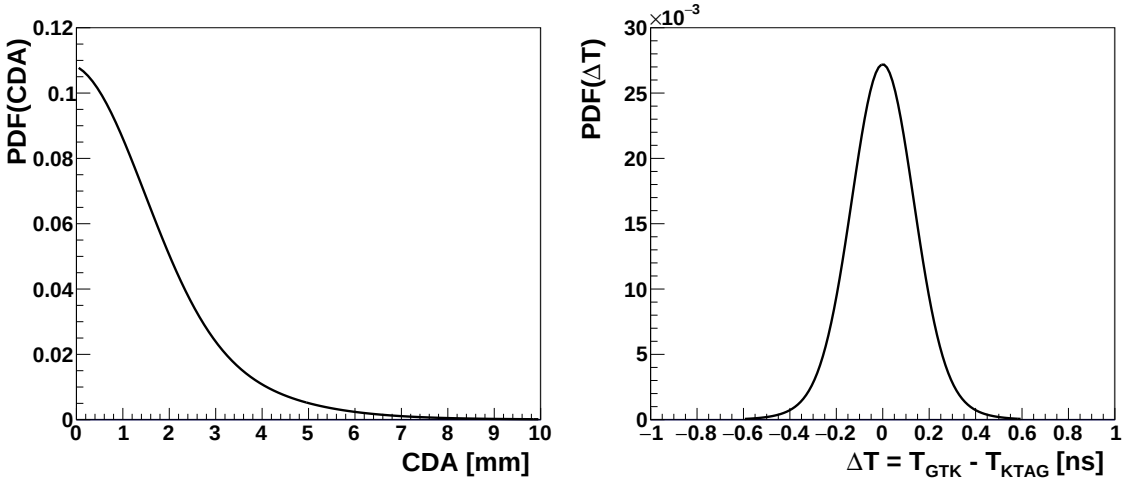

FIGURE 10.2: ***Left:*** Distribution of PDF(CDA) defined in Equation (10.7). ***Right:*** Distribution of PDF(ΔT) defined in Equation (10.8).

The best kaon candidate associated to the downstream track is defined as the one with the highest discriminant ($\mathrm{Discr}_{\mathrm{best}}$) and it must satisfy the following conditions:

- The difference between $\mathrm{Discr}_{\mathrm{best}}$ and the discriminant of any other associated kaon candidate must be greater than 0.01.
- $\mathrm{Discr}_{\mathrm{best}}(\mathrm{CDA}, \Delta T) > 0.01$ and CDA less than 7 mm.

[5] The PDFs are template functions obtained from a $K^+ \to \pi^+\pi^-\pi^+$ analysis [151].

The standard tool ***BlueTubeTracker*** [134] is used to correct the vertex position and the kaon and track three momenta due to residual magnetic field in the decay region. As measured in Reference [1], the efficiency of the kaon-track association procedure is about 85%.

10.1.3 Kinematic refinement

In order to further refine the kinematic selection, additional requests are applied to the STRAW track, to the GTK candidate, and to the reconstructed vertex, as follows.

- The kaon momentum and direction must be compatible with the beam profile. This means p_{k} should lie in the range 72.7–77.2 GeV/c and $\theta_{x,y}$ should differ from the average beam direction by less than 0.35 mrad.
- No more than 4 good GTK candidates must be present in the event (including the candidate associated to the STRAW track).
- $|T_{\mathrm{GTK}} - T_{\mathrm{NA48\text{-}CHOD}}| < 1.1$ ns.
- The slope differences of the STRAW track measured before and after the fit should be less than 0.3 mrad and 1 mrad in the xz and yz planes, respectively.
- The pattern recognition quality of the STRAW track candidate must be greater than 4.
- At least 15 hits and no more than 42 hits must belong to the STRAW track.
- The transverse position of the vertex must lie along the beamline. It is required:

$$-148.53\ \mathrm{mm} + 0.00122\ z_{\mathrm{vertex}} \leq x_{\mathrm{vertex}} \leq -93.9\ \mathrm{mm} + 0.0012\ z_{\mathrm{vertex}} \text{ and}$$
$$-5.4\ \mathrm{mm} - 0.00010\ z_{\mathrm{vertex}} \leq y_{\mathrm{vertex}} \leq 3.6\ \mathrm{mm} + 0.00011\ z_{\mathrm{vertex}}\ .$$

If more than one STRAW track reaches this stage of the selection (a good track with both downstream and upstream associations), only the track with candidates in NA48-CHOD, LKr, RICH single-ring (if any), KTAG and GTK closest in time to the trigger is selected as π^+ track.

Figure 10.3 shows the distributions of the squared missing mass (left panel) and of the longitudinal position of the vertex (right panel) as a function of the STRAW track momentum for the events satisfying the selection of single-track final state events.

10.2 Kaon decays in the fiducial volume

In order to be classified as a good kaon decay, the longitudinal coordinate of the vertex is required to be in the fiducial region: z_{vertex} should lie in the range 105–165 m, representing the region between the last GTK station and the first STRAW chamber. Additional conditions are applied to ensure the correct kaon-track association, rejecting the so-called beam-related background. As shown in the right panel of Figure 10.3, a beam particle can

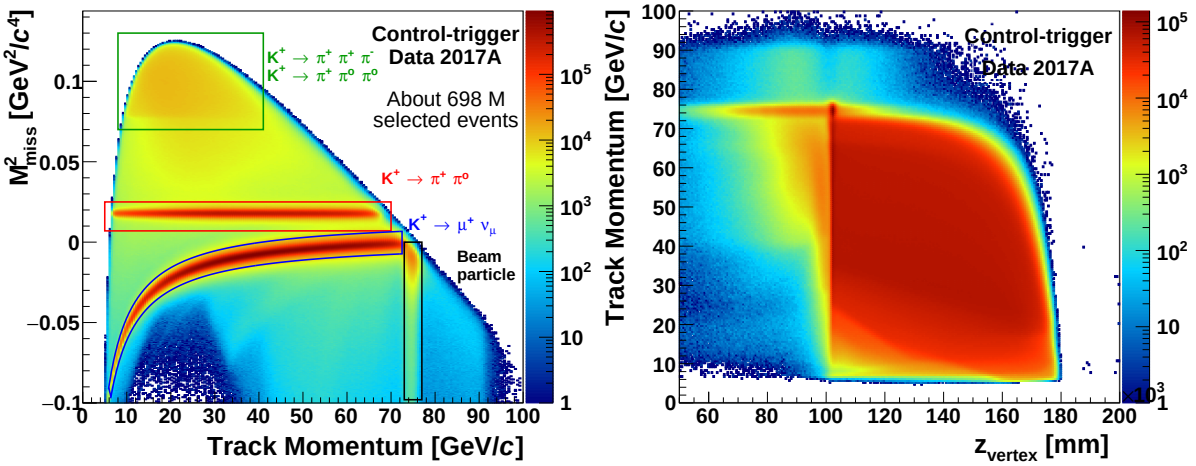

FIGURE 10.3: ***Left:*** Squared missing mass *versus* track momentum for the events passing the single-track selection. The momenta of the track and of the kaon are measured by the STRAW and GTK, respectively. The pion mass hypothesis is assumed for the STRAW 4-momentum. ***Right:*** Longitudinal position of the vertex *versus* STRAW track momentum for the events passing the single-track selection. The 75 GeV/c component is due to elastic scattering of beam particles with material upstream of the GTK3 station ($\simeq$ 102 m). The enhancement around the GTK3 longitudinal position spanning the whole momentum range is due to inelastic interactions of beam particles in the last GTK station. Correctly reconstructed kaon decays populate the region downstream the GTK3 station.

be associated to a downstream track due to different processes, as explained in the following:

- The beam particle does not interact with any material before reaching the fiducial volume and here decays. These are the majority of the events and they populate the z_{vertex} region above 105 m.
- The beam particle interacts with the material in the last GTK station and the products of these interactions are wrongly associated to the downstream track. For these events the longitudinal position of the vertex has a peak at the GTK3 station (z_{vertex} around 102 m) spanning the whole momentum spectrum.
- The beam particle decays upstream of the GTK3 station and its daughter particles, entering the fiducial volume, are wrongly associated to another kaon candidate reconstructed in the GTK detector due to pileup events. These events populate the z_{vertex} region upstream of the last GTK station and have a peak in the momentum spectrum at 75 GeV/c.

The first situation represents the correct kaon-track association and its kinematics are very clean. Instead, the other two require more attention. In order to detect any possible background entering the fiducial volume and coming from an incorrect kaon-track association additional conditions are applied.

10.2.1 CHANTI veto

As described in Section 10.2.1, the CHANTI is a guard ring detector built to veto the inelastic interactions of beam particles in the GTK stations (mostly in GTK3). An event is rejected if at least one coincidence of x and y hits belonging to the same detector plane is found in a time window of ± 3 ns with respect to the STRAW track reference time $T_{\text{downstream}}$.

10.2.2 Residual GTK interactions

Following the $K^+ \to \pi^+\nu\bar{\nu}$ analysis [1], additional conditions are applied to veto residual beam particle interactions in the GTK stations not detected by the CHANTI detector. It is required that any good GTK candidate present in the event must not form a vertex with the STRAW track candidate within the range $100 < z_{\text{vertex}} < 105$ m. The extrapolated STRAW track position at the GTK3 plane has to lie outside of the station sensitive volume. The Time-over-Threshold (ToT) of all the hits of the selected GTK kaon candidate must be smaller than 23 ns and the GTK3 hits must be away from the extrapolated track position at the station plane by more than 24 mm.

10.2.3 Upstream decays

As mentioned above, kaon decays can occur along the beamline upstream of the GTK stations and their products can enter the decay volume and be detected downstream. It can happen that only one charged particle is detected in the final state while all the other decay products are stopped by the passive material along the beamline. Since the parent kaon is not present in the GTK detector, the charged STRAW track can be associated to an unrelated candidate reconstructed in the GTK stations due to pileup activity. These events might be wrongly classified as having one STRAW track in the final state, thus polluting the search for $K^+ \to \pi^+\nu\bar{\nu}$ decays, as well as for $K^+ \to \pi^+\pi^o$ with π^o decaying into invisible particles. Following the studies made on this type of events in the $K^+ \to \pi^+\nu\bar{\nu}$ analysis [1], three additional conditions are applied:

- *Early decay*: using the position of the STRAW track and of the GTK kaon candidate as extrapolated at the TRIM5 and at the last dipole (BEND6) magnets, it is required that the event does not have a vertex with longitudinal coordinate lying in the region 99.5–101.8 m.

- $R_{\text{STRAW}} - z_{\text{vertex}}$ *cut* (Figure 10.4 left panel): the correlation between the STRAW track and the GTK candidate is exploited, and a geometric cut is applied on the track transverse distance with respect to the beamline at the STRAW chamber 1 (R_{STRAW1}) as a function of the z coordinate of the vertex. It is required that:

  $$R_{\text{STRAW1}} > 735 \text{ mm} - 0.004\, z_{\text{vertex}} ,$$
  $$R_{\text{STRAW1}} > 7\,462.5 \text{ mm} - 0.0625\, z_{\text{vertex}} \text{ and}$$
  $$R_{\text{STRAW1}} < 1\,812.5 \text{ mm} - 0.0098333\, z_{\text{vertex}}.$$

- *Box cut* (Figure 10.4 right panel): the STRAW track position as extrapolated at the plane of the TRIM5 magnet has to be outside of the region $|x_{\text{track}}^{TRIM5}| < 100$ mm and $|y_{\text{track}}^{TRIM5}| < 500$ mm.

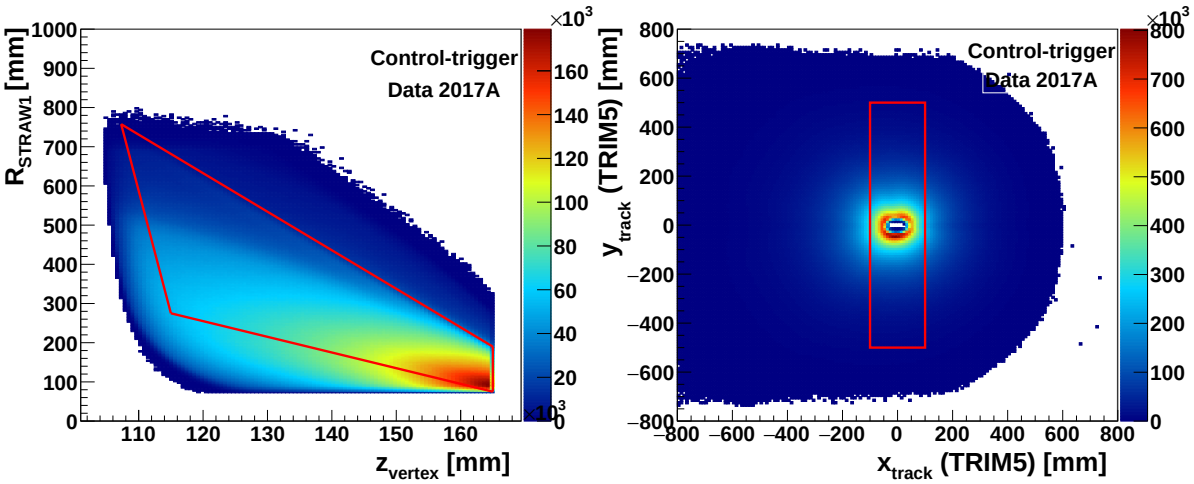

FIGURE 10.4: ***Left:*** Distribution of the STRAW track transverse distance with respect to the beam-line at STRAW chamber 1 *versus* the longitudinal position of kaon-track vertex. The selected events are those inside the red lines. ***Right:*** Distribution of the extrapolated STRAW track position at the TRIM5 magnet mid plane ($z_{\text{TRIM5}} = 101.8$ m). The rejected events are those inside the red box.

Figure 10.5 shows the distribution of the squared missing mass as a function of the STRAW track momentum for the events selected as kaon decays inside the fiducial volume after applying the veto conditions on upstream interactions and decays.

10.3 Particle identification

The information collected in Section 10.1.1 for the LKr, MUVs, and RICH detectors are exploited for particle identification. The most probable kaon decay is into a muon and a muon-neutrino, $\text{BR}(K^+ \to \mu^+\nu_\mu) \simeq 63\%$ [5], and therefore the major task of the particle identification system in NA62 is a good pion/muon separation. For the $K^+ \to \pi^+\nu\bar{\nu}$ analysis a muon suppression of at least $\mathcal{O}(10^7)$ is required with the highest possible efficiency for pion. In order to reach the desired performances for the experiment, a muon suppression of $\mathcal{O}(10^5)$ is required from the calorimeters (LKr and HAC) plus the MUV3 detector, and $\mathcal{O}(10^2)$ from the RICH detector.

10.3.1 Calorimeters PID

The first requirement is the presence of no MUV3 candidates associated to the STRAW track (see MUVs paragraph in Section 10.1.1 for the association). These are events in which the charged particle in the final state is clearly identified as a muon, passing through 80 cm of iron wall and reaching the MUV3 detector. More difficult to suppress are muons that do not reach the MUV3 detector either because of the loss of the majority of their energy in the calorimeters (LKr and HAC), or because of their decay upstream of the MUV3 detector.

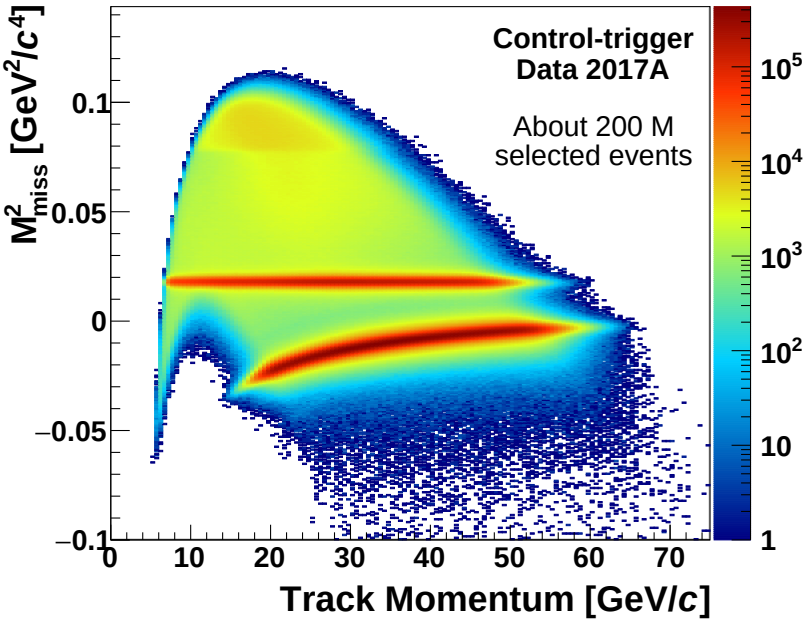

FIGURE 10.5: Squared missing mass distribution *versus* the STRAW track momentum for the selected kaon decays in the fiducial volume. The squared missing mass is computed according to Equation (9.1), using the 3-momenta measured by the STRAW and the GTK detectors for the pion and kaon particles, respectively.

Those events are rejected with the output of the ***SpectrometerCalorimeterAssociation*** tool. The tool provides particle identification probabilities based on a Multivariate analysis [110] using information from the energies deposited in the LKr and HAC calorimeters and from the shape of the induced shower. Given the output of the tool, the probability for pion identification has to satisfy the condition

$$\text{Prob}(\pi) > \text{Max}\left(0.6, 0.956 - 0.4596\, e^{\frac{-(p_{\text{track}}\,[\text{GeV}/c]-11.44)}{5.27}}\right). \tag{10.9}$$

which allows a flat pion identification efficiency around 85% through the entire STRAW track momentum considered. In order to ensure the presence of only one charged particle in the final state, the in-time energy deposited in the HAC calorimeter not associated to the STRAW track must be less than 5 GeV, and the two ratios $E_{\text{HAC}}/p_{\text{track}}$ and $E_{\text{calo}}/p_{\text{track}}$ must be less than 1.2. Here E_{HAC} and E_{calo} are the HAC and the total calorimetric (HAC plus LKr) energies associated to the STRAW track and p_{track} is the track momentum measured by the STRAW spectrometer. Moreover, to further reject positrons, the following condition is applied: $E_{\text{LKr}}/p_{\text{track}} < 0.8$. Here E_{LKr} is the energy of the LKr cluster associated to the STRAW track according to the LKr paragraph in Section 10.1.1.

10.3.2 RICH PID

The presence of both RICH single-ring and RICH-likelihood candidates associated to the STRAW track (see RICH paragraph in Section 10.1.1 for the association) is required for the

RICH detector. In order to identify the charged particle in the final state as a pion, the most probable hypothesis given by the likelihood algorithm must be the pion one, and the ratio between the pion probability and the maximum probability for the muon and electron identification must be greater than 1.2:

$$\frac{\text{Prob}(\pi)}{\text{Max}\left(\text{Prob}(\mu),\ \text{Prob}(e)\right)} > 1.2\ . \tag{10.10}$$

Using the track momentum measured by the STRAW spectrometer (p_{track}) and the ring radius of the associated RICH single-ring candidate (R_{ring}) it is possible to calculate the mass of the charged particle as follows:

$$m_{\text{RICH}} = p_{\text{track}} \sqrt{r_{\text{index}}^2 \cos^2\left(\arctan\left(\frac{R_{\text{ring}}}{f_{\text{length}}}\right)\right) - 1} \tag{10.11}$$

where $f_{\text{length}} = 17.02$ m is the mirrors focal length, and r_{index} the refractive index of the neon gas inside the RICH vessel calibrated on a burst-by-burst basis using electrons under the velocity assumption $\beta = 1$. The mass of the single-ring candidate has to be in the range 133–200 MeV/c^2, for pion identification. In the same way described in Section 10.1.2 for the kaon-track association, a discriminant is built with the time of the RICH single-ring candidate in place of the KTAG. The event is rejected if $\text{Discr}(\text{CDA}, \Delta T_{\text{GTK}-\text{RICH}}) < 0.005$.

10.3.3 PID results

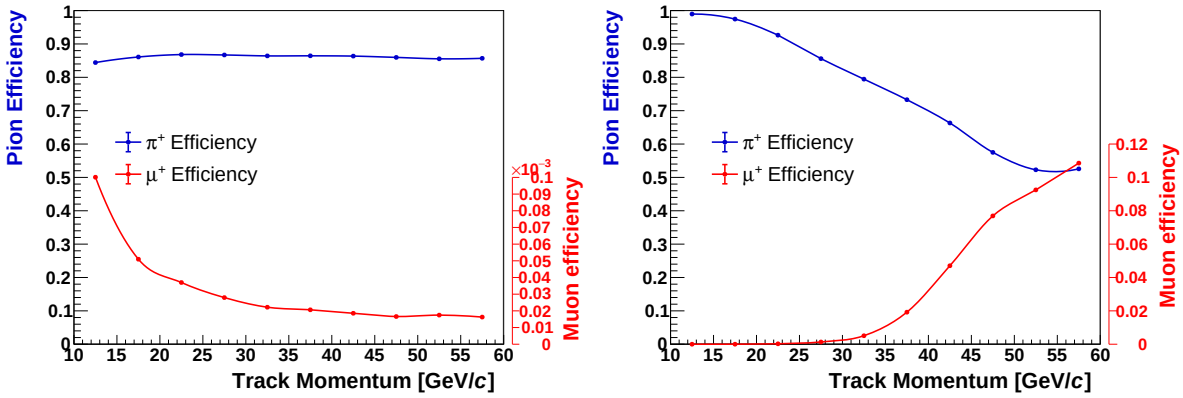

FIGURE 10.6: ***Left:*** Efficiency for the calorimetric-based pion-identification criteria detailed in the text, for π^+ and μ^+. ***Right:*** Efficiency for the RICH-based pion-identification criteria detailed in the text, for π^+ and μ^+.

The efficiency for calorimeter-based particle-identification for pions and muons are measured with the selection of pure samples of $K^+ \to \pi^+\pi^o$ and $K^+ \to \mu^+\nu_\mu$ events on control-trigger data without using calorimeter information. The single-track selection and the requirement of kaon decay in the fiducial volume, described in Sections 10.1 and 10.2, are applied. The results are shown in the left panel of Figure 10.6: a total pion efficiency of about 86.5% is obtained, with a muon rejection inefficiency of 2.7×10^{-5} in the range

10–60 GeV/c for the STRAW track momentum. In a similar way, the efficiency for RICH-based particle-identification is measured for pions and muons with the selection of data control-trigger samples of $K^+ \to \pi^+\pi^o$ and $K^+ \to \mu^+\nu_\mu$ decays without using RICH information. The results are shown in the right panel of Figure 10.6, with a total pion efficiency of about 78.2% and a muon rejection inefficiency of 4.3×10^{-2} in the STRAW track momentum range 10–60 GeV/c.

10.4 $K_{2\pi}$ signal region

The left panel of Figure 10.7 shows the squared missing mass distribution, evaluated according to Equation (9.1) using the STRAW and GTK information as input, as a function of the STRAW track momentum for all the events selected as $K^+ \to \pi^+ + X$. The events population is clearly dominated by $K^+ \to \pi^+\pi^o(\gamma)$ decays. The two-body decay nature of the $K_{2\pi}$ events results in a peak of the missing mass distribution around the π^o mass, $m_{\pi^o} = 134.97$ MeV/c^2 [5].

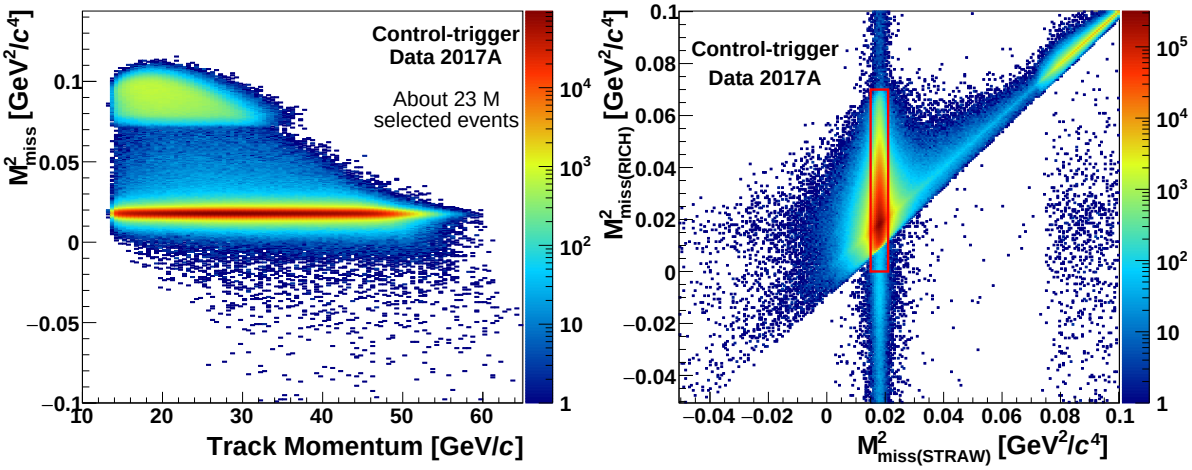

FIGURE 10.7: ***Left:*** Squared missing mass distribution *versus* STRAW track momentum for each selected event of the type $K^+ \to \pi^+ + X$. The pion and kaon 3-momenta are given by the STRAW and GTK candidates, respectively. The selected events are dominated by $K^+ \to \pi^+\pi^o(\gamma)$ events, with a contribution from $K^+ \to \pi^+\pi^o\pi^o$ decays for values of the squared missing mass above two times the π^o mass ($M^2_{\text{miss}} \gtrsim 0.07$ GeV$^2/c^4$). ***Right:*** The $K_{2\pi}$ signal region is defined in the two dimensional plane of $M^2_{\text{miss(RICH)}}$ *versus* $M^2_{\text{miss(STRAW)}}$. The selected events are those inside the red box, as defined in Equation (10.12).

In order to define the $K_{2\pi}$ signal region, two different definitions of the missing mass variable are used: while always using the kaon 4-momentum as measured by the GTK detector, the pion 4-momentum is obtained, assuming the pion mass, in one case using the STRAW track information and in the second case exploiting the momentum, Equation (10.11), given by the RICH single-ring candidate associated to the STRAW track. The latter definition helps to reduce mis-reconstruction effects in the STRAW spectrometer. A

two dimensional $K_{2\pi}$ signal region, shown in the right panel of Figure 10.7, is defined as: [6]

$$\begin{aligned} 0.015 \leq M^2_{\text{miss(STRAW)}} &= \left(P_{K^+} - P^{\text{STRAW}}_{\pi^+}\right)^2 \leq 0.021\ \text{GeV}^2/c^4, \\ 0 \leq M^2_{\text{miss(RICH)}} &= \left(P_{K^+} - P^{\text{RICH}}_{\pi^+}\right)^2 \leq 0.07\ \text{GeV}^2/c^4. \end{aligned} \tag{10.12}$$

In the 2017 Sample A about 21×10^6 $K_{2\pi}$ events are selected on control-trigger data in the STRAW track momentum range 10–60 GeV/c. They correspond to about 8.4×10^9 tagged π^o mesons available for the normalization sample of the $\pi^o \to$ *invisible* analysis, after accounting for the 400 downscaling factor of the control trigger. In the selected sample, the total background contamination for decays different from $K^+ \to \pi^+\pi^o(\gamma)$ with $\pi^o \to \gamma\gamma$ is estimated to be below 10^{-5}, as also confirmed by the background studies made in the $K^+ \to \pi^+\nu\bar{\nu}$ analysis of 2017 data [152]. The π^+ momentum distribution of the selected events is shown in Figure 10.8. Table 10.2 lists the number of tagged π^o mesons in bins of 5 GeV/c of the π^+ momentum.

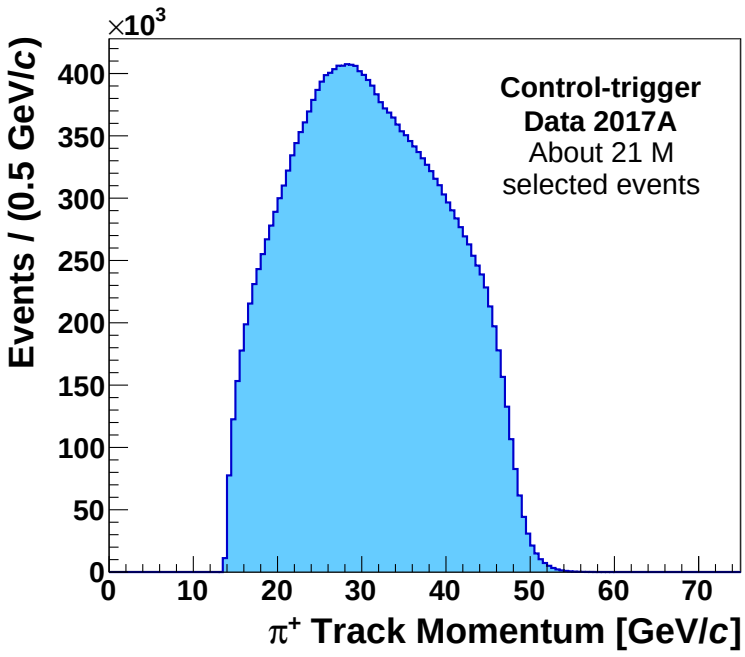

FIGURE 10.8: Distribution of the π^+ momentum, as measured by the STRAW spectrometer, for $K_{2\pi}$ events selected on control-trigger data in the 2017 Sample A.

[6] The conditions applied reduce the contribution of hard photons radiated in the final state.

π^+ Momentum [GeV/c]	$K_{2\pi}$ selected [10^6]	N_{π^o} [10^6]
10 – 15	0.211	84.55
15 – 20	2.309	923.43
20 – 25	3.460	1383.90
25 – 30	4.031	1612.51
30 – 35	3.762	1504.93
35 – 40	3.284	1313.67
40 – 45	2.646	1058.54
45 – 50	1.203	481.37
50 – 55	0.067	26.91
55 – 60	0.001	0.35

TABLE 10.2: Number of tagged π^o mesons, estimated after applying the full $K_{2\pi}$ selection on control-trigger data for the full 2017 Sample A data set. The momentum bins are those used for the estimation of the expected π^o rejection, reported in Chapter 14.

Chapter 11
The Photon-rejection Algorithm

In order to search for $\pi^o \rightarrow$ *invisible* events it is mandatory to veto all the activity due to π^o decays into "visible" particles, namely photons and electron-positron pairs. The detectors dedicated to this purpose are the photon-veto detectors: LKr, LAV, and SAV. The related conditions are given in Section 11.1 and are called *photon-veto conditions*. However, photons from π^o decays can convert in the material before reaching the photon-veto detectors and the emitted electron-positron pair escapes detection. This can happen because the $e^{\pm}$ energy is too low or a shower is initiated with the production of secondaries with small enough energy to be lost to detection. Moreover, if the conversion happens upstream of the STRAW spectrometer magnet, the particles can be deflected by the MNP33 magnet into not instrumented regions in between the LAV stations or inside the beam tube. Very similar situations can occur in case of Dalitz decays of the π^o, $\pi^o \rightarrow \gamma e^+ e^-$, where the electron and the positron can remain inside the beam tube, or be deflected into un-instrumented regions, or can shower and give rise to additional photons, electrons and positrons with smaller and smaller energy to be lost to detection. To achieve the highest efficiency for the detection of visible π^o decays, the combined information from different detectors is used. The related set of conditions is called *photon-conversion conditions* and is detailed in Section 11.2.

The criteria applied to detect and reject any visible π^o decay (photon-rejection algorithm in the following) have been developed following the $K^+ \rightarrow \pi^+ \nu\bar{\nu}$ analysis of 2016 data [1], with slight modifications of the photon-conversion conditions in order to have stronger suppression. Therefore, the detection of photons from π^o decays has not been optimized, on purpose, for the $\pi^o \rightarrow$ *invisible* analysis in order to evaluate the π^o rejection for its use in the $K^+ \rightarrow \pi^+ \nu\bar{\nu}$ analysis.

The signal sample for the search for $\pi^o \rightarrow$ *invisible* events is obtained after applying the $K_{2\pi}$ selection and all the conditions of the photon-rejection algorithm, as veto, on $\pi\nu\bar{\nu}$-trigger data. In order to evaluate the background contribution, single-photon efficiencies for the detectors composing the photon-veto system are measured on data with $K_{2\pi}$ events selected as for the normalization sample (see Chapter 10 for the selection). The conditions of the photon-rejection algorithm are here used to positively detect the presence of a photon and/or a photon conversion, as it will be explained in detail in Chapter 13.

11.1 Photon-veto conditions

11.1.1 Photons in LKr

In the LKr calorimeter photons are detected as clusters (see Section 7.2.2 for the LKr cluster algorithm) that must be at least 10 cm away from the extrapolated π^+ track position at the LKr surface and in time with $T_{\text{downstream}}$, used as reference time for the event. The time window is changed according to the cluster energy as shown in Table 11.1 taking into account that

$$\sigma_{T_{\text{LKr}}}[\text{ns}] = 0.56 + \frac{1.53}{E[\text{GeV}]} - \frac{0.233}{\sqrt{E[\text{GeV}]}} \tag{11.1}$$

is the typical time resolution of an electromagnetic shower in the LKr calorimeter [1].

Cluster energy [GeV]	Timing condition
$E < 1$	$\lvert T_{\text{LKr}} - T_{\text{downstream}}\rvert < 5$ ns
$1 \leq E < 2$	$\lvert T_{\text{LKr}} - T_{\text{downstream}}\rvert < 5\ \sigma_{T_{\text{LKr}}}$
$2 \leq E < 15$	$\lvert T_{\text{LKr}} - T_{\text{downstream}}\rvert < 15\ \sigma_{T_{\text{LKr}}}$
$E \geq 15$	$\lvert T_{\text{LKr}} - T_{\text{downstream}}\rvert < 70\ \sigma_{T_{\text{LKr}}}$
$E > 10$	$\lvert T_{\text{LKr}} - T_{\text{downstream}} + 25\text{ ns}\rvert < 3\ \sigma_{T_{\text{LKr}}}$
$E > 10$	$\lvert T_{\text{LKr}} - T_{\text{downstream}} - 25\text{ ns}\rvert < 3\ \sigma_{T_{\text{LKr}}}$

TABLE 11.1: Timing conditions used to select photons in the LKr calorimeter. The typical time resolution of an electromagnetic shower, $\sigma_{T_{\text{LKr}}}$, is defined in Equation (11.1).

The wide time window at high energy helps to include non-gaussian tails in the time distribution due to mis-reconstruction of the cluster time (in particular, due to pile-up activity) [153]. Particular attention has to be paid to a possible time offset of ± 25 ns due to the wrong assignment of the readout time slot for hits belonging to the same shower (time jitter in the CREAMs) [153]. To further improve the photon detection, an auxiliary (cell-based) reconstruction (see Section 7.2.2) is used. Since its efficiency for low-energy clusters is higher than in the standard reconstruction, it helps to improve the photon detection at low energies. Auxiliary photon clusters must be at least 10 cm away from the extrapolated π^+ track impact point at the LKr surface and in time with $T_{\text{downstream}}$ according to Table 11.1. Additionally, an energy above 700 MeV and a distance greater than 5 cm with respect to any standard photon cluster (if any) are required.

11.1.2 Photons in LAV

In the LAV system photons are detected using the output of the ***LAVMatching*** tool [134]. The tool masks possible noisy blocks on a burst-by-burst basis using a central database and searches for in-time LAV block hits. Given the double threshold setting of the LAV readout, a hit may be reconstructed from up to four time measurements, corresponding to the leading and trailing edge times on the high and low thresholds. Among all the in-time reconstructed hits, only certain combinations of leading/trailing edges are considered in the tool. For this analysis, the in-time LAV hits must be in a ± 5 ns time window with respect to $T_{\text{downstream}}$, used as reference time.

11.1.3 Photons in SAV

In the SAV detectors photons are detected using the information from the two readout systems: the TDC- and the FADC-based readout. In both cases $T_{\text{downstream}}$ is considered as the reference time. For the TDC readout the output of the ***SAVMatching*** [134] tool is used with the requirement of a time window of ± 5 ns. As for the ***LAVMatching*** tool noisy channels are checked on a burst-by-burst basis using a central database, and only certain combinations of leading/trailing edges are considered. Instead, for the FADC readout all the hits with an energy of at least 1 GeV and in a ± 5 ns time window are considered as photon signals.

11.2 Photon-conversion conditions

Information from different detectors are used to detect photon conversions by looking for in-time activity not associated to the π^+ track (extra activity). The conditions include:

- The hit multiplicity from NA48-CHOD, CHOD, LKr, MUV0 and HASC detectors.
- The extra activity reconstructed standalone in the charged hodoscopes, CHOD and NA48-CHOD.
- The extra activity detected by the RICH detector.
- The so-called STRAW-segment and single-particle information.
- The LKr information from merged clusters and extra hits.

11.2.1 Hit multiplicity

Photon conversions are detected in the MUV0, HASC, NA48-CHOD, CHOD and LKr detectors in a similar way as presented in Reference [1]. A photon conversion is detected if at least one of the following conditions is satisfied.

MUV0 and HASC

Hits within ± 10 ns and ± 3 ns with respect to the reference time $T_{\text{downstream}}$ indicate the presence of extra activity in the MUV0 and HASC detectors, respectively.

CHOD–NA48-CHOD association

All hits in a time window of ± 5 ns with respect to $T_{\text{downstream}}$ and 10 cm away from the extrapolated π^+ track impact point are considered as extra activity in the CHOD detector. Each of those hits is tried to be associated to an NA48-CHOD candidate, which is reconstructed in a similar way as described in Section 10.1.1 by using as reference time and position those of the CHOD hit and changing accordingly the resolution to build the discriminant of Equation (10.2). The NA48-CHOD hit pair with smallest discriminant is

associated to the CHOD hit if the time difference and space distance are smaller than 15 ns, 250 mm in the x coordinate, and 140 mm in the y coordinate, respectively. The condition is fulfilled, if at least one CHOD–NA48-CHOD association is found.

CHOD–LKr association

Extra hits in the CHOD detector (as defined above) can be associated to extra activity in the LKr calorimeter. The latter is defined as a sample of hits with more than 50 MeV, at least 100 mm away from the extrapolated π^+ track impact point and in a ± 10 ns time window with respect to $T_{\text{downstream}}$. A CHOD-LKr association exists if the hit time difference is less than 15 ns and their positions at the LKr surface are closer than 250 mm in the x coordinate and 140 mm in the y coordinate.

NA48-CHOD–LKr association

Extra hits in the LKr calorimeter (as defined above) are used to find an association to NA48-CHOD candidates in the same way as for the CHOD–NA48-CHOD association. In this case, an association is found if the NA48-CHOD candidate with smallest discriminant (according to Equation (10.2)) and the LKr hit have time difference and space distance less than 15 ns and 130 mm, respectively.

11.2.2 CHOD and NA48-CHOD standalone extra activity

A CHOD standalone extra activity is detected if there is at least one hit 150 mm away from the extrapolated π^+ track impact point and in ± 5 ns time window with respect to $T_{\text{downstream}}$. For the NA48-CHOD, the presence of more than 3 hits (excluding the two hits associated to the π^+ track) in ± 7 ns with respect to $T_{\text{downstream}}$ determine the standalone extra activity.

11.2.3 RICH extra activity

Extra activity in the RICH detector is present if there are more than 4 hits in time, within a time window of ± 0.5 ns with respect to the time of the π^+ single-ring candidate, but not spatially associated to the ring candidate. [1] A spatial association between an extra RICH hit and the π^+ single-ring candidate is found if $0.9 \leq |\vec{r}_{\text{hit}} - \vec{r}_{\text{ring}}| / R_{\text{ring}} \leq 1.1$, where $\vec{r}_{\text{hit}}$ is the hit position, R_{ring} and $\vec{r}_{\text{ring}}$ are the ring radius and ring center of the single-ring candidate.

11.2.4 STRAW-segment and single-particle information

In order to detect the presence of extra activity in the STRAW spectrometer two methods are used: a procedure to reconstruct track segments [1] and a simple check on the number of reconstructed tracks.

[1] The condition is specific to this analysis and it is not included in the $K^+ \to \pi^+ \nu\bar{\nu}$ selection.

Track segments

Hits not belonging to the π^+ track candidate and with a drift time between 0 and 170 ns are clustered together in the different views of each chamber to form view-clusters. The same pattern recognition algorithm applied for the standard reconstruction (see Section 7.2.1) is used. View-clusters of different view-planes are then combined to form chamber-hits. For each combination of chamber-hits in STRAW 1 and 2, a segment is built with the K^+-π^+ vertex as third point and a least-squared fit is performed in the xz and yz planes. The triplet is accepted if the fitted slopes in the two planes are smaller than 20 mrad, and the fitted segment lies more than 30 mm away from the π^+ track position in chamber 1 and 2. The segment with minimum chi square χ^2_{segment} is defined as *segment12*. A similar procedure is applied for the combination of chamber-hits in STRAW 3 and 4 and the K^+-π^+ vertex. The fitted slope in the yz plane is required to be lower than 20 mrad and the direction of the segment to be compatible either with a negative charged particle with momentum lower than 90 GeV/c or with a positive charged particle with momentum not greater than 10 GeV/c. The segment with minimum chi square is defined as *segment34*.
Extra activity is detected in the STRAW spectrometer if:

$$|T_{\text{segment12}} - T_{\text{GTK}}| < 35 \text{ ns} - 1.4\chi^2_{\text{segment12}} \text{ or}$$

$$|T_{\text{segment34}} - T_{\text{GTK}}| < 40 \text{ ns} - 5.7\chi^2_{\text{segment34}}$$

where T_{segment} is the average time of the two chamber-hits that produce the segment and T_{GTK} the time of the GTK kaon candidate.

Single particle

The detection of photon conversions upstream or in the first STRAW chamber is improved by looking for at least one reconstructed track (with hits in at least three chambers) with positive charge in addition to the π^+ track. If the track is found, a two-track vertex is reconstructed using the closest distance of approach. A photon conversion is detected, if the related CDA is smaller than 30 mm.

11.2.5 LKr merged clusters and extra hits

Merging clusters

As stated in Section 11.1.1, for any photon detected in the LKr calorimeter the distance between the extrapolated position of the π^+ track at the calorimeter surface and the photon cluster must be greater than 100 mm. However, rarely it can happen that the distance between two reconstructed clusters is below 100 mm and therefore the additional activity partially overlapped with the pion cluster is not detected. In order to detect this kind of events, in-time LKr clusters (according to Table 11.1) from the standard reconstruction with more than 2 GeV and between 40 and 100 mm from the π^+ track impact point are classified as additional activity, if they are found together with more than 2 extra in-time NA48-CHOD hits.

Extra hits

To fully exploit the LKr photon-detection capability and to recover residual inefficiencies of the clustering algorithm for soft photons, information from LKr hits is included. [2] All LKr hits with an energy of at least 50 MeV and 300 mm away from the π^+ track impact point [3] are grouped in 20×20 cm^2 regions covering the entire sensitive surface of the calorimeter. Extra activity due to additional LKr hits is found if the sum of the hit energies in at least one of the regions is greater than 500 MeV.

11.3 Efficiency of the photon-rejection algorithm

The effect of wrongly vetoing events actually with no photons nor photon conversions in the final state is evaluated with a sample of $K^+ \to \mu^+\nu_\mu$ ($K_{\mu2}$ in the following) events selected in control-trigger data. According to what is described in Sections 10.1 and 10.2, K^+ decays to a single positively charged daughter particle in the final state are selected. A positive muon identification is obtained by requiring:

- A MUV3 candidate associated to the STRAW track.
- The ratio $E_{\rm LKr}/p_{\rm track}$ to be below 0.8.
- Both a RICH single-ring and a RICH-likelihood candidate associated to the STRAW track.
- The most probable identification provided by the RICH likelihood to be the muon hypothesis.
- The muon probability given by the ***SpectrometerCalorimeterAssociation*** tool to be greater than 0.8 and the HAC energy not associated with the STRAW track less than 5 GeV.
- $|M^2_{\rm miss} = (P_{K^+} - P_{\mu^+})^2| < 0.005$ GeV$^2/c^4$, with the kaon and muon 3-momenta measured by the GTK and STRAW respectively.

About 1×10^8 $K_{\mu2}$ events are selected in the STRAW track momentum region 10–60 GeV/c. The photon-veto and photon-conversion conditions (together referred to as photon-rejection algorithm) described in Sections 11.1 and 11.2 are applied consecutively on the selected events resulting in a 45.8% signal loss due to accidental activity (random veto, RV), with about 29% given by the photon-veto conditions. According to the studies made in the $K^+ \to \pi^+\nu\bar{\nu}$ analysis [154], the corresponding efficiency of the photon-rejection algorithm must be corrected by bias effects specific to the $K_{\mu2}$ and the $K^+ \to \pi^+\pi^o$ with $\pi^o \to$ *invisible* final states. On one side, about 2.5% of the $K_{\mu2}$ events satisfy the photon-rejection conditions as a result of interactions of the muon. This figure is about 10% when

[2] The condition is specific to this analysis and it is not included in the $K^+ \to \pi^+\nu\bar{\nu}$ selection.

[3] For the single-photon efficiency study, described in Chapter 13, an additional photon cluster is required to be present in the LKr calorimeter. Therefore, a distance from the photon position greater than 200 mm is asked to the hits.

considering a π^+ particle in the final state. The two corrections are evaluated with MC simulations. A 3% relative systematic uncertainty is assigned, which accounts for the reliability of the simulation in reproducing the response to π^+ interaction secondaries. After correcting for these biases, the resulting efficiency of the photon-rejection algorithm is

$$\varepsilon_{\text{signal}} = 1 - RV = (50.1 \pm 1.6)\%. \tag{11.2}$$

Chapter 12
The Trigger Efficiency

The signal sample of the search for the decays $\pi^o \rightarrow \textit{invisible}$ is obtained from events triggered by the $\pi\nu\bar{\nu}$-trigger stream. The $\pi\nu\bar{\nu}$-trigger efficiency is determined from data control samples of $K^+ \rightarrow \pi^+\pi^o$ ($K_{2\pi}$) and $K^+ \rightarrow \mu^+\nu_\mu$ ($K_{\mu 2}$) events, respectively for the $\text{L0}_{\pi\nu\bar{\nu}}$ and $\text{L1}_{\pi\nu\bar{\nu}}$ trigger levels. A detailed description of the $\pi\nu\bar{\nu}$-trigger conditions is given in Section 8.1.1.

12.1 $\text{L0}_{\pi\nu\bar{\nu}}$ Trigger

For the 2017 Sample A, the $\text{L0}_{\pi\nu\bar{\nu}}$-trigger conditions require

$$\text{RICH}\times!\text{Q}_x \times \text{UMTC}\times!\text{MUV3}\times!\text{E30}\ ,$$

where the detector primitives are:

- RICH: at least 3 hits clustered in time in the RICH detector.
- Q_x: coincidences in exactly two opposite quadrants of the CHOD hodoscope (condition in veto).
- UMTC: less than 6 in-time hits in the CHOD detector.
- MUV3: coincidences between MUV3 hits in the two PMTs reading the same scintillator tile (condition in veto).
- E30: total energy released in the LKr calorimeter greater than 30 GeV or more than one reconstructed cluster (condition in veto).

A sample of $K_{2\pi}$ events is selected on control-trigger data in the same way as described in Chapter 10 for the normalization sample. In order to clean the sample and avoid events with photon conversions upstream of the NA48-CHOD and CHOD detectors, the following conditions are applied as veto [1]: Hit Multiplicity, RICH extra activity, NA48-CHOD and CHOD standalone extra activity, STRAW segment and single particle. The $\text{L0}_{\pi\nu\bar{\nu}}$-trigger efficiency is obtained from the combination of three conditions: L0RICH, L0Comb (which includes the information from the CHOD and MUV3 primitives) and L0LKr (which includes the LKr primitive condition !E30). The efficiency is evaluated by looking to the primitives information recorded in the L0TP data. For each of the conditions, the presence of the corresponding primitives within 10 ns from the time of the reference detector is used to flag the efficient events. The reference detector is the RICH (the CHOD when computing the

[1] The conditions are described in details in Section 11.2, only the LKr information from merged clusters and extra hits, Section 11.2.5, is not applied.

L0RICH efficiency). The selected $K_{2\pi}$ sample is used to evaluate the efficiencies for the L0RICH and L0Comb conditions as a function of the π^+ momentum. To properly evaluate the signal efficiency for the L0LKr condition, the additional requirement of having the two photons coming from the π^o decay hitting the LAV stations 2–11 is added. Since the additional photons requirement restricts the $K_{2\pi}$ sample to high π^+ momentum (above 40 GeV/c), the L0LKr efficiency is evaluated as a function of the energy released in the LKr calorimeter as shown in the left panel of Figure 12.1. In order to obtain the L0LKr efficiency as a function of the π^+ momentum, the energy-dependent efficiency is weighted, by using the $E_{\rm LKr}/p_{\rm track}$ distribution, for the probability of a pion to release a fraction of its energy in the calorimeter. The $E_{\rm LKr}/p_{\rm track}$ distribution of π^+ mesons is obtained from $K^+ \to \pi^+\pi^-\pi^+$ decays (Figure 12.1 right panel) as derived in Reference [154].

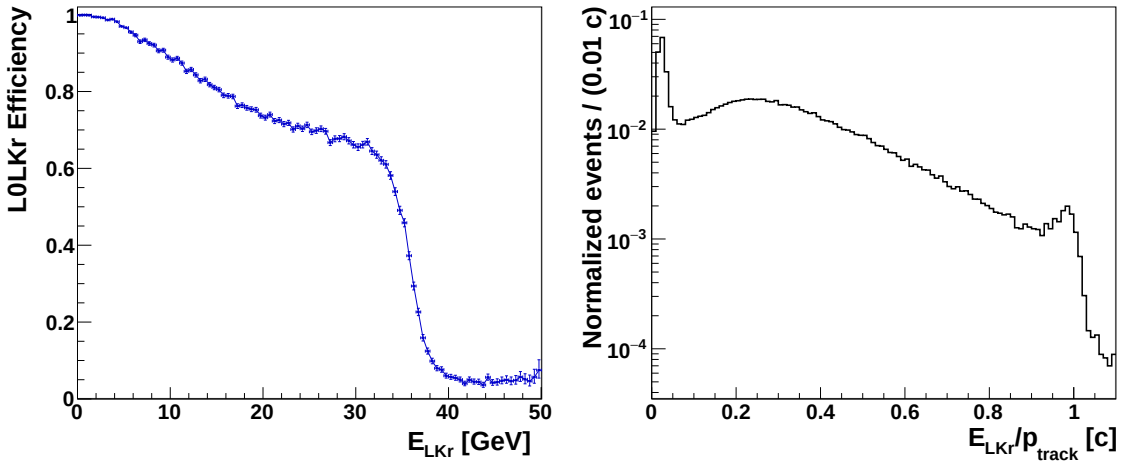

FIGURE 12.1: ***Left:*** L0LKr efficiency as a function of the energy deposited in the LKr calorimeter by the π^+ track. ***Right:*** Ratio of the energy released in the LKr calorimeter over the STRAW track momentum for π^+ particle derived from $K^+ \to \pi^+\pi^-\pi^+$ decays [154].

The L0$_{\pi\nu\bar{\nu}}$-trigger efficiency is shown as a function of the π^+ momentum, as measured by the STRAW spectrometer, in the left panel of Figure 12.2. Table 12.1 lists the L0$_{\pi\nu\bar{\nu}}$ efficiency in 5 GeV/c π^+ momentum bins. Since the L0$_{\pi\nu\bar{\nu}}$-trigger efficiency is not flat in certain 5 GeV/c momentum bins, the total efficiency in each bin is computed by taking into account the π^+ momentum distribution, as shown in Figure 10.8, of $K_{2\pi}$ events selected in data according to the algorithm of Chapter 10. Each event is weighted by the L0$_{\pi\nu\bar{\nu}}$-trigger efficiency shown in the left panel of Figure 12.2, and then for a 5 GeV/c π^+ momentum bin the total efficiency is computed as the weighted average.

12.2 L1$_{\pi\nu\bar{\nu}}$ Trigger

For the 2017 Sample A the L1$_{\pi\nu\bar{\nu}}$-trigger conditions require

$$\text{L1KTAG} \times \text{L1LAV} \times \text{L1STRAW}\ ,$$

where the level one algorithms are:

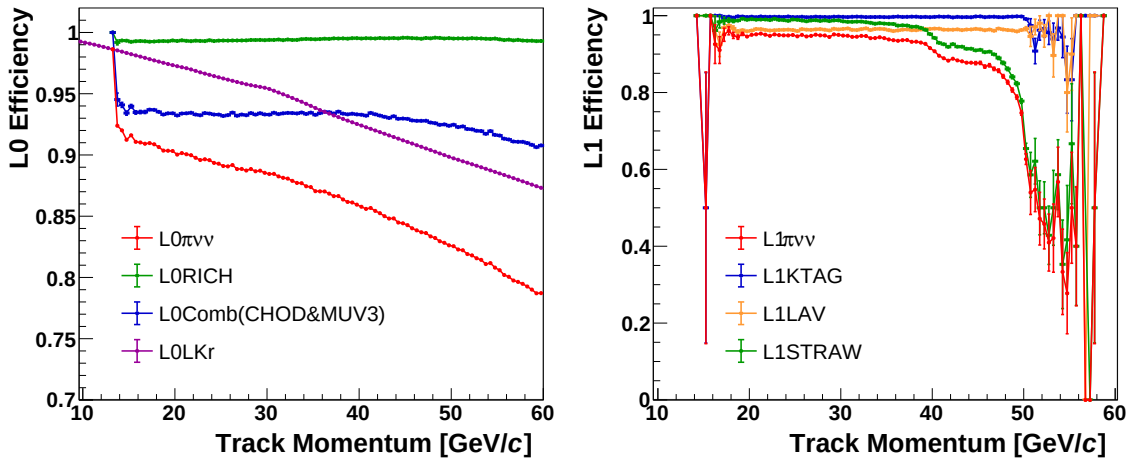

FIGURE 12.2: ***Left:*** $L0_{\pi\nu\bar{\nu}}$-trigger efficiency evaluated as the product of three components L0RICH × L0Comb × L0LKr. The efficiency is obtained from a sample of $K_{2\pi}$ events selected on control-trigger data as described in the text. ***Right:*** $L1_{\pi\nu\bar{\nu}}$-trigger efficiency evaluated as the product of three components L1KTAG × L1LAV × L1STRAW. The efficiency is obtained from a sample of $K_{\mu 2}$ events selected on data triggered by the $L0_{\pi\nu\bar{\nu}}$.

- L1KTAG: in-time KTAG hits in at least 5 out of 8 sectors.
- L1LAV: at most 3 in-time hits in the LAV stations 2–12.
- L1STRAW: a positive charged track reconstructed in the STRAW spectrometer with momentum below 50 GeV/c, CDA $<$ 20 cm, and $z_{\text{vertex}} <$ 180 m as obtained using the nominal beam momentum and directions.

The efficiency of the $L1_{\pi\nu\bar{\nu}}$ is evaluated on a sample of $K_{\mu 2}$ events triggered by the $L0_{\pi\nu\bar{\nu}}$, by requiring the L1-autopass data: these are events in which the L1 algorithms are registered but not enforced. The selection algorithm for $K_{\mu 2}$ events is similar to the one described in Section 11.3. After requiring K^+ decays to a single positively charged daughter particle, the muon PID is performed with the RICH detector and the LKr and HAC calorimeters. Since the presence of a MUV3 signal is asked as veto condition at trigger level in the $L0_{\pi\nu\bar{\nu}}$, no use of the MUV3 detector is made for the muon identification. The full photon-rejection conditions are applied as veto to the $K_{\mu 2}$ sample. The presence of the three $L1_{\pi\nu\bar{\nu}}$ components are checked and the results of the $L1_{\pi\nu\bar{\nu}}$-trigger efficiency as a function of the muon track momentum are shown in the right panel of Figure 12.2. As done for the $L0_{\pi\nu\bar{\nu}}$, the momentum distribution of $K_{2\pi}$ events (Figure 10.8) is used to compute the $L1_{\pi\nu\bar{\nu}}$-trigger efficiency in 5 GeV/c momentum bins. The results are listed in Table 12.1 together with the value of the total $\pi\nu\bar{\nu}$-trigger efficiency (L0+L1) in 5 GeV/c π^+ momentum bins.

As shown in Figure 12.3, the $\pi\nu\bar{\nu}$-trigger efficiency depends on the π^+ track momentum and varies from about 90% at 10 GeV/c to about 40% at 60 GeV/c, mainly due to the L0LKr and to the L1STRAW conditions. A 3.5% relative systematic uncertainty is assigned to the total trigger efficiency, due to the reliability of the technique used to reproduce offline the hardware conditions applied at the L0-trigger level.

π^+ **Momentum [GeV/c]**	10–15	15–20	20–25	25–30	30–35	35–40	40–45	45–50	50–55	55–60
$\varepsilon_{\mathbf{L0}}$ [%]	91.6	90.8	89.7	88.9	87.9	86.6	85.2	83.7	82.2	80.2
$\varepsilon_{\mathbf{L1}}$ [%]	100	95.2	95.0	94.8	94.5	93.2	88.7	85.4	54.0	43.9
$\varepsilon_{\mathbf{trigger}}$ [%]	91.6 ± 3.2	86.3 ± 3.0	85.2 ± 3.0	84.3 ± 3.0	83.1 ± 2.9	80.7 ± 2.8	75.5 ± 2.6	71.5 ± 2.5	44.4 ± 1.6	35.2 ± 1.2

TABLE 12.1: $L0_{\pi\nu\bar{\nu}}$, $L1_{\pi\nu\bar{\nu}}$ and total $\pi\nu\bar{\nu}$-trigger efficiencies evaluated for a $\pi^o \to$ *invisible* signal in 5 GeV/c bins of the π^+ momentum. The binning is the same used in Figure 14.5 for the evaluation of the expected π^o rejection inefficiency.

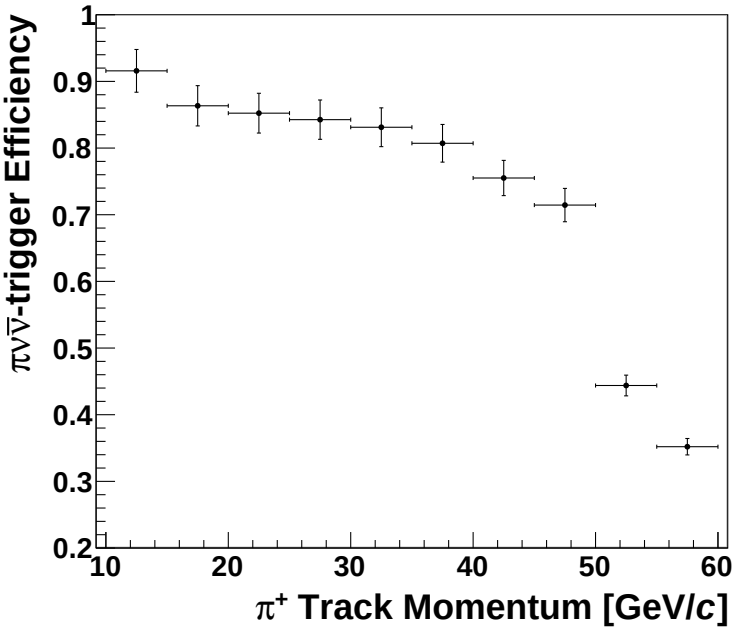

FIGURE 12.3: Total $\pi\nu\bar{\nu}$-trigger efficiency (L0+L1) evaluated for a $\pi^o \to$ *invisible* signal in 5 GeV/c bins of the π^+ momentum. The binning is the same as that used for the evaluation of the expected π^o rejection inefficiency (Figure 14.5).

Chapter 13
The Single-Photon Efficiencies: the Tag&Probe Method

About 2×10^7 $K_{2\pi}$ events are selected following the algorithm of Chapter 10 on control-trigger data in the π^+ momentum range 10–60 GeV/c and available to study the single-photon efficiencies of the photon-veto system. Additional criteria applied on top of the $K_{2\pi}$ algorithm allow to select π^o decays into two photons with at least one photon cluster well reconstructed in the LKr, so that a Tag&Probe method can be used. One photon from the π^o is used as "tagging" (indicated by $\gamma_{\rm tag}$) to determine the expected position and energy of the second photon ($\gamma_{\rm probe}$) pointing towards one of the photon-veto detectors.

13.1 Tagging photon

Events with one or two photon clusters reconstructed (from the standard reconstruction) in the LKr calorimeter are selected. If the event contains two photon clusters, the tagging photon is randomly chosen. Specific requirements are made on the tagging photon in order to precisely determine the position and energy of the probed photon:

- The energy of the tagging photon $E_{\gamma\rm tag}$ has to be between 5 and 50 GeV.
- To prevent effects of possible reconstruction biases at the border of the LKr sensitive volume, the tagging photon must be well inside the LKr sensitive region: the photon transverse position $r_{\gamma\rm tag}$ must be between 25 and 90 cm.
- To be sure that the cluster is consistent with a true photon cluster, it must not be associated to in-time extra activity in the NA48-CHOD or CHOD detectors (see Section 11.2.1 for the definition of extra activity). The cluster is not considered due to a true photon if:

  $$|T_{\gamma\rm tag} - T^{\rm extra}_{\rm NA48\text{-}CHOD}| < 10 \text{ ns and } |\vec{r}_{\gamma\rm tag} - \vec{r}^{\rm extra}_{\rm NA48\text{-}CHOD}| < 13 \text{ cm or,}$$
  $$|T_{\gamma\rm tag} - T^{\rm extra}_{\rm CHOD}| < 10 \text{ ns, } |x_{\gamma\rm tag} - x^{\rm extra}_{\rm CHOD}| < 25 \text{ cm and } |y_{\gamma\rm tag} - y^{\rm extra}_{\rm CHOD}| < 14 \text{ cm.}$$

- A distance of at least 5 cm from any LKr cell marked as dead cell by the official reconstruction is required. As a result of the study described in Appendix B, additional four regions are spotted and marked as dead cells, too.
- A timing cut, tighter than the standard photon cluster selection, is applied: $|T_{\gamma\rm tag} - T_{\rm downstream}| < 3\ \sigma_{T_{\rm LKr}}$, with $\sigma_{T_{LKr}}$ defined in Equation (11.1).

- In the decay of π^o into two photons, the energy of each photon can be related to its direction with respect to the π^o momentum as follows:

$$E_\gamma^{\text{true}} = \frac{m_{\pi^o}^2}{2\left(E_{\pi^o} - |\vec{p}_{\pi^o}|\cos\theta_{\pi^o\text{-}\gamma}\right)}. \tag{13.1}$$

  Given the π^o 4-momentum as $P_{\pi^o} = (P_{K^+} - P_{\pi^+})$, the consistency between the energy of the tagging photon as measured by the LKr and the one expected for a decay $\pi^o \to \gamma\gamma$ is enforced by the requirement that $0.7 \leq E_{\gamma\text{tag}}^{\text{true}}/E_{\gamma\text{tag}}^{\text{LKr}} \leq 1.3$.

Figure 13.1 shows selected distributions of the tagging photon cluster. In total about 8×10^6 events are selected after the requirements on the tagging photon.

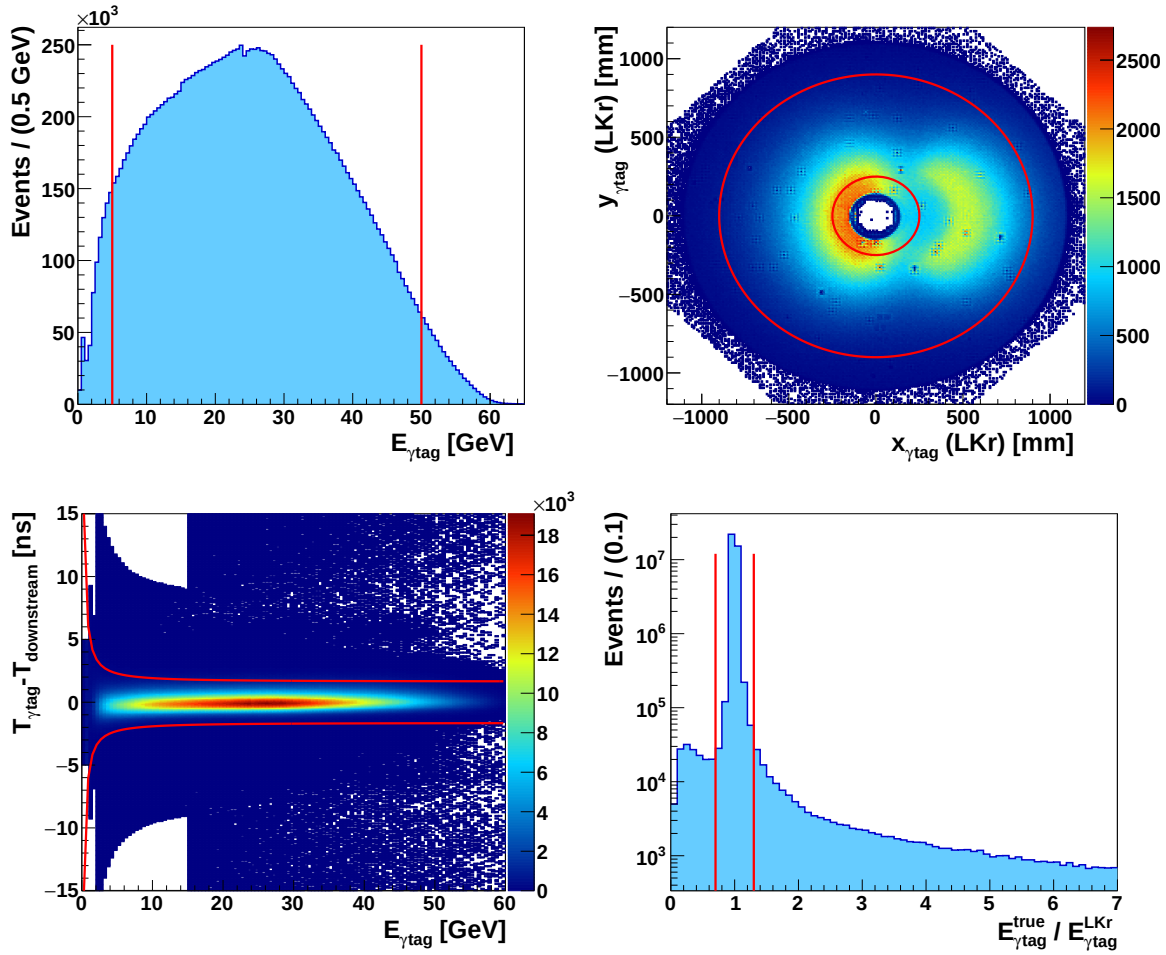

FIGURE 13.1: Distributions for the tagging photon: energy (***top left***), transverse position at the LKr plane (***top right***), timing (***bottom left***), and ratio $E_{\gamma\text{tag}}^{\text{true}}/E_{\gamma\text{tag}}^{\text{LKr}}$ between expected and reconstructed photon energy (***bottom right***). The selected photons are those which lie in the regions delimited by red lines.

13.2 Extrapolation of the probed photon

The 4-momentum of the missing photon is computed as

$$P_{\gamma\text{probe}} = (P_{K^+} - P_{\pi^+} - P_{\gamma\text{tag}}), \tag{13.2}$$

where the 3-momenta of the kaon and pion are measured by the GTK and STRAW detectors, respectively. Instead, the 3-momentum of the tagging photon is evaluated by combining the energy and position of the LKr photon cluster with the position of the K^+-π^+ vertex.

To further constrain the missing 4-momentum of Equation (13.2) to be compatible with that of a photon, the kinematic condition $M^2_{\gamma\text{probe}} = |P^2_{\gamma\text{probe}}| < 0.0025\ \text{GeV}^2/c^4$ is added. Figure 13.2 shows the mass distribution of the probed photon before the kinematic cut and its energy.

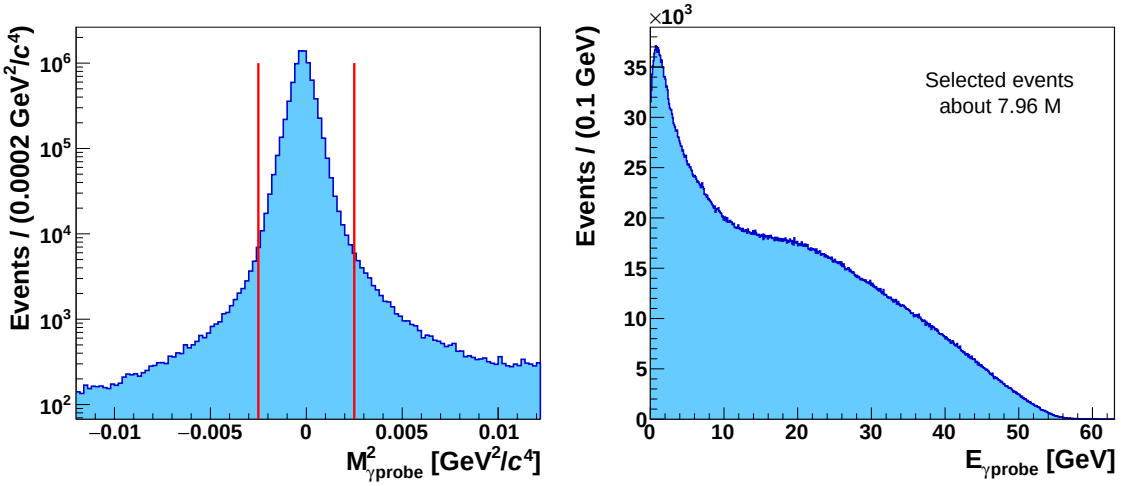

FIGURE 13.2: Distributions of the invariant mass $M^2_{\gamma\text{probe}}$ (***left***) and of the energy (***right***), after the mass cut, for the probed photon.

Using the position of the K^+-π^+ vertex as starting point, the position of the missing photon is extrapolated to the planes of the photon-veto detectors to determine the detector to which the photon is pointing, probed detector. [1] If, after the extrapolation, no sensitive area of any photon-veto detector is found being hit by the probed photon, this is considered out of acceptance. In this case the event is classified as "missing" and discarded in the efficiency evaluation. The effect of wrongly labeling the events as missing or conversely assign a detector when in reality the photon is out of acceptance is taken into account by applying the method-bias correction to the single-photon efficiency measured in data as

[1] The extrapolation technique adopted in this work was compared with a more sophisticated kinematic fitting technique used to refine the estimate of the momentum of the photon to be searched for [155]. However, the observed improvement of the resolution was not enough to further divide the LAV system in sub-structures when evaluating the single-photon efficiency. Possible resolution effects are taken into account by applying the method-bias correction (see Section 13.4.2) to the measured single-photon efficiency. Since the uncertainties due to this correction do not dominate the total error budget of the expected π^0 rejection inefficiency, the idea of importing the kinematic fit treatment was discarded.

explained in Section 13.4.2. In Table 13.1, the detector positions and the transverse radii used for the acceptance conditions are listed. The acceptance conditions for both the inner and the outer radii are tightened by 10 mm to reduce mis-tagging effects.

Detector Name	Position (x, y, z) [mm]	Inner radius [mm]	Outer radius [mm]	Acceptance type
LAV1	(0, 0, 121 363)	536.5	906.5	annular
LAV2	(0, 0, 128 973)	536.5	906.5	annular
LAV3	(0, 0, 136 583)	536.5	906.5	annular
LAV4	(0, 0, 144 193)	536.5	906.5	annular
LAV5	(0, 0, 151 803)	536.5	906.5	annular
LAV6	(0, 0, 165 313)	767.5	1 137.5	annular
LAV7	(0, 0, 172 823)	767.5	1 137.5	annular
LAV8	(0, 0, 180 333)	767.5	1 137.5	annular
LAV9	(0, 0, 192 709)	980	1 350	annular
LAV10	(0, 0, 203 102)	980	1 350	annular
LAV11	(0, 0, 217 528)	980	1 350	annular
LAV12	(0, 0, 238 315)	1 070	1 440	annular
IRC module1	(12, 0, 239 706)	60	145	annular
IRC module2	(12, 0, 239 900)	61	145	annular
LKr	(0, 0, 241 093)	150	1 130*	annular / octagon
SAC	(0, 0, 261 210)	–	205 **	box

TABLE 13.1: Position of the photon-veto detectors used for the extrapolation of the probed photon. For the LAV stations, the z coordinate of the back face is considered. For the IRC detector, both front and back modules are taken into account. *Length corresponding to the apothem of the octagon. **Length corresponding to the side of the box.

13.3 Matching criteria

Detector-level single-photon efficiencies are measured on the data, as a function of the photon energy. Since the available statistics is not enough to accurately study each LAV station individually, the LAV system is considered as a whole, without distinguishing the particular station towards which the probed photon is pointing. The IRC and SAC detectors are treated separately, according to the specific detector to which the probed photon is pointing. However, the matching condition is unique for both IRC and SAC, as it uses candidates from both detectors. While selecting the sample for the efficiency evaluation for a given photon-veto detector (LAV, SAV, LKr), the events with in-time photon candidates additional to the tagging photon reconstructed in the photon-veto detectors other than the probed one (SAV–LKr, LAV–LKr, LAV–SAV, respectively) are rejected. Figure 13.3 shows the energies of the probed photons, as defined in Equation (13.2), for all the events selected in the four samples used for the efficiencies evaluation.

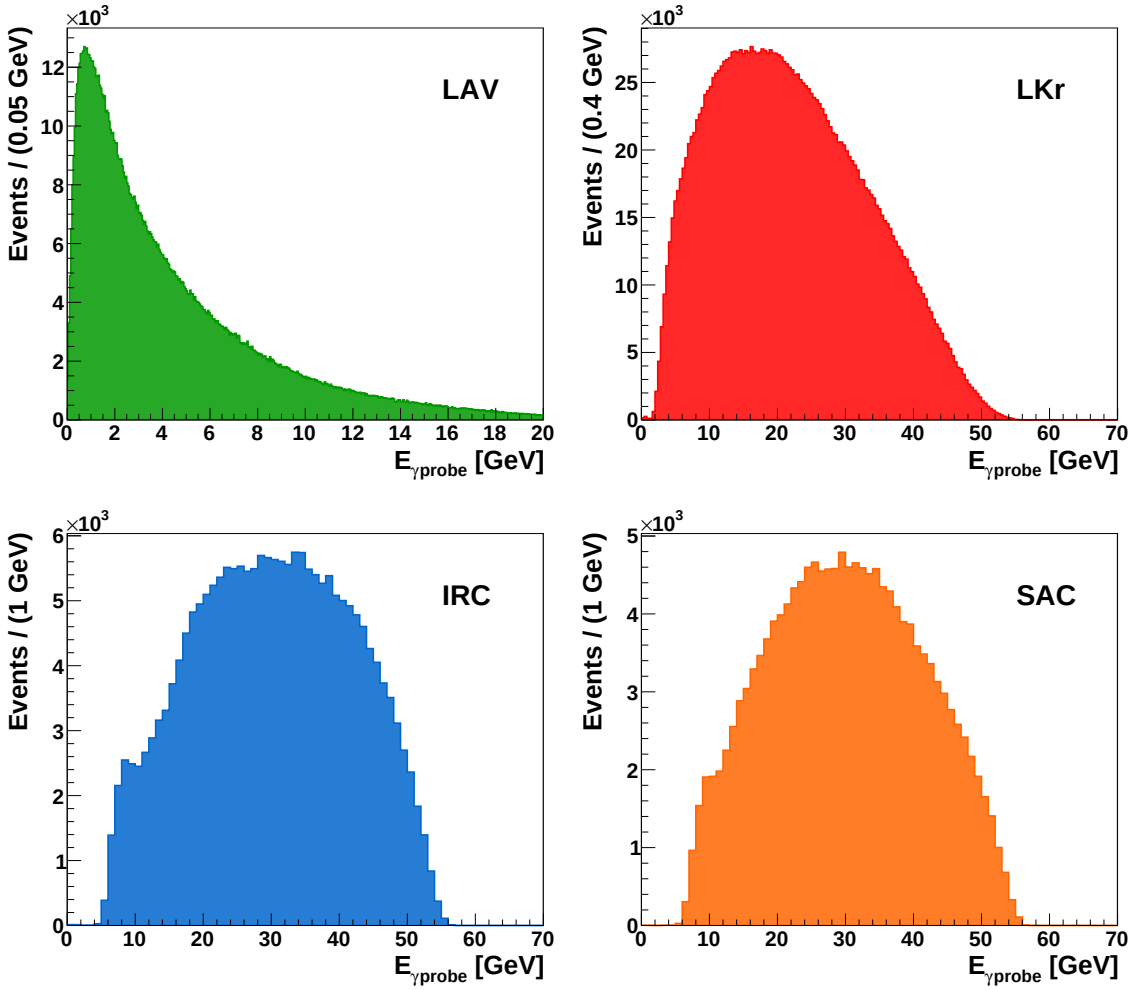

FIGURE 13.3: Energy distributions of the probed photon when pointing to the LAV system (***top left***), to the LKr calorimeter (***top right***), and to the IRC (***bottom left***) and SAC (***bottom right***) detectors.

Once the probed detector is known and no additional photons are detected in the other vetoes, the presence of a photon candidate is verified exploiting the information from both the photon-veto and photon-conversion conditions described in Chapter 11. To summarize, the conditions are:

LAV is the probed detector: γ_{tag} is the only photon detected in the LKr calorimeter, the IRC and SAC detectors are used as vetoes. The probed photon is matched if a photon is found in the LAV (Section 11.1.2) or if the photon-conversion flag is raised (Section 11.2).

IRC is the probed detector: γ_{tag} is the only photon detected in the LKr calorimeter, the LAV system is used in veto. The probed photon is matched if a photon is found in the IRC or SAC detectors (Section 11.1.3), or if the photon-conversion flag is raised (Section 11.2).

SAC is the probed detector: γ_{tag} is the only photon detected in the LKr calorimeter, the LAV system is used in veto. The probed photon is matched if a photon is found in the IRC

or SAC detectors (Section 11.1.3), or if the photon-conversion flag is raised (Section 11.2).

LKr is the probed detector: LAV, IRC, and SAC detectors are used in veto. Since these events have three particles in the LKr calorimeter, an isolation condition is applied to the expected position of the probed photon by requiring a distance of at least 45 cm from the position of both the pion and the tagging photon clusters. Moreover, the expected transverse position of the probed photon must be between 25 and 90 cm to ensure full sensitivity. The probed photon is matched if a photon is found in the LKr calorimeter (Section 11.1.1) or if the photon-conversion flag is raised (Section 11.2).

A measurement of the efficiencies as a function of the expected energy of the probed photon is performed. A total of 31, 30 and 5 energy bins are used for the LAV, LKr, and both IRC and SAC, respectively:

- LAV: bin width of 50 MeV for $E_{\gamma\text{probe}}$ between 0 and 1 GeV, 500 MeV between 1 and 6 GeV, and one single bin above 6 GeV.
- LKr: bin width of 400 MeV in the region $0 < E_{\gamma\text{probe}} < 10$ GeV, 5 GeV between 10 and 35 GeV, and one single bin above 35 GeV.
- IRC and SAC: bin width of 5 GeV below 10 GeV, one bin between 10 and 20 GeV, one between 20 and 40 GeV, and one single bin above 40 GeV.

The splitting in bins of energy is chosen as a compromise between an accurate description of the efficiency as a function of the energy and the available statistics in each bin. The efficiencies are evaluated with the Feldman-Cousins method [156] imposing 68% of confidence level. The measured efficiency for data will be referred to as $\varepsilon^{\text{TP}}_{\text{data}}$.

13.4 Efficiency corrections

Two different effects need to be taken into account in order to estimate the true single-photon efficiencies of the data ($\varepsilon^{\text{true}}_{\text{data}}$). The first one is the so-called random veto: an event is classified as efficient even in absence of a photon-induced signal due to the detection of in-time signal from accidental activity. The second is correlated with the Tag&Probe method itself: since the expected energy and position of the probed photon is evaluated from the information on the tagging photon as measured by the LKr calorimeter, an inaccurate reconstruction of the tagging energy and position leads to a wrong evaluation of the probed energy and of the probed detector. The method-bias is significant for low energies of the probed photon, and therefore affects the low energy region of the LAV and LKr efficiencies.

The following formula is used to correct the measured efficiencies and to evaluate the true one:

$$1 - \varepsilon_{\text{data}}^{\text{true}} = \frac{1 - \varepsilon_{\text{data}}^{\text{TP}}}{(1 - RV)\, b}$$
$$\varepsilon_{\text{data}}^{\text{true}} = 1 - \frac{1 - \varepsilon_{\text{data}}^{\text{TP}}}{(1 - RV)\, b} \tag{13.3}$$

where RV and b are the random veto and the method-bias corrections, respectively. The two effects have opposite impacts on the efficiencies. The effect of the random veto is mostly independent from the photon energy while depends on the probed detector. The random veto systematically leads to an efficiency higher than the true one. After the related correction RV is applied, the measured efficiencies must decrease. The method-bias depends both on the photon energy and on the probed detector. The related correction b accounts for the different sources of bias inefficiency and can lead to an efficiency higher or lower than the true one. In an ideal situation, where no random veto is introduced with the matching criteria ($RV = 0$) and no bias is due to the method ($b = 1$) the true data efficiencies coincide with the measured one.

13.4.1 Effect of the random veto on single-photon efficiencies

The random veto is evaluated in control-trigger data with $K_{\mu 2}$ events selected in a way similar to what described in Section 11.3. The difference is that, here, only the random veto due to the matching criteria (Section 13.3) used for the efficiency measurement is considered. This means that, for example the LKr efficiency is not affected by the random veto due to accidental activity in the LAV and SAV detectors. The measured random veto is about $(32.8 \pm 1.0)\%$, $(35.3 \pm 1.1)\%$, and $(26.4 \pm 0.8)\%$ when evaluating the LKr, LAV, and SAV efficiencies, respectively. Figure 13.4 shows the measured single-photon inefficiencies of LAV, LKr, IRC, and SAC detectors after the random veto correction is applied (in Equation (13.3) the method-bias b is considered equal to 1). For comparison the inefficiencies obtained by applying the Tag&Probe method on reconstructed $K_{2\pi(\gamma)}$ MC simulated events are also shown. [2] A good agreement between data and MC simulation is visible for the low-energy part of the probed photon spectrum. A disagreement is observed for the high-energy part. However, it is to be underline that the statistical uncertainty of the MC inefficiencies is not negligible when evaluating the observed disagreement, in particular for the very high-energy part of the spectrum.

[2] The random veto correction is not applied in this case, since no accidental activity is simulated in the downstream part of the detector apparatus. As mentioned in Section 7.1.1, in the MC sample analyzed for this analysis accidental activity is only simulated in the upstream detectors, GTK and KTAG, with the ***UpstreamPileupGenrator*** tool, which is described in Section 7.3.2.

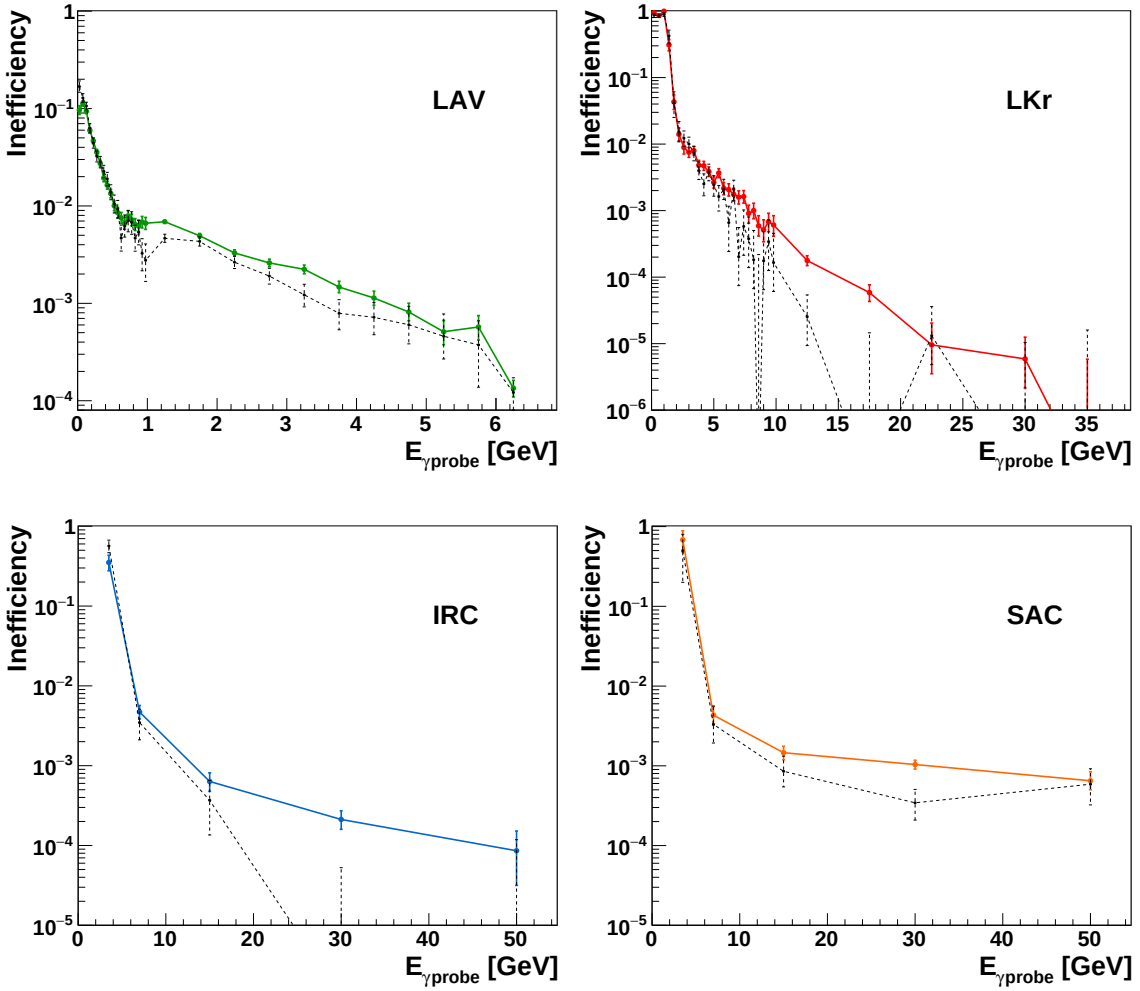

FIGURE 13.4: Measured inefficiencies as a function of the energy of the probed photon ($E_{\gamma probe}$) for data (solid line) and MC (dotted line). The data inefficiencies are corrected for the random veto according to Equation (13.3) (the method-bias b correction is set equal to 1) which is not present in the MC simulation.

13.4.2 Bias of the Tag&Probe method

The bias of the Tag&Probe method is studied with $K_{2\pi(\gamma)}$ MC simulated events. The Tag&Probe method is applied to the reconstructed MC events and the corresponding single-photon efficiency (ε^{TP}_{MC}) are computed as for the data. [3] For inefficient events, the MC truth information on the photon energies and directions is compared to that expected from the Tag&Probe, thus allowing the various sources of the method-bias to be isolated, as described in the following.

Figure 13.5 shows the true end point of the photons in the rz plane, plotted for the events found to be inefficient while probing the LAV detector by applying the Tag&Probe

[3] The $K_{2\pi}$ selection described in Chapter 10 is applied to the reconstructed MC events as for data in order to select the sample for the efficiencies evaluation.

method in the MC. The approximate shape of the detector sensitive volumes are also plotted for comparison. Three main categories of inefficient events are found:

i) Photons wrongly assumed as pointing to the sensitive volume of a LAV station, so-called mis-tagging.

ii) Photons truly pointing to one of the LAV stations and converting to e^+e^- pairs upstream of the station sensitive volume.

iii) Photons with end points within one of the LAV station sensitive volume undergoing photo-nuclear interactions.

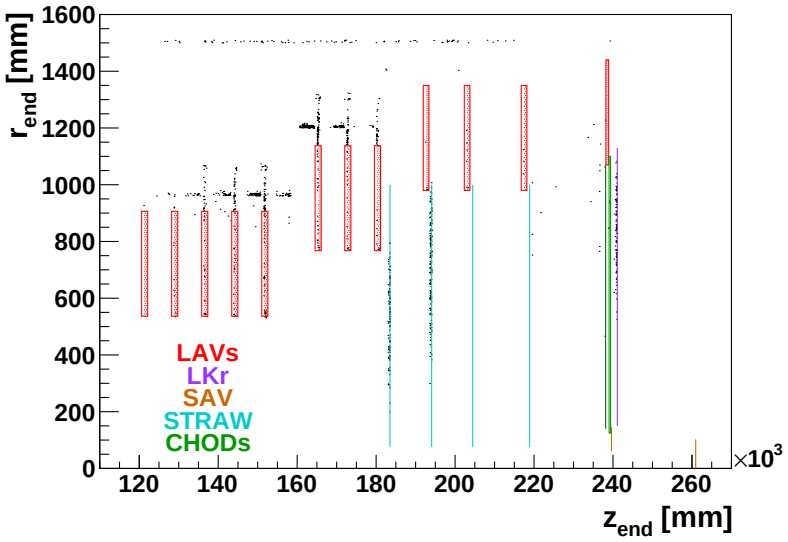

FIGURE 13.5: Events flagged as inefficient, while probing the LAV detector within the MC to evaluate $\varepsilon^{\mathrm{TP}}_{\mathrm{MC}}$. Distribution of the transverse and longitudinal coordinates of the end points of the probed photons, from MC truth information. Photons not pointing to any LAV station and photons converting upstream of a station (whose products are lost detection) are dominant. Photons escaping the apparatus are shown in the plot at $r_{\mathrm{end}} = 1\,500$ mm.

The above categories are related to well understood effects. First of all, a resolution effect of the Tag&Probe method, resulting in an incorrect detector assignment (category i)). For these events, the momentum of the probed photon (as defined in Equation (13.2)) is expected to point towards one of the LAV stations, whereas the geometrical extrapolation of the true MC momentum is outside the LAV acceptance: either the true photon line of flight misses the LAV stations at large angle (since the photon momentum has been overestimated) or it is actually pointing to the LKr calorimeter (since the photon momentum has been underestimated). The first case dominates below $\simeq$ 200 MeV and the second above $\simeq$ 1 GeV, as shown in the left panel of Figure 13.6. The first case directly leads to events of category i) as defined above, and these events automatically introduce an inefficiency. For the second case to produce events of category i), the LKr calorimeter must be inefficient, too, otherwise the events would have been rejected in advance by the veto condition

against additional in-time activity in the LKr calorimeter: this inefficiency happens mostly because the probed photon converts. Category ii) is relevant in the energy range 1–3 GeV, where upstream conversions can be lost to detection because the e^+e^- pair is severely bent by the MNP33 spectrometer magnet. Category iii) is mostly relevant in the energy range 500 MeV–1 GeV. The right panel of Figure 13.6 shows the energy of the inefficient photons, as taken from the MC truth, for the three categories defined above. The region most affected by the method-bias correction is that at low energy where category i) is the most abundant case.

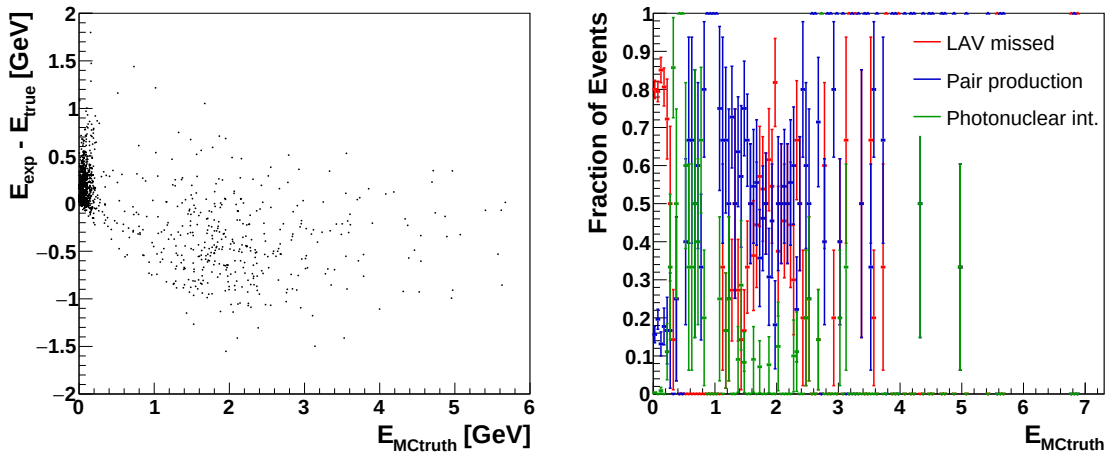

FIGURE 13.6: MC events flagged as inefficient, when probing the LAV detector to evaluate ε_{MC}^{TP}. ***Left:*** Difference between the expected and true energy of the probed photon *versus* the true energy. ***Right:*** Fractional contribution to the inefficiency for the three categories defined in the text as a function of the true energy of the probed photon.

Similar studies to those shown in Figures 13.5 and 13.6 for the LAV system are also performed for the other detectors. The different contributions to the inefficiencies of the LAV, LKr and SAV are listed in Table 13.2. For each of the detectors, the dominant source of inefficiency is due to the mis-tagging contribution. While photon interactions are real detection inefficiencies, the mis-tagging contribution is an intrinsic bias of the Tag&Probe method for which the data single-photon efficiencies must be corrected.

	LAV	**LKr**	**SAV**
Total inefficiency	4.5×10^{-3}	5.8×10^{-4}	6.3×10^{-4}
Sources of inefficiency [%]			
Mis-tagging	61.83	56.21	61.54
Photon-conversion	32.19	31.70	38.46
Photon-nuclear int.	4.66	12.09	–
Other interactions	1.32	–	–

TABLE 13.2: Sources of the MC inefficiency. The mis-tagging contribution is taken into account by the method-bias correction.

The method-bias correction is defined as the ratio between the MC inefficiencies obtained from the Tag&Probe method and the true one ($1 - \varepsilon^{\text{true}}_{\text{MC}}$):

$$b = \frac{1 - \varepsilon^{\text{TP}}_{\text{MC}}(E)}{1 - \varepsilon^{\text{true}}_{\text{MC}}(E)}. \tag{13.4}$$

The efficiencies $\varepsilon^{\text{TP}}_{\text{MC}}$ are evaluated as for the data, with the Tag&Probe method applied to the reconstructed $K_{2\pi(\gamma)}$ MC events. Instead, for $\varepsilon^{\text{true}}_{\text{MC}}$ the probed-photon energy and the probed detector to which the photon is pointing are given by the MC truth. [4] Figure 13.7 shows the method-bias obtained for the LAV and LKr efficiencies. It significantly differs from unity in the low-energy regions, namely $E_{\gamma\text{LAV}} < 2$ GeV and $E_{\gamma\text{LKr}} < 4$ GeV, where the effect of the mis-tagging is relevant. For the high-energy regions of LAV and LKr, namely $E_{\gamma\text{LAV}} > 2$ GeV and $E_{\gamma\text{LKr}} > 4$ GeV, the observed bias is compatible with 1 within the statistical uncertainties. For the IRC and SAC efficiencies, the bias ratio is assumed to be 1 in the following. Extremely large statistics would be needed to evaluate the bias related to those detectors. As demonstrated by the method validation of Chapter 17, the systematic uncertainty due to the IRC-SAC bias is expected to be a sub-leading effect after the optimization of the signal momentum region (Chapter 18).

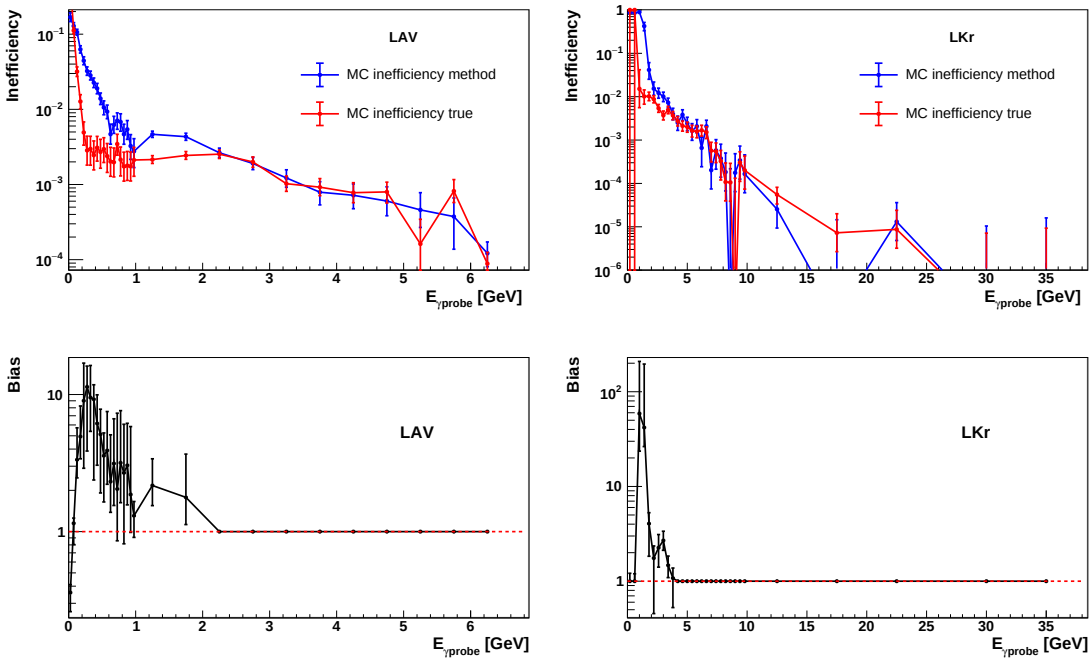

FIGURE 13.7: MC inefficiency (***top***), as measured with the Tag&Probe method (blue) and with the MC truth information (red), and measured method-bias (***bottom***) for the LAV and LKr detectors. [5] The bias plays a role in the low-energy region of the probed photon, recovering the inefficiency related to mis-tagging of the Tag&Probe method.

[4] The MC sample is treated using the ***UpstreamPileupGenerator*** tool (see Section 7.3.2 for the description). This affects the reconstruction of the GTK detector and the matching with the STRAW track, but there is no direct implication on the photon-veto capability. Obviously, a bias can be generated, as the resolution of the probed photon receives contributions from the reconstruction of the two charged particles. This possible effect is accounted for by the method-bias correction in the related data-based systematic uncertainty evaluation.

The statistical uncertainty on the LAV and LKr method-bias corrections are evaluated accounting for the partial correlation between $\varepsilon_{\mathrm{MC}}^{\mathrm{TP}}$ and $\varepsilon_{\mathrm{MC}}^{\mathrm{true}}$. Each event is flagged to whether or not it can be used for the evaluation of the true and/or method efficiency and for which energy bins of the probed photon. The efficiency is evaluated separately: i) for the events only usable for the method (true) efficiency as a function of the method (true) probed energy, E_i^{TP} (E_i^{true}); and ii) for the events usable for both the method and true efficiency as a function of the pair E_i^{TP}–E_j^{true}, where i and j can refer to different energy bins. The method and true efficiencies are obtained as statistical-weighted average of the efficiencies for the "only" and "both" categories. The statistical uncertainty is then propagated by means of a toy MC simulation. The propagated error can be regarded as a conservative estimate, since no parametrization of the measured efficiencies is done in order to reduce the statistical uncertainties. As the energy of the probed photon increases, the error of the method-bias decreases thanks to the correlation induced by the "both" category of events. As a consequence, for the final LAV and LKr single-photon efficiencies, the MC statistical uncertainty is dominant at low energy, while the data statistical uncertainty dominates at high energy.

Systematic and statistical uncertainties on the method-bias and on the random veto corrections are evaluated and accounted for when evaluating the expected π^o rejection in Chapter 14. Since the π^o rejection inefficiency is dominated by the single-photon detector inefficiencies at high energy, for this work the MC statistics induces a marginal contribution to the uncertainty on the estimated background.

13.5 Results for the single-photon efficiencies

The behavior of the LAV and LKr inefficiency is separately studied. At extremely low energies, the energy distribution of the probed photon is very steep in the LAV. Therefore, the average energy in each bin is seen to differ from and is used in place of the bin center. The analysis results are completely insensitive to this treatment. A further consistency check is performed by smoothing the LAV and LKr efficiency curves, inclusive of the related statistical uncertainties. Details are given in Appendix D. None of the analysis results (background expectations and uncertainties, optimization of the momentum signal region) shows any significant variation whether or not such a treatment is applied. Therefore, the LAV and LKr inefficiencies obtained with the smooth treatment are used in the analysis.

[5] In the LAV, the zig-zag behavior stems from the MC truth inefficiency, not from the Tag&Probe evaluation. Apparently this effect is beyond the statistical fluctuations (evaluated using the Feldman-Cousins method with 68% coverage). The step observed above 750 MeV is due to the photo-nuclear effect: a bump is observed in the true inefficiency, which is spread onto several bins in the Tag&Probe evaluation. The effect is less pronounced in the Tag&Probe evaluation in data as seen in Figure 13.4.

The results of the single-photon efficiency study are shown in Figure 13.8 after the corrections of the efficiencies for the random veto and the method-bias, according to Equation (13.3). [6] The summarized results are:

- in the LKr an inefficiency of $\mathcal{O}(10^{-4})$ between 10 and 20 GeV and below 10^{-5} above 20 GeV.
- in the LAV an inefficiency of $\mathcal{O}(10^{-3})$ between 1 and 4 GeV and below 10^{-3} above 4 GeV.
- in the IRC an inefficiency below 10^{-3} above 10 GeV.
- in the SAC an inefficiency of $\mathcal{O}(10^{-3})$ above 10 GeV.

Numerical values of the inefficiency as a function of the probed photon energy are given in Appendix C in Table C.1 and Table C.2.

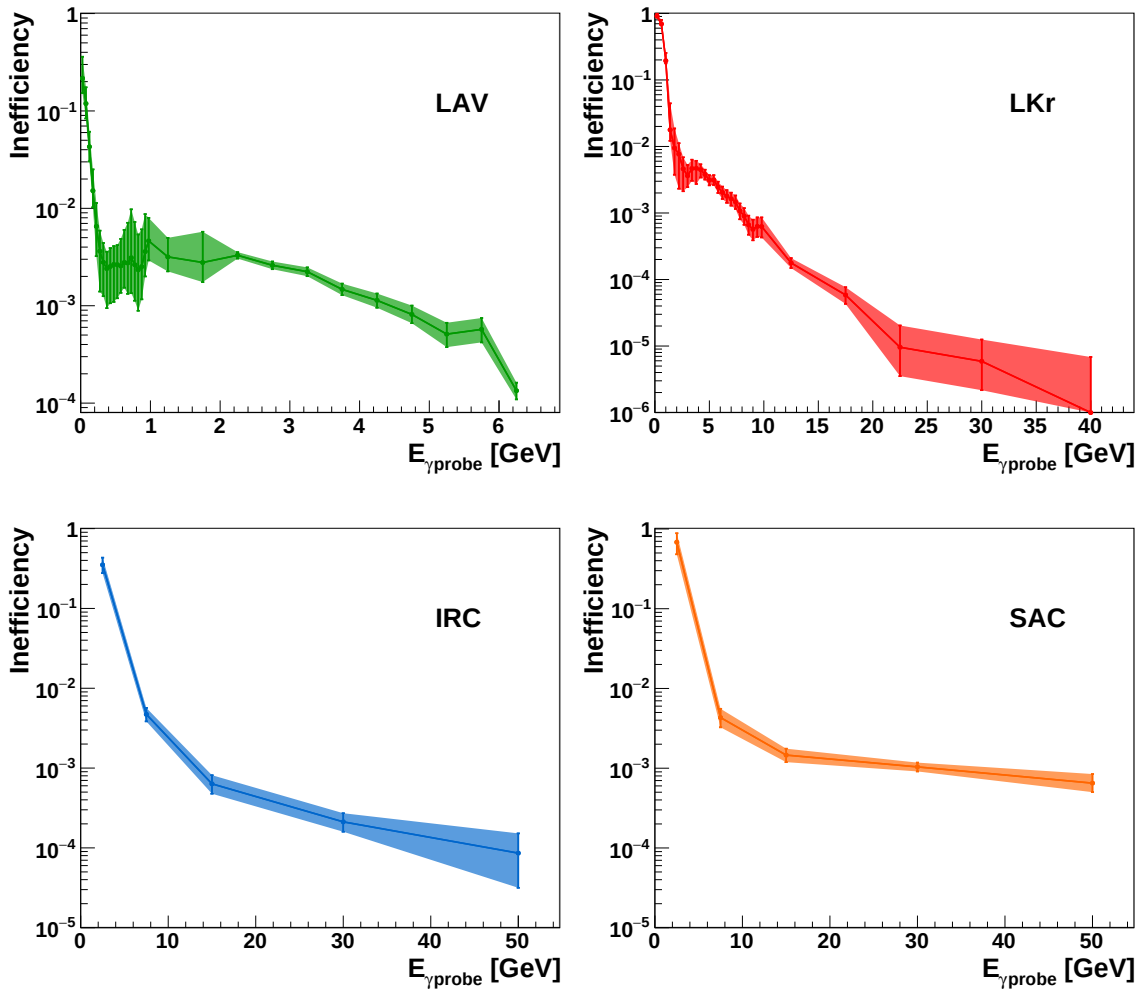

FIGURE 13.8: Inefficiency *versus* the energy of the probed photon ($E_{\gamma probe}$) as a result of the single-photon efficiency study.

[6] Only the statistical uncertainties are shown. The systematic uncertainties on the expected background rejection induced by the single-photon efficiencies are discussed in Chapter 14.

Chapter 14
The Expected π^o Rejection

The single-photon efficiencies of the data are used as input to evaluate the expected π^o rejection inefficiency by weighting $K^+ \to \pi^+\pi^o(\gamma)$, $K_{2\pi(\gamma)}$, MC events. The MC sample consists of about 60 million generated events. [1] The selection described in Chapter 10 is applied to the MC reconstructed events. The MC truth information is, instead, exploited to geometrically extrapolate each photon of the event to the LKr, LAVs and SAV detectors. Using the photon energies (given by the MC truth) and the respective detector, the event is weighted by the probability w of detecting at least one photon:

$$\begin{aligned} w &= \varepsilon_{\gamma_1} + \varepsilon_{\gamma_2} + \varepsilon_{\gamma_{\text{rad}}} - \varepsilon_{\gamma_1}\varepsilon_{\gamma_2} - \varepsilon_{\gamma_1}\varepsilon_{\gamma_{\text{rad}}} - \varepsilon_{\gamma_2}\varepsilon_{\gamma_{\text{rad}}} + \varepsilon_{\gamma_1}\varepsilon_{\gamma_2}\varepsilon_{\gamma_{\text{rad}}} = \\ &= w_{\pi^o} + \varepsilon_{\gamma_{\text{rad}}} - w_{\pi^o}\varepsilon_{\gamma_{\text{rad}}} \end{aligned} \tag{14.1}$$

where $w_{\pi^o} = \varepsilon_{\gamma 1} + \varepsilon_{\gamma 2} - \varepsilon_{\gamma 1}\varepsilon_{\gamma 2}$ is the probability of detecting at least one photon coming from the π^o and ε_{γ_i} is the efficiency of the i-photon. In case no detectable radiative photon γ_{rad} is present in the MC event (which corresponds to radiation of a photon with energy softer than 10 keV in the kaon rest frame), the total weight coincides with w_{π^o}.

The expected rejection inefficiency ε_{π^o} is obtained in bins of the π^+ momentum, as a function of the involved photon-veto detectors, and of the energy of the radiative photon. Numerical results are listed in Table 14.1 for the π^+ momentum range 15–35 GeV/c, which is the momentum range used in the $K^+ \to \pi^+\nu\bar{\nu}$ analysis. The numbers provided correspond to the central values, while the related uncertainties are provided only for the total rejection inefficiency. The uncertainty evaluation is discussed in Section 14.1.

A difference is observed in the K^+ momentum distribution of $K^+ \to \pi^+\pi^o(\gamma)$ events selected in data and MC, as shown in Figure 14.1. The difference arises from the beam simulation being tuned on the beam setup used during the 2016 data taking. In order to avoid a possible bias induced by this discrepancy, the MC events are weighted with the data/MC ratio. The impact of this correction on the estimate of the expected rejection inefficiency is negligible with respect to the total uncertainty.

14.1 Uncertainties on the expected π^o rejection

Three sources of uncertainty are considered when evaluating the rejection inefficiency ε_{π^o}:

- The statistical uncertainty due to the limited statistics of the $K_{2\pi(\gamma)}$ MC sample used to obtain the average π^o rejection inefficiency.

[1] As described in Section 7.1, for this sample π^o mesons are forced to decay into two photons.

$E^*_{\gamma\text{rad}}$ [MeV]	π^o categories	π^o rejection inefficiency		Fraction of events
		Intrinsic	Total contribution	
< 0.01	All categories	2.70×10^{-8}	2.59×10^{-8}	0.957
	LKr-LKr	4.86×10^{-10}	3.52×10^{-10}	0.7236
	LKr-LAV	1.09×10^{-10}	1.76×10^{-11}	0.1608
	LKr-SAV	$8.94 \times 10-8$	9.55×10^{-9}	0.1068
	LKr-Missing*	–	–	0.0022
	LAV-SAV	7.86×10^{-7}	5.11×10^{-9}	0.0065
	SAV-Missing	1.24×10^{-4}	1.24×10^{-8}	0.0001
0.01 – 2	All categories	2.19×10^{-8}	9.08×10^{-10}	4.15×10^{-2}
2 – 4	All categories	1.06×10^{-8}	1.10×10^{-11}	1.04×10^{-3}
4 – 6	All categories	3.12×10^{-9}	8.91×10^{-13}	2.86×10^{-4}
6 – 8	All categories	2.41×10^{-10}	1.77×10^{-14}	7.34×10^{-5}
8 – 10	All categories	5.18×10^{-11}	1.56×10^{-15}	3.01×10^{-5}
≥ 10	All categories	2.55×10^{-10}	6.90×10^{-15}	2.72×10^{-5}
Total π^o rejection inefficiency: $\left(2.68^{+1.46}_{-1.90}\right) \times 10^{-8}$				

TABLE 14.1: Expected π^o rejection inefficiency for the π^+ momentum range 15–35 GeV/c in the different categories of the two π^o photons and as a function of the energy of the radiative photon, provided for the single category (intrinsic) and as contribution to the total rejection inefficiency. $E^*_{\gamma\text{rad}}$ is given in the K^+ center of mass. In the events with photon radiation softer than 10 keV, the photon in not propagated in the GEANT4 simulation. The uncertainties of the total π^o rejection inefficiency combine statistical and systematic uncertainties. *The category LKr-Missing does not contribute to the evaluated rejection, but only to its uncertainty. This happens because in such events the photon detected by the LKr has an energy above 35 GeV, where only an upper limit to the LKr detection inefficiency could be set.

- The statistical uncertainty due to the statistical errors of the data single-photon efficiencies.
- The systematic uncertainty due to the method-bias correction applied on the data single-photon efficiencies.

The study of the uncertainties on the expected π^o rejection inefficiency described in Sections 14.1.1, 14.1.2, and 14.1.3 takes as example the π^+ momentum region 15–35 GeV/c. However, this procedure is repeated in each of the π^+ momentum bin in which the expected π^o rejection inefficiency is computed.

14.1.1 Statistical uncertainty of the MC

The uncertainty induced by the limited MC statistics is obtained by dividing in 20 subsamples the $K_{2\pi(\gamma)}$ MC events and computing for each sub-sample the expected π^o rejection inefficiency. The average of the 20 measurements is considered as the central value of the rejection inefficiency ε_{π^o} while its standard deviation is taken as statistical uncertainty induced by the available MC statistics. For the π^+ momentum region 15–35 GeV/c given in Table 14.1, the result for the rejection inefficiency including only the MC statistical uncertainty is $\varepsilon_{\pi^o} = (2.68 \pm 0.13) \times 10^{-8}$.

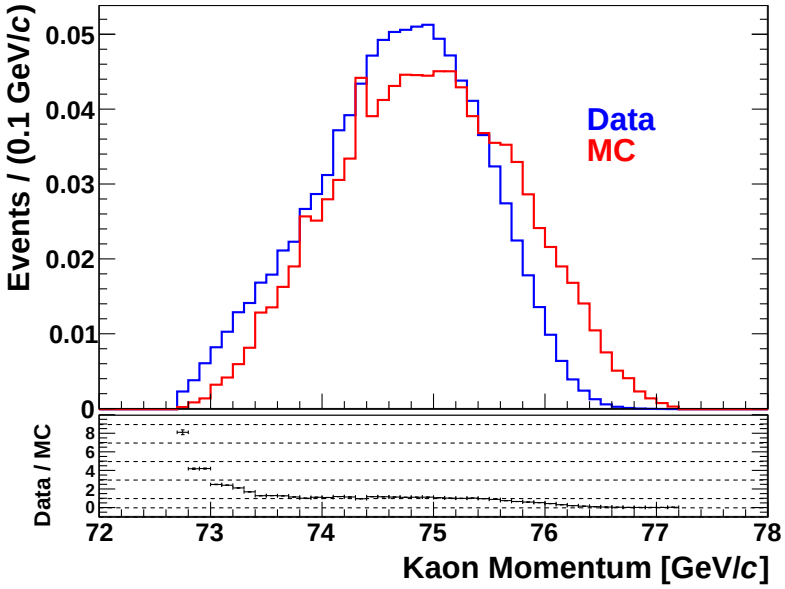

FIGURE 14.1: Kaon momentum of $K_{2\pi(\gamma)}$ events selected as described in Chapter 10 for data (blue) and MC (red). The expected π^0 rejection inefficiency is corrected to account for the difference observed between data and MC.

14.1.2 Statistical uncertainty of the single-photon efficiencies

When evaluating the expected π^0 rejection inefficiency, the single-photon efficiencies measured on data are used. In order to propagate the error of the single-photon efficiencies, the evaluation is repeated 1 000 times randomly sampling the efficiencies with an asymmetric distribution centered on the measured value and with left and right gaussian spreads determined by the corresponding (asymmetric) uncertainties. From the distribution of the 1 000 obtained rejection inefficiencies, left- and right-asymmetric uncertainties are derived by taking 1 sigma confidence interval with 34.1% coverage on both sides of ε_{π^0} (obtained with the mean value of the single-photon efficiencies). In the momentum region 15–35 GeV/c, the result for the rejection inefficiency including such an uncertainty is $\varepsilon_{\pi^0} = \left(2.68^{+1.46}_{-1.90}\right) \times 10^{-8} = \left(2.68 \pm 0.13_{(\text{MCstat.})} \pm^{1.45}_{1.89(\text{Datastat.})}\right) \times 10^{-8}$.

14.1.3 Systematic uncertainty of the single-photon efficiencies

The determination of the π^0 rejection inefficiency based on MC simulation is sensitive to systematic effects in the Tag&Probe method used to determine the single-photon efficiency. The LKr calorimeter, a central detector in this work, can be considered as the most important source of systematic effects. In particular, the reliability of the MC in simulating non-gaussian tails of the LKr energy resolution has been carefully studied. The LKr energy resolution is evaluated in data and MC from the selection of $K^+ \to \pi^+\pi^0(\gamma)$ events with π^0 undergoing Dalitz decay ($K_{2\pi_D}$ events). The following data and MC samples have been analyzed:

- Data 2017 Sample A. The filter *POS3TVFilter* [134] has been used during the central reprocessing of the data in order to identify three-track events with a positron in

the final state. The filter requires data collected within the *Control*, *Multi-track* and *Electron-multi track* trigger streams (see Section 8.1.1 for the details of the trigger configurations). Data are reconstructed with the software revision *v1.0.2*.

- MC sample of $K^+ \to \pi^+\pi^0(\gamma)$ events with the π^0 meson forced to have Dalitz decay ($\pi^0 \to \gamma e^+ e^-$). About 5×10^7 events centrally produced with the software revision *v0.11.1* have been analyzed.

After applying the selection described in Appendix E, the expected 4-momentum of the Dalitz photon $P_{\gamma\text{expected}} = (P_{K^+} - P_{\pi^+} - P_{e^+} - P_{e^-})$ is required to point to the LKr sensitive volume. A distance greater than 20 cm is required between the expected photon position and the impact point at the LKr surface of each of the three charged particles. The photon is searched among the LKr photon clusters of the standard reconstruction. Only one photon must be present in time with the event [2] and at least 15 cm away from the pion, electron, and positron clusters. The photon cluster is required to be within 50 cm from its expected position, as computed with the charged particles, and all the conditions imposed to the tagging photon of the Tag&Probe method are applied (see Section 13.1).

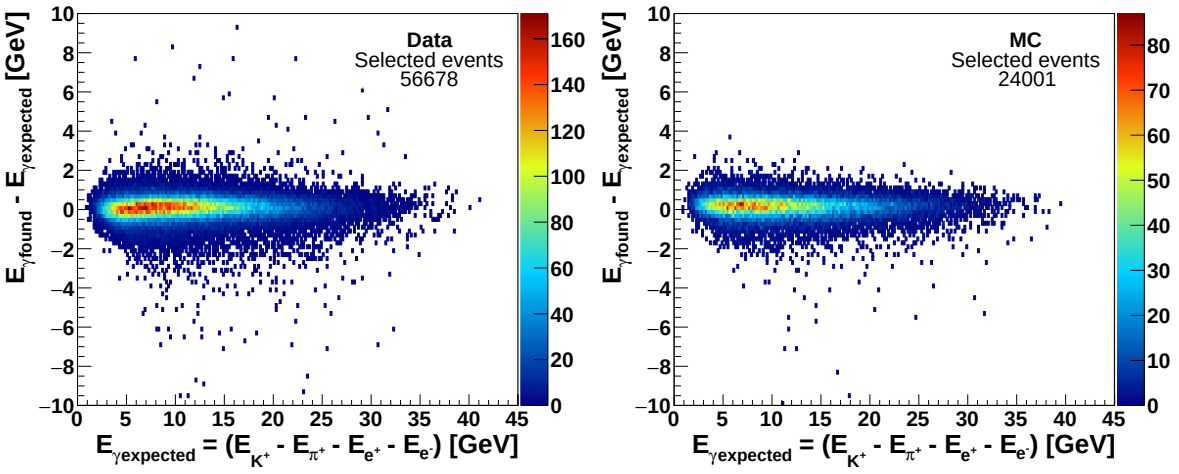

FIGURE 14.2: Difference between expected and reconstructed LKr photon energy as function of the expected energy (computed with the charged particle 4-momenta) for selected $K_{2\pi_D}$ events in data (***left***) and MC (***right***).

The difference between the reconstructed and expected photon energy is evaluated in bins of the expected energy, as shown in Figure 14.2 for the data (left panel) and MC (right panel). The data distribution is populated by events in the very far tails of the resolution, which are not present with the same rate (negative values of the y axis) or are absent altogether (positive values of the y axis) in the simulation. [3] In order to correctly account for this effect in the calculation of the method-bias correction (described in Section 13.4.2), the

[2] The timing-*versus*-energy conditions are used, according to the list in Table 11.1.

[3] Possible contributions from the STRAW track reconstruction to the far tails of the energy residual distributions were studied in the context of the search for $K^+ \to \pi^+\pi^0$ with $\pi^0 \to \gamma A'$, as explained in Reference [157]. Using the MC truth for the π^+ or $e^\pm$ in place of the reconstructed tracks, no difference was observed in the resolution evaluated in the MC and the data-MC comparison was unchanged.

LKr resolution tails are parameterized from the $K_{2\pi_D}$ data selection and then applied to the $K_{2\pi(\gamma)}$ MC sample used to evaluate the MC efficiencies as described in the following.

The resolution of the measured LKr photon energy in data is studied in 4 bins of the expected energy (0–5 GeV, 5–10 GeV, 10–20 GeV, and above 20 GeV) as shown in Figure 14.3. The LKr resolution is described by the histogram itself for the bulk of the distribution (gaussian central region delimited by the dashed black lines) and by the fit of the tails with an inverted second order polynomial, $f(x) = 1/(p_2x^2 + p_1x + p_0)$.

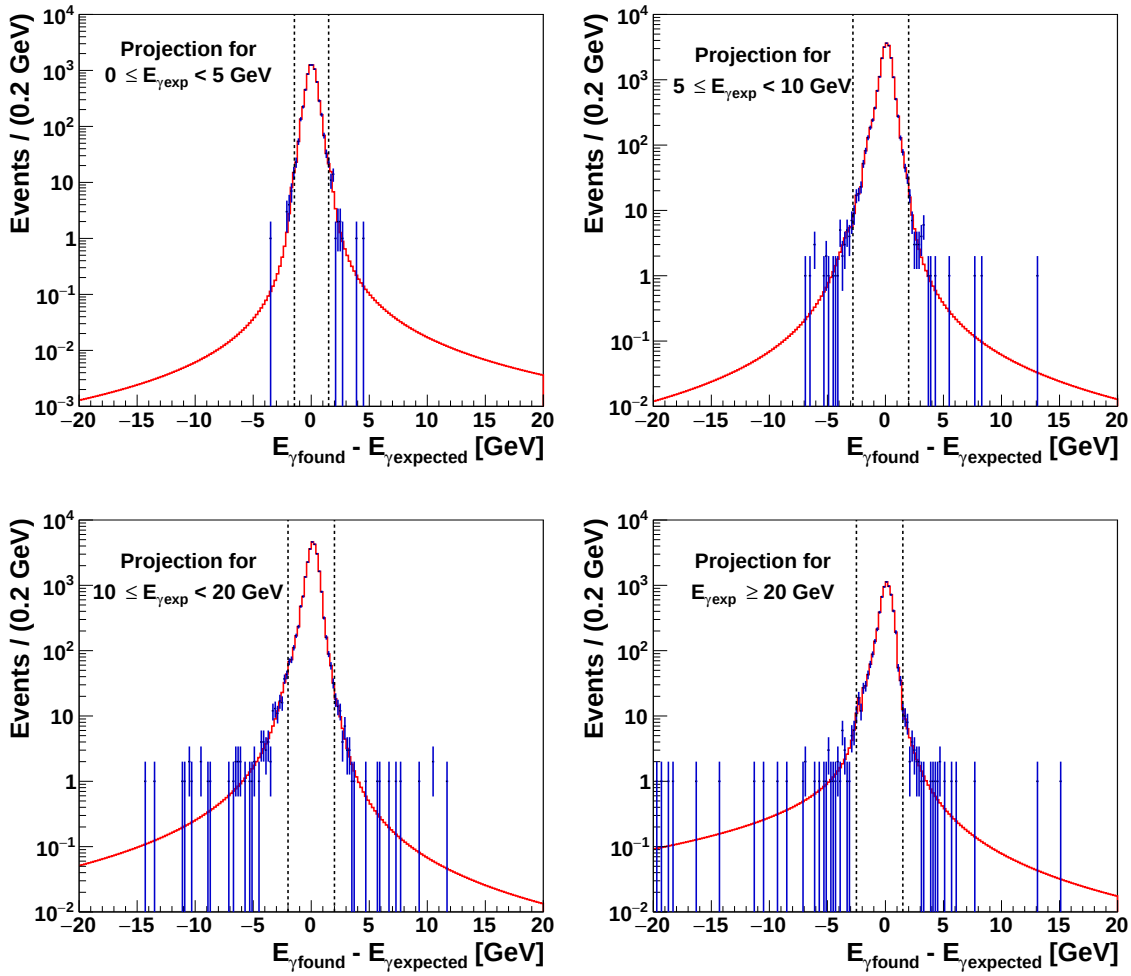

FIGURE 14.3: LKr energy resolution as evaluated in data with $K_{2\pi_D}$ events selected as described in the text. The difference between the reconstructed and expected photon energy is plotted in four different bins of the expected energy. The blue points represent the data, while the red curve is the result of the fit.

The parameterized LKr energy resolution obtained in data is inserted in the $K_{2\pi(\gamma)}$ MC sample used for the evaluation of the single-photon efficiencies within the MC, with the goal to correct the reconstructed energy of the tagging photon and determine the effect

on the method-bias correction. Given the true energy of the photon cluster a new reconstructed energy is randomly sampled according to the parameterization of the data resolution. Events in the far tails of the energy resolution are rare, but can affect the Tag&Probe method. Given the limited MC statistics available for the evaluation of the method-bias correction, and to avoid that the result is being driven by few events moved to the far tails of the resolution, the energy smearing procedure is repeated 1 000 times for each event.
The single-photon efficiencies of the Tag&Probe method are evaluated for this smeared MC, providing an alternative method-bias correction (with respect to that defined in Section 13.4.2) to be applied to the data efficiencies according to Equation (13.3). To control the statistical uncertainty of this procedure, the total available $K_{2\pi(\gamma)}$ MC statistics (60 million of events) is divided into two (equal sized) sub-samples and the method-bias is evaluated separately in each of them, as shown in Figure 14.4. The data-MC resolution discrepancy clearly affects the region 300 MeV–1 GeV of the method-bias for the LAV efficiency at the level of a factor up to 2, while the effect is smaller when evaluating the method-bias for the LKr efficiency. Given the LAV expected inefficiency and the method-bias correction extent, a systematic uncertainty of $<^{+0.5}_{-0.2}$ % on the low-energy region of the LAV inefficiency is derived.

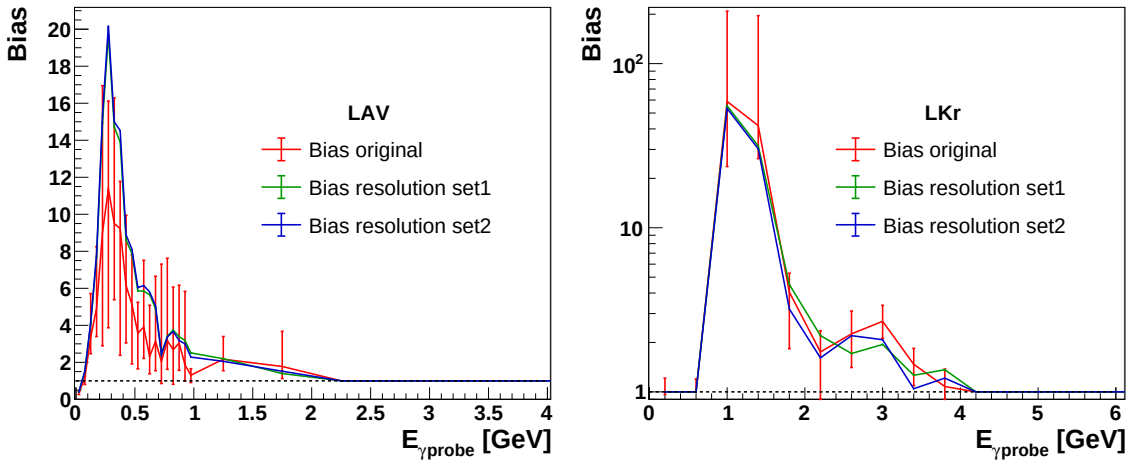

FIGURE 14.4: Method-bias for the LAV (***left***) and LKr (***right***) efficiencies. The green and blue lines represent the method-bias correction once the parameterized LKr resolution measured in the data is inserted in the two (equal sized) $K_{2\pi(\gamma)}$ MC sub-samples for the evaluation of $\varepsilon^{\mathrm{TP}}_{\mathrm{MC}}$. The red line is the measured method-bias obtained in Section 13.4.2 without considering any resolution effect.

The π^o rejection inefficiency is evaluated after correcting the efficiency for each of the two alternative method-bias factors. A corresponding systematic uncertainty is estimated as the difference between the mean of the π^o rejection inefficiency using the two alternative method-bias values and that obtained without including any correction for the different data and MC LKr energy resolution. This procedure is applied for each of the π^+ momentum ranges where the π^o rejection inefficiency is evaluated. For the π^+ momentum region 15–35 GeV/c, given as example in Table 14.1, the rejection inefficiency obtained after

including also the systematic uncertainty is

$$\varepsilon_{\pi^o} = \left(2.68^{+1.46}_{-1.90}\right) \times 10^{-8} = \left(2.68 \pm 0.13_{(\text{MCstat.})} \pm^{1.45}_{1.89(\text{Datastat.})} \pm 0.05_{(\text{Datasyst.})}\right) \times 10^{-8}.$$

After considering the impact of the LKr resolution on the method-bias correction, the result for the rejection inefficiency uncertainties is practically unchanged. The statistical uncertainty due to the data single-photon efficiencies is seen to dominate the total uncertainty. Other tests for systematic effects are performed by comparing the expected background events with the observed counts in data sidebands, as will be explained in Chapter 17.

14.2 Expected π^o rejection as a function of the π^+ momentum

The expected π^o rejection inefficiency is computed in 5 GeV/c bins of the π^+ momentum. An additional source of rejection in the data is given by accidental in-time activity in the photon-veto detectors, the so-called random veto. The π^o rejection inefficiency evaluated with the MC is therefore scaled by a factor $\varepsilon_{\text{signal}} = (1 - RV) = (0.501 \pm 0.016)$, as obtained in Section 11.3. For the π^+ momentum range 15–35 GeV/c the corresponding π^o rejection inefficiency is $\varepsilon_{\pi^o} = \left(1.34^{+0.73}_{-0.95}\right) \times 10^{-8}$.

A possible source of rejection present in data but not accounted for by the MC evaluation is given by the $\pi\nu\bar{\nu}$-trigger conditions, which perform an online photon veto both at L0 and at L1, with the L0LKr and L1LAV algorithms respectively. If the trigger conditions are partly orthogonal to the offline conditions of the photon-rejection algorithm, the trigger would induce an additional rejection. This possibility is investigated by selecting, according to Chapter 10, $K_{2\pi}$ events on control-trigger data and looking for at least one event which survives all the photon-rejection conditions but it is discarded by the $\pi\nu\bar{\nu}$ trigger. After applying the full photon-rejection algorithm no event is seen to survive out of 21 million selected events before any $\pi\nu\bar{\nu}$-trigger requirement is applied. Therefore, with the available statistics, any trigger effect on the rejection (if present) must be below 1×10^{-7} at 90% of confidence level.

The total expected rejection inefficiency as a function of the charged pion momentum (5 GeV/c momentum bins) is shown in Figure 14.5. Table 14.2 lists the numerical values. The result strongly depends on the π^+ momentum. Increasing the π^+ momentum above 40 GeV/c corresponds to decrease the π^o momentum below 35 GeV/c and to enhance the probability that one of the π^o photons escapes detection passing in the regions not instrumented between two LAV stations. Instead, decreasing the π^+ momentum below 15–20 GeV/c increases the probability that the hardest of the two π^o-daughter photons touches the beam pipe and converts therein into an e^+e^- pair which is then lost to detection. [4]

[4] The e^+e^- pair can be bent away from any sensitive volume of the detectors by the dipole magnet placed between the MUV3 and SAC detectors.

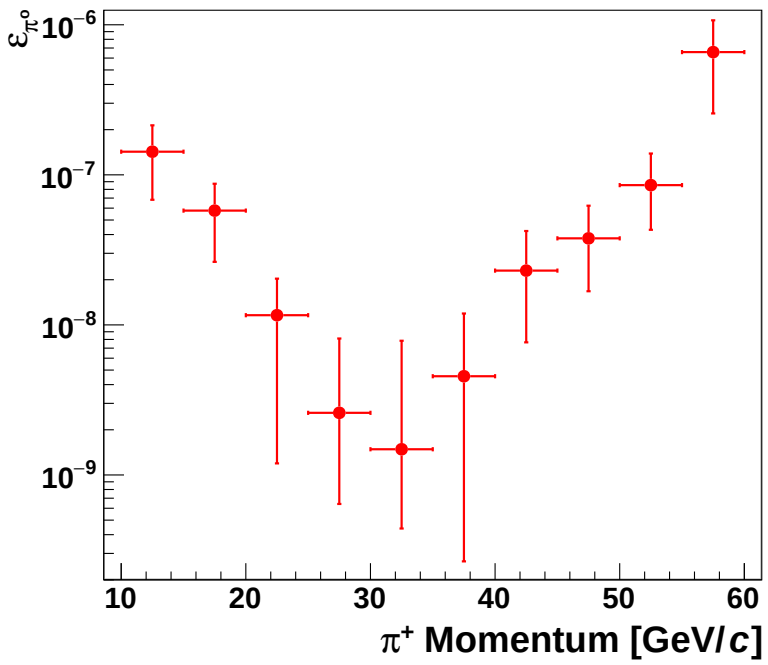

FIGURE 14.5: Overall expected rejection inefficiency of π^o from $K^+ \to \pi^+\pi^o(\gamma)$ events estimated from a combination of data single-photon efficiencies and MC simulation. The rejection inefficiency is studied as a function of the charged pion momentum (5 GeV/c momentum bins).

The reliability of the rejection obtained with the Tag&Probe method needs to be verified. Control regions with an expected π^o rejection inefficiency in-line (or above) the current limit of $\mathcal{O}(10^{-7})$ [41] on the physical process are identified at the edges of the π^+ momentum spectrum:

- left sideband: π^+ momentum 10–15 GeV/c, $\varepsilon_{\pi^o} = \left(1.43^{+0.71}_{-0.74}\right) \times 10^{-7}$.
- right sideband: π^+ momentum 55–60 GeV/c, $\varepsilon_{\pi^o} = \left(6.6^{+4.1}_{-4.0}\right) \times 10^{-7}$.

The left sideband at low π^+ momentum allows validation of the IRC and SAC efficiencies, which are the leading contributors to the total π^o inefficiency, as shown in the left panel of Figure 14.6. The LKr efficiency, instead, dominates the inefficiency at high π^+ momentum with a sub-leading contribution from the LAV (Figure 14.6 right panel) and might be validated in the right sideband. [5] The validation studies are described in detail in Chapter 17. After the validation, the momentum cut is optimized in the central region (π^+ momentum 20–45 GeV/c) to obtain the optimal signal region for the final measurement of the $\pi^o \to$ *invisible* decay, as discussed in Chapter 18.

[5] As it will explained in Chapter 17, the 50 GeV/c cut applied by the L1STRAW algorithm in the $\pi\nu\bar{\nu}$-trigger stream, on whose data the $\pi^o \to$ *invisible* is based, excludes this possibility and a different approach for the validation of the LKr and LAV efficiencies is followed.

π^+ Momentum [GeV/c]	ε_{π^0} [10^{-8}]
10 – 15	$14.3^{+7.1}_{-7.4}$
15 – 20	$5.8^{+3.0}_{-3.2}$
20 – 25	$1.16^{+0.87}_{-1.04}$
25 – 30	$0.26^{+0.55}_{-0.20}$
30 – 35	$0.15^{+0.64}_{-0.10}$
35 – 40	$0.45^{+0.74}_{-0.43}$
40 – 45	$2.3^{+1.9}_{-1.5}$
45 – 50	$3.8^{+2.5}_{-2.1}$
50 – 55	$8.5^{+5.3}_{-4.2}$
55 – 60	66^{+41}_{-40}

TABLE 14.2: Values of the expected overall π^0 rejection inefficiency, as reported in Figure 14.5. The total uncertainties include the statistical contribution from MC, and the statistical and systematic contributions from the data single-photon efficiencies.

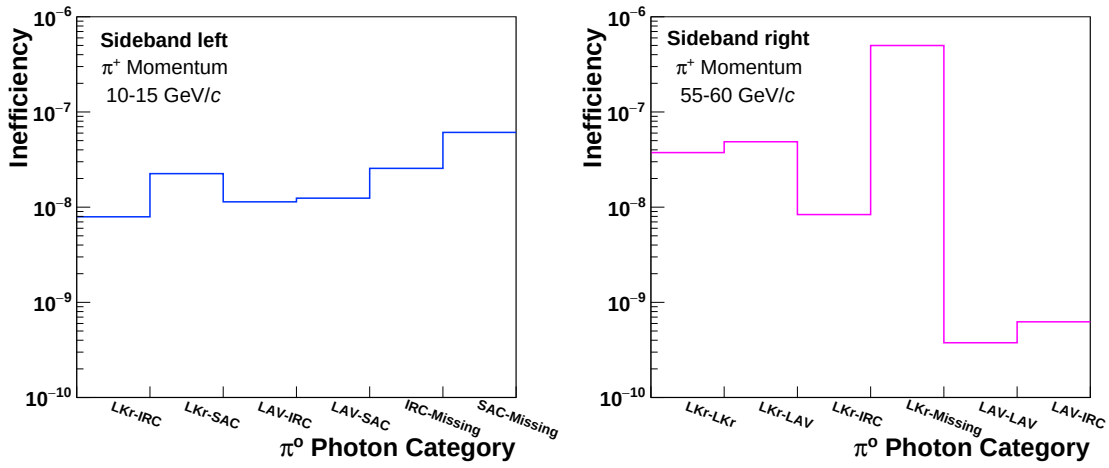

FIGURE 14.6: Inefficiency contributions to the total π^0 rejection in different categories of the two π^0-daughter photons for the two sideband regions. The inefficiency is dominated by the IRC&SAC and LKr in the low (***left***) and high (***right***) π^+ momentum sideband region, respectively. Only the categories with an inefficiency contribution greater than 10^{-10} are shown.

Chapter 15
The Background Expectation

The signal sample for the search for $\pi^o \to$ *invisible* events is obtained after applying the $K_{2\pi}$ selection and the conditions of the photon-rejection algorithm, as veto, to $\pi\nu\bar{\nu}$-trigger data. After signal selection, the dominant background contribution of the residual events is due to $K^+ \to \pi^+\pi^o(\gamma_{\rm IB})$ events with $\pi^o \to \gamma\gamma$ decays, where the photons emitted from the π^o decay, as well as through the inner bremsstrahlung (IB) amplitude, are undetected. The estimated background rejection is seen to strongly depend on the momentum of the radiative photon from the IB amplitude (see Table 14.1): decays with a radiative photon harder than 10 keV/c in the K^+ rest frame are rejected at the level of 10^{10} or better. [1] Given the rejection power on hard radiated photons, the background contribution from the radiative process $K^+ \to \pi^+\pi^o\gamma$ mediated by a structure-dependent direct-emission transition amplitude (DE) and by the interference (INT) between DE and IB amplitudes [158–160] is negligible.

Any background source other than undetected $K^+ \to \pi^+\pi^o(\gamma), \pi^o \to \gamma\gamma$ decays can also be considered negligible. This point is studied as an extension of the background estimation of the $K^+ \to \pi^+\nu\bar{\nu}$ search [161]. From the procedure described in Reference [152], which produces a first estimate of the $M^2_{\rm miss}$ expected distribution as a function of the π^+ momentum, the background contributions other than the dominant π^o-induced background are evaluated. [2] As shown in Table 15.1, it turns out that the $K^+ \to \pi^+\nu\bar{\nu}$ channel is the largest single background contributor (as evaluated assuming the SM central value for its branching ratio [3]). Throughout the entire π^+ momentum window considered, the overall number of expected background events slowly varies with the momentum and is well below 0.1 events for each π^+ momentum bin considered. Normalized to the expected π^o-induced background, the contribution of any other background is seen to be always below 1.5%.

As discussed in Chapters 13 and 14, to evaluate the expected number of background events, single-photon detection efficiencies are determined from a Tag&Probe method on data, and the expected rejection for $K^+ \to \pi^+\pi^o(\gamma)$, $\pi^o \to \gamma\gamma$ decays is obtained by

[1] In the MC simulation, the IB transition includes the effect of multiple soft photon emission by QED [141]. The energy of all the soft photons is summed up and provides the energy of the single photon emitted. The momentum spectrum of the charged pion accounts for the total energy radiated. Since the $\pi^o \to$ *invisible* analysis is insensitive to IB photons of energy harder than 10 keV, any effect induced by multiple photon emission might be relevant only if all of the photons are softer than 10 keV. Any bias due to multiple photon emission on the evaluation of the expected background events is therefore negligible.

[2] The $M^2_{\rm miss}$ shape distributions has been obtained from private discussion with Giuseppe Ruggiero and Tommaso Spadaro.

[3] ${\rm BR}_{\rm SM}(K^+ \to \pi^+\nu\bar{\nu}) = (8.4 \pm 1.0) \times 10^{-11}$.

Decay	Background contribution
$K^+ \to \pi^+\nu\bar{\nu}$	0.214
$K^+ \to \mu^+\nu(\gamma)$	0.012
$K^+ \to \mu^+\nu(\gamma)$ $(\mu^+ \to e^+\nu)$	0.003
$K^+ \to \pi^+\pi^o\pi^o$	0.001
Upstream decays	0.084
Total background	0.314

TABLE 15.1: Summary of the background contributions other than the dominant one, undetected $K^+ \to \pi^+\pi^o(\gamma)$ and $\pi^o \to \gamma\gamma$ events, for the full π^+ momentum spectrum considered. The estimate of the number of background events is obtained by extension of the procedure adopted in the $K^+ \to \pi^+\nu\bar{\nu}$ analysis of 2017 data.

weighting simulated events for the probability that all photons escape detection. The expected number of background events N_{bkg} is evaluated after accounting for the trigger efficiency according to Equation (9.2), here reported,

$$N_{\text{bkg}} = N_{\pi^o} \times \varepsilon_{\pi^o} \times \varepsilon_{\text{trigger}}$$

where ε_{π^o} is the expected π^o rejection inefficiency; $\varepsilon_{\text{trigger}}$ is the trigger efficiency; N_{π^o} is the number of tagged π^o mesons evaluated in data before any photon-rejection condition is applied. The estimated number of background events in 5 GeV/c π^+ momentum bins are listed in Table 15.2. The uncertainties on the expected π^o rejection inefficiency and on the trigger efficiency are propagated in the estimation on the number of background events.

π^+ Momentum [GeV/c]	N_{π^o} [10^6]	ε_{π^o} [10^{-8}]	$\varepsilon_{\text{trigger}}$ [%]	N_{bkg}
10 – 15	84.55 ± 0.18	$14.3^{+7.1}_{-7.4}$	91.6 ± 3.2	$11.1^{+5.5}_{-5.8}$
15 – 20	923.43 ± 0.61	$5.8^{+3.0}_{-3.2}$	86.3 ± 3.0	46^{+24}_{-25}
20 – 25	$1\,383.90 \pm 0.74$	$1.16^{+0.87}_{-1.04}$	85.2 ± 3.0	14^{+10}_{-12}
25 – 30	$1\,612.51 \pm 0.80$	$0.26^{+0.55}_{-0.20}$	84.3 ± 3.0	$3.5^{+7.5}_{-2.7}$
30 – 35	$1\,504.93 \pm 0.78$	$0.15^{+0.64}_{-0.10}$	83.1 ± 2.9	$1.9^{+7.9}_{-1.3}$
35 – 40	$1\,313.67 \pm 0.73$	$0.45^{+0.74}_{-0.43}$	80.7 ± 2.8	$4.8^{+7.8}_{-4.5}$
40 – 45	$1\,058.54 \pm 0.66$	$2.3^{+1.9}_{-1.5}$	75.5 ± 2.6	18^{+15}_{-12}
45 – 50	481.37 ± 0.44	$3.8^{+2.5}_{-2.1}$	71.5 ± 2.5	$12.9^{+8.4}_{-7.2}$
50 – 55	26.91 ± 0.10	$8.5^{+5.3}_{-4.2}$	44.4 ± 1.6	$1.02^{+0.64}_{-0.51}$
55 – 60	0.35 ± 0.01	66^{+41}_{-40}	35.2 ± 1.2	$0.082^{+0.052}_{-0.050}$

TABLE 15.2: Summary of the number of tagged π^o mesons N_{π^o}, expected background rejection inefficiency ε_{π^o}, $\pi\nu\bar{\nu}$-trigger efficiency $\varepsilon_{\text{trigger}}$, and estimated number of background events N_{bkg} evaluated in 5 GeV/c π^+ momentum bins.

Chapter 16
The Statistical Treatment of Data: the CL_s Method

Given the estimated number of background events, the statistical treatment of the CL_s method [103] is used to evaluate the expected number of signal events N_s to a certain confidence level (CL). The method is widely used in statistically limited searches, where the transitions between exclusion, observation, discovery, and measurement are small. It consists of two hypothesis tests:

- the null, or background-only, hypothesis (b) which here implies that the data can be understood in terms of SM physics: π^o decays into *visible* particles that are undetected.
- the alternative, signal-plus-background, hypothesis ($s+b$) which here means that new physics can explain the observed data: π^o decays to *invisible* particles. Since the background from $\pi^o \to \gamma\gamma$ decays cannot be completely rejected, the alternative hypothesis must include both signal and background.

The CL_s method makes use of a modified frequentist statistics where the confidence level observed for the signal-plus-background hypothesis ($CL_{(s+b)}$) is normalized to the confidence level observed for the background-only hypothesis (CL_b):

$$CL_s = \frac{CL_{s+b}}{CL_b} = \frac{\text{Prob}(Q_{s+b} \geq Q_{\text{obs}})}{\text{Prob}(Q_b \geq Q_{\text{obs}})} \tag{16.1}$$

where Q is a test statistics and Q_{obs} the observed value of Q. It gives an approximation to the confidence, in the signal hypothesis, one might have obtained if it would have been possible to discard, with absolute certainty, that the selected events are due to background processes. In this sense, conservative exclusion limits on the signal are obtained and the signal hypothesis is excluded at a certain confidence level CL when $CL_s = 1 - \text{CL}$.

In order to determine CL_b, MC-toy simulations are used to generate 1 million of possible background event counts (N_{b_i}) evaluated from a Poisson distribution with mean equal to the expected number of background events (N_b). For each generation, the test statistics Q_b must be evaluated: it is defined as the likelihood ratio (ratio of the probability densities) of the two hypotheses signal-plus-background and background-only, assuming that N_{b_i} counts are observed

$$Q_b = -2\ln(Q_{b_i}) = 2\left[N_s - N_{b_i}\ln\left(\frac{N_s}{N_b}+1\right)\right], \tag{16.2}$$

where

$$Q_{b_i} = \frac{e^{-(N_s+N_b)}\,(N_s+N_b)^{N_{b_i}}}{N_{b_i}!} \times \frac{N_{b_i}!}{e^{-N_b}\,N_b^{N_{b_i}}} = \frac{e^{-N_s}\,(N_s+N_b)^{N_{b_i}}}{N_b^{N_{b_i}}}. \tag{16.3}$$

The test statistics Q_b is constructed to decrease monotonically for increasingly signal-like experiments. Therefore, the confidence in the signal hypothesis is given by the probability that the test statistics is greater than or equal to the value Q_{obs} observed in the experiment:

$$Q_{\text{obs}} = 2\left[N_s - N_{\text{obs}} \ln\left(\frac{N_s}{N_b}+1\right)\right]. \tag{16.4}$$

The same procedure is applied to the alternative hypothesis of signal+background. $CL_{(s+b)}$ is obtained with 1 million of MC-toy simulations used to generate $N_{(s+b)_i}$ counts from a Poisson distribution with mean $N_s + N_{b_i}$ (where N_{b_i} is defined as in the null hypothesis). The test statistics Q_{s+b} is defined according to Equations (16.2) and (16.3) by replacing N_{b_i} with $N_{(s+b)_i}$. The probability of observing a test statistics Q_b ($Q_{(s+b)}$) greater or equal than Q_{obs} is computed by means of an integration given the Q_b ($Q_{(s+b)}$) distribution for different values of N_{b_i} ($N_{(s+b)_i}$).

A comparison between the achieved limits and those in the background-only hypothesis is performed. Since the expected limits are computed supposing the absence of signal (i.e. signal events are due to a background fluctuation), the number of observed events N_{obs} is assumed equal to a fluctuation of the background events N_b, according to a Poisson distribution. This procedure is repeated 200 times by generating independent MC-toy simulations. In each generation the number N_b of background events is randomly extracted from an asymmetric gaussian distribution centered on the value of the estimated background events N_{bkg} as given in Equation (9.2) and with left and right standard deviations determined by its uncertainties. In order to evaluate the observed limit after the unblinding of the signal region, the CL_s is computed with N_{obs} equal to the number of residual $K_{2\pi}$ events on $\pi\nu\bar{\nu}$-trigger data after applying all the photon-rejection conditions. Both for the expected and observed limits, for a given value of N_b a scan on the number of signal events is done, resulting in a two dimensional distribution of the CL_s value as a function of N_s. From this distribution, the median value of CL_s together with the regions with 68% and 95% statistical coverage are evaluated for each tested N_s (as shown in Figure 17.1 for the validation of the low-momentum sideband region).

The CL_s method is used in Chapter 17 and Chapter 18 for the validation of the π^+ low-momentum sideband and for the optimization of the π^+ signal region, respectively.

Chapter 17
The Validation of the Background Estimate

As a consequence of the trend of the expected π^o rejection inefficiency as a function of the charged pion momentum (shown in Figure 14.5) three momentum regions are identified: two sideband regions at the edges of the π^+ momentum distribution and a central region.

17.1 Low-momentum region

In order to validate the rejection estimate and, therefore, the number of expected background events, the number of events expected in absence of a signal is compared to the number of events observed in the data in the sideband momentum region 10–15 GeV/c. Here the expected rejection inefficiency is $\varepsilon_{\pi^o} = (1.43^{+0.71}_{-0.74}) \times 10^{-7}$ and, considering the uncertainties, the presence of $\pi^o \to invisible$ signal events can be excluded at 90% CL by the experimental limit from the BNL experiment E949 [41]. Therefore a direct comparison between expectation and observed events in the data can be done. In total about 85×10^6 tagged π^o mesons are collected in data, as estimated by applying the $K_{2\pi}$ selection on control-trigger data and before any of the condition of the photon-rejection algorithm, and given the estimated π^o rejection $11.1^{+5.5}_{-5.8}$ background events are expected (see Table 15.2). From the CL_s method computed in absence of signal (the number of observed events in data is taken as a fluctuation of the number of background events), the 90% CL limit on the number of expected signal events is: $N_{\text{s-exp}} \leq 7.1^{+3.9(+7.6)}_{-2.7(-4.1)}$, where the uncertainties correspond to the intervals with 68% (95%) statistical coverage. In the data signal sample, 14 events survive the $K_{2\pi}$ selection after all the photon-rejection conditions are applied, resulting from the CL_s method in an observed 90% CL limit on signal events of $N_{\text{s-obs}} \leq 9.4$. Figure 17.1 shows the two-dimensional distribution of the CL_s as a function of N_{s} for the expected and observed limits. No excesses are observed, meaning that the observed signals are compatible with a statistical fluctuation of the sole background.

Given the number of signal events N_{s} one can derive the branching ratio according to Equation (9.3) here reported:

$$\text{BR}(\pi^o \to invisible) = \text{BR}(\pi^o \to \gamma\gamma) \times \frac{N_{\text{s}}}{N_{\pi^o} \times \varepsilon_{\text{signal}} \times \varepsilon_{\text{trigger}}}$$

where N_{π^o} is the number of π^o mesons tagged on control-trigger data as estimated by applying the $K_{2\pi}$ selection before any photon-rejection conditions; $\varepsilon_{\text{trigger}}$ and $\varepsilon_{\text{signal}}$ are the efficiencies of the $\pi\nu\bar{\nu}$ trigger and of the photon-rejection algorithm evaluated for a $\pi^o \to invisible$ signal, respectively.
In the sideband region of π^+ momentum 10–15 GeV/c, the expected and observed upper

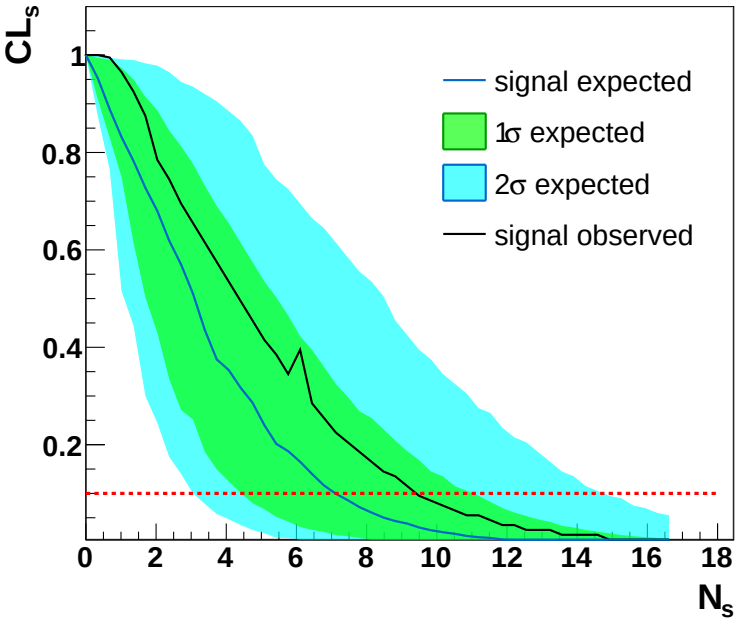

FIGURE 17.1: Two dimensional distribution of CL_s *versus* N_s for the expected and observed upper limits in the low-momentum sideband region 10–15 GeV/c. The number of expected background events is $11.1^{+5.5}_{-5.8}$ while 14 events are observed in the data after all the signal selection. The CL_s results of the data (black line) are compared to the expected fluctuations in absence of a signal. The band of the expected limit is obtained from a combination of MC simulation and data single-photon efficiencies. The green (light blue) area is defined as having a statistical coverage of 34% (47.5%) on either side from the statistical median. The red dashed line corresponds to set the limit at 90% CL ($CL_s = 1 - \mathrm{CL} = 0.1$).

limits at 90% CL are:

$$\mathrm{BR}_{\mathrm{expected}}(\pi^o \to \mathit{invisible}) \leq \left(1.81^{+1.00(+1.95)}_{-0.68(-1.03)}\right) \times 10^{-7}, \tag{17.1}$$

$$\mathrm{BR}_{\mathrm{observed}}(\pi^o \to \mathit{invisible}) \leq 2.39 \times 10^{-7}. \tag{17.2}$$

The expected and observed limits are compatible within one sigma. The comparison between expected and observed limits translates into the validation of the single-photon efficiencies of the IRC and SAC detectors, which are the leading contributions to the background in the π^+ momentum bin 10–15 GeV/c, as shown in the left panel of Figure 14.6: the events with one photon pointing to the IRC or SAC detectors and the other photon escaping detection at large angle are dominating the veto performance for the low-momentum sideband, with expected contributions to the π^o rejection inefficiency of $\simeq 3 \times 10^{-8}$ and $\simeq 8 \times 10^{-8}$, respectively. A systematic uncertainty on the IRC (SAC) inefficiency above $\simeq^{+2.0}_{-1.0} \times 10^{-4}$ ($\simeq^{+5.0}_{-2.5} \times 10^{-4}$) would produce a one-sigma discrepancy between the observed and expected branching ratios. These figures correspond to a factor of $\simeq^{+3.0}_{-2.0}$ ($\simeq^{+2.5}_{-1.7}$) times the total uncertainty quoted for the IRC (SAC) efficiency (here, the two most energetic bins of Table C.2 contribute to the quoted π^o rejection inefficiency). Therefore the test performed translates into an upper limit on the systematic uncertainty for the IRC and SAC efficiency. The results obtained can be translated into a maximum

systematic uncertainty on the LKr calorimeter efficiency, too. The fraction of events with one photon pointing to the LKr and the other escaping detection at large angle ("missing") is $\simeq 0.11\%$. A systematic uncertainty on the LKr efficiency above $\simeq^{+5.0}_{-0.0} \times 10^{-5}$ would produce a one-sigma discrepancy between the observed and expected branching ratios. This figure corresponds to a factor of 4 to 10 times the upper total uncertainty quoted for the LKr efficiency for the three highest energy bins of Table C.1.

17.2 High-momentum region

The LKr and LAV efficiencies drive the rejection inefficiency for high values of the π^+ momentum (Figure 14.6 right panel) and can be validated with the sideband region between 55–60 GeV/c. However, this cannot be done as for the low-momentum sideband region due to the cut at 50 GeV/c applied on the data by the L1STRAW algorithm used in the $\pi\nu\bar{\nu}$ trigger. Different possibilities have been investigated in order to overcome this issue. One possibility would be to extend the sideband to the momentum region 50–60 GeV/c [1], gaining in statistics, and use the L1-autopass data (the events in which the L1 algorithms are registered but not enforced), which correspond to about 25% of the L0$_{\pi\nu\bar{\nu}}$-trigger events. Since about 7×10^4 $K_{2\pi}$ events are selected in the high-momentum region on control-trigger data (see Chapter 10), the number of corresponding L1-autopass data is around 7 million events, which would be barely sufficient to validate an expected rejection inefficiency of $\mathcal{O}(10^{-7})$. However, this would imply a re-filter of the data used, since at the moment the *PNNFilter* itself applies a cut at 50 GeV/c on the momentum of the STRAW tracks. Obviously, the validation cannot be performed using the control-trigger stream itself, given the statistics. The lack of statistics in the π^+ high-momentum region would make the results of the two attempts (L1-autopass and pure control-trigger data) inconclusive and therefore a different approach needs to be used to validate the LKr and LAV efficiencies by using the central π^+ momentum region.

17.3 Central-momentum region

In the central π^+ momentum region of Figure 14.5, momentum between 20 and 45 GeV/c, the LKr inefficiency starts to dominate the expected background rejection with a subleading contribution from the LAV inefficiency. [2] The two inefficiencies increase their contributions to the π^o rejection with the momentum, as shown in Figure 17.2. Given an expected π^o rejection inefficiency on the order of 10^{-8}–10^{-9}, the present experimental limit [41] does not provide a useful constraint and a different test is performed with respect to the validation of the low-momentum region.

[1] Given the estimated rejection, the presence of signal is still excluded by the present experimental limit.

[2] As it will be discussed in Chapter 18, the signal momentum region for the final search for $\pi^o \to$ *invisible* decays is chosen after the optimization of the momentum region 20–45 GeV/c.

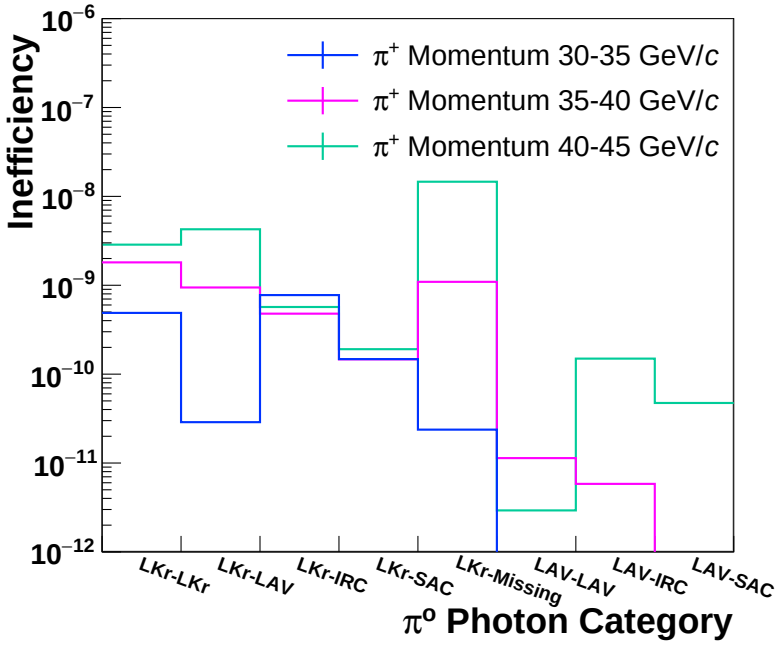

FIGURE 17.2: Inefficiency contributions to the expected π^o rejection for three bins of the π^+ momentum in the central momentum region. Only the contributions above 10^{-12} are shown.

A particular approach [162] has been applied to validate the background expectations in the 5 GeV/c π^+ momentum bins of the central momentum region. The idea is to add an artificial and energy-independent inefficiency ε_x to the LAV and LKr detectors, one at a time, such that the corresponding π^o rejection inefficiency is weakened to the level of 10^{-7} to 10^{-6} also in the central momentum region. The presence of signal events is excluded at this level by the current experimental limit [41], and the background estimation obtained in this way can be directly validated by comparison to data in which the LAV and LKr efficiencies are similarly artificially decreased. The procedure is performed slightly differently for the evaluation of the expected and observed π^o rejection inefficiency as explained in the following.

Expected LAV-induced π^o rejection While analyzing the MC $K_{2\pi(\gamma)}$ sample used to evaluate the expected π^o rejection, the LAV single-photon efficiency as measured in Chapter 13 is decreased by a constant value ε_x. For each value of ε_x tested, the corresponding π^o rejection inefficiency is obtained, as shown in the left panel of Figure 17.3. By construction, for $\varepsilon_x = 0$ the rejection is equal to that obtained in Chapter 14.

Observed LAV-induced π^o rejection When applying the photon-rejection algorithm of Chapter 11 to the $K_{2\pi}$ data signal sample, the events are flagged as pertaining to the LAV, and/or to the LKr, and/or the other vetoes if at least one photon is detected therein. An artificial inefficiency ε_x is introduced for LAV-flagged events: in a fraction of cases equal to ε_x, the LAV flag is switched off. These altered events can still be rejected if they are flagged by one of the other detectors, otherwise they determine an artificial contribution

to the global inefficiency and therefore a worsening of the π^o rejection inefficiency. Since this test makes use of events which would be rejected in standard conditions and since the expected π^o rejection inefficiency is artificially increased at the level of 10^{-7} as checked before with the MC, the blind analysis principle is preserved.

Expected LKr-induced π^o rejection The same procedure described above for the LAV cannot be applied for the validation of the LKr efficiency, since for the data events with one or two photons detected by the LKr calorimeter would have to be carefully distinguished to be compared with the expectation. [3] Therefore a different approach is explored. While analyzing the MC $K_{2\pi(\gamma)}$ sample used to evaluate the expected π^o rejection, events with one or more photons pointing to the LKr calorimeter are altered: the probability w, defined in Equation (14.1), is decreased for these events by a constant value ε_x. For each value of ε_x tested, the corresponding π^o rejection inefficiency is obtained, as shown in the right panel of Figure 17.3. By construction, for $\varepsilon_x = 0$ the rejection is equal to that obtained in Chapter 14.

Observed LKr-induced π^o rejection Exactly as for the LAV, when applying the photon-rejection algorithm of Chapter 11 to the $K_{2\pi}$ data signal sample, the events are flagged as pertaining to the LAV, and/or to the LKr, and/or to the other vetoes if at least one photon is detected therein. An artificial *global* inefficiency ε_x is introduced for LKr-flagged events: in a fraction of cases equal to ε_x, the LKr flag is switched off. These altered events can still be rejected if they are flagged by one of the other detectors, otherwise they determine an artificial contribution to the global inefficiency and therefore a worsening of the π^o rejection inefficiency. Also in this case the blind analysis principle is preserved, since the test makes use of events which would be rejected in standard conditions and since the expected π^o rejection inefficiency is artificially increased at the level of 10^{-7} as checked before with the MC. However, introducing a global inefficiency to the expected LKr-induced π^o rejection enhances mostly the contribution of the events with two photons in the LKr calorimeter (since they are the majority of events with at least one photon in the detector acceptance). Anyway, the dominant contribution from the LKr to the final π^o rejection comes from the category with only one photon inside the calorimeter and the second lost at large angle (the so-called LKr-Missing category), therefore this study on the LKr cannot provide an estimate on the systematic uncertainty due to the LKr efficiency. Only the test on the LAV can be used to validate the background rejection.

A complication arises for the test of the observed π^o rejection. The $\pi\nu\bar{\nu}$ trigger already applies a veto on the photons in the LKr and LAV detectors (through the L0LKr and L1LAV requests), so that the sample used for the signal search is biased. For this validation to be implemented with reasonable simplicity, data from a different trigger stream must be used.

[3] For the test of the LAV efficiency, the contribution of the events with two photons detected in the LAV system is negligible, see Figure 17.2 and Table 14.1.

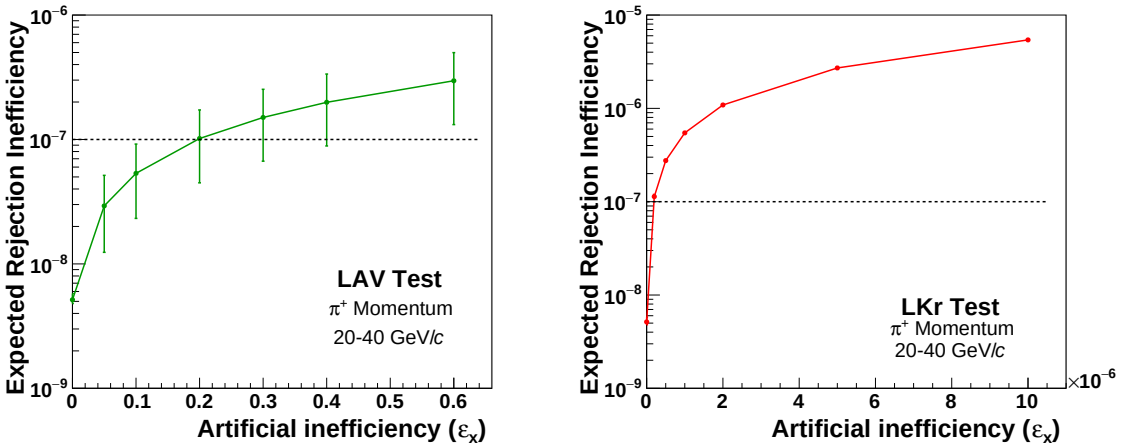

FIGURE 17.3: An artificial single-photon and a global inefficiencies ε_x are introduced, one at a time, for the LAV (***left***) and LKr (***right***) respectively, and the expected π^0 rejection inefficiency is recomputed as ε_x varies. Regions in which the expected rejection inefficiency is of $\mathcal{O}(10^{-7})$ or greater can now be cross-checked with the data. For $\varepsilon_x = 0$ a π^0 rejection inefficiency of about 5×10^{-9} is obtained according to the procedure described in Chapter 14. The momentum region between 20–40 GeV/c is used for this test.

Two alternatives are explored: data from the *Non-Muon* trigger and from the control trigger.

A large amount of $K_{2\pi}$ events is collected with the *Non-Muon* trigger mask (see Section 8.1.1 for the details on the trigger configurations). The conditions for the 2017 Sample A required by this trigger stream are:

- L0: RICH $\times$ Q$_1$ $\times$!MUV3
- L1: KTAG

A downscaling factor of 200 is applied at L0-trigger level. The number of $K_{2\pi}$ selected events is roughly a factor of 3 more than those counted in the control-trigger stream. The filter *OneTrackNotMuonFilter* [134] has been specifically developed for the *Non-Muon* trigger stream, with the main purpose of selecting a sample useful for accidental activity (random veto) studies on the LAV system and the LKr calorimeter. The filter requires single-track events with momentum below 40 GeV/c and no in-time activity in the SAV detector. However, at the moment this analysis is done no reconstructed data are available for the 2017 Sample A since the filter was not included in the central reprocessing of the data. For this reason, the background validation with this trigger stream cannot be performed.

The second possibility investigated for the validation of the background rejection is the use of pure control-trigger data. Due to the downscaling factor of 400, the validation procedure described above cannot be applied separately for each 5 GeV/c π^+ momentum bin of the central momentum region, since at least $\mathcal{O}(10^7)$ selected $K_{2\pi}$ events are needed. In order to have a reasonable amount of statistics, the momentum region under validation is extended to the range 20–40 GeV/c. In the data sample of 2017 A about 1.5×10^7

$K_{2\pi}$ events are selected in this region before applying any of the conditions of the photon-rejection algorithm. The estimated π^o rejection inefficiency from the MC simulation and the single-photon efficiencies is about 5×10^{-9}, with contributions given in Table 17.1: the IRC and LKr detectors are the relevant sources for the estimated π^o rejection inefficiency, with a sub-leading contribution at the level of 20% from the LAV.

$E^*_{\gamma\text{rad}}$ [MeV]	π^o categories	π^o rejection inefficiency		Fraction of events
		Intrinsic	Total contribution	
< 0.01	All categories	4.83×10^{-9}	4.62×10^{-9}	0.957
–	LKr – LKr	0.80×10^{-9}	0.57×10^{-9}	0.712
–	LKr – LAV	1.05×10^{-9}	0.22×10^{-9}	0.210
–	LKr – SAV	2.53×10^{-8}	1.85×10^{-9}	0.073
–	LKr – Missing	8.00×10^{-8}	0.24×10^{-9}	0.003
–	LAV – SAV	3.15×10^{-7}	0.63×10^{-9}	0.002
–	SAV – Missing	4.33×10^{-5}	1.30×10^{-9}	3×10^{-5}
0.01–2	All categories	3.45×10^{-9}	1.45×10^{-10}	4.2×10^{-2}
2–4	All categories	1.88×10^{-9}	1.88×10^{-12}	1.0×10^{-3}
4–6	All categories	6.68×10^{-10}	1.87×10^{-13}	2.8×10^{-4}
6–8	All categories	7.82×10^{-10}	0.61×10^{-13}	7.8×10^{-5}
8–10	All categories	1.16×10^{-10}	3.59×10^{-15}	3.1×10^{-5}
≥ 10	All categories	7.96×10^{-11}	2.15×10^{-15}	2.7×10^{-5}
Total π^o rejection inefficiency*: $\left(4.8^{+6.2}_{-3.7}\right) \times 10^{-9}$				

TABLE 17.1: Contributions to the expected π^o rejection inefficiency in the π^+ momentum region 20–40 GeV/c used for the validation of the background rejection. *Statistical and systematic uncertainties are combined.

After applying the method described above for the LAV, the observed π^o rejection inefficiency is computed in control-trigger data and shown as a function of the artificial inefficiency ε_x in Figure 17.4, allowing a comparison with the expected π^o rejection inefficiency after the LAV efficiency is worsened. The numerical values are listed in Table 17.2. For the observed rejection inefficiencies the uncertainties are dominated by the data statistics and are partially correlated when ε_x varies. The uncertainties on the expected rejection inefficiencies are dominated by the statistical contribution of the single-photon detector efficiencies and are mostly correlated when ε_x varies.

Throughout the ε_x values tested, expected and observed rejections are compatible within the quoted uncertainties, and two consequences can be derived:

- The LAV inefficiency had to be increased by 20%, to induce a 10^{-7} rejection inefficiency. This is due to the sub-leading contribution of the LAV efficiency to the π^o rejection as shown in Table 17.1. The worsening of the rejection inefficiency linearly depends on the average LAV artificial inefficiency. An absolute systematic uncertainty of 1.5% on the LAV inefficiency would bias the rejection inefficiency by 6×10^{-9}, i.e.

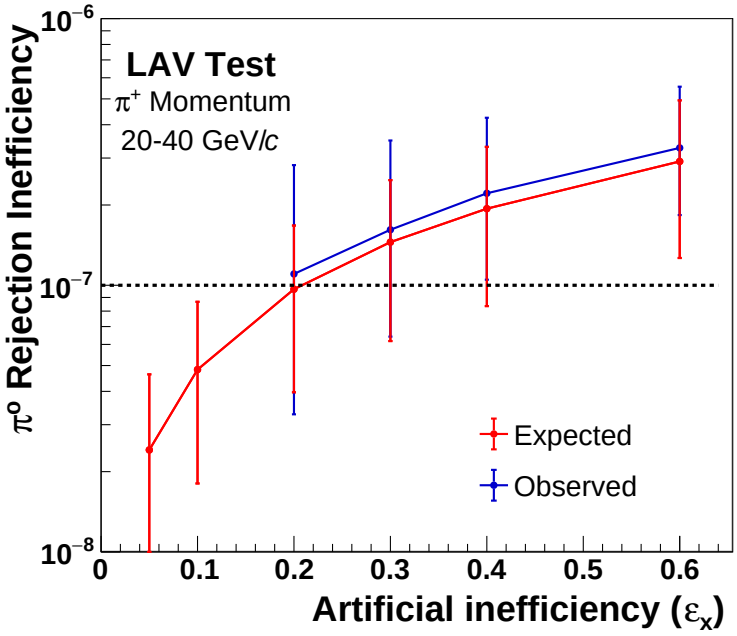

FIGURE 17.4: Observed (blue) and expected (red) π^0 rejection inefficiency as a function of an artificial LAV inefficiency ε_x, introduced as explained in the text. The π^+ momentum range 20–40 GeV/c is considered for the validation test.

ε_x	Expected rejection inefficiency [10^{-7}]	Observed rejection inefficiency [10^{-7}]
0.05	$0.24^{+0.22}_{-0.17}$	–
0.1	$0.48^{+0.38}_{-0.30}$	–
0.2	$0.97^{+0.71}_{-0.57}$	$1.10^{+1.72}_{-0.78}$
0.3	$1.45^{+1.03}_{-0.83}$	$1.62^{+1.88}_{-0.97}$
0.4	$1.9^{+1.4}_{-1.1}$	$2.2^{+2.0}_{-1.2}$
0.6	$2.9^{+2.0}_{-1.6}$	$3.3^{+2.3}_{-1.4}$

TABLE 17.2: Numerical values for the expected and observed π^0 rejection inefficiencies as a function of an artificial LAV inefficiency introduced as explained in the text. The π^+ momentum region 20–40 GeV/c is considered for the validation test.

by one standard deviation. The agreement observed when evaluating the systematic uncertainty of the rejection from the method-bias correction allows setting the systematic error for the LAV inefficiency at $^{+0.5}_{-0.2}$%, thus implying a systematic uncertainty on the π^0 rejection inefficiency of $^{+2.0}_{-0.8} \times 10^{-9}$.

- Given a 20% increase in the LAV inefficiency, the dominant contributors to the π^0 rejection inefficiency are given by the LKr–LAV and LAV–SAV (LAV–IRC indeed) configurations, as shown in Table 17.3. A one-sigma variation of the difference between observed and expected π^0 rejections would be obtained after varying the LKr inefficiency by a factor $^{+4.0}_{-1.0} \times 10^{-6}$. This is less than the approximate absolute uncertainty on the LKr efficiency, see Table C.1. The test performed allows concluding that

any systematic error on the LKr efficiency is below the quoted statistical uncertainty. Similarly, a variation of $^{+1.5}_{-1.0} \times 10^{-4}$ of the IRC inefficiency would correspond to a one-sigma variation of the difference between observed and expected π^0 rejection inefficiencies. This allows a slightly more stringent constraint on the IRC systematic uncertainty than the test using the low-momentum region.

Therefore, from the test performed on the LAV inefficiency upper limits are derived on the systematic uncertainties for the LKr and IRC inefficiencies.

The effect of the random veto when evaluating the observed rejection is seen to be well below the quoted uncertainties.

$E^*_{\gamma\text{rad}}$ [MeV]	π^0 categories	π^0 rejection inefficiency		Fraction of events
		Intrinsic	Total contribution	
< 0.01	All categories	0.95×10^{-7}	0.91×10^{-7}	0.957
–	LKr – LKr	0.08×10^{-8}	0.06×10^{-8}	0.712
–	LKr – LAV	3.10×10^{-7}	6.46×10^{-8}	0.210
–	LKr – SAV	2.60×10^{-8}	0.19×10^{-8}	0.073
–	LKr – Missing	6.67×10^{-8}	0.02×10^{-8}	0.003
–	LAV – SAV	1.32×10^{-5}	2.64×10^{-8}	0.002
–	SAV – Missing	4.33×10^{-5}	0.13×10^{-8}	3×10^{-5}
0.01–2	All categories	7.88×10^{-8}	3.31×10^{-9}	4.2×10^{-2}
2–4	All categories	4.97×10^{-8}	4.97×10^{-11}	1.0×10^{-3}
4–6	All categories	2.75×10^{-8}	0.77×10^{-11}	2.8×10^{-4}
6–8	All categories	4.52×10^{-8}	3.53×10^{-12}	7.8×10^{-5}
8–10	All categories	0.64×10^{-8}	1.98×10^{-13}	3.1×10^{-5}
≥ 10	All categories	0.17×10^{-8}	4.54×10^{-14}	2.7×10^{-5}
Total π^0 rejection inefficiency*: $\left(0.97^{+0.71}_{-0.57}\right) \times 10^{-7}$				

TABLE 17.3: Contributions to the expected π^0 rejection inefficiency in the π^+ momentum region 20–40 GeV/c after increasing the LAV inefficiency by 20%. *Statistical and systematic uncertainties are combined.

17.4 Summary of the validation

The systematic uncertainties on the expected π^0 rejection inefficiency derived from the validation of the analysis as discussed in Sections 17.1 and 17.3 are found to be smaller than the combined uncertainty derived from the MC statistics, the statistical uncertainty of the single-photon efficiencies, and the systematics of the Tag&Probe method. The results for the π^+ momentum region 20–40 GeV/c, used in the validation of the central momentum region, are summarized in Table 17.4.

Source	$\Delta(1-\varepsilon^{\text{true}}_{\text{data}})$	$\Delta(\varepsilon_{\pi^o})$	**Validation method**
LAV	$^{+0.5}_{-0.2}\times 10^{-2}$, $E>1$ GeV	$^{+2.0}_{-0.8}\times 10^{-9}$	Data-driven method-bias Section 14.1.3
LKr	$<^{+4.0}_{-1.0}\times 10^{-6}$, $E>20$ GeV	$<^{+4.0}_{-1.0}\times 10^{-9}$	LAV-artificial inefficiency Section 17.3
IRC	$<^{+1.5}_{-1.0}\times 10^{-4}$, $E>10$ GeV	$<^{+4.5}_{-3.0}\times 10^{-9}$	LAV-artificial inefficiency Section 17.3
SAC	$<^{+5.0}_{-5.0}\times 10^{-4}$, $E>10$ GeV	$<^{+3.0}_{-3.0}\times 10^{-9}$	Low-momentum sideband Section 17.1
MC stat. Data stat. Data syst.		$^{+6.2}_{-3.7}\times 10^{-9}$	Chapter 14
Total π^o rejection inefficiency: $\left(4.8^{+6.2}_{-3.7}\right)\times 10^{-9}$			

TABLE 17.4: Summary of the systematic uncertainties (Δ) derived from the background validation on the single-photon detector inefficiencies $1-\varepsilon^{\text{true}}_{\text{data}}$, and on the expected rejection inefficiency ε_{π^o}, in the π^+ momentum region 20–40 GeV/c. The uncertainties on ε_{π^o} are compared to the combined uncertainty derived from the MC statistics, the statistical uncertainty on the single-photon efficiencies, and the systematics on the Tag&Probe method.

Chapter 18
The Optimization of the π^+ Momentum Signal Region

The optimization of the π^+ momentum signal region is performed before the unblinding of the final number of candidate events in the data signal sample. Given the dependence of the expected π^o rejection inefficiency on the π^+ momentum shown in Figure 14.5, three signal regions are tested with lower edge at 20 GeV/c and upper edge value set at 35, 40, and 45 GeV/c, respectively. Table 18.1 summarizes the number of tagged π^o mesons and the estimated background rejection for the three regions under study.

π^+ **Momentum [GeV/c]**	N_{π^o} $[\mathbf{10^6}]$	ε_{π^o} $[\mathbf{10^{-9}}]$	$\varepsilon_{\mathbf{trigger}}$ **[%]**	$N_{\mathbf{bkg}}$
20 – 35	$4\,501.3 \pm 1.3$	$4.9^{+6.0}_{-4.0}$	84.2 ± 3.0	19^{+23}_{-15}
20 – 40	$5\,815.0 \pm 1.5$	$4.8^{+6.2}_{-3.7}$	83.4 ± 2.9	23^{+30}_{-18}
20 – 45	$6\,873.6 \pm 1.7$	$7.7^{+7.5}_{-6.6}$	82.2 ± 2.9	44^{+42}_{-37}

TABLE 18.1: Expected background events computed according to Equation (9.2) for the tested π^+ momentum regions.

For each of the three π^+ momentum regions, the CL_s method is applied in order to determine the limit on the number of expected $\pi^o \to$ *invisible* signal events. It is important to remark that the CL_s technique is applied under the assumption of absence of signal and with N_{obs} equal to a fluctuation of the estimated background. The results of the CL_s are listed in Table 18.2 and allows selecting the momentum region with upper edge at 40 GeV/c, as it provides the upper limit on the $\pi^o \to$ *invisible* branching ratio with the lowest median and 68% coverage upper bound. The upper limit on the expected branching ratio, evaluated according to Equation (9.3), are also listed in Table 18.2.

π^+ **Momentum [GeV/c]**	$N_{\mathbf{s\text{-}expected}}$	$\mathbf{BR}_{\mathbf{expected}}$ $[\mathbf{10^{-9}}]$
20 – 35	$9.4^{+4.9(+14.2)}_{-4.2(-6.4)}$	$4.9^{+2.6(+7.4)}_{-2.2(-3.4)}$
20 – 40	$10.1^{+5.8(+19.1)}_{-4.2(-6.3)}$	$4.1^{+2.3(+7.8)}_{-1.7(-2.6)}$
20 – 45	$12.9^{+7.6(+18.8)}_{-5.0(-7.9)}$	$4.5^{+2.6(+6.6)}_{-1.8(-2.8)}$

TABLE 18.2: Expected 90% CL upper limits on the number of signal events and on the branching ratio for $\pi^o \to$ *invisible*, computed according to Equation (9.3), for the three π^+ momentum regions under study. The median values obtained by the CL_s method is quoted together with the bands with 68% and 95% coverage, given as first and second set of uncertainties, respectively, with the latter in parentheses.

After fixing the upper edge of the π^+ momentum signal region at 40 GeV/c, according to the optimization, the lower edge has been increased by 5 GeV/c and for the new momentum region under test the expected performance are evaluated. [1] The estimated background events are listed in Table 18.3 and compared with those obtained previously in 20–40 GeV/c. The CL_s method is again applied to determine the limit on the number of expected $\pi^o \to invisible$ signal events in the new momentum region under study. The results of the CL_s are listed in Table 18.4 and compared with those obtained in 20–40 GeV/c.

π^+ Momentum [GeV/c]	N_{π^o} [10^6]	ε_{π^o} [10^{-9}]	$\varepsilon_{\text{trigger}}$ [%]	N_{bkg}
20 – 40	$5\,815.0 \pm 1.5$	$4.8^{+6.2}_{-3.7}$	83.4 ± 2.9	23^{+30}_{-18}
25 – 40	$4\,431.1 \pm 1.3$	$2.8^{+5.9}_{-2.1}$	82.8 ± 2.9	10^{+22}_{-8}

TABLE 18.3: Expected background events computed according to Equation (9.2) for the tested π^+ momentum regions.

π^+ Momentum [GeV/c]	$N_{\text{s-expected}}$	$\text{BR}_{\text{expected}}$ [10^{-9}]
20 – 40	$10.1^{+5.8(+19.1)}_{-4.2(-6.3)}$	$4.1^{+2.3(+7.8)}_{-1.7(-2.6)}$
25 – 40	$7.2^{+4.8(+10.5)}_{-2.9(-4.8)}$	$3.8^{+2.6(+5.7)}_{-1.5(-2.6)}$

TABLE 18.4: Expected 90% CL upper limits on the number of signal events and on the branching ratio for $\pi^o \to invisible$, computed according to Equation (9.3), for the two π^+ momentum regions under study. The median values obtained by the CL_s method is quoted together with the bands with 68% and 95% coverage, given as first and second set of uncertainties, respectively, with the latter in parentheses.

Given the results of the CL_s technique for the regions under study, shown in Figure 18.1, the optimal choice of the π^+ momentum range for the search for $\pi^o \to invisible$ decays is the region between 25 and 40 GeV/c.

18.1 Signal momentum region 25–40 GeV/c: summary of the systematic uncertainties

Variations in the results obtained for the validation procedure described in Section 17.3 are verified for the signal π^+ momentum region 25–40 GeV/c, and the corresponding systematics are derived. About 11×10^6 $K_{2\pi}$ events are selected according to the criteria of Chapter 10 on control-trigger data, still enough to apply the validation procedure for the background estimation described in Section 17.3. After applying an artificial increase in the LAV inefficiency by ε_x the expected and observed rejection inefficiencies are computed.

[1] Since the present best upper limit is at the 10^{-7} level [41], using a lower edge of less than 20 GeV/c would worsen the analysis sensitivity. Conversely, increasing the lower edge above 25 GeV/c would not guarantee to have the statistics needed for the background validation in the central momentum region described in Section 17.3.

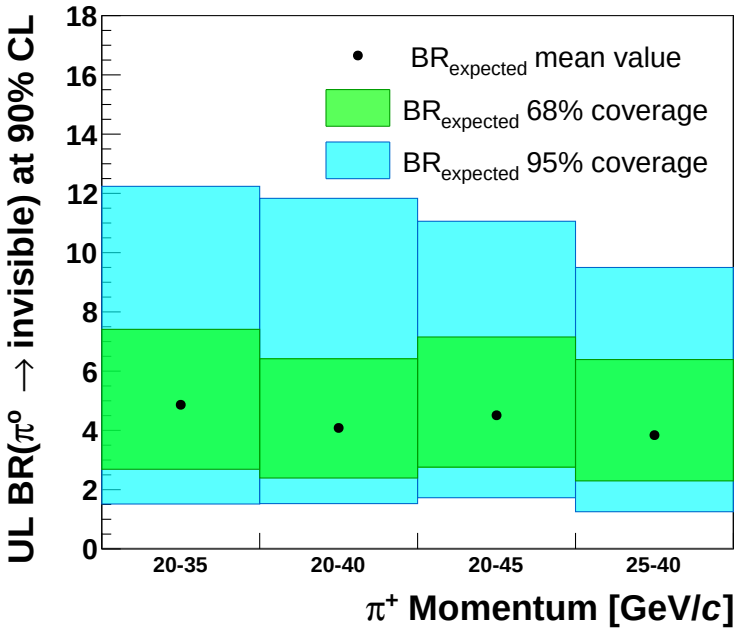

FIGURE 18.1: Expected 90% CL upper limits on the $\pi^o \to$ *invisible* branching ratio, computed according to Equation (9.3), as a results of the optimization of the π^+ momentum region. The median values obtained by the CL_s method is shown together with the bands with 68% (light green) and 95% (light blue) coverage. After the optimization of both the upper and lower edges, the region between 25 and 40 GeV/c is chosen as signal momentum region for the analysis.

The observed rejection inefficiency agrees with the expected one within the statistical uncertainty and their numerical values are listed in Table 18.5.

ε_x	**Expected rejection inefficiency [10^{-7}]**	**Observed rejection inefficiency [10^{-7}]**
0.05	$0.26^{+0.24}_{-0.15}$	–
0.1	$0.52^{+0.43}_{-0.28}$	–
0.2	$1.03^{+0.82}_{-0.55}$	$1.4^{+2.3}_{-1.0}$
0.3	$1.55^{+2.00}_{-0.81}$	$2.2^{+2.5}_{-1.3}$
0.4	$2.1^{+1.6}_{-1.1}$	$2.9^{+2.7}_{-1.5}$
0.6	$3.1^{+2.3}_{-1.6}$	$4.4^{+3.0}_{-1.9}$

TABLE 18.5: Numerical values for the expected and observed π^o rejection inefficiencies as a function of an artificial LAV inefficiency, introduced as explained in Section 17.3, for the π^+ momentum range 25–40 GeV/c.

The contributions to the expected π^o rejection inefficiency for $\varepsilon_x = 0.2$ are listed in Table 18.6. The inefficiency of the LKr–LAV component is higher than that for the 20–40 GeV/c region (see Table 17.3): 0.84×10^{-7} with respect to 0.65×10^{-7}. As seen, the statistical uncertainty of the test worsens by $\sim 30\%$ with respect to the range 20–40 GeV/c. Nevertheless

the systematic uncertainty implied by the agreement observed is still lower than the statistical uncertainty on the detector single-photon inefficiencies, as summarized in Table 18.7. The SAV–Missing contribution for the bin 25–40 GeV/c is lower than that for 20–40 GeV/c by a factor of 5. Therefore, the effect of the IRC and SAC systematic uncertainties is greatly reduced.

$E^*_{\gamma\text{rad}}$ [MeV]	π^o categories	π^o rejection inefficiency		Fraction of events
		Intrinsic	Total contribution	
< 0.01	All categories	0.99×10^{-7}	0.95×10^{-7}	0.957
–	LKr – LKr	1.05×10^{-9}	0.74×10^{-9}	0.702
–	LKr – LAV	3.53×10^{-7}	8.41×10^{-8}	0.238
–	LKr – SAV	1.91×10^{-8}	1.07×10^{-9}	0.056
–	LKr – Missing	1.03×10^{-7}	0.31×10^{-9}	0.003
–	LAV – SAV	2.05×10^{-5}	1.23×10^{-8}	0.0006
–	SAV – Missing	2.40×10^{-5}	0.24×10^{-9}	1×10^{-5}
0–2	All categories	8.31×10^{-8}	3.49×10^{-9}	4.2×10^{-2}
2–4	All categories	5.30×10^{-8}	0.53×10^{-10}	1.0×10^{-3}
4–6	All categories	2.03×10^{-8}	0.59×10^{-11}	2.9×10^{-4}
6–8	All categories	5.51×10^{-8}	0.43×10^{-11}	7.8×10^{-5}
8–10	All categories	0.75×10^{-8}	0.21×10^{-12}	2.8×10^{-5}
≥ 10	All categories	0.26×10^{-8}	0.70×10^{-13}	2.7×10^{-5}
Total π^o rejection inefficiency*: $\left(1.03^{+0.82}_{-0.55}\right) \times 10^{-7}$				

TABLE 18.6: Contributions to the expected π^o rejection inefficiency in the π^+ momentum region 25–40 GeV/c after increasing the LAV inefficiency by 20%. *Statistical and systematic uncertainties are combined.

Source	$\Delta(1 - \varepsilon^{\text{true}}_{\text{data}})$	$\Delta(\varepsilon_{\pi^o})$	Validation method
LAV	$^{+0.5}_{-0.2} \times 10^{-2}, E > 1$ GeV	$^{+0.6}_{-0.3} \times 10^{-9}$	Data-driven method-bias Section 14.1.3
LKr	$<^{+4.6}_{-1.0} \times 10^{-6}, E > 20$ GeV	$<^{+4.6}_{-1.0} \times 10^{-9}$	LAV-artificial inefficiency Section 17.3
IRC	$<^{+1.7}_{-1.0} \times 10^{-4}, E > 10$ GeV	$<^{+0.5}_{-0.2} \times 10^{-9}$	LAV-artificial inefficiency Section 17.3
SAC	$<^{+5.0}_{-5.0} \times 10^{-4}, E > 10$ GeV	$<^{+0.1}_{-0.1} \times 10^{-9}$	Low-momentum sideband Section 17.1
MC stat. Data stat. Data syst.		$^{+5.9}_{-2.1} \times 10^{-9}$	Chapter 14
Total π^o rejection inefficiency: $\left(2.8^{+5.9}_{-2.1}\right) \times 10^{-9}$			

TABLE 18.7: Summary of the systematic uncertainties (Δ) derived from the background validation on the single-photon detector inefficiencies $1 - \varepsilon^{\text{true}}_{\text{data}}$, and on the expected rejection inefficiency ε_{π^o}, in the momentum signal region 25–40 GeV/c. The uncertainties on ε_{π^o} are compared to the combined uncertainty derived from the MC statistics, the statistical uncertainty on single-photon efficiencies, and the systematics on the Tag&Probe method.

18.2 Comparison of the analysis method with the present experimental result

A different technique is used in this work with respect to the most sensitive present experimental result of $\pi^o \to$ *invisible* decays from the BNL experiment E949 [41]. The analysis described in this work makes use of a "*background-expectation*" technique in order to determine the background contribution of $\pi^o \to \gamma\gamma$ decays with both photons undetected. This is done with the combination of MC simulation and single-photon efficiencies measured on control-trigger data as described in Chapters 13 and 14. The number of estimated background events are then used together with the number of tagged π^o mesons selected in data to compute with the CL_s method the upper limit on the number of expected signal events. As described in Section 2.3, the E949 experiment at BNL used a "*non-background-expectation*" technique for $\pi^o \to \gamma\gamma$ decays where the number of remaining events after applying the signal selection are all interpreted as $\pi^o \to$ *invisible* signal events [41].

A comparison with the E949 experimental technique is done as described in the following. A scan on the number of observed data events, N_{obs}, is performed in the range 0–54, corresponding to a $\simeq 2\sigma$ variation of the number of estimated background events $N_{\text{bkg}} = 10^{+22}_{-8}$. The expected limit at 90% CL on the number of signal events are computed in two ways:

- in the *background-expectation* approach, the CL_s method is applied giving in input the expected number of background events (evaluated as described in Chapter 15) and the tested value of N_{obs}.
- in the *no-background-expectation* approach, the Poisson statistics is used to determine the 90% CL upper limit on the number of signal events for each tested value of N_{obs}.

From Equation (9.3), the upper limits on the branching ratio are evaluated and the comparison of the two approaches is shown in Figure 18.2. It can be seen that more stringent limits can be set with the *background-expectation* technique if the number of observed data events is below 30. The transition observed corresponds to the discovery scenario given the estimated background, which obviously is not possible in the *non-background-expectation* method.

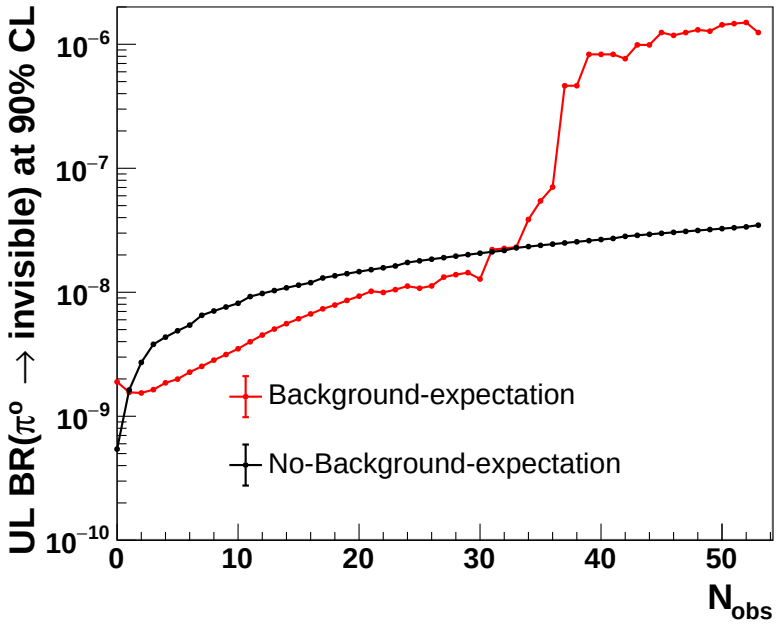

FIGURE 18.2: Comparison of the upper limits on the branching ratio of $\pi^0 \rightarrow$ *invisible* decays between the analysis technique described in this work (red line) and that used by the E949 experiment at BNL (black line).

Chapter 19
Results

19.1 BR($\pi^o \rightarrow invisible$)

The optimization of the π^+ momentum region described in Chapter 18 defines the signal region for the measurement of $\pi^o \rightarrow invisible$ as the π^+ momentum range 25–40 GeV/c. Given an expected π^o rejection inefficiency of $\varepsilon_{\pi^o} = \left(2.8^{+5.9}_{-2.1}\right) \times 10^{-9}$, the background estimation is $N_{\text{bkg}} = 10^{+22}_{-8}$. After applying the full photon-rejection algorithm described in Chapter 11 on the signal sample of $\pi\nu\bar{\nu}$-trigger data, 12 events are observed as shown in Figure 19.1. The number of observed events are compared to the expectation from a pure-background scenario in 5 GeV/c momentum bins, see Table 19.1.
Additional sources of systematic uncertainties specific to the photon-rejection conditions are considered. In particular, the criteria defining the LKr region spatially unrelated to the charged pion when defining the "Hit multiplicity" condition (see Section 11.2.1) are varied. The results of this study are described in Appendix F. Since any variation in the event count is negligible if compared to the quoted uncertainties, no additional systematic uncertainties need to be added.

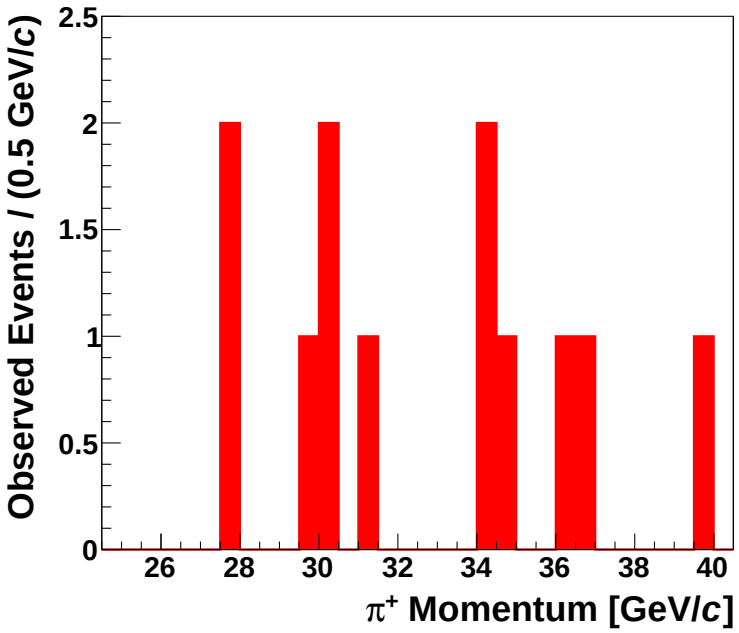

FIGURE 19.1: Unblinding of the signal region. Momentum distribution of $K_{2\pi}$ events after applying the full photon-rejection conditions on $\pi\nu\bar{\nu}$-trigger data: 12 events are observed in the π^+ momentum range 25–40 GeV/c.

π^+ **Momentum [GeV/c]**	$N_{\mathbf{bkg}}$	$N_{\mathbf{obs}}$
25 – 30	$3.5^{+7.5}_{-2.7}$	3
30 – 35	$1.9^{+8.0}_{-1.3}$	6
35 – 40	$4.8^{+7.8}_{-4.5}$	3

TABLE 19.1: Number of expected background events and number of observed events in 5 GeV/c bins in the π^+ momentum signal region 25–40 GeV/c.

Given the number of the expected background and observed events the CL_s method is applied to determine a frequentist 90% confidence interval for the number of signal events. No deviation of the observed counts beyond the uncertainty from a pure-background scenario is detected and the upper limit on the number of observed signal events is set to $N_s < 8.24$ at 90% CL. Figure 19.2 shows the results of the CL_s method on the limit of observed signal events, together with the median of the expected signal events and the bands at 68% and 95% coverage.

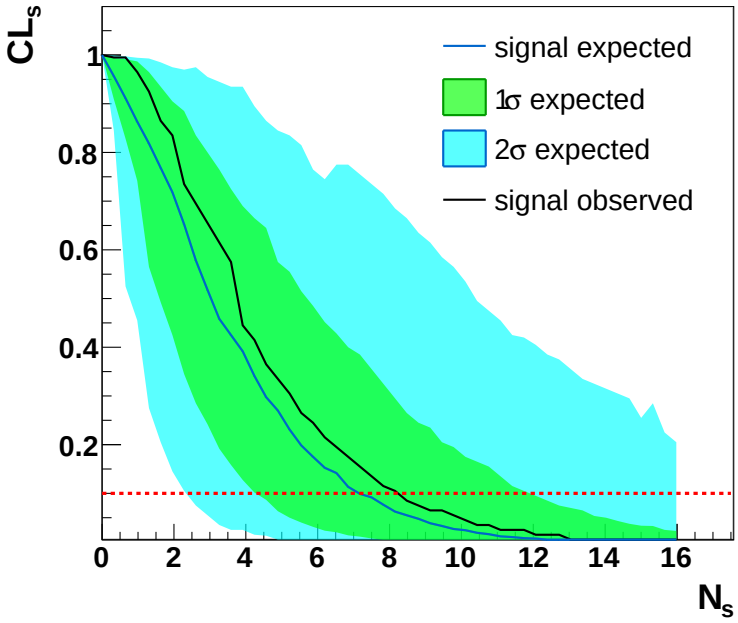

FIGURE 19.2: Two dimensional distribution of CL_s *versus* N_s for the expected and observed upper limits for the signal events in the π^+ momentum range 25–40 GeV/c. The number of expected background events is 10^{+22}_{-8} while 12 events are observed in the data after the signal selection. The CL_s results of the data (black line) is compared to the expected fluctuations in absence of signal (blue line). The band of the expected limit is obtained from a combination of MC simulation and data single-photon efficiencies. The green (light blue) area is defined as having a statistical coverage of 34% (47.5%) on either side from the statistical median. The red dashed line corresponds to set the limit at 90% CL ($CL_s = 1 - \mathrm{CL} = 0.1$).

The observed upper limit from Equation (9.3) on the $\pi^o \to invisible$ branching ratio at 90% confidence level is:

$$\mathrm{BR}_{\mathrm{observed}}(\pi^o \to invisible) \leq 4.4 \times 10^{-9}, \tag{19.1}$$

while the 90% CL expected upper limit in absence of signal is: [1]

$$\mathrm{BR}_{\mathrm{expected}}(\pi^o \to invisible) \leq \left(3.8^{+2.6(+5.7)}_{-1.5(-2.6)}\right) \times 10^{-9}. \tag{19.2}$$

This result improves on the present most stringent upper limit, from the E949 experiment at BNL [41], by a factor of about 60.

19.2 Rejection studies within the $K^+ \to \pi^+\nu\bar{\nu}$ analysis

In the measurement of the $K^+ \to \pi^+\nu\bar{\nu}$ branching ratio, $K^+ \to \pi^+\pi^o(\gamma)$ events represent one of the most dangerous background contributions. In the analysis of both 2016 [89] and 2017 [102] data, this is, indeed, the dominant background from kaon decays in the fiducial volume. Therefore a robust validation of the reliability of the estimation for this background source is needed and is provided by this work. In addition, within the $K^+ \to \pi^+\nu\bar{\nu}$ analysis, a data-driven approach has been adopted. The π^o rejection has been measured as the ratio between the observed residual events after applying all of the photon-rejection conditions on $\pi\nu\bar{\nu}$-trigger data and those observed without the photon-rejection conditions on control-trigger data for events with M^2_{miss} compatible with the squared π^o mass (M^2_{miss} ranging from 0.015 to 0.021 GeV$^2/c^4$), corrected for the signal and trigger efficiency. $K^+ \to \pi^+\pi^o$ events where the π^o decays into two photons both reconstructed in the LKr calorimeter are then used to evaluate the reconstruction tails of the kinematic variable M^2_{miss}, that was combined with the observed residual $K^+ \to \pi^+\pi^o$ events to evaluate the expected background for this channel in the two signal regions. However, this method does not allow inclusion of the radiative tails from $K^+ \to \pi^+\pi^o\gamma$ events, which affect mostly the so-called *Signal Region 2* with M^2_{miss} above the squared π^o mass. This contribution was estimated in this work by the evaluation of the π^o rejection as described in Chapters 13 and 14, in the squared missing mass region $0.026 < M^2_{\mathrm{miss}} = (P_{K^+} - P_{\pi^+})^2 < 0.068$ GeV$^2/c^4$ [163]. The inclusion of this contribution in the background evaluation of the $K^+ \to \pi^+\nu\bar{\nu}$ analysis is discussed in Reference [154].

After unblinding the present analysis, the comparison between the π^o rejection estimated as described in this work and that obtained with the data-driven method within the $K^+ \to \pi^+\nu\bar{\nu}$ analysis [2] has been done for the same data set (2017 Sample A). It must be emphasized that the LKr information is treated slightly differently in the $K^+ \to \pi^+\nu\bar{\nu}$ analysis of 2017 data [164] with respect to the 2016 selection, and therefore to this work.

[1] The median values obtained by the CL_s method is quoted together with the bands with 68% and 95% coverage, given as first and second set of uncertainties, respectively, with the latter in parentheses.

[2] Numbers are obtained from private discussion with Giuseppe Ruggiero and Radoslav Marchevski.

Instead, the analysis documented in this work involves two conditions which are not used for the $K^+ \to \pi^+\nu\bar{\nu}$ analysis: one allows rejecting photon conversions by looking for extra activity in the RICH detector (see Section 11.2.3); the other, so-called "LKr extra hit" (see Section 11.2.5), allows vetoing photons in the LKr calorimeter with point of impact up to 30 cm from the charged pion on the basis of their hit energy distribution, without using any of the official cluster algorithms. The absence of the RICH-based conversion condition cannot impact by more than 10% on the total rejection as the total contribution of photon conversions to the single-photon inefficiency is about 30%, as shown in Table 13.2. The impact of the LKr extra hit condition has been determined by counting the observed events without applying this condition. The results are shown in Table 19.2. The variations are tiny for the low π^+ momentum region, dominated by the IRC-SAC inefficiency. An increase by 40% is observed in the signal region 25–40 GeV/c without the LKr extra hit cut, which is compatible in size and sign with the observed difference shown in Figure 19.3. After including the contributions from the two additional conditions, the π^o rejection inefficiency estimated in this work is compared with that observed within the $K^+ \to \pi^+\nu\bar{\nu}$ analysis in 5 GeV/c momentum bins for the π^+ momentum region 15–40 GeV/c. As shown in Figure 19.3, the two results agree within the quoted uncertainties.

π^+ Momentum range [GeV/c]	Observed events	
	Standard analysis	No LKr extra hit cut
15 – 20	66	67
20 – 25	11	14
25 – 30	3	5
30 – 35	6	7
35 – 40	3	5

TABLE 19.2: Observed event counts for this analysis and for a modified version without the LKr extra hit condition.

19.3 New-physics searches in $K^+ \to \pi^+ X \to \pi^+ + invisible$ decay

With no modifications to the analysis described in this work, the result of Section 19.1 can be converted into a limit for the decay $K^+ \to \pi^+ X$, where X stands for any system with mass m_X around the π^o mass and assumed to escape detection, being long-lived or feebly interacting with SM particles. The signature for the decay $K^+ \to \pi^+ X$ corresponds to a charged pion in the final state and nothing else. The kinematic condition of Equation (10.12) on the squared missing mass restricts the search to the mass range m_X between 0.109 and 0.155 GeV/c^2. From Equation (9.3), the branching ratio for a $K^+ \to \pi^+ X$ decay

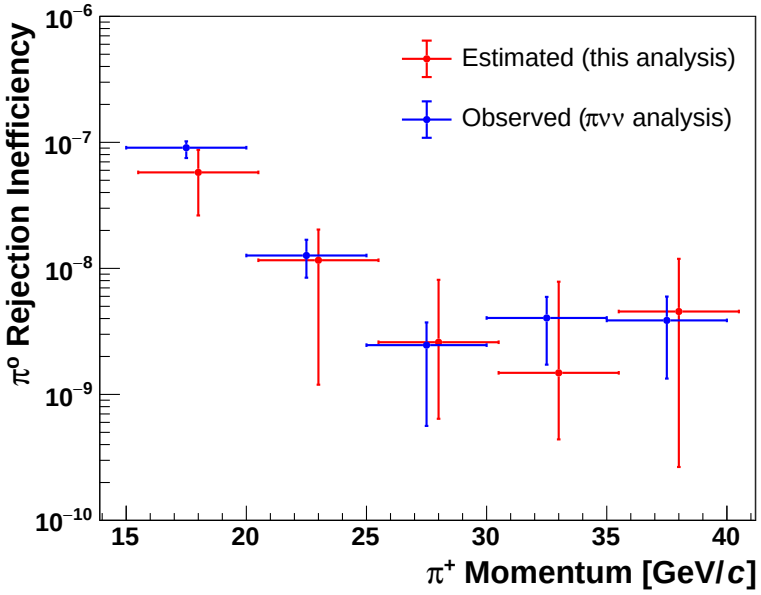

FIGURE 19.3: π^o rejection inefficiency as a function of the charged pion momentum in 5 GeV/c bins: red points refer to the π^o rejection inefficiency estimated in the analysis of this work, blue points to that observed within the $K^+ \to \pi^+ \nu\bar{\nu}$ analysis using the data sample 2017 A.

can be computed as:

$$\begin{aligned} \mathrm{BR}(K^+ \to \pi^+ X) &= \frac{N_\mathrm{s}}{N_{K^+} \times R(m_X) \times \varepsilon_\mathrm{signal} \times \varepsilon_\mathrm{trigger}} = \\ &= \frac{\mathrm{BR}(K^+ \to \pi^+ \pi^o) \times \mathrm{BR}(\pi^o \to invisible)}{R(m_X)} \end{aligned} \tag{19.3}$$

where N_s is the number of $\pi^o \to invisible$ signal events; N_{K^+} the number of kaon decays in the sample used; $\varepsilon_\mathrm{signal}$ and $\varepsilon_\mathrm{trigger}$ the efficiency of the conditions of the photon-rejection algorithm and of the $\pi\nu\bar{\nu}$ trigger, respectively; $R(m_X)$ the acceptance of the kinematic condition on the squared missing mass in Equation (10.12) for the emission of a particle with mass m_X in the process $K^+ \to \pi^+ X$ normalized to $K^+ \to \pi^+ \pi^o$ with $\pi^o \to invisible$ decays. [3]

From the result of Section 19.1, $\mathrm{BR}_\mathrm{observed}(\pi^o \to invisible) \leq 4.4 \times 10^{-9}$, a 90% CL upper limit on $\mathrm{BR}(K^+ \to \pi^+ X)$ is obtained, shown as solid line in Figure 19.4, as a function of m_X in the mass range 0.109 – 0.155 GeV/c^2. In the hypothesis that X is a single particle dominantly decaying to SM particles, different hypotheses have been made for the value of its lifetimes, τ_X. The corresponding upper limits are shown as dashed lines in Figure 19.4. As τ_X decreases, the probability that the X decay products satisfy the conditions to veto the event increases, and therefore the corresponding upper limit on the branching ratio weakens. The shape of the upper limits is a direct consequence of the trend of the acceptance $R(m_X)$ as a function of the mass m_X.

[3] In a model-independent approach, the radiative effects are assumed to cancel.

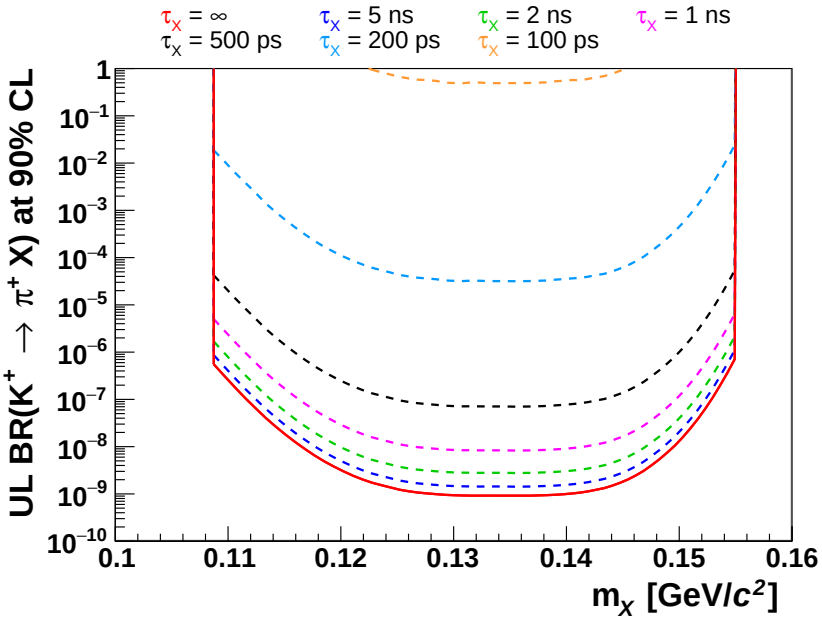

FIGURE 19.4: Upper limit at 90% CL on the branching ratio for the decays $K^+ \to \pi^+ X$, where X stays for any system with mass m_X long-lived or invisibly decaying inside the NA62 experimental apparatus (solid line). Assuming X being a single particle dominantly decaying to SM particles, different hypotheses are made on the X rest lifetime τ_X (dashed lines). The search is restricted to the mass region 0.109 – 0.155 GeV/c^2 for m_X.

The result shown in Figure 19.4 is obtained as a direct by-product of the $\pi^o \to invisible$ search: no changes to the selection are made and the search is done treating the squared missing mass window $0.015 < M^2_{\text{miss}} = (P_{K^+} - P_{\pi^+})^2 < 0.021$ GeV$^2/c^4$ as a single bin. [4] The limit obtained is therefore conservative throughout the mass range. It has to be underlined that Equation (19.3), and the corresponding values for the branching ratio, are independent from any model of new physics: the results for finite lifetimes rely on the only assumption that the escaping system is made of a single particle dominantly decaying to SM visible daughters with the quoted lifetime. The decay width for the process $K^+ \to \pi^+ X$ is given in Equation (2.4) and reported here for convenience [42, 47]:

$$\Gamma(K^+ \to \pi^+ X) = \frac{1}{16\pi\, m^3_{K^+}} \times \lambda^{1/2}\left(m^2_{K^+}, m^2_{\pi^+}, m^2_X\right) \times \left(\frac{m^2_{K^+} - m^2_{\pi^+}}{m_s - m_d}\right)^2 \times |h^S_{ds}|^2 \qquad (19.4)$$

where $\lambda(a,b,c) = (a-b-c)^2 - 4\,bc$ and h^S_{ds} is the model-dependent effective coupling for the $s \to d$ transition.

The results presented are interpreted as a search for axion-like particles (ALPs) with dominant fermion coupling and for dark scalars, decaying to invisible final state in the

[4] An analysis with missing-mass sliding window has been performed on signal and background simulated spectra. Window widths of ±1 and ±1.5 units of the missing mass resolution have been considered. The projected sensitivity is seen to only marginally improve over the limit obtained when treating the entire missing mass range as a single bin.

experimental apparatus or escaping detection being feebly interacting and long lived, according to the models presented in Section 2.4 [42, 43].

19.3.1 Interpretation in term of ALP production in K^+ decays

Following Reference [42], the excluded parameters regions are evaluated for the three coupling scenarios: Yukawa-like, Quark universal, and Quark third generation. According to the theoretical calculations of Reference [42] the coupling strengths for the transition $s \to d$ are: [5]

$$h^S_{ds} = (3.5 \times 10^{-9} + i\, 1.5 \times 10^{-9}) g_Y \tag{19.5}$$

for the Yukawa-like couplings,

$$h^S_{ds} \approx (4.6 \times 10^{-6} + i\, 2.0 \times 10^{-6}) g_q \tag{19.6}$$

for the Quark-universal couplings and

$$h^S_{ds} \approx (1.7 \times 10^{-9} + i\, 7.6 \times 10^{-10}) g_Q \tag{19.7}$$

for the Quark-third-generation couplings.
Inserting the upper limits obtained (Figure 19.4 red line) in Equation (2.4) and using Equations (19.5), (19.6), and (19.7) the excluded parameters regions for the coupling *versus* the mass are computed. Figure 19.5 shows the results obtained (labeled as "This result") together with the most updated searches for ALPs in K and B decays as extrapolated from Reference [42]. [6] Stronger constraints on the couplings are given by the kaon sector for $m_a \lesssim 0.3$ GeV/c^2 in the scenarios of Yukawa-like and Quark-universal couplings. In the scenario of Quark-third-generation couplings, where ALPs are assumed to be solely and universally coupled to quarks from the third family, the effective coupling h^S_{ds} is reduced by more than three orders of magnitudes with respect to the Quark-universal couplings scenario and therefore the bounds on g_Q are three orders of magnitudes weaker than those obtained for g_q where the coupling to the light quarks is also included. This is not the case for B mesons, for which the corresponding h^S_{sb} effective coupling is dominated by the ALP coupling with heavy-quarks and the bounds on $B \to Xa$ are unchanged when the light quarks are excluded.

For the corresponding Yukawa-like scenario of Reference [43], the so-called *BC10* model, the excluded regions for the parameter space of coupling *versus* mass have been computed, too. The upper limits obtained (Figure 19.4 red line) are inserted in Equation (2.4) and according to the Lagrangian of Equation (2.6) the value [7]

$$|h^S_{ds}| \approx 1 \times 10^{-9} g_Y \tag{19.8}$$

[5] For the computation of h^2_{ds} see Equation (A.2) in the Appendix A.
[6] The NA62 results including 2016 and 2017 data for $K^+ \to \pi^+ X$ in the region far from the π^o mass should increase the sensitivity for invisible-ALP searches by a factor of $\sim \sqrt{2}$ [165].
[7] For the computation of h^2_{ds} see Appendix A.

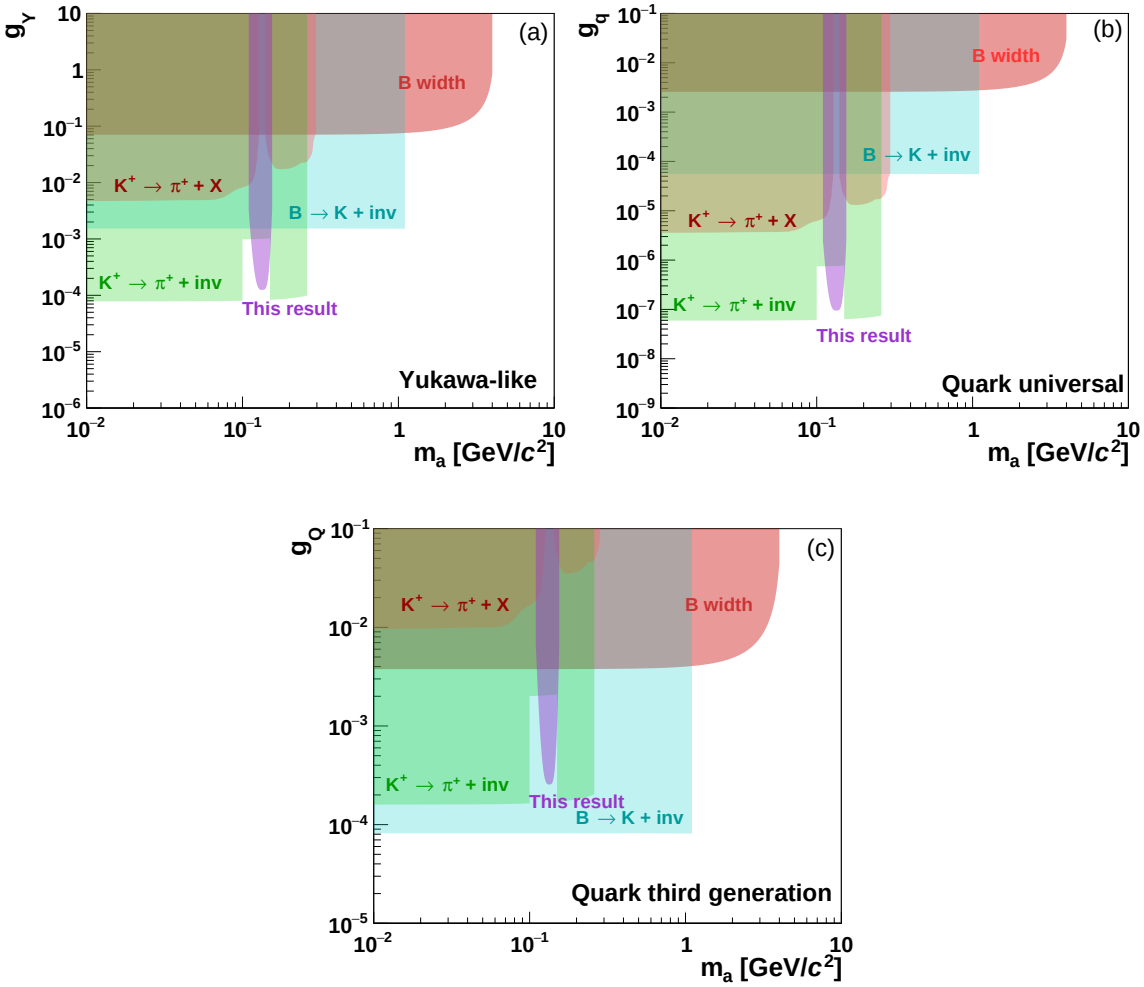

FIGURE 19.5: Excluded parameter regions for an invisibly decaying pseudoscalar a produced in K and B FCNC decays as presented in Reference [42]. Contributions from $K^+ \to \pi^+ + invisible$ (E949 experiment [41, 52, 53]), $K^+ \to \pi^+ X$ ($K_{\mu 2}$ experiment [54]), $B \to K + inivisible$ (CLEO experiment [55]), and the B width measurement (PDG [5]) are shown. Three different coupling scenarios are considered as explained in Section 2.4.1: (a) Yukawa-like; (b) Quark universal; (c) Quark third generation. The results on the search for ALPs in the channel $K^+ \to \pi^+ + invisible$ around the π^o mass presented in this work are labeled as "This result".

is used for the coupling strength for the transition $s \to d$. Figure 19.7 shows the results obtained (labeled as "This result") together with the most updated searches for ALPs in K and B decays as extracted from Reference [43].

If, within the accessible mass range, the ALP width is assumed to be dominated by decays to SM particles [8], the corresponding rest lifetime, shown in Figure 19.6 is expected to be well above a few ns for g_Y coupling below $\simeq 0.02$. Therefore, the upper limit in Figure 19.4 for infinite lifetime can be directly translated into a corresponding upper limit for the coupling g_Y as a function of the ALP mass m_a. The present analysis allows to exclude a previously unexplored region of the parameter space, as shown in the top panel of Figure 19.7. To derive the upper edge of the excluded region, no sensitivity is assumed for

[8] The ALP decay width to SM particles is given in Equations (A.3) and (A.4) in the Appendix A.

ALP lifetimes shorter than 2 ns.

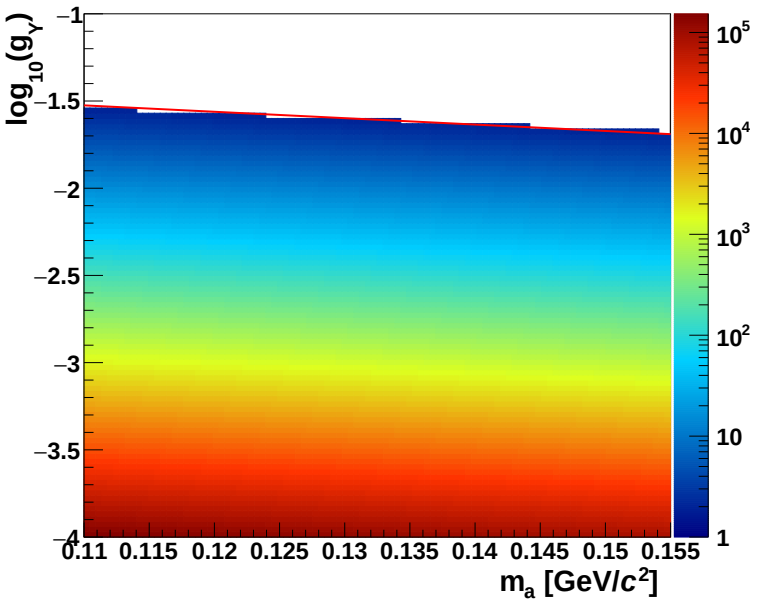

FIGURE 19.6: Lifetime of the ALP particle (in ns) according to Equations (A.3) and (A.4), as a function of $\log_{10}(g_Y)$ and of the ALP mass. The red line corresponds to ALP lifetimes of 2 ns.

If, within the accessible mass range, the ALP width is assumed to be dominated by decays to invisible particles, the corresponding ALP lifetime can be assumed to be significantly lower than that for the previous scenario. Nevertheless, the branching fractions for ALP decays to SM particles would be suppressed, so that the ALP would effectively be an invisible particle for the whole parameter space. The present analysis allows excluding an even larger region of unexplored parameter space than for the previous scenario, as shown in the bottom panel of Figure 19.7: all of the constraints from previous searches for ALP visible decays would be significantly weakened.

19.3.2 Interpretation in term of dark scalar production in K^+ decays

Following the model presented in Section 2.4.2, refereed to as *BC4* model in Reference [43], the production of light dark scalars S is investigated in the channel $K^+ \to \pi^+ S$. Using Equation (2.4) and, according to the Lagrangian of Equation (2.7), the value [9]

$$|h^S_{ds}|^2 \approx 3.8 \times 10^{-19} \sin^2\theta \tag{19.9}$$

for the coupling strength in the $s \to d$ transition, the relation between the branching ratio and the coupling is of the form [44]:

$$\sin^2\theta = \mathrm{BR}(K^+ \to \pi^+ S) \times \frac{m_K}{0.004\ |\vec{p}_S|} \tag{19.10}$$

[9] For the computation of h^2_{ds} see Equation (A.7) in the Appendix A.

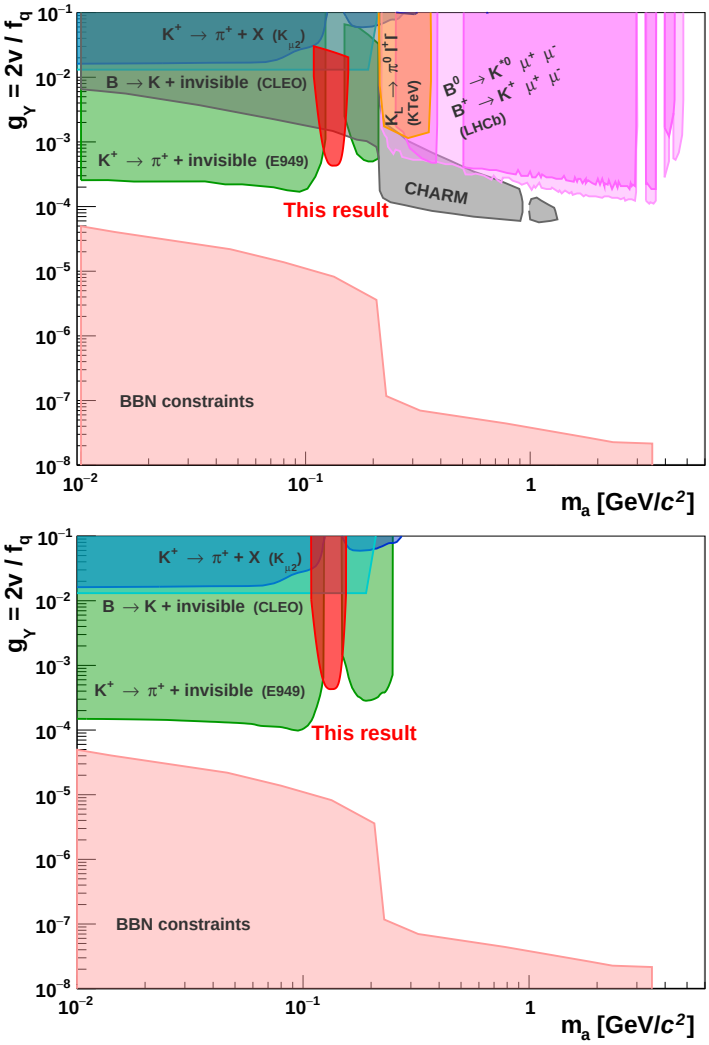

FIGURE 19.7: Search for an axion-like particle a according to the *BC10* model of Reference [43]. ***Top:*** Excluded parameter regions for an axion-like particle dominantly decaying to SM particles. Contributions from $K^+ \to \pi^+ + invisible$ (E949 experiment [52, 53]), $K^+ \to \pi^+ X$ ($K_{\mu 2}$ experiment [54]), $B \to K + invisible$ (CLEO experiment [55]), the search for visible a decays (CHARM experiment [56]), $K_L \to \pi^0 \ell^+ \ell^-$ (KTeV experiment [57]), $B \to K^{(*)} \mu^+ \mu^-$ decays (LHCb experiment [58–60]), and constraints from the Big Bang nucleosynthesis are shown. ***Bottom:*** Excluded parameter regions for an axion-like particle dominantly decaying to invisible particles, with contributions from $K^+ \to \pi^+ + invisible$ (E949 experiment [52, 53]), $K^+ \to \pi^+ X$ ($K_{\mu 2}$ experiment [54]), $B \to K + invisible$ (CLEO experiment [55]), and constraints from the Big Bang nucleosynthesis. For both panels, the exclusion bound from the present search for the decay $K^+ \to \pi^+ + a$ is labeled as "This result".

where $\vec{p}_S$ is the 3-momentum of the S particle in the K^+ rest frame.

Inserting the upper limits obtained (Figure 19.4 red line) in Equation (19.10), the excluded parameters regions for the coupling *versus* the mass are computed. Figure 19.8 shows the results obtained (labeled as "This result") together with the most updated searches for S in K and B decays as extracted from Reference [43].

If in the accessible mass range, the width of the scalar is assumed to be dominated by

decays to visible particles, a lifetime of $\simeq 0.003$ ns/$\sin^2\theta$ is obtained. [10] With the coupling range shown in the top panel of Figure 19.8, infinite lifetimes for the dark scalar can be safely assumed. The results obtained extend in a region still unexplored by past experiments. If, as for the ALP search, dark scalar decays to invisible particles are assumed to dominate, the analysis results exclude an even larger region of unexplored parameter space, as shown in the bottom panel of Figure 19.8.

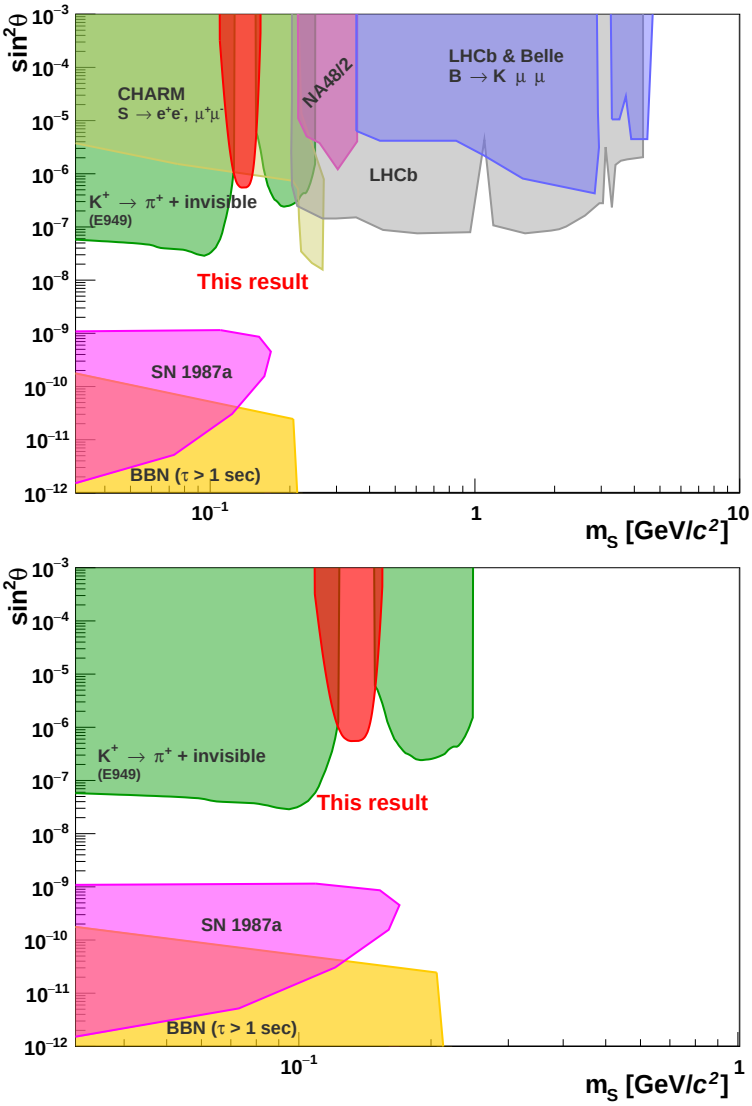

FIGURE 19.8: Search for a dark scalar S according to the *BC4* model of Reference [43]. ***Top:*** Excluded parameter regions for a dark scalar dominantly decaying to SM particles. Contributions from $K^+ \to \pi^+ + invisible$ (E949 experiment [63]), the search for visible S decays (CHARM experiment [56, 64]), $K \to \pi\mu\mu$ (NA48/2 experiment [65]), $B \to K\mu\mu$ (LHCb [59, 60] and Belle [66] experiments), astrophysical constraints (SN1987a [67–70]), and constraints from the Big Bang nucleosynthesis are shown. ***Bottom:*** Excluded parameter regions for a dark scalar dominantly decaying to invisible particles, with contributions from $K^+ \to \pi^+ + invisible$ (E949 experiment [63]), astrophysical constraints (SN1987a [67–70]), and constraints from the Big Bang nucleosynthesis. For both panels, the exclusion bound from the present search for the decay $K^+ \to \pi^+ + S$ is labeled as "This result".

[10] The scalar decay width to SM particles is given in Equation (A.8) in the Appendix A. For the mass range considered in this work, the electron channel dominates the decay width of the S particle.

Chapter 20
Conclusions

A search for invisible decays of π^o mesons tagged via the decay chain $K^+ \to \pi^+\pi^o(\gamma)$, $\pi^o \to invisible$ performed within the NA62 experiment has been presented in this work. From a fraction of data collected in the 2017 data taking, a sample of about 21×10^6 $K^+ \to \pi^+\pi^o(\gamma)$ events (corresponding to about 8.4×10^9 tagged π^o mesons) have been selected in the π^+ momentum region 10–60 GeV/c on control-sample data. The photon-rejection algorithm has been developed following the $K^+ \to \pi^+\nu\bar{\nu}$ analysis of 2016 data [1] and, therefore, not optimized by purpose for the $\pi^o \to invisible$ search, so that the π^o rejection evaluated in this work can be used in the $K^+ \to \pi^+\nu\bar{\nu}$ analysis.

A different experimental technique has been adopted with respect to that leading to the current most stringent upper limit: the background contribution from $\pi^o \to \gamma\gamma$ events is evaluated by the combination of the response, studied in data, of the photon-veto system in detecting the visible products of π^o decays with MC simulation. This procedure allows the evaluation of the expected π^o rejection and of the estimated number of background events. The validation of the background expectation shows that the single-photon detection efficiencies have been measured in data with a systematic uncertainty sub-dominant with respect to the statistical fluctuations, and the topologies of the detector signals generated by the two photons from $\pi^o \to \gamma\gamma$ decays can be reproduced in the data as expected in the MC.

After the optimization of the π^+ momentum region, the search for $\pi^o \to invisible$ has been performed in the signal region with π^+ momentum between 25 and 40 GeV/c. Here, the estimated π^o rejection inefficiency is

$$\varepsilon_{\pi^o} = \left(2.8^{+5.9}_{-2.1}\right) \times 10^{-9}, \tag{20.1}$$

and the number of estimated background events is $N_{\text{bkg}} = 10^{+22}_{-8}$. Using the CL_s method, in absence of signal, the expected upper limit at 90% CL on the branching ratio is

$$\text{BR}_{\text{expected}}(\pi^o \to invisible) \leq \left(3.8^{+2.6(+5.7)}_{-1.5(-2.6)}\right) \times 10^{-9}, \tag{20.2}$$

where the uncertainties represent 68% and 95% statistical coverage of the upper limit, given as first and second set of uncertainties, respectively, with the latter in parentheses.
After the unblinding of the signal region, 12 events are observed in the signal sample. The resulting 90% CL upper limit on the branching ratio for $\pi^o \to invisible$ is

$$\text{BR}_{\text{observed}}(\pi^o \to invisible) \leq 4.4 \times 10^{-9} \tag{20.3}$$

which improves by a factor of about 60 on the present most stringent experimental result [41].

The analysis has also been interpreted as a search for $K^+ \to \pi^+ X$ decays, where X stands for any system with mass m_X in the range 0.109 – 0.155 GeV/c^2 assumed to escape detection being long-lived or invisibly decaying. Model-independent limits are derived for the $K^+ \to \pi^+ X$ branching ratio for different X lifetimes. Using the models discussed in References [42, 43], the productions of axion-like particles (ALP, a) with fermionic couplings is investigated in the channel $K^+ \to \pi^+ a$ and excluded parameter regions are computed for the ALP coupling with SM fermions as a function of the ALP mass. Similarly, using the model discussed in Reference [43] the productions of dark scalars S with mixing with the SM Higgs boson is investigated in the channel $K^+ \to \pi^+ S$ and an excluded parameter region is computed for the S coupling to the Higgs as a function of the S mass. The results obtained improve on the previous experimental limits for a wide class of models.

As a perspective, to further improve on the results here presented the uncertainties on the detector single-photon efficiencies should be reduced. This is particularly true for the high-energy part of the LKr single-photon efficiency, the uncertainty of which drives the error on the expected π^o rejection inefficiency. Achieving such an improvement would require on one side a significant increase of the statistics of the data control sample and, on the other side, a validation of the measured single-photon efficiency more stringent than it is possible at present, with the possibility to include in the validation procedure a sideband region at high π^+ momentum. An increase of the MC statistics would also be needed in order to better study the systematic uncertainties induced by the method-bias correction.

Appendix A
Formulae for Axion-Like and Dark Scalar Particles

Flavor-changing neutral currents $s \to d$ and $b \to s$ transitions are investigated in the search for axion-like particles (ALPs) and dark scalar particles as discussed in the models presented in Section 2.4 [42, 43]. In this work the channel $K^+ \to \pi^+ X$ is considered, where X stands for any system with mass m_X around the π^o mass assumed to escape detection, being long-lived or feebly interacting with SM particles. The main formulae used to compute the excluded parameter regions for the coupling *versus* the X mass are reported in the following.

Axion-like particles

Following Reference [42], the ALP-fermion interaction given in Equation (2.5) can be written as: [1]

$$\mathcal{L} \supset a\, \bar{d}_L\, s_R \times \frac{\alpha(m_d - m_s)}{4\sqrt{2}\pi\, v\, m_W^2 \sin^2\theta_W} \left(m_t^2 V_{ts} V_{td}^* \log\left(\frac{\Lambda_{\rm UV}^2}{m_t^2}\right) + m_c^2 V_{cs} V_{cd}^* \log\left(\frac{\Lambda_{\rm UV}^2}{m_c^2}\right)\right) \times g_Y \tag{A.1}$$

in case of the the Yukawa-like scenario, where a, $\bar{d}$ and s are the ALP, $\bar{d}$-quark and s-quark fields, respectively; m_d, m_s, m_c and m_t the masses of the *down*, *strange*, *charm* and *top* quark, respectively; m_W^2 the mass of the W boson and θ_W the Weinberg angle; α is the fine-structure constant; v the vacuum expectation value of the Higgs field; V_{ij} is the CKM matrix parameter for the quarks i and j; g_Y the ALP-fermion coupling; and $\Lambda_{\rm UV}$ is the new-physics scale. [2] In Reference [42] the new-physics scale is assumed at $\Lambda = 1$ TeV. Similar expressions can be derived for the Quark-universal and Quark-third-generation scenarios. From Equation (A.1), one can derive:

$$h_{ds}^S = \frac{\alpha(m_d - m_s)}{4\sqrt{2}\pi\, v\, m_W^2 \sin^2\theta_W} \left(m_t^2 V_{ts} V_{td}^* \log\left(\frac{\Lambda_{\rm UV}^2}{m_t^2}\right) + m_c^2 V_{cs} V_{cd}^* \log\left(\frac{\Lambda_{\rm UV}^2}{m_c^2}\right)\right) \times g_Y \tag{A.2}$$

to be used in Equation (2.4) for the evaluation of the excluded parameter regions of the coupling strength as function of the ALP mass. In the Yukawa-like scenario of Reference [43], the expression of h_{ds}^S can be obtained from Equation (A.2) multiplied by a factor 1/4.

[1] In Reference [42], the limit $m_t \gg m_b \gg m_s$ is considered.

[2] Equation (2.5) is seen as part of a more general theory which manifests at a higher energy scale, Λ, where the new physics is assumed to appear. The divergences of the one loop contribution of the effective theory are canceled at the new-physics scale Λ.

For m_a values lower than three times the pion mass, as the ALP mass range considered in this work, the only decay possible for the ALP is into pairs of leptons and photons. The ALP decay width is of the form [42]

$$\Gamma(a \to \ell^+\ell^-) = \frac{g_f^2}{8\pi} m_a \sqrt{1 - \frac{1}{\tau_\ell}} \tag{A.3}$$

in case of a decay to a lepton pair, where g_f is the ALP-fermion coupling, m_a the ALP mass and $\tau_\ell = m_a^2/(4m_\ell^2)$ the lepton lifetime, respectively, and

$$\Gamma(a \to \gamma\gamma) = \frac{\alpha^2 m_a^3}{256\pi^3} \left| \sum_f \frac{N_c\, Q_f^2\, g_f}{m_f} F_a(\tau_f) \right|^2 \tag{A.4}$$

in case of a decay to a photon pair, with f running over all fermions and where g_f is the ALP-fermion coupling; m_a and m_f the ALP and fermion masses, respectively; Q_f the fermion charge; N_c the number of color; α the fine-structure constant; $\tau_f = m_a^2/(4m_f^2)$ the fermion lifetime and

$$F_a(\tau) = \frac{2}{\tau} \times \begin{cases} \arcsin^2 \sqrt{\tau}, & \tau \leq 1 \\ -\frac{1}{4}\left[\log \frac{1+\sqrt{1-\tau^{-1}}}{1-\sqrt{1-\tau^{-1}}} - i\pi\right]^2, & \tau > 1 \end{cases} \tag{A.5}$$

Equations (A.3) and (A.4) are used to derive the ALP lifetime for a given coupling and mass as shown in Figure 19.6.

Dark scalar particles

In Reference [43], the production of a light dark scalar particle arises from the mixing with the SM Higgs as given in Equation (2.7). In the channel $K^+ \to \pi^+ + S$, considered in this work, the $s \to d$ transition can be written as [45]:

$$\mathcal{L}_{sd} \supset S\, \bar{d}_L\, s_R \times \frac{3\alpha(m_d - m_s)}{32\pi\, v\, m_W^2 \sin^2\theta_W} \left(m_t^2 V_{ts} V_{td}^* + m_c^2 V_{cs} V_{cd}^*\right) \times \sin\theta \tag{A.6}$$

where S, $\bar{d}$ and s are the dark scalar, $\bar{d}$-quark and s-quark fields respectively; m_d, m_s, m_c and m_t the masses of the *down*, *strange*, *charm* and *top* quark, respectively; m_W^2 the mass of the W boson and θ_W the Weinberg angle; α is the fine-structure constant; v the vacuum expectation value of the Higgs field; V_{ij} is the CKM matrix parameter for the quarks i and j; and $\sin\theta$ the coupling parameter of the S-Higgs mixing. From Equation (A.6), one can derive:

$$h_{ds}^S = \frac{3\alpha(m_d - m_s)}{32\pi\, v\, m_W^2 \sin^2\theta_W} \left(m_t^2 V_{ts} V_{td}^* + m_c^2 V_{cs} V_{cd}^*\right) \times \sin\theta \tag{A.7}$$

to be used in Equation (2.4) for the evaluation of the excluded parameter regions of the coupling strength as function of the dark scalar mass.

The dark scalar decay width into leptons is of the form [44]

$$\Gamma(S \to \ell^+\ell^-) = \sin^2\theta \times \frac{m_\ell^2\, m_S}{8\pi\, v^2}\beta_\ell^2 \tag{A.8}$$

where $\sin\theta$ is the S-Higgs mixing parameter; m_ℓ and m_S are the lepton and dark scalar masses, respectively; v the vacuum expectation value of the SM Higgs; and β_ℓ a kinematic parameter equals to $\beta_\ell = \sqrt{1 - 4m_\ell^2/m_S^2}$. For m_s values lower than two times the muon mass, as the S mass range considered in this work, the dark scalar dominantly decay to an electron-positron pair.

Appendix B
LKr Dead Cells

The effect of the LKr dead cells on the Tag&Probe method is studied with the selection of $K_{2\pi}$ events on control-trigger data as described in Chapter 10. Exactly two photon clusters (from the standard reconstruction) must be present in the LKr calorimeter according to Section 11.1.1 and veto conditions are applied on the LAV and SAV detectors as described in Sections 11.1.2 and 11.1.3. A distance greater than 20 cm is required between the two LKr photon clusters. One of them is randomly chosen as the tagging photon and must satisfy the conditions described in Section 13.1 (except the minimum distance from any dead cell), while the other is considered as the probe photon. The expected 4-momentum of the probed photon is computed according to Equation (13.2) and its extrapolated position at the LKr plane must be inside the detector sensitive volume.

For the selected events, a two dimensional plot is filled with the x and y position of the tagging photon with and without the weight for $\Delta E^{\text{probe}}_{\text{expected}-\text{found}}$, where $E^{\text{probe}}_{\text{expected}}$ and $E^{\text{probe}}_{\text{found}}$ are the energy of the probed photon as computed from Equation (13.2) and as given by the reconstructed LKr photon cluster. The ratio of the two plots, shown in Figure B.1, represents the average value of $\Delta E^{\text{probe}}_{\text{expected}-\text{found}}$. From this ratio, four regions are seen to have an energy response much lower than expected and they are identified as dead cells in addition to those already marked as dead by the LKr reconstruction (green/yellow spots in Figure B.1). Table B.1 gives the definition of the four regions and the position of the tagging photon is required not to be inside any of them.

x [mm]	y [mm]
$210 < x < 240$	$-350 < y < -310$
$700 < x < 740$	$-150 < y < -110$
$-320 < x < -290$	$-500 < y < -470$
$-730 < x < -710$	$290 < y < 320$

TABLE B.1: LKr regions with an energy response much lower than expected marked as additional dead-cell regions.

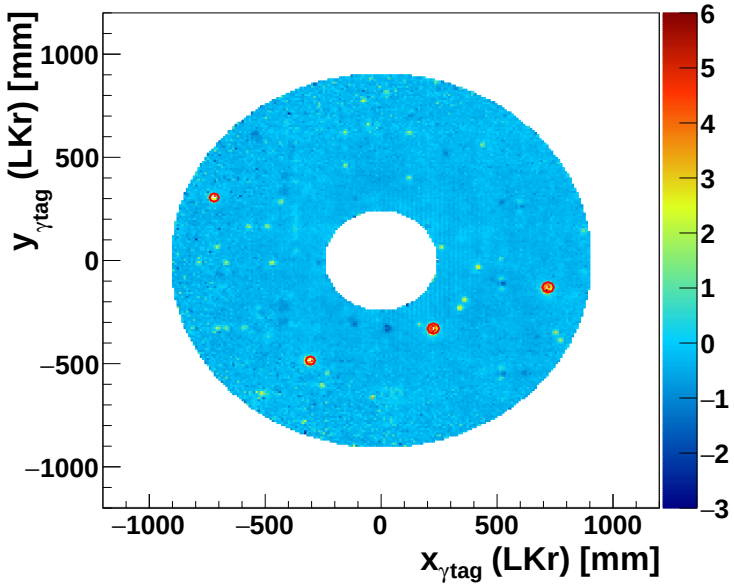

FIGURE B.1: Position of the tagging photon at the LKr surface. Each bin is filled with the average value of the difference in GeV units between the expected and reconstructed energy of the probed photon ($\langle \Delta E^{\text{probe}}_{\text{expected}-\text{found}} \rangle$), which should peak at 0 GeV. In four regions, values of $\langle \Delta E \rangle$ greater than 5 GeV are seen. These are declared dead-cell regions in addition to those already known in the LKr reconstruction (green/yellow spots).

Appendix C
Results of the Single-Photon Inefficiencies

Energy [GeV]	Inefficiency LAV
0.00 – 0.05	$(2.16^{+1.44}_{-0.64}) \times 10^{-1}$
0.05 – 0.10	$(1.19^{+0.56}_{-0.35}) \times 10^{-1}$
0.10 – 0.15	$(4.29^{+1.83}_{-1.26}) \times 10^{-2}$
0.15 – 0.20	$(1.52^{+0.99}_{-0.49}) \times 10^{-2}$
0.20 – 0.25	$(6.53^{+4.82}_{-3.30}) \times 10^{-3}$
0.25 – 0.30	$(3.63^{+2.28}_{-2.23}) \times 10^{-3}$
0.30 – 0.35	$(2.79^{+1.62}_{-1.54}) \times 10^{-3}$
0.35 – 0.40	$(2.41^{+1.17}_{-1.46}) \times 10^{-3}$
0.40 – 0.45	$(2.53^{+1.38}_{-1.47}) \times 10^{-3}$
0.45 – 0.50	$(2.65^{+1.44}_{-1.56}) \times 10^{-3}$
0.50 – 0.55	$(2.64^{+1.55}_{-1.45}) \times 10^{-3}$
0.55 – 0.60	$(2.56^{+2.29}_{-1.20}) \times 10^{-3}$
0.60 – 0.65	$(2.78^{+3.23}_{-1.25}) \times 10^{-3}$
0.65 – 0.70	$(2.75^{+4.36}_{-1.42}) \times 10^{-3}$
0.70 – 0.75	$(3.11^{+6.66}_{-1.77}) \times 10^{-3}$
0.75 – 0.80	$(2.64^{+4.60}_{-1.51}) \times 10^{-3}$
0.80 – 0.85	$(2.34^{+3.05}_{-1.45}) \times 10^{-3}$
0.85 – 0.90	$(2.52^{+3.57}_{-1.35}) \times 10^{-3}$
0.90 – 0.95	$(3.60^{+5.12}_{-1.60}) \times 10^{-3}$
0.95 – 1.00	$(4.63^{+3.34}_{-1.71}) \times 10^{-3}$
1.0 – 1.5	$(3.17^{+1.80}_{-0.92}) \times 10^{-3}$
1.5 – 2.0	$(2.78^{+2.97}_{-1.03}) \times 10^{-3}$
2.0 – 2.5	$(3.30^{+0.26}_{-0.25}) \times 10^{-3}$
2.5 – 3.0	$(2.60^{+0.24}_{-0.23}) \times 10^{-3}$
3.0 – 3.5	$(2.24^{+0.24}_{-0.23}) \times 10^{-3}$
3.5 – 4.0	$(1.47^{+0.22}_{-0.19}) \times 10^{-3}$
4.0 – 4.5	$(1.14^{+0.20}_{-0.18}) \times 10^{-3}$
4.5 – 5.0	$(8.14^{+1.90}_{-1.53}) \times 10^{-4}$
5.0 – 5.5	$(5.11^{+1.58}_{-1.35}) \times 10^{-4}$
5.5 – 6.0	$(5.72^{+1.76}_{-1.51}) \times 10^{-4}$
$\geq$ 6.0	$(1.34^{+0.28}_{-0.25}) \times 10^{-4}$

Energy [GeV]	Inefficiency LKr
0.0 – 0.4	$(9.09^{+0.80}_{-0.65}) \times 10^{-1}$
0.4 – 0.8	$(6.93^{+1.04}_{-0.44}) \times 10^{-1}$
0.8 – 1.2	$(1.94^{+0.60}_{-0.17}) \times 10^{-1}$
1.2 – 1.6	$(1.78^{+2.67}_{-0.56}) \times 10^{-2}$
1.6 – 2.0	$(9.49^{+9.16}_{-5.73}) \times 10^{-3}$
2.0 – 2.4	$(7.67^{+3.53}_{-5.35}) \times 10^{-3}$
2.4 – 2.8	$(4.61^{+2.26}_{-2.49}) \times 10^{-3}$
2.8 – 3.2	$(3.63^{+1.65}_{-1.18}) \times 10^{-3}$
3.2 – 3.6	$(4.66^{+1.67}_{-1.62}) \times 10^{-3}$
3.6 – 4.0	$(4.69^{+1.40}_{-1.96}) \times 10^{-3}$
4.0 – 4.4	$(4.49^{+0.91}_{-1.07}) \times 10^{-3}$
4.4 – 4.8	$(3.80^{+0.68}_{-0.62}) \times 10^{-3}$
4.8 – 5.2	$(3.12^{+0.58}_{-0.52}) \times 10^{-3}$
5.2 – 5.6	$(3.14^{+0.56}_{-0.51}) \times 10^{-3}$
5.6 – 6.0	$(2.45^{+0.50}_{-0.45}) \times 10^{-3}$
6.0 – 6.4	$(2.03^{+0.46}_{-0.41}) \times 10^{-3}$
6.4 – 6.8	$(1.79^{+0.41}_{-0.37}) \times 10^{-3}$
6.8 – 7.2	$(1.63^{+0.39}_{-0.34}) \times 10^{-3}$
7.2 – 7.6	$(1.47^{+0.36}_{-0.32}) \times 10^{-3}$
7.6 – 8.0	$(1.08^{+0.31}_{-0.27}) \times 10^{-3}$
8.0 – 8.4	$(9.00^{+2.83}_{-2.35}) \times 10^{-4}$
8.4 – 8.8	$(6.62^{+2.50}_{-1.90}) \times 10^{-4}$
8.8 – 9.2	$(5.68^{+2.26}_{-1.79}) \times 10^{-4}$
9.2 – 9.6	$(6.29^{+2.30}_{-1.92}) \times 10^{-4}$
9.6 – 10.0	$(6.25^{+2.33}_{-1.96}) \times 10^{-4}$
10 – 15	$(1.78^{+0.32}_{-0.29}) \times 10^{-4}$
15 – 20	$(5.86^{+1.81}_{-1.55}) \times 10^{-5}$
20 – 25	$(9.59^{+10.79}_{-6.06}) \times 10^{-6}$
25 – 30	$(5.89^{+6.63}_{-3.73}) \times 10^{-6}$
$\geq$ 30	$\leq 5.84 \times 10^{-6}$

TABLE C.1: Results of the single-photon inefficiencies for the LAV (***left***) and the LKr (***right***) detectors.

Energy [GeV]	**Inefficiency IRC**	**Inefficiency SAC**
0 – 5	$(3.52^{+0.81}_{-0.75}) \times 10^{-1}$	$(6.82^{+2.01}_{-2.01}) \times 10^{-1}$
5 – 10	$(4.72^{+0.96}_{-0.87}) \times 10^{-3}$	$(4.32^{+1.25}_{-1.06}) \times 10^{-3}$
10 – 20	$(6.35^{+1.80}_{-1.57}) \times 10^{-4}$	$(1.46^{+0.30}_{-0.27}) \times 10^{-3}$
20 – 40	$(2.12^{+0.60}_{-0.53}) \times 10^{-4}$	$(1.04^{+0.14}_{-0.13}) \times 10^{-3}$
$\geq$ 40	$(8.60^{+6.60}_{-5.44}) \times 10^{-5}$	$(6.50^{+1.95}_{-1.49}) \times 10^{-4}$

TABLE C.2: Results of the single-photon inefficiencies for the IRC and SAC detectors.

Appendix D
Smooth of the LAV and LKr Single-Photon Efficiencies

As stated in Section 13.5, a consistency check of the analysis results is performed by smoothing the LAV and LKr efficiency curves inclusive of the related statistical uncertainties. The *SmoothKern* method of the *TGraphSmooth* ROOT class [166] is used. The idea is to substitute the evaluated inefficiency with a gaussian-kernel weighted average: for each energy point, the average is performed using $\pm 4\sigma$ interval, where the resolution σ is set to 100 MeV for the LAV and 750 MeV for the LKr. Figure D.1 shows the LAV and LKr inefficiency with and without applying the treatment described above.

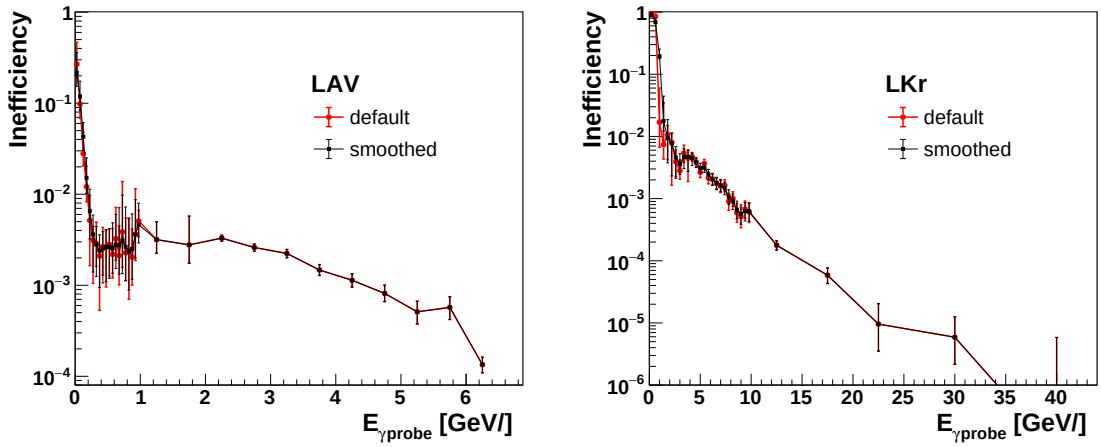

FIGURE D.1: LAV (***left***) and LKr (***right***) inefficiency: the original result (red) is compared with a smoothed curve (black) obtained as described in the text.

The expected π^o rejection is then evaluated as described in Chapter 14 with both inefficiencies of Figure D.1 for the LAV and LKr. The results are shown in Figure D.2 and no significant variations are observed in the estimated π^o rejection inefficiency. Since the analysis results in term of background rejection and uncertainties, and optimization of the momentum signal region do not show any significant variation whether or not the smooth treatment is applied, the LAV and LKr smoothed inefficiencies are used in the analysis.

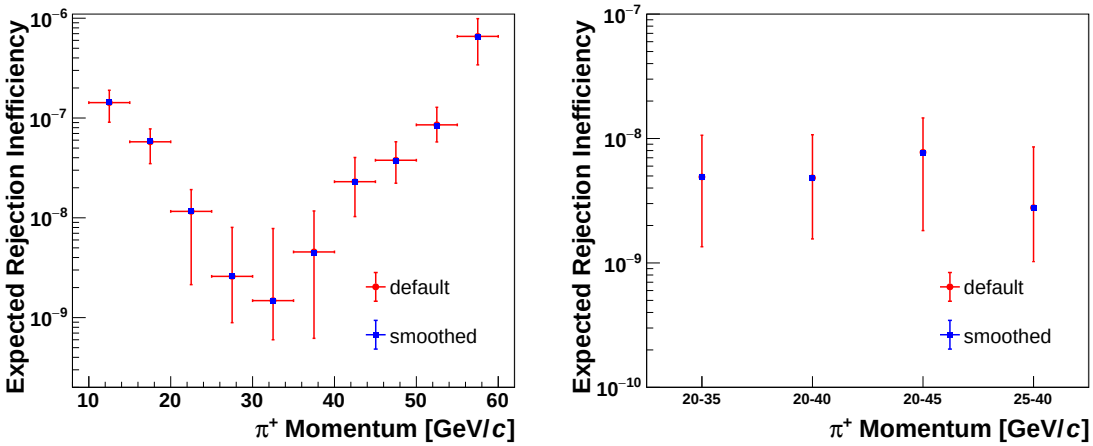

FIGURE D.2: Background rejection inefficiency evaluated as described in Chapter 14 from the original result (red points) and from the smoothed inefficiency curves (blue points) of the LAV and LKr, as a function of the π^+ momentum in 5 GeV/c bins (***left***) and in the momentum intervals tested for the analysis optimization as given in Chapter 18 (***right***).

Appendix E
Dalitz Selection

$K^+ \to \pi^+\pi^o(\gamma)$ Dalitz ($\pi^o \to \gamma e^+ e^-$) events are selected similarly to the $K_{2\pi}$ normalization sample (see Chapter 10). The main difference is that, instead of a single STRAW track in the final state, a triplet of STRAW tracks is required. The three-track combination is formed by requiring for each of the STRAW tracks the following conditions:

- A good quality track. This means that the track must satisfy the conditions: $|\Delta p_{\rm fit}| \leq 20$ GeV/c , $\chi^2_{\rm fit} \leq 20$, and to have hits in at least 3 chambers.
- The track must be in the acceptance of the NA48-CHOD, LKr, and MUV3 detectors.
- The track must be associated to NA48-CHOD, CHOD, LKr candidates but not to a MUV3 candidate.

Among all the three-track combinations only those with total charge equal to the K^+ charge, $Q_{\rm triplet} = 1$, are considered. For each selected triplets a three-track vertex is defined as the median point at their closest distance of approach (CDA). The best triplet is the one with minimum CDA and has to satisfy $\mathrm{CDA}_{\rm triplet} < 30$ mm. The longitudinal position of the three-track vertex must lie between 100 and 170 m.

At least one of the STRAW tracks must be associated to candidates in the RICH, MUV1, and MUV2 detectors, and is identified as the pion track if it satisfies the conditions:

- The most probable hypothesis given by the ***SpectrometerRICHAssociation*** tool is equal to 3 (pion hypothesis).
- The pion probability given by the ***SpectrometerCalorimeterAssociation*** tool is greater than 0.8.

The positron and electron track must have $E_{\rm LKr}/p_{\rm track} \geq 0.8$. In addition, the positron track must be associated to a RICH candidate and the most probable hypothesis given by the ***SpectrometerRICHAssociation*** tool must be equal to 1 (positron hypothesis).

A KTAG candidate with at least 5 fired sectors is required in time (within 2 ns time window) with the tracks triplet. The association of the pion track to a GTK kaon candidate is made exactly as for the single-track events as described in Section 10.1. The longitudinal position of the K–π vertex is required to be between 105 and 165 m and the squared missing mass $M^2_{\rm miss} = (P_{K^+} - P_{\pi^+})^2$ to be between 0.015 and 0.021 GeV$^2/c^4$. No activity is allowed in the CHANTI, LAVs and SAV detectors.

Appendix F
Study of the Systematics due to the LKr Hit Multiplicity

Additional sources of systematic uncertainties specific to the photon-rejection conditions are considered. In particular, the criteria defining the region of the LKr spatially unrelated to the charged pion when defining the "Hit multiplicity" condition (Section 11.2.1) are varied. The LKr hit multiplicity condition allows detection of photons not reconstructed by the LKr standard and auxiliary reconstruction algorithms (see Section 7.2.2 for the algorithms description) due to photon-pion merging. Anyway, inelastic interactions of the charged pion downstream the STRAW spectrometer magnet (in particular in the RICH mirrors) could induce a systematic loss of signal acceptance, due to detection of additional activity in the NA48-CHOD, CHOD, and LKr detectors. The impact of this effect is studied by varying the distance cut used in Section 11.2.1 to define the LKr hit multiplicity associated to NA48-CHOD and CHOD extra activity. The default cut at 10 cm, used in this work, corresponds to look for extra in-time activity in the LKr starting from about 5 cells away from the pion cluster. This is considered the minimum distance that can be applied given the matrix of cells used for the cluster reconstruction, otherwise the cells belonging to the pion cluster would be also included. The cut on the distance is increased to 15, 20, and 30 cm. Changing the definition of the LKr hit multiplicity condition, the LKr single-photon efficiency as computed in Chapter 13 is not touched, given the 45 cm isolation distance required between the expected position of the probed photon and that of both the charged pion and the tagging photon clusters. On the contrary, the number of observed events after applying all the conditions of the photon-rejection algorithm is expected to vary due to the change of the LKr hit multiplicity definition: events previously rejected are now kept if a looser cut is used. The number of events remained in the π^+ momentum signal region 25–40 GeV/c are counted as a function of the distance cut used. The results of this study are reported in Table F.1.

Distance cut [cm]	10	15	20	30
π^+ Momentum [GeV/c]		$N_{\mathbf{obs}}$		
25 – 30	3	5	6	6
30 – 35	6	6	6	6
35 – 40	3	3	3	3
25 – 40	12	14	15	15

TABLE F.1: Observed events in the π^+ momentum signal region 25–40 GeV/c after applying the full photon-rejection algorithm on $\pi\nu\bar{\nu}$-trigger data as a function of the LKr hit multiplicity distance cut.

The number of observed events increases by extending the area belonging to the pion cluster. In particular, the lower π^+ momentum region is more affected by the change of the LKr hit multiplicity cut: this can be due to kinematic considerations or statistical fluctuations. The variation of N_{obs} saturates at $+25\%$ when the distance cut is loosened, as shown in Figure F.1.

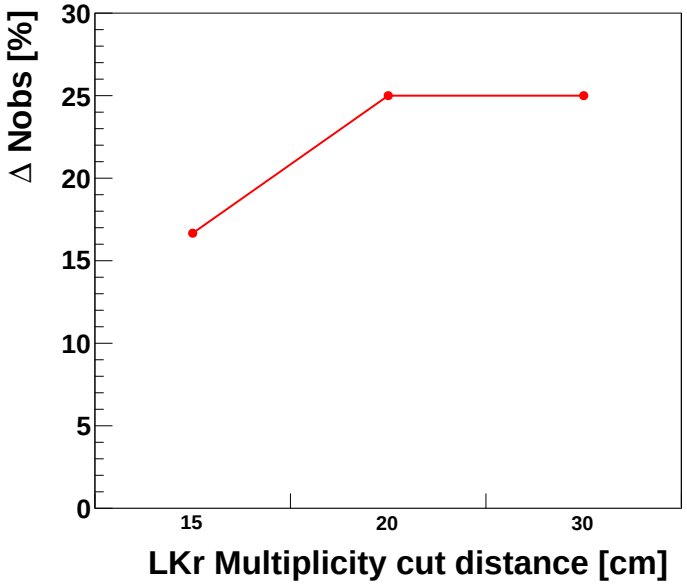

FIGURE F.1: Variation of the numbers of observed events in the π^+ momentum signal region 25–40 GeV/c as a function of the distance cut applied to define the LKr hit multiplicity cut.

A systematic effect induced by the LKr hit multiplicity distance cut, if present, is not affecting the uncertainty quoted and some considerations are in order:

- A maximum increase of $+25\%$ on the expected π^o rejection inefficiency would remain totally sub-leading with respect to the fluctuations on the estimated number of background events, $N_{\text{bkg}} = 10^{+22}_{-8}$ in the π^+ momentum signal region 25–40 GeV/c, since the main source of uncertainty on the π^o rejection inefficiency is due to the statistical contribution of the single-photon efficiencies.

- The cut variation for the LKr hit multiplicity condition would have an impact on the $\pi^o \to \textit{invisible}$ signal efficiency due to the effect of accidental activity ($\varepsilon_{\text{signal}}$), for which a systematic error of 3% is quoted. The corresponding change induced by the cut variation is sub-leading with respect to the quoted uncertainty.

- The problem of determining the variation of the efficiency for photons closer and closer to the pion impact point is difficult to solve with the necessary uncertainty, given the statistics available. Indirect information might be obtained from the study of the distribution of the minimum angle between the pion and the expected photon.

List of Figures

List of Tables

Bibliography

[1] R. Marchevski and G. Ruggiero. *"$K^+ \to \pi^+ \nu\bar{\nu}$ Selection"*. NA62 internal note NA62-18-04. URL: https://na62.web.cern.ch/na62/restricted/NotesDoc/NA62-18-04.pdf.

[2] R. Marchevski. "First measurement of the $K^+ \to \pi^+ \nu\bar{\nu}$ decay with the NA62 experiment at CERN". PhD Thesis. Johannes Gutenberg Universität Mainz, 2019.

[3] D. H. Perkins. *Introduction to high energy physics*. Addison-Wesley, 1982.

[4] F. Halzen and A. D. Martin. *Quarks and leptons: an introductory course in modern particle physics*. Wiley, 1984.

[5] M. Tanabashi *et al.* (Particle Data Group). "Review of Particle Physics". In: *Phys. Rev. D* 98 (2018), p. 030001. DOI: 10.1103/PhysRevD.98.030001.

[6] G. Arnison *et al.* (UA1 Collaboration). "Experimental observation of isolated large transverse energy electrons with associated missing energy at $s = 540$ GeV". In: *Phys. Lett. B* 122 (1983), pp. 103–116. DOI: 10.1016/0370-2693(83)91177-2.

[7] M. Banner *et al.* (UA2 Collaboration). "Observation of single isolated electrons of high transverse momentum in events with missing transverse energy at the CERN pp collider". In: *Phys. Lett. B* 122 (1983), pp. 476–485. DOI: 10.1016/0370-2693(83)91605-2.

[8] Ch. Berger *et al.* (PLUTO Collaboration). "Jet analysis of the $\Upsilon(9.46)$ decay into charged hadrons". In: *Phys. Lett. B* 82 (1979), pp. 449–455. DOI: 10.1016/0370-2693(79)90265-X.

[9] J. E. Augustin *et al.* "Discovery of a Narrow Resonance in e^+e^- Annihilation". In: *Phys. Rev. Lett.* 33 (1974), pp. 1406–1408. DOI: 10.1103/PhysRevLett.33.1406.

[10] J. J. Aubert *et al.* "Experimental Observation of a Heavy Particle J". In: *Phys. Rev. Lett.* 33 (1974), pp. 1404–1406. DOI: 10.1103/PhysRevLett.33.1404.

[11] S. Herb *et al.* "Observation of a Dimuon Resonance at 9.5 GeV in 400-GeV Proton-Nucleus Collisions". In: *Phys. Rev. Lett.* 39 (1977), pp. 252–255. DOI: 10.1103/PhysRevLett.39.252.

[12] F. Abe *et al.* (CDF Collaboration). "Observation of Top Quark Production in $\overline{p}p$ Collisions with the Collider Detector at Fermilab". In: *Phys. Rev. Lett.* 74 (1995), pp. 2626–2631. DOI: 10.1103/PhysRevLett.74.2626.

[13] S. Abachi *et al.* (D∅ Collaboration). "Search for High Mass Top Quark Production in $p\overline{p}$ Collisions at $\sqrt{s} = 1.8$ TeV". In: *Phys. Rev. Lett.* 74 (1995), pp. 2422–2426. DOI: 10.1103/PhysRevLett.74.2422.

[14] G. Aad *et al.* (ATLAS Collaboration). "Observation of a new particle in the search for the Standard Model Higgs boson with the ATLAS detector at the LHC". In: *Phys. Lett. B* 716 (2012), pp. 1–29. DOI: 10.1016/j.physletb.2012.08.020.

[15] S. Chatrchyan *et al.* (CMS Collaboration). "Observation of a new boson at a mass of 125 GeV with the CMS experiment at the LHC". In: *Phys. Lett. B* 716 (2012), pp. 30–61. DOI: 10.1016/j.physletb.2012.08.021.

[16] J. Ellis and T. You. "Updated global analysis of Higgs couplings". In: *JHEP* 06 (2013), p. 103. DOI: 10.1007/JHEP06(2013)103.

[17] H. Yukawa. "On the Interaction of Elementary Particles. I". In: *Progress of Theoretical Physics Supplement* 01 (1955), pp. 1–10. DOI: 10.1143/PTPS.1.1.

[18] C. Y. Chao. "Mixed Cosmic-Ray Showers at Sea Level". In: *Phys. Rev.* 75 (1949), pp. 581–590. DOI: 10.1103/PhysRev.75.581.

[19] W. B. Fretter. "Penetrating Showers". In: *Phys. Rev.* 76 (1949), pp. 511–517. DOI: 10.1103/PhysRev.76.511.

[20] H. W Lewis, J. R. Oppenheimer, and S. A. Wouthuysen. "The Multiple Production of Mesons". In: *Phys. Rev.* 73 (1948), pp. 127–140. DOI: 10.1103/PhysRev.73.127.

[21] R. Bjorklund *et al.* "High Energy Photons from Proton-Nucleon Collisions". In: *Phys. Rev.* 77 (1950), pp. 213–218. DOI: 10.1103/PhysRev.77.213.

[22] K. Kampf. "On Decays of Light Unflavoured Pseudoscalar Mesons". In: *Proceedings, 2nd International Workshop on Physics of fundamental Symmetries and Interactions at low energies and the precision frontier (PSI2010): PSI, Villigen, Switzerland, October 11-14, 2010*. arXiv: 1109.4370 [hep-ph].

[23] E. Minucci and T. Spadaro. "π^0 *neutral decays at NA62*". NA62 internal note NA62-16-07. URL: https://na62.web.cern.ch/na62/restricted/NotesDoc/NA62-16-07.pdf.

[24] T. Kalogeropoulos, J. Schechter, and J. Valle. "A test for neutrino masses". In: *Phys. Lett. B* 86 (1979), pp. 72–74. DOI: 10.1016/0370-2693(79)90623-3.

[25] P. Herczeg and C. M. Hoffman. "On the decays $\pi^0 \to \nu\nu'$". In: *Phys. Lett. B* 100 (1981), pp. 347–350. DOI: 10.1016/0370-2693(81)90102-7.

[26] L. Arnellos, W. J. Marciano, and Z. Parsa. "The decay $\pi^0 \to \nu\nu\gamma$". In: *Nuclear Physics B* 196 (1982), pp. 365–377. DOI: 10.1016/0550-3213(82)90495-3.

[27] W. J. Marciano and Z. Parsa. "Rare kaon decays with "missing energy"". In: *Phys. Rev. D* 53 (1996), R1–R5. DOI: 10.1103/PhysRevD.53.R1.

[28] R. Barate *et al.* (ALEPH Collaboration). "An Upper limit on the tau-neutrino mass from three-prong and five-prong tau decays". In: *Eur. Phys. J. C* 02 (1998), pp. 395–406. DOI: 10.1007/s100520050149.

[29] E. Fischbach *et al.* "Helicity-flipping neutral currents and $\gamma\gamma \to \nu\bar{\nu}$". In: *Phys. Rev. D* 13 (1976), pp. 1523–1526. DOI: 10.1103/PhysRevD.13.1523.

[30] E. Fischbach *et al.* "Implications of a nonzero neutrino mass for the process $\gamma\gamma \to \nu\bar{\nu}$". In: *Phys. Rev. D* 16 (1977), pp. 2377–2378. DOI: 10.1103/PhysRevD.16.2377.

[31] W. P. Lam and K. W. Ng. "Cosmological bound on Dirac neutrino mass via $\gamma\gamma \to \pi^0 \to \nu\bar{\nu}$". In: *Phys. Rev. D* 44 (1991), pp. 3345–3347. DOI: 10.1103/PhysRevD.44.3345.

[32] A. A. Natale. "Limit on $\Gamma(\pi^0 \to \nu\nu)$ from SN 1987A". In: *Phys. Lett. B* 258 (1991), pp. 227–230. DOI: 10.1016/0370-2693(91)91237-P.

[33] F. Arretche, A. A. Natale, and D. N. Voskresensky. "Medium effects in the pion-pole mechanism $[\gamma\gamma \to \pi^0 \to \nu_R\bar{\nu}_L(\nu_L\bar{\nu}_R)]$ of neutron star cooling". In: *Phys. Rev. C* 68 (2003), p. 035807. DOI: 10.1103/PhysRevC.68.035807.

[34] A. C. Kalloniatis, J. D. Carroll, and B. Y. Park. "Neutral pion decay into $\nu\bar{\nu}$ in dense Skyrmion matter". In: *Phys. Rev. D* 71 (2005), p. 114001. DOI: 10.1103/PhysRevD.71.114001.

[35] B. Kayser *et al.* "Are neutrons always left-handed?" In: *Phys. Lett. B* 52 (1974), pp. 385–388. DOI: 10.1016/0370-2693(74)90105-1.

[36] U. Camerini *et al.* "Experimental Search for Semileptonic Neutrino Neutral Currents". In: *Phys. Rev. Lett.* 23 (1969), pp. 326–329. DOI: 10.1103/PhysRevLett.23.326.

[37] J. H. Klems, R. H. Hildebrand, and R. Stiening. "Limits on the $K^+ \to \pi^+ + \nu + \overline{\nu}$ and $K^+ \to \pi^+ + n\gamma$ Decay Rates". In: *Phys. Rev. D* 04 (1971), pp. 66–80. DOI: 10.1103/PhysRevD.4.66.

[38] G. D. Cable *et al.* "Search for Rare K^+ Decays. II. $K^+ \to \pi^+\nu\bar{\nu}$". In: *Phys. Rev. D* 08 (1973), pp. 3807–3812. DOI: 10.1103/PhysRevD.8.3807.

[39] Y. Asano *et al.* "Search for a rare decay mode $K^+ \to \nu\bar{\nu}$ and axion". In: *Phys. Lett. B* 107 (1981), pp. 159–162. DOI: 10.1016/0370-2693(81)91172-2.

[40] M. S. Atiya *et al.* (E787 Collaboration). "Upper limit on the branching ratio for the decay $\pi^0 \to \nu\bar{\nu}$". In: *Phys. Rev. Lett.* 66 (1991), pp. 2189–2192. DOI: 10.1103/PhysRevLett.66.2189.

[41] A. V. Artamonov *et al.* (E949 Collaboration). "Upper limit on the branching ratio for the decay $\pi^0 \to \nu\bar{\nu}$". In: *Phys. Rev. D* 72 (2005), p. 091102. DOI: 10.1103/PhysRevD.72.091102.

[42] M. J. Dolan *et al.* "A taste of dark matter: flavour constraints on pseudoscalar mediators". In: *JHEP* 03 (2015), p. 171. DOI: 10.1007/JHEP03(2015)171. arXiv: 1412.5174v3 [hep-ph].

[43] J. Beacham *et al. Physics beyond colliders at CERN: beyond the Standard Model working group report*. 2019. DOI: 10.1088/1361-6471/ab4cd2. arXiv: 1901.09966 [hep-ex].

[44] J. C. Clarke, R. Foot, and R. R. Volkas. "Phenomenology of a very light scalar (100 MeV $< m_h <$ 10 GeV) mixing with the SM Higgs". In: *JHEP* 02 (2014). DOI: 10.1007/jhep02(2014)123.

[45] B. Batell, M. Pospelov, and A. Ritz. "Multilepton signatures of a hidden sector in rare B decays". In: *Phys. Rev. D* 83 (2011). DOI: 10.1103/physrevd.83.054005.

[46] G. Krnjaic. "Probing light thermal dark matter with a Higgs portal mediator". In: *Phys. Rev. D* 94 (2016). DOI: 10.1103/physrevd.94.073009.

[47] N. G. Deshpande, G. Eilam, and J. Jiang. "On the possibility of a new boson X^o (214 MeV) in $\Sigma \to p\mu^+\mu^-$". In: *Phys. Lett. B* 632 (2006), pp. 212–214. DOI: 10.1016/j.physletb.2005.10.050.

[48] R. D. Peccei and H. R. Quinn. "CP Conservation in the Presence of Pseudoparticles". In: *Phys. Rev. Lett.* 38 (1977), pp. 1440–1443. DOI: 10.1103/PhysRevLett.38.1440.

[49] S. Weinberg. "A New Light Boson?" In: *Phys. Rev. Lett.* 40 (1978), pp. 223–226. DOI: 10.1103/PhysRevLett.40.223.

[50] F. Wilczek. "Problem of Strong P and T Invariance in the Presence of Instantons". In: *Phys. Rev. Lett.* 40 (1978), pp. 279–282. DOI: 10.1103/PhysRevLett.40.279.

[51] E. Izaguirre, T. Lin, and B. Shuve. "Searching for Axionlike Particles in Flavor-Changing Neutral Current Processes". In: *Phys. Rev. Lett.* 118 (2017), p. 111802. DOI: 10.1103/PhysRevLett.118.111802.

[52] A. V. Artamonov *et al.* (E949 Collaboration). "Study of the decay $K^+ \to \pi^+\nu\bar{\nu}$ in the momentum region 140 $< P_\pi <$ 199 MeV/c". In: *Phys. Rev. D* 79 (2009), p. 092004. DOI: 10.1103/PhysRevD.79.092004.

[53] V. V. Anisimovsky *et al.* (E949 Collaboration). "Improved Measurement of the $K^+ \to \pi^+\nu\bar{\nu}$ Branching Ratio". In: *Phys. Rev. Lett.* 93 (2004), p. 031801. DOI: 10.1103/PhysRevLett.93.031801.

[54] T. Yamazaki *et al.* "Search for a Neutral Boson in a Two-Body Decay of $K^+ \to \pi^+ X^0$". In: *Phys. Rev. Lett.* 52 (1984), pp. 1089–1091. DOI: 10.1103/PhysRevLett.52.1089.

[55] R. Ammar *et al.* (CLEO Collaboration). "Search for the Familon via $B^\pm \to \pi^\pm X^0$, $B^\pm \to K^\pm X^0$, and $B^0 \to K^0_S X^0$ Decays". In: *Phys. Rev. Lett.* 87 (2001), p. 271801. DOI: 10.1103/PhysRevLett.87.271801.

[56] F. Bergsma *et al.* (CHARM Collaboration). "Search for axion-like particle production in 400 GeV proton-copper interactions". In: *Phys. Lett. B* 157 (1985), pp. 458–462. DOI: 10.1016/0370-2693(85)90400-9.

[57] A. Alavi-Harati *et al.* "Search for the Decay $K_L \to \pi^0\mu^+\mu^-$". In: *Phys. Rev. Lett.* 84 (2000), pp. 5279–5282. DOI: 10.1103/PhysRevLett.84.5279.

[58] R. Aaij *et al.* (LHCb Collaboration. "Differential branching fraction and angular analysis of the $B^+ \to K^+\mu^+\mu^-$ decay". In: *JHEP* 02 (2013), p. 105. DOI: 10.1007/JHEP02(2013)105.

[59] R. Aaij *et al.* (LHCb Collaboration). "Search for long-lived scalar particles in $B^+ \to K^+\chi\mu^+\mu^-$) decays". In: *Phys. Rev. D* 95 (2017), p. 071101. DOI: 10.1103/PhysRevD.95.071101.

[60] R. Aaij *et al.* (LHCb Collaboration). "Search for Hidden-Sector Bosons in $B^0 \to K^{*0}\mu^+\mu^-$ Decays". In: *Phys. Rev. Lett.* 115 (2015), p. 161802. DOI: 10.1103/PhysRevLett.115.161802.

[61] D. O'Connell, M. J. Ramsey-Musolf, and M. B. Wise. "Minimal extension of the standard model scalar sector". In: *Phys. Rev. D* 75 (2007). DOI: 10.1103/physrevd.75.037701.

[62] C. Bird *et al.* "Dark Matter Particle Production in $b \to s$ Transitions with Missing Energy". In: *Phys. Rev. Lett.* 93 (2004). DOI: 10.1103/physrevlett.93.201803.

[63] A. V. Artamonov *et al.* (E949 Collaboration). "New Measurement of the $K^+ \to \pi^+\nu\bar{\nu}$ Branching Ratio". In: *Phys. Rev. Lett.* 101 (2008), p. 191802. DOI: 10.1103/PhysRevLett.101.191802.

[64] M. W. Winkler. "Decay and detection of a light scalar boson mixing with the Higgs boson". In: *Phys. Rev. D* 99 (2019). DOI: 10.1103/physrevd.99.015018.

[65] J. R. Batley *et al.* (NA48/2 Collaboration). "Searches for lepton number violation and resonances in $K^\pm \to \pi\mu\mu$ decays". In: *Phys. Lett. B* 769 (2017), pp. 67–76. DOI: 10.1016/j.physletb.2017.03.029.

[66] J. T. Wei *et al.* (Belle Collaboration). "Measurement of the Differential Branching Fraction and Forward-Backward Asymmetry for $B \to K^{(*)}\ell^+\ell^-$". In: *Phys. Rev. Lett.* 103 (2009), p. 171801. DOI: 10.1103/PhysRevLett.103.171801.

[67] M. S. Turner. "Axions from SN1987A". In: *Phys. Rev. Lett.* 60 (1988), pp. 1797–1800. DOI: 10.1103/PhysRevLett.60.1797.

[68] J. A. Frieman, S. Dimopoulos, and M. S. Turner. "Axions and stars". In: *Phys. Rev. D* 36 (1987), pp. 2201–2210. DOI: 10.1103/PhysRevD.36.2201.

[69] A. Burrows, M. S. Turner, and R. P. Brinkmann. "Axions and SN 1987A". In: *Phys. Rev. D* 39 (1989), pp. 1020–1028. DOI: 10.1103/PhysRevD.39.1020.

[70] R. Essig *et al.* "Discovering new light states at neutrino experiments". In: *Phys. Rev. D* 82 (2010), p. 113008. DOI: 10.1103/PhysRevD.82.113008.

[71] G. D. Rochester and C. C. Butler. "Evidence for the Existence of New Unstable Elementary Particles". In: *Nature* 160 (1947), pp. 855–857. DOI: 10.1038/160855a0.

[72] M. Gell-Mann. "A schematic model of baryons and mesons". In: *Phys. Lett.* 08 (1964), pp. 214–215. DOI: 10.1016/S0031-9163(64)92001-3.

[73] N. Cabibbo. "Unitary Symmetry and Leptonic Decays". In: *Phys. Rev. Lett.* 10 (1963), pp. 531–533. DOI: 10.1103/PhysRevLett.10.531.

[74] S. L. Glashow, J. Iliopoulos, and L. Maiani. "Weak Interactions with Lepton-Hadron Symmetry". In: *Phys. Rev. D* 02 (1970), pp. 1285–1292. DOI: 10.1103/PhysRevD.2.1285.

[75] J. H. Christenson *et al.* "Evidence for the 2π Decay of the K_2^0 Meson". In: *Phys. Rev. Lett.* 13 (1964), pp. 138–140. DOI: 10.1103/PhysRevLett.13.138.

[76] M. Kobayashi and T. Maskawa. "CP-Violation in the Renormalizable Theory of Weak Interaction". In: *Progress of Theoretical Physics* 49 (1973), pp. 652–657. DOI: 10.1143/PTP.49.652.

[77] KOTO Experiment. URL: http://koto.kek.jp.

[78] F. Ambrosino *et al.* (KLEVER Project). *"KLEVER: An experiment to measure* BR($K_L \to \pi^0\nu\bar{\nu}$) *at the CERN SPS"*. KLEVER-PUB-18-02. arXiv: 1901.03099 [hep-ex].

[79] KAON 2019, International Conference on Kaon Physics. Perugia (Italy), 10–13 September 2019. URL: https://indico.cern.ch/event/769729/.

[80] H. Burkhardt *et al.* (NA31 Collaboration). "The beam and detector for a high-precision measurement of CP violation in neutral-kaon decays". In: *Nucl. Inst. & Meth. in Phys. Res. A* 268 (1988), pp. 116–143. DOI: 10.1016/0168-9002(88)90598-0.

[81] V. Fanti *et al.* (NA48 Collaboration). "The beam and detector for the NA48 neutral kaon CP violation experiment at CERN". In: *Nucl. Inst. & Meth. in Phys. Res. A* 574.3 (2007), pp. 433–471. DOI: 10.1016/j.nima.2007.01.178.

[82] J. R. Batley *et al.* (NA48 Collaboration). "A Precision measurement of direct CP violation in the decay of neutral kaons into two pions". In: *Phys. Lett. B* 544 (2002), pp. 97–112. DOI: 10.1016/S0370-2693(02)02476-0.

[83] J. R. Batley *et al.* (NA48/2 Collaboration). "Search for direct CP violating charge asymmetries in $K^\pm \to \pi^\pm\pi^+\pi^-$ and $K^\pm \to \pi^\pm\pi^0\pi^0$ decays". In: *Eur. Phys. J. C* 52 (2007), pp. 875–891. DOI: 10.1140/epjc/s10052-007-0456-7.

[84] G. Anelli *et al.* (NA62 Collaboration). *Proposal to measure the rare decay $K^+ \to \pi^+\nu\bar{\nu}$ at the CERN SPS*. Tech. rep. CERN-SPSC-2005-013. SPSC-P-326. Geneva: CERN, 2005. URL: http://cds.cern.ch/record/832885.

[85] C. Lazzeroni *et al.* (NA62 Collaboration). "Test of lepton flavour universality in $K^+ \to \ell^+\nu$ decays". In: *Phys. Lett. B* 698 (2011), pp. 105–114. DOI: 10.1016/j.physletb.2011.02.064.

[86] E. Cortina Gil *et al.* (NA62 Collaboration). "Searches for lepton number violating K^+ decays". In: *Phys. Lett. B* 797 (2019), p. 134794. DOI: https://doi.org/10.1016/j.physletb.2019.07.041.

[87] E. Cortina Gil *et al.* (NA62 Collaboration). "Search for heavy neutral lepton production in K^+ decays". In: *Phys. Lett. B* 778 (2018), pp. 137–145. DOI: https://doi.org/10.1016/j.physletb.2018.01.031.

[88] E. Cortina Gil *et al.* (NA62 Collaboration). "Search for production of an invisible dark photon in π^0 decays". In: *JHEP* 05 (2019), p. 182. DOI: 10.1007/JHEP05(2019)182.

[89] E. Cortina Gil *et al.* (NA62 Collaboration). "First search for $K^+ \to \pi^+\nu\bar{\nu}$ using the decay-in-flight technique". In: *Phys. Lett. B* 791 (2018), pp. 156–166. DOI: 10.1016/j.physletb.2019.01.067.

[90] E. Cortina Gil *et al.* (NA62 Collaboration). "Search for heavy neutral lepton production in K^+ decays to positrons". In: *Phys. Lett. B* 807 (2020), p. 135599. DOI: 10.1016/j.physletb.2020.135599.

[91] A. J. Buras *et al.* "$K^+ \to \pi^+\nu\bar{\nu}$ and $K_L \to \pi^0\nu\bar{\nu}$ in the Standard Model: status and perspectives". In: *JHEP* 11 (2015), p. 33. DOI: 10.1007/JHEP11(2015)033.

[92] F. Mescia and C. Smith. "Improved estimates of rare K decay matrix-elements from $K_{\ell 3}$ decays". In: *Phys. Rev. D* 76 (2007), p. 034017. DOI: 10.1103/PhysRevD.76.034017.

[93] A. J. Buras, D. Buttazzo, and R. Knegjens. "$K \to \pi\nu\bar{\nu}$ and ε'/ε in simplified new physics models". In: *JHEP* 11 (2015), p. 166. DOI: 10.1007/JHEP11(2015)166.

[94] M. Blanke, A. J. Buras, and S. Recksiegel. "Quark flavour observables in the Littlest Higgs model with T-parity after LHC Run 1". In: *Eur. Phys. J. C* 76 (2016), p. 182. DOI: 10.1140/epjc/s10052-016-4019-7.

[95] M. Blanke *et al.* "Rare K and B Decays in a warped extra dimension with custodial protection". In: *JHEP* 03 (2009), pp. 108–108. DOI: 10.1088/1126-6708/2009/03/108.

[96] T. Blazek and P. Matak. "Left-left squark mixing, $K^+ \to \pi^+\nu\bar{\nu}$ and minimal supersymmetry with large $\tan\beta$". In: *International Journal of Modern Physics A* 29 (2014), p. 1450162. DOI: 10.1142/S0217751X14501620.

[97] G. Isidori *et al.* "Exploring the flavour structure of the MSSM with rare K decays". In: *JHEP* 08 (2006), pp. 064–064. DOI: 10.1088/1126-6708/2006/08/064.

[98] T. Morimitsu and K. Yamamoto. "Probing SUSY with 10 TeV stop mass in rare decays and CP violation of kaon". In: *Progress of Theoretical and Experimental Physics* 12 (2016). 123B02. DOI: 10.1093/ptep/ptw160.

[99] M. Bordone *et al.* "Probing lepton-flavour universality with $K \to \pi\nu\bar{\nu}$ decays". In: *Eur. Phys. J. C* 77 (2017), p. 618. DOI: 10.1140/epjc/s10052-017-5202-1.

[100] S. Fajfer *et al.* "Footprints of leptoquarks: from $R_{K^{(*)}}$ to $K \to \pi\nu\bar{\nu}$". In: *Eur. Phys. J. C* 78 (2018), p. 275. DOI: 10.1140/epjc/s10052-018-5757-5.

[101] S. Adler *et al.* "Measurement of the $K^+ \to \pi^+\nu\bar{\nu}$ branching ratio". In: *Phys. Rev. D* 77 (2008), p. 052003. DOI: 10.1103/PhysRevD.77.052003.

[102] G. Ruggiero. *"New Result on $K^+ \to \pi^+\nu\bar{\nu}$ from the NA62 Experiment"*. Talk at conference KAON 2019, Perugia (Italy), September 2019. URL: https://indico.cern.ch/event/769729/contributions/3510938/attachments/1905346/3146619/kaon2019_ruggiero_final.pdf.

[103] A. L. Read. "Presentation of search results: the CL_s technique". In: *J. Phys. G* 28 (2002), pp. 2693–2704. DOI: 10.1088/0954-3899/28/10/313.

[104] E. Cortina Gil *et al.* (NA62 Collaboration). "The Beam and detector of the NA62 experiment at CERN". In: *JINST* 12 (2017), P05025. DOI: 10.1088/1748-0221/12/05/P05025.

[105] N. Doble and G. Brianti. *NAHIF: The SPS North Area High Intensity Facility*. Tech. rep. CERN-SPS-EA-77-2. Geneva: CERN, 1977.

[106] B. Döbrich (for the NA62 Collaboration). "Dark Sectors at fixed targets: The example of NA62". In: *Frascati Phys. Ser.* 66 (2018), pp. 312–327. arXiv: 1807.10170 [hep-ex].

[107] F. Anghinolfi *et al.* "NINO: An ultra-fast and low-power front-end amplifier/discriminator ASIC designed for the multigap resistive plate chamber". In: *Nucl. Inst. & Meth. in Phys. Res. A* 533 (2004), pp. 183–187. DOI: 10.1016/j.nima.2004.07.024.

[108] J. R. Fry *et al.* "Precision magnetic field mapping for CERN experiment NA62". In: *J. Phys. G* 43 (2016), p. 125004. DOI: 10.1088/0954-3899/43/12/125004.

[109] Picture provided by R. Wanke.

[110] R. Aliberti. "Particle Identification with Calorimeters for the Measurement of the Rare Decay $K^+ \to \pi^+ \nu\bar{\nu}$ at NA62". PhD Thesis. Johannes Gutenberg Universität Mainz, 2019.

[111] Picture provided by M. B. Brunetti.

[112] F. Ambrosino *et al.* "A Prototype large-angle photon veto detector for the P326 experiment at CERN". In: *Proceedings, 2007 IEEE Nuclear Science Symposium and Medical Imaging Conference (NSS/MIC 2007): Honolulu, Hawaii, October 28-November 3, 2007*. Vol. 1. 2007, pp. 57–64. DOI: 10.1109/NSSMIC.2007.4436288.

[113] A. Antonelli *et al.* "Study of the performance of the NA62 small-angle calorimeter at the DAΦNE Linac". In: *Nucl. Inst. & Meth. in Phys. Res. A* 877 (2018), pp. 178–182. DOI: 10.1016/j.nima.2017.09.065.

[114] A. Ceccucci *et al.* (NA62 Collaboration). *NA62/P-326 Status Report*. Tech. rep. CERN-SPSC-2007-035. SPSC-M-760. 2007. URL: http://cds.cern.ch/record/1070584.

[115] NA62 Collaboration. Tech. rep. Technical Design Document. CERN: NA62 Collaboration, 2010. URL: https://na62.web.cern.ch/na62/Documents/TD_Full_doc_v10.pdf.

[116] K. Ahmet *et al.* (OPAL Collaboration). "The OPAL detector at LEP". In: *Nucl. Inst. & Meth. in Phys. Res. A* 305 (1991), pp. 275–319. DOI: 10.1016/0168-9002(91)90547-4.

[117] F. Ambrosino *et al.* "The Large-Angle Photon Veto System for the NA62 Experiment at CERN". In: *Proceedings, 2011 IEEE Nuclear Science Symposium and Medical Imaging Conference (NSS/MIC 2011): Valencia, Spain, October 23-29, 2011*, pp. 1159–1166. DOI: 10.1109/NSSMIC.2011.6154594.

[118] A. Antonelli *et al.* "Performance of the NA62 LAV front-end electronics". In: *JINST* 08 (2013), p. C01020. DOI: 10.1088/1748-0221/8/01/C01020.

[119] Picture from NA62 shifer training website. URL: https://na62st.web.cern.ch/na62st/.

[120] B. G. Taylor (RD12 Collaboration). "TTC distribution for LHC detectors". In: *IEEE Trans. Nucl. Sci.* 45 (1998), pp. 821–828. DOI: 10.1109/23.682644.

[121] URL: http://alicetrigger.web.cern.ch/alicetrigger/alice_main.htm.

[122] B. Angelucci *et al.* "TEL62: an integrated trigger and data acquisition board". In: *JINST* 07 (2012), pp. C02046–C02046. DOI: 10.1088/1748-0221/7/02/c02046.

[123] J. Christiansen. High Performance Time to Digital Converter, CERN/EP-MIC, March 2004. URL: http://tdc.web.cern.ch/TDC/hptdc/docs/hptdc_manual_ver2.2.pdf.

[124] D. Moraes *et al. "The CARIOCA Front End Chip for the LHCb muon chambers"*. CERN-LHCb-2003-009 (2003).

[125] P. Lichard *et al.* "Performance evaluation of multiple (32 channels) sub-nanosecond TDC implemented in low-cost FPGA". In: *JINST* 09 (2014), pp. C03013–C03013. DOI: 10.1088/1748-0221/9/03/c03013.

[126] A. Kluge *et al.* "The TDCpix readout ASIC: A 75 ps resolution timing front-end for the NA62 Gigatracker hybrid pixel detector". In: *Nucl. Inst. & Meth. in Phys. Res. A* 732 (2013), pp. 511–514. DOI: 10.1016/j.nima.2013.06.089.

[127] A. Ceccucci *et al.* "The NA62 Liquid Krypton calorimeter readout module". In: *JINST* 06 (2011), pp. C12017–C12017. DOI: 10.1088/1748-0221/6/12/c12017.

[128] D. Soldi. "The FPGA-based first level trigger for the NA62 Experiment at CERN SPS". PhD Thesis. Università degli Studi di Torino, 2017.

[129] V. Bonaiuto *et al.* "Status of the NA62 liquid krypton electromagnetic calorimeter Level 0 trigger processor". In: *JINST* 08 (2013), p. C02054. DOI: 10.1088/1748-0221/8/02/C02054.

[130] URL: http://information-technology.web.cern.ch/services/castor-service.

[131] N. Lurkin (for the NA62 Collaboration). "The Run Control system of the NA62 experiment". In: *Journal of Physics: Conference Series* (2017), p. 012045. DOI: 10.1088/1742-6596/800/1/012045.

[132] ETM Controls, *SIMATIC WinCC Open Architecture (previously PVSS)* SCADA software from ETM (Siemens subsidiary). http://www.etm.at.

[133] P. Golonka *et al.* "Detector and Run Control Systems for the NA62 Fixed-Target Experiment at CERN". In: *Proocedings, 2015 ICALEPCS: Melbourne, Australia*. DOI: 10.18429/JACoW-ICALEPCS-MOPGF020.

[134] The NA62 Software Framework Documentation. URL: https://na62-sw.web.cern.ch.

[135] R. Brun and F. Rademakers. "ROOT - An Object Oriented Data Analysis Framework". In: *Nucl. Inst. & Meth. in Phys. Res. A* 389 (1997), pp. 81–86. DOI: 10.1016/S0168-9002(97)00048-X. URL: http://root.cern.ch/.

[136] URL: https://git-scm.com.

[137] K. L. Brown and F. C. Iselin. *DECAY TURTLE (Trace Unlimted Rays Through Lumped Elements): a computer program for simulating charged-particle beam transport systems, including decay calculations*. CERN Yellow Reports: Monographs. Geneva: CERN, 1974. DOI: 10.5170/CERN-1974-002.

[138] J. Allison *et al.* "Recent developments in Geant4". In: *Nucl. Inst. & Meth. in Phys. Res. A* 835 (2016), pp. 186–225. DOI: 10.1016/j.nima.2016.06.125.

[139] NA62 GRID. URL: http://na62.gla.ac.uk/index.php?task=production.

[140] NA62 Monte Carlo Twiki Page. URL: https://twiki.cern.ch/twiki/bin/view/NA62/MonteCarloSamples.

[141] F. E. Low. "Bremsstrahlung of Very Low-Energy Quanta in Elementary Particle Collisions". In: *Phys. Rev.* 110 (1958), pp. 974–977. DOI: 10.1103/PhysRev.110.974.

[142] C. Gatti. "Monte Carlo simulation for radiative kaon decays". In: *Eur. Phys. J. C* 45 (2006), pp. 417–420. DOI: 10.1140/epjc/s2005-02435-2.

[143] URL: http://information-technology.web.cern.ch/services/eos-service.

[144] H. Danielsson. *"Garfield Simulation of the NA62 STRAW Tracker"*. NA62 internal note NA62-14-12. URL: https://na62.web.cern.ch/na62/restricted/NotesDoc/NA62-14-12.pdf.

[145] R. E. Kalman. "A New Approach to Linear Filtering and Prediction Problems". In: *Journal of Fluids Engineering* 82 (1960), pp. 35–45. DOI: 10.1115/1.3662552.

[146] G. Ruggiero. *"Straw Spectrometer Reconstruction"*. NA62 internal note NA62-12-01. URL: https://na62.web.cern.ch/na62/restricted/NotesDoc/NoteNA62-12-01.pdf.

[147] G. Unal (NA48-98-01) redistributed by R. Fantechi as NA62 internal note NA62-15-02. *"Reconstruction program for LKr"*. URL: https://na62.web.cern.ch/na62/restricted/NotesDoc/NA62_15_02.pdf.

[148] M. Perrin-Terrin. NA62 Analysis Meeting, June 2017. URL: https://indico.cern.ch/event/649875/contributions/2643714/attachments/1485568/2306513/perrin-terrin$_$13-06-2017.pdf.

[149] A. Sturgess. NA62 Analysis Meeting, March 2016. URL: https://indico.cern.ch/event/508889/contributions/2021722/attachments/1244098/1831245/andyalphabeta.pdf.

[150] U. Müller *et al.* "Particle identification with the RICH detector in experiment WA89 at CERN". In: *Nucl. Inst. & Meth. in Phys. Res. A* 343 (1994), pp. 279–283. DOI: 10.1016/0168-9002(94)90565-7.

[151] G. Ruggiero. NA62 Analysis Meeting, May 2017. URL: https://indico.cern.ch/event/641378.

[152] G. Ruggiero. NA62 Analysis Meeting, September 2019. URL: https://indico.cern.ch/event/844179/contributions/3544398/attachments/1898748/3133434/PinunuWG_28_08_2019_II.pdf.

[153] M. Corvino. NA62 Analysis Meeting, March 2019. URL: https://indico.cern.ch/event/803305/contributions/3340350/attachments/1807044/2950100/CorvinoPiNuNu-06.03.2019.pdf.

[154] R. Marchevski and G. Ruggiero. *"$K^+ \to \pi^+ \nu\bar{\nu}$ Analysis"*. NA62 internal note NA62-18-05. URL: https://na62.web.cern.ch/na62/restricted/NotesDoc/NA62-18-05.pdf.

[155] T. Spadaro *et al.* NA62 Collaboration Meeting, September 2018. URL: https://indico.cern.ch/event/703563/sessions/276807/attachments/1708891/2754350/LAVEffiStudies_final.pdf.

[156] G. J. Feldman and R. D. Cousins. "Unified approach to the classical statistical analysis of small signals". In: *Phys. Rev. D* 57 (1998), pp. 3873–3889. DOI: 10.1103/PhysRevD.57.3873.

[157] M. Mirra and T. Spadaro. *"Search for invisible dark photons at NA62"*. NA62 internal note NA62-18-08. URL: https://na62.web.cern.ch/na62/restricted/NotesDoc/NA62-18-08_rev2.pdf.

[158] J. D. Good. "Pion Spectrum in Radiative K_π^+ Decay". In: *Phys. Rev.* 113 (1959), pp. 352–355. DOI: 10.1103/PhysRev.113.352.

[159] N. Christ. "Possible CP Violation in $K^\pm \to \pi^\pm \pi^0 \gamma$". In: *Phys. Rev.* 159 (1967), pp. 1292–1296. DOI: 10.1103/PhysRev.159.1292.

[160] M. McGuigan and A. I. Sanda. "$K \to \pi\pi\gamma$ in the six-quark model". In: *Phys. Rev. D* 36 (1987), pp. 1413–1421. DOI: 10.1103/PhysRevD.36.1413.

[161] R. Marchevski. NA62 Analysis Meeting, September 2019. URL: https://indico.cern.ch/event/844179/contributions/3544397/attachments/1898746/3133431/WeeklyMeeting_28_08_2019.pdf.

[162] Private discussion with Matthew Moulson and Tommaso Spadaro.

[163] L. Peruzzo, S. Martellotti, and T. Spadaro. NA62 Analysis Meeting, February 2018. URL: https://indico.cern.ch/event/703625/contributions/2888904/attachments/1596867/2529872/PhysicsPeruzzo.pdf.

[164] M. Corvino. *"Optimization of the π^0 rejection and random veto for $K^+ \to \pi^+ \nu\bar{\nu}$ analysis"*. NA62 internal note NA62-19-12. URL: https://na62.web.cern.ch/na62/restricted/NotesDoc/NA62-19-12%20.pdf.

[165] R. Volpe. *"Search for $K^+ \to \pi^+ X$ reinterpreting $K^+ \to \pi^+ \nu\bar{\nu}$ 2017 data analysis"*. NA62 internal note NA62-20-08. URL: https://na62.web.cern.ch/restricted/NotesDoc/NA62-20-08.pdf.

[166] URL: https://root.cern.ch/doc/master/classTGraphSmooth.html.